



HAL
open science

Modelling challenges of stationary combustion in inert porous media

Pierre-Alexandre Masset

► **To cite this version:**

Pierre-Alexandre Masset. Modelling challenges of stationary combustion in inert porous media. Other. Institut National Polytechnique de Toulouse - INPT, 2022. English. NNT: 2022INPT0060. tel-04247408

HAL Id: tel-04247408

<https://theses.hal.science/tel-04247408>

Submitted on 18 Oct 2023

HAL is a multi-disciplinary open access archive for the deposit and dissemination of scientific research documents, whether they are published or not. The documents may come from teaching and research institutions in France or abroad, or from public or private research centers.

L'archive ouverte pluridisciplinaire **HAL**, est destinée au dépôt et à la diffusion de documents scientifiques de niveau recherche, publiés ou non, émanant des établissements d'enseignement et de recherche français ou étrangers, des laboratoires publics ou privés.



Université
de Toulouse

THÈSE

En vue de l'obtention du

DOCTORAT DE L'UNIVERSITÉ DE TOULOUSE

Délivré par :

Institut National Polytechnique de Toulouse (Toulouse INP)

Discipline ou spécialité :

Energétique et Transferts

Présentée et soutenue par :

M. PIERRE-ALEXANDRE MASSET

le mardi 20 septembre 2022

Titre :

Modelling challenges of stationary combustion in inert porous media

Ecole doctorale :

Mécanique, Energétique, Génie civil, Procédés (MEGeP)

Unité de recherche :

Institut de Mécanique des Fluides de Toulouse (IMFT)

Directeur(s) de Thèse :

M. LAURENT SELLE

M. THIERRY POINSOT

Rapporteurs :

MME CARMEN JIMENEZ, CIEMAT MADRID

M. RONAN VICQUELIN, CENTRALESUPELEC GIF SUR YVETTE

Membre(s) du jury :

MME PASCALE DOMINGO, CORIA, Président

M. CHRISTOPHE ALMARCHA, IRPHE MARSEILLE, Membre

M. LAURENT SELLE, CNRS TOULOUSE, Membre

M. THIERRY POINSOT, CNRS TOULOUSE, Membre

Modelling challenges of stationary combustion in inert porous media

Abstract

Thanks to strong heat recirculation, submerged combustion within porous media presents unique technological features such as broadened flammability limits and extended power range. The associated possibility to burn ultra-lean mixtures with minimal CO/NO_x emissions makes porous media combustion a potential alternative in the industry, for instance in domestic heat generation or clean aviation where low pollutant emissions and robust operability are of paramount importance. However, even though this combustion mode has been studied for decades, there remains many open questions regarding the intertwined flame structure and the validity of associated low-order modelling. To date, volume-averaged models are mostly based upon *ad hoc* hypotheses and still present large discrepancies with experiments. Aiming to challenge and strengthen these models, the present work presents analytical and numerical studies of the volume-averaged equations, followed by 3D direct pore-level simulations of methane-air and hydrogen-air combustion.

Chapters 1 and 2 provide a critical review of concepts associated to flows and flames within porous media, with a focus on non-adiabatic combustion and macroscopic effective characterization. A classification of gaseous flames in terms of the thermal Péclet number is proposed, and the upscaling procedure on the pointwise equations is presented. Chapter 3 presents asymptotic results based on the volume-averaged equations, and the proposed theoretical framework unveils the first fully-explicit formulae for flame speed in infinite and finite-length porous burners. Multi-layered burners are also considered theoretically for the first time, and the important concept of contact resistance between two stacked porous plates is underlined. Chapter 4 proposes a general classification of porous media combustion in three distinct regimes for increasing inter-phase heat transfer, only based on two reduced parameters, in order to reconcile the literature frameworks of local thermal equilibrium (LTE) and non-equilibrium (LTNE).

Chapter 5, 6 and 7 present 3D pore-level direct numerical simulations of flames within porous media using complex kinetics, for various structural topologies and pore sizes. As a major technical hurdle encountered during the thesis, the meshing workflow from X-ray tomography to conformal computational mesh is given for practical use in the community. These DNS unveil the internal flame structure of methane-air and hydrogen-air flames within typical porous burners, and it is shown that when the pore size is larger than the flame thickness, sharp and locally-anchored flame fronts are observed. These local discontinuities related to the strongly non-linear reaction rates are shown to be in direct violation of the classical volume-averaged hypotheses. This demonstrates that new volume-averaged models are required, and accordingly a closure for reaction rates based upon phenomenology and observations in the 3D DNS is proposed. Eventually, the pore-level specificities of hydrogen combustion at pore scale are described.

Keywords: porous media combustion, volume-averaged models, heat recirculation, asymptotic analysis, 3D coupled gas/solid pore-level simulations.



Remerciements

Un travail de thèse n'est pas une aventure solitaire. Qu'aurais-je compris, entrepris et accompli sans le reste de la communauté scientifique, et sans le soutien indéfectible de mes proches et de mes amis ? Ces quelques remerciements resteront incomensurables à ce que j'ai reçu.

Mes premières pensées se tournent vers mes deux directeurs de thèse Laurent Selle et Thierry Poinot. Sans Thierry, pas de stage LBM au CERFACS, pas de thèse à l'IMFT. Merci d'avoir cru en moi, et d'avoir su m'orienter vers le passionnant sujet de la combustion. Et que dire de Laurent, qui malgré la naissance d'Elisa, a su sacrifier tant d'espace mental sous la douche pour répondre à mes questionnements métaphysiques ? Le moins qu'on puisse dire est que je fus un thésard fatiguant - mais j'espère que tu t'es bien marré et que mes futurs encadrants auront ton humour et ta sympathie. Certes, j'attends toujours la plaque de chocolat promise depuis Noël 2020, mais ne serait-ce pas là un apprentissage sensé subtil pour guérir mon impatience ? Aussi, comment ne pas remercier Thierry Schuller, l'alsacien souriant tout aussi insomniaque que moi ? Ton soutien, tes idées et tes encouragements m'auront été d'une aide précieuse.

Concernant la chair à canon (amis doctorants), je ne sais pas si j'aurais tenu ces trois années de thèse sans vous. Comment rester éveillé sans Titouan pour vous rappeler toutes les quinze minutes d'aller lire le dernier ouvrage d'Emmanuel Todd ou de Frédéric Lordon ? Si mes cauchemars sont remplis d'équations mal équilibrées, les siens sont à coup sûr tapissés de capitalisme libéral. Comment garder l'espoir que l'humanité est finalement belle, sans la virilité presque indécente d'Andrea, qui en plus d'être beau gosse, bosse plus qu'un japonais en période de rush ? Nous avons eu la chance de te connaître - mais ce n'est rien comparé à la chance de Monica ! Je pense ensuite au troisième homme des débuts de SCIROCCO : merci Sylvain de m'avoir appris ce qu'était un tournevis ! Tes traits de génie pour les manip m'impressionneront toujours. Je remercie également François, la constante universelle du bureau Nougaro ! Je n'oublie pas l'honorable Victor, coureur cycliste infatigable et une des personnes les mieux intentionnées que je connaisse : j'espère que nous resterons proches sur le long terme.

Je remercie également les nouvelles et encore optimistes recrues. Antoine et Hervé, les deux acolytes aux photos de soirées... intéressantes. Mon ami Hugo, excellent pax, qui escalade la monture des portes du laboratoire d'une main comme pour me rappeler que je dois encore progresser pour les noires d'Arkose. Gillien et Enrique pour leur sympathie au quotidien : vous avez su revigorer la démographie déclinante de notre bureau. Francesco - expert italien en informatique des souris. Mais aussi Clément, Mariano, Tarik, Pablo, Enrica, Benoît, Ilyass... et bien d'autres que j'oublie. Je pense aussi à Bastien, feu mon colocataire, qui va bientôt finir d'enregistrer le taux horaire le plus élevé de France et de Monaco. Son amitié et nos discussions restent un soutien indélébile.

Enfin, je remercie ma famille. Mes deux parents, Marie-Claude et Jacques-Olivier, qui sont le dénominateur commun de tous mes succès. L'humilité impose que je m'incline devant leur constance, amour et dévotion. Je remercie mon frère Thomas-Xavier, qui est venu nous faire un petit coucou pour un stage M1, et Anne-Sophie, qui me remontait le moral avec de délicieuses vidéos de mon neveu grandissant. J'espère avoir plus de temps pour lui après ma thèse.

A tous, je vous souhaite une belle carrière dans un domaine qui fera sens pour vous, qui vous donnera l'envie de vous lever le matin et qui vous rendra fiers. N'oubliez jamais que lorsque la maison brûle, nous avons besoin de pompiers et d'eau.

Enfin, merci à toi, Maeva. Tu sais ce que je te dois.

Contents

Abstract	i
Remerciements	iii
Nomenclature	x
1. Introduction	1
1.1. Current societal context	2
1.1.1. High constraints on energy	2
1.1.2. Combustion, economy and global warming	2
1.1.3. Hydrogen potential to carbon-neutral targets	3
1.1.4. Why studying porous media combustion?	5
1.1.5. Scope of the thesis	5
1.2. Concepts of porous media combustion	6
1.2.1. Small-scale combustion systems	6
1.2.2. Advantages/drawbacks of small-scale combustors	7
1.2.3. Principle of heat recirculation	7
1.2.4. Applications of heat-recirculating burners	9
1.2.4.1. Radiant heating	9
1.2.4.2. Ultra-lean or ultra-rich combustion	9
1.2.4.3. Low-emission burners	10
1.2.4.4. Other applications	12
1.2.5. Materials suitable for porous media combustion	12
1.2.6. Non-adiabaticities in premixed laminar combustion	13
1.2.6.1. Adiabatic laminar flames	13
1.2.6.2. Laminar flame speed	14
1.2.6.3. Heat loss/gain and multiple flame speeds for laminar flames	15
1.2.6.4. 1D structure of a flame inside a porous burner	17
1.2.6.5. Heat recirculation, multiple flame speeds and solutions	17
1.2.6.6. Sub-adiabatic combustion	18
1.2.7. Stabilization mechanisms in porous burners	19
1.2.7.1. Hydrodynamic vs. thermal stabilization	19
1.2.7.2. Stability of the solutions	20
1.2.7.3. Burner design variations	20
1.3. Motivations and objectives of the thesis	23
1.4. Outline of the manuscript	24
1.5. Publications during the thesis	26
1.5.1. Works related to porous media combustion	26
1.5.2. Other works	26
2. From micro to macroscopic scale	27
2.1. Flow, flames and heat transfer within porous media	28
2.1.1. Physical phenomena at micro and macroscales	28
2.1.2. Flow regimes	29

2.1.3.	Pressure drop	29
2.1.4.	Turbulence	30
2.1.5.	Interphase heat exchange	32
2.1.6.	Dispersion in the gas phase	33
2.1.6.1.	Phenomenology of dispersion	33
2.1.6.2.	Case $Pe_{p,\psi} \ll 1$	35
2.1.6.3.	Case $Pe_{p,\psi} \gg 1$	35
2.1.6.4.	Interpretation of dispersion at the microscale	36
2.1.7.	Influence of the pore diameter	36
2.1.8.	Summary of reduced parameters	38
2.1.9.	Heat transfer through the solid matrix	39
2.1.9.1.	Heat conduction - effective conductivity	39
2.1.9.2.	Radiation	40
2.2.	Modelling equations and upscaling hypotheses	41
2.2.1.	Classical stationary volume-averaged equations	41
2.2.2.	Pointwise governing equations	42
2.2.2.1.	Equations in the gas phase - AVBP	42
2.2.2.2.	Stationary version with temperature	43
2.2.2.3.	Stationary isobaric version for low Mach numbers	43
2.2.2.4.	Heat equation in the solid phase - AVTP	44
2.2.2.5.	Boundary conditions	44
2.2.3.	Volume-averaging	44
2.2.3.1.	Notations	44
2.2.3.2.	Deviations from the average	45
2.2.3.3.	Spatial averaging theorem	46
2.2.3.4.	Volume-averaging in the solid phase	47
2.2.3.5.	Volume-averaging in the gas phase	48
2.2.4.	Conclusions of the chapter	50
2.A.	Geometrical proof of the spatial averaging theorem	51
2.B.	Deviation terms for products of N quantities	52
3.	Asymptotic analysis of flames in infinite, finite and multi-staged porous burners	53
3.1.	Chapter introduction	54
3.2.	Fully explicit formulae for flame speed in infinite porous media	57
3.2.1.	Configuration	57
3.2.2.	Modelling assumptions and decoupled methodology	57
3.2.3.	Thermal problem \mathcal{T}	58
3.2.3.1.	Equations and boundary conditions	58
3.2.3.2.	Dimensionless equations	58
3.2.3.3.	Numerical solutions of the thermal problem	61
3.2.4.	Length scales separation and approximation of η_{rec}	63
3.2.4.1.	Length scales separation	63
3.2.4.2.	Approximation of η_{rec}	63
3.2.5.	Chemical problem - model closure	64
3.2.5.1.	Single-step kinetics	64
3.2.5.2.	Power law approximation	66
3.2.6.	Discussion and validation	67
3.3.	Effects of flame wrinkling	68
3.3.1.	Taking into account flame wrinkling	68

3.3.2.	Theoretical influence of the wrinkling factor Γ_w	68
3.3.2.1.	Single-step Arrhenius	69
3.3.2.2.	Power law	69
3.3.2.3.	Conclusion on flame wrinkling	70
3.4.	Effects of finite length & multi-staged burners	70
3.4.1.	Single-staged burner: problem formulation	70
3.4.2.	Influence of flame position	73
3.4.3.	Universal behavior of finite-length effects in the decoupled regime	74
3.4.4.	Multi-staged burners: problem formulation	75
3.4.5.	Boundary conditions	76
3.4.6.	Interest of the present modelling for stability discussions	76
3.4.7.	Influence of the thermal resistance	77
3.4.8.	Porosity step	79
3.4.9.	Interphase heat transfer & solid conductivity step	79
3.4.10.	A “realistic” two-step burner?	80
3.4.11.	Case $N \rightarrow \infty$: topology gradation	81
3.5.	Conclusions of the chapter	83
3.A.	Gas temperature continuity	84
3.B.	Maximum of gas temperature at $x = 0$	84
3.C.	Characteristic polynomial	86
3.D.	Description of the coupled solver	87
3.E.	Matrix for resolution of the single-layer finite porous	88
4.	Combustion regimes of the 1D volume-averaged equations	89
4.1.	Chapter introduction	90
4.2.	Methodology	91
4.2.1.	Simplified analytical model (AM)	92
4.2.2.	Dimensionless parametrization	93
4.2.3.	1D numerical simulations (SIM)	94
4.2.4.	Relations between (AM) and (SIM)	94
4.2.4.1.	Choice of constant properties for (AM)	94
4.2.5.	Exploration of the parametric space	95
4.2.5.1.	Definition of the parametric space	95
4.2.5.2.	Numerical strategy (SIM)	95
4.2.5.3.	Baseline case	95
4.3.	From decoupled to hyperdiffusive regimes	95
4.3.1.	General description of the regimes	95
4.3.1.1.	Decoupled regime - Figure 4.2(b) and (f)	96
4.3.1.2.	Hyperdiffusive regime - Figure 4.2(d) and (h)	97
4.3.1.3.	Intermediate regime - Figure 4.2(c) and (g)	97
4.3.1.4.	Summary of observations	97
4.3.2.	Transitions between the regimes	97
4.3.2.1.	Classification using speed-up convergence and preheating	97
4.3.2.2.	Classification using an equivalent resistive model	98
4.3.2.3.	Comparison between the two classifications	100
4.4.	Detailed structure of the various regimes	101
4.4.1.	Porous media as Lewis-changing devices	101
4.4.1.1.	Equivalent gaseous equation	101
4.4.1.2.	Effective Lewis number	102
4.4.1.3.	Lewis-changing effect at the flame front - (\bar{Y}_F, θ_g) space	102

4.4.2.	Broadening effects in porous media	103
4.4.2.1.	Reaction length scale	103
4.4.2.2.	Conclusion on broadening effects	104
4.4.3.	Effects of equivalence ratio, fuel and complex chemistry	105
4.4.3.1.	Effects of equivalence ratio	105
4.4.3.2.	Effects of fuel	105
4.4.3.3.	Effects of detailed chemistry	105
4.4.3.4.	Conclusions on γ and further remark	107
4.5.	Generalized formulae for flame speed in all regimes	107
4.5.1.	Flame acceleration due to preheating - F	107
4.5.2.	Flame acceleration due to hyperdiffusion - G	107
4.5.3.	Validation of the formula	108
4.6.	Conclusions of the chapter	109
4.A.	Approximations of the analytical model (AM)	110
4.A.1.	Decoupled regime	110
4.A.2.	Hyperdiffusive regime	110
4.B.	Criterion for regime discrimination of Figure 4.3	110
4.C.	Flame structure in the space (\mathbf{Y}_F, θ_g)	111
5.	Towards high fidelity simulations of reacting fronts within porous media	113
5.1.	Meshing challenges	114
5.1.1.	An issue common to the field of porous media	114
5.1.2.	Specificities of porous media combustion	114
5.1.3.	Specific case of this thesis	115
5.2.	From porous foam to computational mesh	118
5.2.1.	Constraints on the computational mesh	118
5.2.2.	Step 1: scanning of an actual burner	118
5.2.3.	Step 2: 3D voxels filtering	118
5.2.4.	Step 3: STL generation and meshing strategies	120
5.2.4.1.	STL generation	120
5.2.4.2.	STL topological cleaning	121
5.2.4.3.	Meshing strategies	123
5.3.	Generation of lattice-based porous media	124
5.4.	Conclusions of the chapter	125
6.	Relating 3D simulations and 1D models	127
6.1.	Introduction	128
6.2.	Microscopic and macroscopic models	130
6.2.1.	3D Direct Pore-Resolved Simulations	130
6.2.1.1.	Computational domains	130
6.2.1.2.	Gaseous phase	131
6.2.1.3.	Solid phase	133
6.2.1.4.	A word on radiation	133
6.2.1.5.	Coupling strategy	134
6.2.2.	1D Volume-Averaged Model	134
6.2.2.1.	Governing equations	135
6.3.	Results and discussion	136
6.3.1.	Macroscopic effective properties	136
6.3.1.1.	Effective thermal conductivity	136
6.3.1.2.	Dispersion coefficient	137

6.3.1.3.	Interphase heat transfer coefficient	138
6.3.2.	Structure of the submerged flame	139
6.4.	DPLS vs. VAM	142
6.4.1.	Burning rate	142
6.4.2.	Profiles in physical space	144
6.4.3.	Other sources of error for the volume-averaged framework	145
6.4.4.	Discussion on the thermal Péclet number	146
6.5.	A new model for reaction rates?	147
6.5.1.	Phenomenology of burning rate: DPLS vs.VAM	147
6.6.	Conclusions of the chapter	152
6.A.	Energy and mass budgets micro vs. macro	153
6.B.	Additional plots local flame structure on \mathcal{A}	153
7.	Specificities of hydrogen combustion within porous media	157
7.1.	Chapter introduction	158
7.1.1.	Freely-propagating flows	160
7.1.2.	Meso and microcombustion	160
7.1.3.	Laminar burner-stabilized flames	161
7.1.4.	Turbulent combustion	161
7.2.	Hydrogen-air 1D laminar flames	162
7.3.	Methodology	164
7.4.	Results and discussion	164
7.4.1.	Unsteady flames	164
7.4.2.	Steady flames?	167
7.4.3.	Local flame structure	169
7.4.4.	Burning rates	170
7.4.5.	Modelling of the reaction rates	172
7.4.6.	Burning below the flammability limit	173
7.5.	Conclusions of the chapter	173
7.A.	Local flame structure in geometry D1	174
	Conclusions and future research directions	175
	Conclusions	175
	Future research directions	176
	Appendices	181
	A. Characteristics of CH4_15_138_9_AP mechanism	183
	List of Figures	190
	List of Tables	197
	Bibliography	199

Nomenclature

Abbreviations

ARC	Analytically-Reduced Chemistry
DPLS	Direct Pore-Level Simulations
HR(R)	Heat Release Rate
LFL	Lean Flammability Limit
LT(N)E	Local Thermal (Non-)Equilibrium
PMC	Porous Media Combustion
PPI	Pores Per Inch (pore density)
REV	Representative Elementary Volume
RFL	Rich Flammability Limit
RTE	Radiative Transfer Equation
VAM	Volume-Averaged Model(ling)

Operators/exponents

$\langle \cdot \rangle^A$	surface average
$\langle \cdot \rangle_t$	time average
$\mathcal{A}(\cdot)$	pure commutation with the volume average
$\mathcal{D}(\cdot)$	deviations from pure commutation with the volume average
$\mathcal{R}(\cdot)$	relative value in a 3D field compared to the 1D adiabatic flame at the same fuel progress
n_T	temperature exponent in response to preheating
N_{τ_g}	tortuosity exponent

Reactive fluid mechanics

ΔT	preheating temperature in excess of T_u
$\dot{\omega}_k$	species reaction rate per unit volume
$\dot{\omega}_T$	heat release rate per unit volume in the temperature equation
$\dot{\omega}_T^0$	heat release rate per unit volume in the total energy equation

κ	flame stretch
λ_g	gas thermal conductivity
$\mathbf{J}_k^{\text{eff}}$	effective macroscale species diffusion flux
\mathbf{J}_k	species mass flux
\mathbf{q}	pointwise thermal heat flux in the gas phase
\mathbf{u}	velocity vector
\mathbf{V}_c	correction velocity
μ	dynamic viscosity
ν	kinematic viscosity
ϕ	equivalence ratio
ρ_g	gas density
$\underline{\underline{\tau}}$	viscous stress tensor
$\underline{\underline{\mathbf{D}}}_{\text{th}}^{\text{eff}}$	effective macroscale thermal diffusion tensor
$c_{p_g,k}$	individual species gas heat capacity per mass unit
c_{p_g}	gas heat capacity per mass unit
D_ψ^{intr}	intrinsic diffusivity of a quantity ψ
E	total energy
$J.$	1D heat flux on each side of the finite porous medium
P	pressure
S_L^P	intrinsic velocity at the infinite upstream in the infinite porous media
T_a	activation temperature
T_g	gas temperature
T_u	inlet temperature
$T_{\text{preheating}}$	preheated temperature ($= T_u + \Delta T$)
T_{ad}	equilibrium temperature
T_{max}	maximum temperature reached in the domain
W_k, W	species and mean molecular weights
Y_k, X_k	species mass and molar fractions

Volume-averaging

\dot{m}	intrinsic mass flux per surface unit of premixed gas ($= \langle \rho_g \rangle^g \langle u \rangle^g$)
$\langle \cdot \rangle$	superficial volume-average
$\langle \cdot \rangle^g, \langle \cdot \rangle^s$	intrinsic volume-averages
\mathbf{n}	normal on the flame surface orientated towards the fresh gases
\mathbf{n}_{gs}	gas/solid normal at the interface

\mathbf{x}	REV center location
\mathbf{y}	REV space integration variable
\mathcal{A}_{ge}	gas/gas surface of the REV
\mathcal{A}_{gs}	gas/solid interface
\mathcal{A}_{se}	solid/solid surface of the REV
\mathcal{V}	REV volume
$\mathcal{V}_g, \mathcal{V}_s$	gas and solid REV volumes
Q_x^{DNS}	transverse-averaged longitudinal heat flux
Q_{gs}	interphase heat transfer

Porous matrix characterization

β_F	non-Darcy coefficient
ϵ	porosity
λ_s	solid thermal conductivity
λ_s^{eff}	macroscale effective thermal conductivity
\mathcal{S}_V	surface density
τ_g	gas-phase tortuosity
A^{dis}	dispersion proportionality constant
D_ψ^{eff}	effective macroscale diffusivity of a quantity ψ
h	surface heat transfer coefficient
h_V	volume heat transfer coefficient
k_p	permeability factor
S_L^0	laminar adiabatic free-flame speed
T_s	solid temperature

Length scales

δ_L	flame thickness
δ_R	reaction thickness
d_p	pore diameter
L	length of the finite porous media
l_{diff}	gas diffusion length scale
$l_{\text{re-eq}}$	interphase re-equilibration length scale
l_{reac}	reaction length scale
$L_{g,s}$	gas and solid macroscopic gradient length scale

$l_{g,s}$ gas and solid microscopic gradient length scale

Other symbols

χ = $1 + 1/r_\lambda$
 \dot{m}_0 mass flux of the reference 1D laminar flame
 \dot{m}_∞ mass flux at the infinite upstream, outside of the porous medium
 \dot{m}_n mass flux normal to the flame surface
 λ_i roots of the characteristic polynomial (eigenvalues)
 $\mathcal{A}, \mathcal{A}^*$ flame surfaces for methane and hydrogen
 \mathcal{C} chemical problem (kinetic closure)
 \mathcal{T} thermal problem
 σ Stefan-Boltzmann constant
 A_i^\bullet amplitude coefficients for the solutions
 P_0 ambient pressure = 1 atm
 R_g universal gas constant
 x longitudinal abscissa
 x_p flame position in the finite case
 y, z transverse abscissae

Reduced parameters

α reduced heat release ($= (T_{ad} - T_u)/T_{ad}$)
 β Zel'dovich number
 η_{rec} recirculation efficiency
 η_{rec}^0 theoretical recirculation efficiency in the decoupled regime for $\dot{m} = \dot{m}_0$
 η_{rec}^{max} maximum recirculation efficiency for all flame positions in the finite case
 Γ total flame acceleration within the porous medium
 γ ratio of diffusion to reaction length scale
 Γ_d flame acceleration related to dispersion
 Γ_p flame acceleration related to preheating
 Γ_w flame acceleration related to wrinkling
 $Pe_{p,th}$ pore-based thermal Péclet number
 Pr Prandtl number
 Re_p pore-based Reynolds number
 Da Damkholer number
 Le_k species Lewis number

Nomenclature

Sc_k	species Schmidt number
θ	dimensionless temperatures
c	progress variable
$r_{\dot{m}}$	reduced mass flux
r_λ	ratio of conductivities (includes porosity)

Sub/superscripts

$\bar{\cdot}$	mean property in the solid matrix
'	deviations from the average
*	dimensionless variable
$^0, 0$	reference 1D adiabatic laminar flame
(AM)	analytical/asymptotic model with constant coefficients
(SIM)	1D simulations with non-constant coefficients and resolved kinetics
1	zone 1 ($x < 0$) in the infinite case
2	zone 2 ($x > 0$) in the infinite case
eff	effective property at the macroscopic scale
G1	inlet gaseous zone 1 in the finite case
G2	outlet gaseous zone 2 in the finite case
S1	solid-gas zone 1 in the finite case
S2	solid-gas zone 2 in the finite case
g	gas related
i, j	indices
k	related to species k
n	n^{th} layer in multi-staged burners
s	solid related

Introduction

This first chapter proposes a critical review of the concepts related to porous media burners, with a special attention given to heat recirculation and non-adiabatic combustion. It is the occasion to come back to the unique features and applications of porous burners, as well as other heat-recirculating devices. The various burner designs found in the literature and afferent stabilization mechanisms are reviewed in detail. But in order to take a step back, the chapter begins with an overview of the current societal context regarding combustion and energy, so as to investigate how porous burners may - or may not - be helpful regarding various emission targets and technological challenges. Eventually, the objectives, outline and contributions of the manuscript to the literature are described.

Overview

1.1. Current societal context	2
1.1.1. High constraints on energy	2
1.1.2. Combustion, economy and global warming	2
1.1.3. Hydrogen potential to carbon-neutral targets	3
1.1.4. Why studying porous media combustion?	5
1.1.5. Scope of the thesis	5
1.2. Concepts of porous media combustion	6
1.2.1. Small-scale combustion systems	6
1.2.2. Advantages/drawbacks of small-scale combustors	7
1.2.3. Principle of heat recirculation	7
1.2.4. Applications of heat-recirculating burners	9
1.2.5. Materials suitable for porous media combustion	12
1.2.6. Non-adiabaticities in premixed laminar combustion	13
1.2.7. Stabilization mechanisms in porous burners	19
1.3. Motivations and objectives of the thesis	23
1.4. Outline of the manuscript	24
1.5. Publications during the thesis	26
1.5.1. Works related to porous media combustion	26
1.5.2. Other works	26

“Science without conscience is but the ruin to the soul.”

RABELAIS, *Pantagruel*, II, 8

1.1. Current societal context

Before delving into technical details of this thesis topic - namely *porous media combustion*, we provide in this first section some contextual elements regarding the place of combustion in our modern economies, and the subsequent timeless need to design combustion devices in a flexible, safe, fuel-efficient, CO₂ and pollutant-free manner. Interestingly, porous burners may be helpful in reaching those goals. And because they are arguably a serious candidate to harness hydrogen flames, the potential of this alternative, decarbonized and trendy fuel is briefly discussed.

1.1.1. High constraints on energy

The period of this Ph.D. thesis has seen two major crises hit the world successively: the Covid-19 outbreak and the war in Ukraine. Somehow, both remind us of the predatory nature of mankind over our planet, coupled to an ever growing, intertwined globalization. Indeed, Covid-19 may have originated from zoonosis [1], itself stemming from deforestation, soil artificialization, demographic explosion, noise and light pollution. And whilst a large portion of humanity was locked down in 2020, the resulting global decrease in CO₂ emissions was only of the order of what would be required *on a yearly basis* to reach carbon-neutral targets by 2050 [2, 3]. Concerning Ukraine, the hesitations of Europeans to set an embargo on Russian fossil fuels is a strong reminder that our economies and daily lives are very dependent upon carbon-intensive resources, and of the strong intertwining of politics with energy fluxes. This makes energy efficiency and decarbonization challenges of utmost importance - keeping in mind that they may hardly be reached without some degree of sobriety. In addition, due to the finite nature of fossil fuels, a supply crunch is expected to occur in the near future [4]. According to the International Energy Agency, the production of conventional crude oil peaked around 2006 (70 million barrels/day [5]), while oilfield discoveries peaked as early as in the 1960s (55 billion barrels/year [6]). Those have been decreasing ever since. Simultaneously, the Energy Return On Investment (EROI) of oil, defined as the ratio of extracted-to-spend energy during production, has fallen steadily throughout the last decade. This partly originates from the growing share of shale oil - showing 5 to 10 times less EROI than conventional oil [7] for 1.75 times more CO₂ emitted per energy unit. These looming prospects urge for the development of fuel-efficient, clean, and decarbonized energy systems, in order to move away from fossil fuels rapidly. This poses large societal challenges, because the development of carbon-resilient economies has shown difficult - whatever is the rest of the scenario regarding anthropogenic environmental impact.

1.1.2. Combustion, economy and global warming

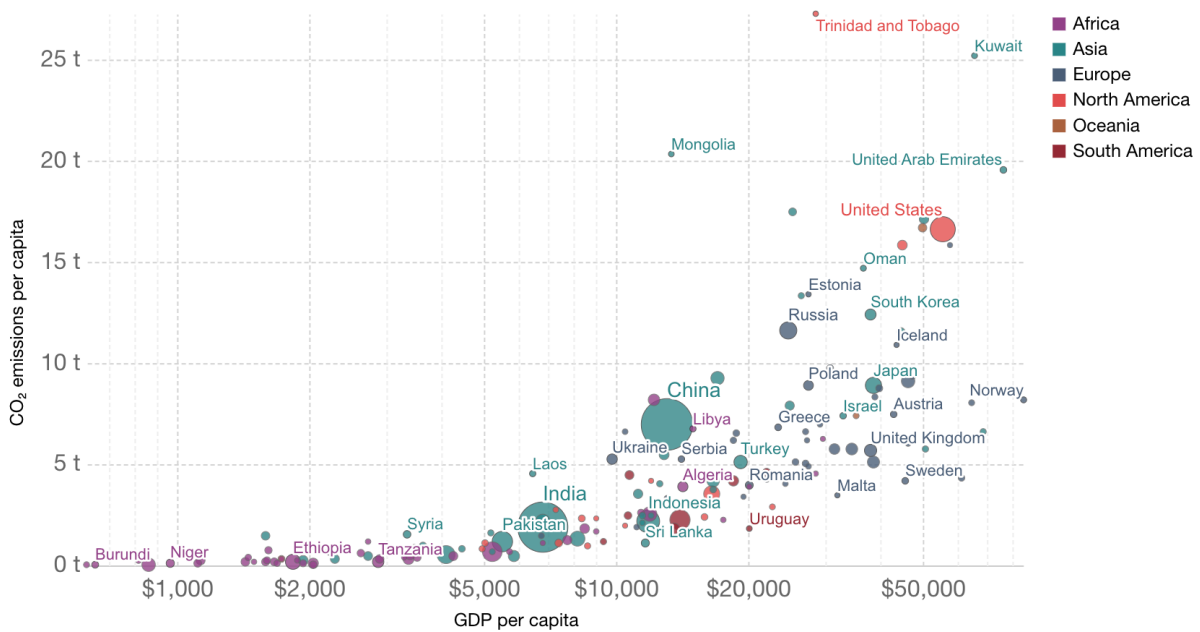
Global warming is an additional constraint posed upon human civilization. In the 2021 IPCC report II on Impacts, Adaptation and Vulnerability [8], one reads: *“human-induced climate change, including more frequent and intense extreme events, has caused widespread adverse impacts and related losses and damages to nature and people, beyond natural climate variability. [...] The rise in weather and climate extremes has led to some irreversible impacts as natural and human systems are pushed beyond their ability to adapt”*. Accordingly, there is not a day scientists do not try and raise awareness regarding climate change and the need to move away from fossil fuels. However, this is far from being an easy task: as shows Figure 1.1, economic

prosperity is strongly correlated to CO₂ emissions [9]. And since the general trend is to favor economic growth rather than environmental concerns, the only way out is to try and *decouple* economic growth from CO₂. This may be achieved by redefining the notion of growth, but also by a swift development of decarbonized energies, such as renewables, nuclear, biomass, and alternative fuels such as ammonia [10], metals [11] and, subject of much attention today in the combustion community, hydrogen [12].

CO₂ emissions per capita vs GDP per capita, 2018



This measures CO₂ emissions from fossil fuels and cement production only – land use change is not included. Gross domestic product (GDP) per capita is measured in international-\$ in 2011 prices to adjust for price differences between countries and adjust for inflation.



Source: Global Carbon Project; Maddison Project Database 2020 (Bolt and van Zanden (2020))
OurWorldInData.org/co2-and-other-greenhouse-gas-emissions/ • CC BY

Figure 1.1. – CO₂ emissions *vs.* GDP per capital throughout the world.

1.1.3. Hydrogen potential to carbon-neutral targets

Hydrogen and energy share long history. Electrolysis and its reverse process (fuel cells) were already subject of research in the 1800s, and the first internal combustion engine developed by François de Rivaz in 1806 was powered by a hydrogen/oxygen mixture [13]. Due to its low density at ambient conditions, hydrogen has been used to lift aircrafts, and thanks to its highest energy density per mass unit among all fuels (120 MJ kg⁻¹), it propelled humanity to the Moon. Hydrogen is also used to produce ammonia, essential for fertilisers, and more generally it is one of the key starting materials in the chemical industry. Concerning combustion applications, H₂ has seen ups and downs, but is now being seriously considered by governments as a lever to decarbonize the industry, transport and domestic appliances [14]. Unfortunately, H₂ does not constitute a primary energy source but an *energy carrier*: it must be produced from another energetic resource. There exists to that end myriad pathways, including steam reforming, pyrolysis, photolysis, and of course, electrolysis [15]. Today, only 5% of H₂ is obtained by electrolysis, the rest coming mostly from fossil fuels [16]. Considering the fact that electric grids are not yet fully decarbonized, it means that only a small fraction of current hydrogen production can be considered as sustainable. This urges for heavy and rapid deployment of

decarbonized electric sources, but also suggests that one should carefully consider the entire energy/ CO_2 cycles from primary source to end usage. Notably, the current electrification of industries, vehicles and domestic appliances is a potential source of usage conflicts in the near future. Note that because of the relatively low efficiencies of electrolyzers (60-80% [17]), fuel cells (50-70% [18]) and internal combustion engines (10-30% [19]), hydrogen as a fuel for light mobility seems much less energy-efficient than batteries from the point of view of global energy production. So in a context of large constraints on energy volumes, H_2 is of course not a silver bullet given the short time scales required for decarbonization.

There exists, nonetheless, situations where hydrogen can make both economical and environmental sense. Because electricity cannot be stored easily in large quantities, the intermittent production from renewables and excess energy from nuclear plants can be converted to hydrogen, when production exceeds demand [20]. Once stored, H_2 constitutes a ready-to-use, versatile energy resource. This strategy is often referred to as *power-to-gas* [21], and is illustrated in Figure 1.2. The stored hydrogen can be used in multiple ways: converted back to electricity, used as a fuel for heavy transports, but also, used as a *green heat production source* in domestic and industrial contexts. This heat production is of particular interest to us, because porous media may be well-suited to burn this hydrogen [22].

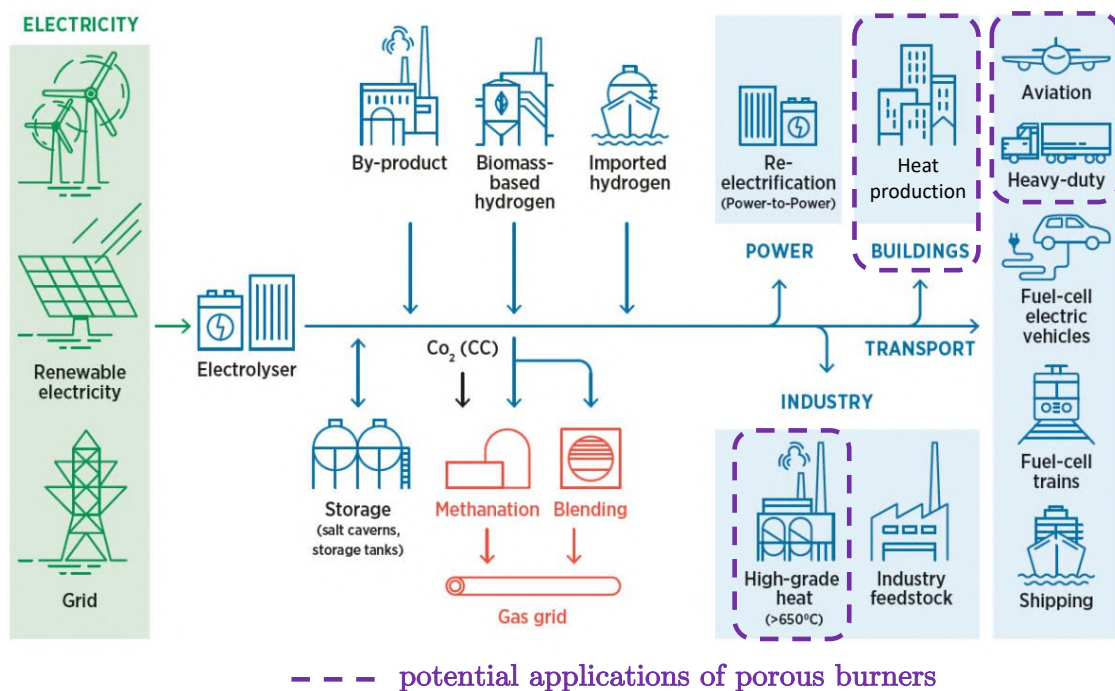


Figure 1.2. – Power-to-gas strategy, from the International Renewable Energy Agency (IRENA). Fields of application for porous burners are shown in dashed purple.

Moreover, in the realistic scenario of a “smooth” transition from fossil fuels to hydrogen-based combustion applications, intermediate technologies capable of supporting hydrocarbons/hydrogen blends are often considered. This concept is referred to as *hybridation* or *substitution*. Note that the partial injection of hydrogen into existing natural gas distribution networks and current devices has been proven safe up to 6% in volume [23], but this is of course insufficient. Combustion devices capable of sustaining both hydrocarbons and hydrogen are thus necessary. This fuel-flexibility is - justly - another known feature of porous burners [24].

Note that although hydrogen has received much attention from officials and the general public, its negative consequences and external dependencies must be considered with attention. As

predicted by Cherry in [25], a technicist precipitation into H₂ technologies may show major side an rebound effects such as “*delayed development of other energy alternatives, hazards of catalyst or hydride metals, disruptive employment shifts, land usage conflicts, and increased vehicle usage*”. In addition, hydrogen presents a series of safety concerns which must be handled. H₂ is a small, colorless and odorless molecule which leaks easily, diffuses rapidly, is subject to buoyancy effects, cannot be liquid at ambient temperature, ignites in air for very low fuel concentrations, and swiftly transitions to hazardous detonations [26, 27]. Moreover, in case of leakage, H₂ may react with tropospheric hydroxyl radicals, disturbing the distributions of methane and ozone leading to a large warming potential in the short term [28]. All things considered, the question of whether hydrogen is a temporary hype or a real game-changer is left to the reader’s appreciation.

1.1.4. Why studying porous media combustion?

Compared to classical, “free-flame” combustion devices, porous burners present a series of advantages that may help harnessing hydrocarbon and hydrogen flames in a safe, clean and efficient fashion [29, 30]. For example, because hydrogen flames are mostly invisible to the eye, internal combustion inside a porous matrix which heats up and radiates is particularly appreciable - notably for domestic appliances. Also, since flame stabilisation and burning rates are partly dictated by the temperature of the solid matrix and its geometry, porous burners may serve as fuel-independent flame stabilizers, enabling the design of *universal burners* adapted to hydrocarbons, hydrogen, and blends [22, 24, 31, 32]. In addition, porous burners allow the combustion of mixtures of extremely low fuel content [33]. From a safety point of view, this may reduce explosion risks, because even in the case of leaks or flame extinction, the unburnt mixture would be less to not flammable [34] - and from a pollution point of view, this enables a drastic reduction in CO and NO_x emissions [33, 35]. Also, in the context of heat production, porous burners show a high radiant output, which is of interest for some domestic and industrial applications [30, 36, 37].

From here, a “hands-on” work direction could have been to try and design porous burners fulfilling all these remarkable features simultaneously for a specific application (*e.g.* a domestic boiler) - but because some basic questions regarding the modelling of porous media combustion and structure of the flame within the porous matrix are still open, a somewhat *academic* standpoint was adopted, with the aim of clarifying concepts and help building a sound approach to the domain. The general question driving this thesis may be summarized as follows:

“What is the behavior of flames within porous media and how to model it?”

1.1.5. Scope of the thesis

This work addresses steady premixed submerged combustion within inert porous media. *Steady*, in opposition to the related topic of filtration combustion, *i.e.* when the combustion wave is mobile in the frame of the solid matrix. *Premixed*, because the oxidizer and the fuel are supposed perfectly mixed before entering in the porous medium - diffusion flames and liquid fuels are excluded. *Submerged combustion*, because we focus mainly on situations where the chemical reactions occur completely inside of the porous matrix. *Inert porous media*, because we exclude the complex topics of catalytic or heterogeneous reactions - that is, no surface kinetic enhancement nor combustion of the surface material itself. Although this situation appears to be quite restrictive, it still opens a vast field of investigation and useful applications, with many basic questions still open.

1.2. Concepts of porous media combustion

This section introduces concepts and applications related to combustion within porous burners. First is discussed the more general field of small-scale combustors, which present high levels of interphase heat transfer due to the large surface-to-volume ratios. Then, the mechanism of heat recirculation taking place in those burners is presented, along with its technological implications. It is also the occasion to discuss the influence of non-adiabaticity on premixed laminar flames and their stabilization mechanisms within the hot porous matrix.

1.2.1. Small-scale combustion systems

When a flame is placed inside a combustion chamber or a tube, the degree of interaction between combustion and the walls is directly linked to the size of the device. The smaller the system, the larger the surface-to-volume ratio thus more heat leaving the system by conduction to the walls. Sometimes, when the system size reaches the order of a few flame thicknesses, the exothermic reaction from combustion is not strong enough to overcome the losses and flame extinction is observed - also called flame *quenching* [38]. Intuitively, the quenching distance - defined as the threshold size of the system leading to extinction - depends on the temperature of the walls, the temporal history of the flame-wall interactions, the geometry of the system, the fuel used and other parameters [39]. If the losses do not act as a perfect sink, and contrarily accumulate and diffuse heat within the walls, quenching may be prevented and stable combustion throughout time possible. For instance, if the hot walls increase the temperature of the incoming reactants, it is not excluded that reaction can take place in systems of arbitrarily small size, where the notion of quenching becomes irrelevant [40]. Examples of combustion devices allowing stable combustion whilst presenting large surface-to-volume ratio include micro and mesoscale tubes, single or multi-step mesoscale burners, honeycombs, and of course *porous media burners*. Figure 1.3 shows examples of such devices in operation with the corresponding length scale of flow interstices. Interestingly, steady combustion appears to be possible over a very wide range of interstitial sizes - here from about 0.01 to 10 mm. It means that small combustion devices are intrinsically ambivalent: albeit presenting *a priori* larger heat losses unfavorable to

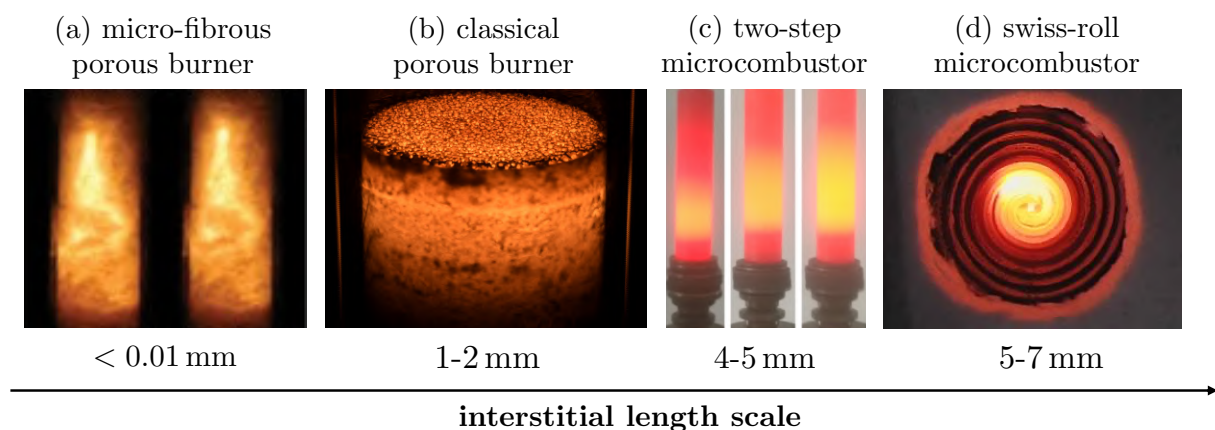


Figure 1.3. – Examples of combustion devices of large surface-to-volume ratio. (a) from [41]: a silica micro-fibrous porous burner of characteristic fiber size $4\ \mu\text{m}$ / (b) a classical porous burner made of reticulated alumina foam (credits F. Muller, IMFT) / (c) from [42]: a two-backward-step microcombustor using hydrogen as fuel / (d) from [43]: a swiss-roll microcombustor with very low flammability limit and strong heat recirculation.

combustion, these can end up in fact beneficial for reaction if properly accumulated and recycled to increase the reactivity of the incoming reactants and decrease the local losses in the reaction zone. Nevertheless, it does not mean that all small-scale devices are capable of sustaining this particular type of combustion - for example in the presence of excessive external heat losses or cooling. Also, the large thermal inertia of the solid may present hysteresis and require external triggering for stable combustion to occur [44]. This is somewhat reassuring, given the fact that the opposite situation - when extinction is wanted - is based upon similar devices, namely small inlet tubes or porous media placed upstream of combustion chambers. These are called *flame arresters*, which are aimed at preventing spurious and potentially dangerous propagation of reaction in critical regions in or outside of the combustion system.

1.2.2. Advantages/drawbacks of small-scale combustors

Small-scale burners such as presented in Figure 1.3 might possess certain drawbacks, such as large thermal inertia, high manufacturing costs and low material durability due to the high thermal shocks and stresses. Fortunately, these are balanced by some unique technological features which cannot be obtained otherwise in classical “free-flame” burners [45]:

- a high radiant output and efficiency, due to the high temperatures of the walls ;
- a large fuel flexibility, where methane, hydrogen, propane, ethylene may be burnt with the same device but also liquid fuels ;
- broadened flammability limits in terms of mixture fuel content ;
- lowered pollutant emissions, especially CO/NO_x in the lean limit ;
- a very large power range, up to 1-50 ratio ;
- a high energy density ;
- a submerged combustion, where reaction does not occur at the exterior. This has safety and control advantages, because the system may be less dependent upon external and inlet conditions.

Though such achievements may be more or less reached to some degree for a specific technology, these are all enabled by the same fundamental mechanism: *heat recirculation*.

1.2.3. Principle of heat recirculation

Many combustion systems are subject to some degree of heat recirculation. Consider for instance the classical situation of a bunsen flame stabilised at the outlet of a tube in Figure 1.4(a). Black arrows show the flow direction and red lines mark the flame reaction zone. Yellow arrows illustrate directly the phenomenon of heat recirculation: a fraction of the combustion heat is extracted from the base of the flame, which diffuses through the walls and is finally transferred back to the incoming reactants. These reactants are therefore *preheated* in excess of the inlet temperature before reaching the reaction zone. Of course, this effect is not very strong for bunsen flames: the exchange from the hot products to the tube remains limited to the base of the reaction

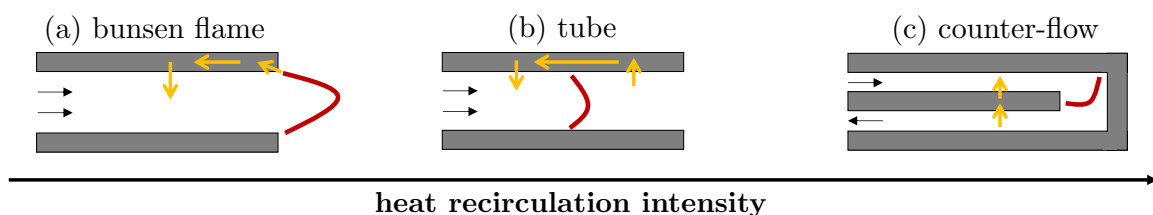


Figure 1.4. – Principle of heat recirculation on various configurations.

zone only. A situation more favourable to heat recirculation is shown in Figure 1.4(b), when a flame is stabilised inside a tube: here the hot products are in direct and prolonged contact with the tube walls, what enhances greatly heat recirculation. However, in the tube the heat still needs to travel upstream so the intensity of the phenomenon is mostly governed by the solid thermal conductivity. A situation even more favourable is shown in Figure 1.4(c), where the combustion products are in direct contact with the incoming reactants in a counter-flow reactor. This corresponds for instance to the swiss-roll presented in Figure 1.3(d).

Due to the highly non-linear dependency of reaction rates to temperature [46], heat recirculation may increase greatly reaction kinetics, leading to *enhanced burning rates*. This explains why heat-recirculating reactors are capable of burning below and beyond the classical flammability limits, why a very high energy density and power range can be reached, and why the system may become less fuel-dependent. Note that heat recirculation is *not* equivalent to the mixing/dilution of the fresh gases with a fraction of the burnt gases, what would change drastically the mixture composition and may on the contrary reduce reaction rates [47, 48]. Also, because the reactants are preheated, the burnt gases may reach *locally* a temperature *larger* than the adiabatic equilibrium computed from the inlet state of the mixture [49]. This is illustrated in Figure 1.5, which shows schematically the temperature profiles of a 1D flame with and without heat recirculation. This explains why the terms *superadiabatic* or *excess enthalpy* are often used to characterize this type of combustion. Importantly, the fact that superadiabatic temperatures can be obtained in steady state does not mean that the burner is capable of violating the first law of thermodynamics: any upstream preheating is readily equilibrated downstream, even though from ignition a transient local accumulation of enthalpy is required. Metaphorically, heat recirculation in combustion devices shares the same purpose than wearing clothes: *feel warmer locally for a given heat production*. Indeed, while clothes do not change the rate of metabolic heat production in humans - which is almost a constant $\simeq 40$ cal/s [50] - they allow for a fraction of this heat to stay in the neighborhood of the skin. That way, the solid phase described before can be viewed as “clothes for flames”. But the analogy stops here.

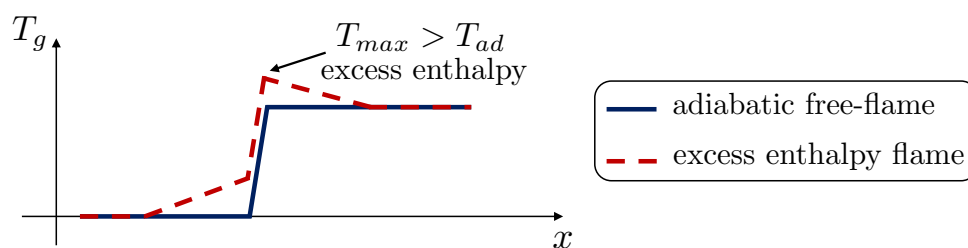


Figure 1.5. – Effect of heat recirculation on a premixed flame.

It is worth mentioning situations where heat recirculation may be favourable or unfavourable to combustion applications. Even in classical burners such as shown in Figure 1.4(a), there exists some degree of interaction between the flame and the walls, leading to a certain preheating of the incoming reactants. In operation, if the flame heats up the solid too much, then the flame front may flash back or self-ignition may be observed near the heated inlet region. This detrimental mechanism is illustrated in Figure 1.6, which shows the operation of a conventional free-flame burner inside a domestic appliance, from ignition (a) to flashback (c). On the other hand, this heat recirculation may also prevent blow-off, so in general it is difficult to say whether heat recirculation be beneficial or detrimental in a given situation. Designing a burner which delays blow-off (allowing increased burning rates) with low flashback propensity is the general design goal which, as we will see, is also sought for in porous media combustion but hard to achieve.

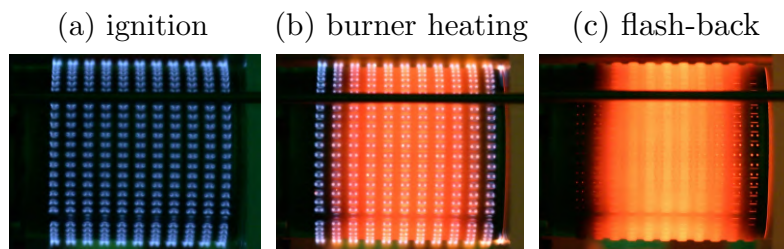


Figure 1.6. – Heat recirculation in a classical free-flame burner leading to flashback. Credits: H. Pers, IMFT.

1.2.4. Applications of heat-recirculating burners

1.2.4.1. Radiant heating

Because of the strong flame-wall coupling in heat-recirculating reactors, the walls may reach very high temperatures - typically above 1000 K. Beyond the consequence that not all materials are suitable for these applications [51], such high temperatures may lead to large amounts of thermal radiation which are of interest in some industrial applications where high radiant output is required - for instance in glass manufacturing [52], infrared radiators [53], thermophotovoltaic power generation [54], household domestic heating [55], efficient cooking appliances [56, 57] or paper drying [58]. Note that porous burners of the sort are already commercially available [59–61], with typical thermal loads reaching 1000 kW m^{-2} and radiation temperatures of 1750 K. A view of these burners is provided in Figure 1.7. As reported in several studies [30, 36, 37], the radiation efficiency reached by porous burner can be as high as 30-40%, and seems to decrease with pore size and burning rate.



Figure 1.7. – From [59–61]: examples of commercial and industrial solutions based upon porous media combustion.

1.2.4.2. Ultra-lean or ultra-rich combustion

It is notorious that adiabatic, unstretched laminar free-flames cannot burn below or above certain proportions of fuel content, respectively called lean (LFL) and rich flammability limit (RFL). These limits depend on the fuel considered, pressure, temperature, and the relative proportion of inert molecules such as nitrogen, argon, etc. By noting ϕ the equivalence ratio, one finds for example $\phi_{\text{LFL}} = 0.52$ and $\phi_{\text{RFL}} = 1.67$ for methane-air combustion at ambient conditions (300 K, 1 atm) [62]. This flammability range is classically a limitation for conventional burners: they cannot operate too lean to avoid blow-off and produce sufficient power, while ultra-rich combustion is sometimes required for example with syngas production. To that regard, heat recirculation can be much beneficial, because the enhanced kinetics may allow a stable combustion way beyond these flammability limits [33]. Figure 1.8 reports values of ϕ attained by

various heat-recirculating reactors in the literature, either below the LFL or above the RFL. They show, in agreement with Figure 1.4, that *steady* porous media combustion is tendentially less efficient for lean-burn applications than counter-flow designs (here, under the form of swiss-roll), and that an *unsteady* porous media combustion allows, to the best of the author's knowledge, achievement of the lowest equivalence ratio ($\phi = 0.028$, which is only 5% of the LFL [63]). This performance, obtained by transient recuperation of heat accumulated in the solid, requires the management of a moving frame front - what can be done by reversing successively the flow direction [63]. Incidentally, it is worth mentioning that an outstanding performance of 1-100 ratio in fuel content and 1-1000 in flow rates was attained by a swiss-roll for propane combustion, but it made use of a catalytic surface in the central burning zone [64]. As an original application, it was proposed that swiss-rolls be integrated in gas masks to destroy chemical or biological agents passing in the high-temperature combustion region [65, 66]. Thanks to their compact size, low equivalence ratio attainable and low emissions, the exhaust gases are deemed breathable.

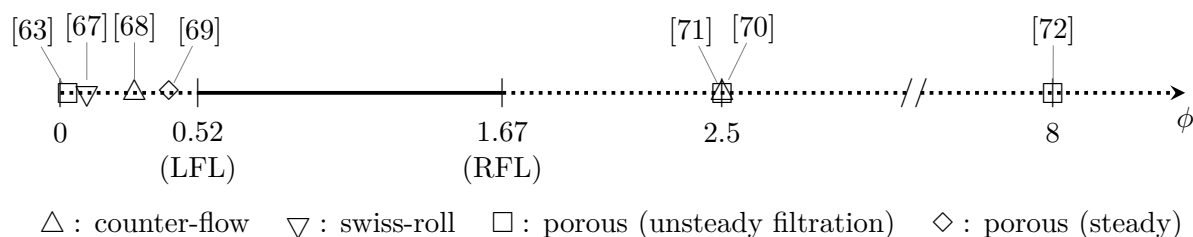


Figure 1.8. – Equivalence ratios attained by various heat recirculating devices for methane combustion, reported from the literature. Solid line: flammability limits.

Nevertheless, heat recirculating devices are not always synonym of increased flammability range. For instance, the experimental study performed in [32] on a cylindrical, uniform 1 cm-long NiCrAl porous foam found no stable combustion outside the classical flammability limits. It shows that even if a system can recirculate some heat, in the presence of sufficient heat losses and in specific geometries it may not exhibit remarkable features compared to conventional burners.

1.2.4.3. Low-emission burners

The combustion of hydrocarbons releases various types of pollutants - primarily CO_2 , which presents substantial global warming potential and cannot be avoided to produce a certain amount of energy. Also, the burning of heavy hydrocarbons leads to the formation of soot and other unburnt compounds (UHC), but those are usually absent for light gaseous combustion (methane, propane). For the latter, the two major remaining pollutants are CO and NOx, which are not the least because directly harmful to nature and humans. Their direct inhalation can be dangerous (and even lethal for CO), cause asthma, cardiovascular problems, and other issues [73–75]. In addition, NOx may produce ozone in altitude and show a large warming potential throughout time [76]. For hydrogen combustion, only NOx emissions remain but they may be larger than hydrocarbon-based combustion in practical applications [77].

In the literature, it is often observed that heat-recirculating systems show lower CO and NOx emissions compared to conventional burners with typical values often under 30 ppm [78–82]. To understand how this is possible, it is important to recall their formation mechanisms. CO results from the incomplete oxidation of the fuel, and typically occurs when oxygen is in default or when flames are highly modified by the flow (stretch, local extinctions). NOx, for their part, are mainly formed at high temperatures due to oxygen-nitrogen interactions (thermal pathway), but also to a lesser extent through more direct nitrogen-hydrocarbon interactions (prompt pathway,

marginal in the lean-burn regime) [83–87]. As shows Figure 1.9, the adiabatic post-combustion equilibrium computed with CANTERA with GriMech3.0 for methane-air predicts a reduction in CO and NO_x concentrations with decreasing equivalence ratio. Conceptually, it is thus reasonable to assume that heat-recirculation, enabling ultra-lean combustion with lower peak temperatures, is the main mechanism allowing a reduction of these emissions. Of course, in realistic applications, the adiabatic equilibrium is rarely reached, and emissions may depend upon operating conditions and local features of the interstitial flow. For instance, it was observed in porous burners that CO formation increases with burning rate at a fixed equivalence ratio [30, 78, 86, 87], hinting that lowered residence time may prevent the complete oxidation of CO into CO₂. Nonetheless, there is an opposite trend for lower equivalence ratios (and thus lower burning rates) where incomplete combustion is more likely to happen, leading to values far away from the equilibrium of Figure 1.9. This can originate from the high curvature and strain of the flame at pore scale, the temperature distribution or the local extraction of heat from the reaction zone, and may lead to larger CO emissions, as observed in experiments [35, 88, 89]. For NO_x emissions, there seems to be experimental consensus over its decrease for decreasing equivalence ratio, which is coherent with its formation pathways and adiabatic equilibrium, and a relative independence upon burning rate, which is less evident to explain though it has been argued that there may be a compensation mechanism between residence time and local temperatures [33]. Overall, the reported trends for emissions follow qualitatively Figure 1.10. As pointed out in [33], the fact that some measurements lie within measurement errors and the discrepancy between burner technologies/geometries does not exclude atypical situations where the trends are different [86]. Note that almost zero emissions were obtained in [81] in a step porous burner, but the exact underpinning mechanisms remain unclear.

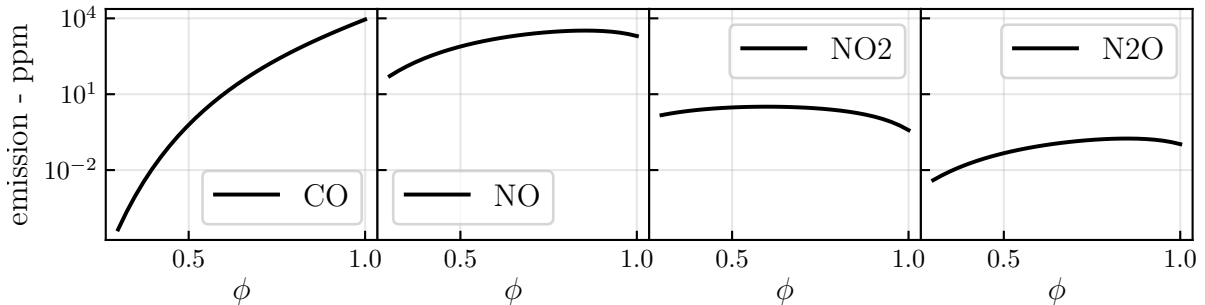


Figure 1.9. – Adiabatic equilibrium computations, computed with CANTERA, chemical scheme GriMech3.0. Here ppm = molar fractions $\times 10^6$.

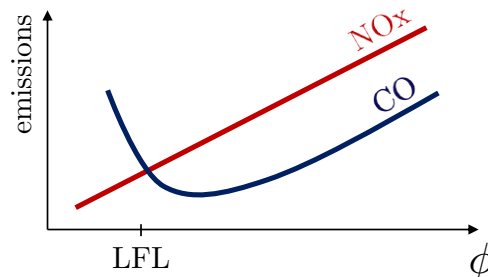


Figure 1.10. – Typical trends of emissions in porous burners found in the literature.

1.2.4.4. Other applications

Heat-recirculating burners find a variety of other applications, including:

- hydrogen production from rich mixtures, as described in [90] - methanol, methane, octane and automotive-grade petrol are burnt inside inert porous burners, yielding up to 66% of conversion to syngas (H_2 , CO). Thanks to heat-recirculation, reaction can be sustained for equivalence ratios way beyond the RFL. In the same line of thought, the synthesis of hydrogen chloride was also performed inside porous media [91] ;
- internal combustion engines using porous media [92, 93], where the porous medium may be utilized in various ways (dispersion of the injected fuel, submerged combustion, etc.) ;
- low-emission LPG combustion - in [94] very similar operating ranges and CO/NO_x emissions were reported for both methane and LPG combustion in a rectangular single-layered porous burner. Other similar studies are reported in [95, 96] ;
- powering of portable electronics and micro-mechanical systems. Because hydrocarbon fuels contain nearly 50 times more chemical energy per mass unit than most recent batteries, systems of low electrical conversion efficiency may still present a certain advantages [97] in terms of lifetime. This may be useful, for instance, for military personnel in regions where electrical generation is difficult ;
- micro-combustion applications [98] also include the development of microscale gas turbines for power generation and micro-propulsion [99, 100], or the original creation of micro-rockets weighing less than 1 gram [101].

The list of possible usages for heat-recirculating burners is very long and the reader is referred to some reviews for additional references [58, 62, 102].

1.2.5. Materials suitable for porous media combustion

The material selected for the solid matrix plays a role in the overall performance of the burner, mostly through its thermal conductivity and radiative properties [29, 103]. The solid must sustain prolonged high temperatures, many short operating cycles with substantial thermal shocks, must possess a certain resistance against corrosion and show thermal expansions compatible with an integration into practical combustion devices. Needless to say, the material should also present sufficient mechanical strength and, for prospected aeronautical applications, should be as lightweight as possible. Table 1.1 provides main thermal properties of the most common materials encountered in porous burners. Expectedly, the two classes of materials used for porous media burners are *metals* (e.g. NiCrAl, stainless steel) and *ceramics* (e.g. aluminium oxide Al_2O_3 , silicon carbide SiC, zirconium dioxide ZrO_2). Visuals are given in Figure 1.11. Due to the large experimental variability, the values of Table 1.1 were rounded and should only be

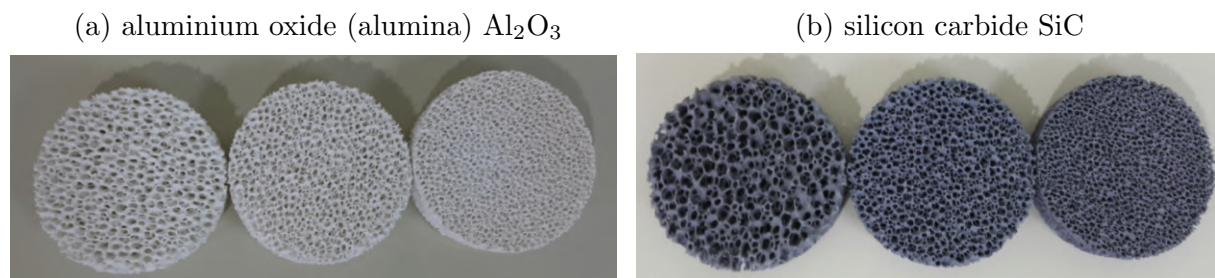


Figure 1.11. – From [104]: examples of porous foams used in experiments - each 10, 20 and 30 pores per inch (PPI).

viewed in terms of order of magnitude. Overall, it is seen that metals show much lower melting points, limiting their use to lean-burn applications. Note that impurities in metal alloys may reduce their allowable operating temperature, so ceramic materials are often preferred because of their very high melting point - up to 3000-4000 K. A sintering stage during manufacturing, which increases the material strength, thermal conductivity and resistance, is beneficial and common practice for all materials. For ceramics, sintering is necessary. Also, Table 1.1 shows that heat capacity it is not a discriminatory characteristic. Noticeably, SiC shows particularly high thermal conductivity, topped only by a few other materials such as diamond [105].

Table 1.1. – Properties of typical materials used in porous media combustion (at ~ 600 K).

material	thermal conductivity ($\text{W m}^{-1} \text{K}^{-1}$)	heat capacity ($\text{J K}^{-1} \text{kg}^{-1}$)	melting temperature (K)	Refs.
NiCrAl	10	500	1800	[32, 60, 106]
stainless steel	15	600	1500	[107, 108]
Al_2O_3	10	700	3700	[93, 103, 104]
SiC	100	600	3100	[103, 104, 109]
ZrO_2	3	500	4700	[103, 110]

Unfortunately, it is often difficult to assess the exact local properties of the porous structure. Depending on the manufacturing process (a possible combination of melting, molding, printing, chemically-active processes, the use of adjuvants, etc.), material inhomogeneities and inner pores inaccessible to the fluid may appear, leading to local properties substantially different from the bulk material. For instance, aluminum oxide Al_2O_3 shows a 10-fold ratio of thermal conductivity depending on the degree of crystal arrangement. Noteworthy, in some cases the production of ceramic materials may be cheaper than metallic counterparts, an increasing tendency due to the progressive depletion and stress on demand of metallic resources [110, 111]. As a main drawback, porous ceramics are brittle and show rapid propagation of cracks after onset [103] - which in turn alters the material macroscopic conductivity.

1.2.6. Non-adiabaticities in premixed laminar combustion

Because the present work addresses laminar combustion within porous media, a thorough understanding of the fundamental influence of heat losses and recirculation on the structure and speed of laminar flames is mandatory. This section recalls notions and concepts associated to adiabatic and non-adiabatic combustion, showing that heat losses and recirculation may lead to a multiplicity of burning rates for a given inlet mixture, and a multiplicity of flame positions for a given burning rate.

1.2.6.1. Adiabatic laminar flames

Adiabatic laminar flames are probably the most fundamental objects underpinning combustion technologies. They refer to the ideal one-dimensional combustion of a mixture defined by its mass fractions Y_k , unburnt temperature T_u and pressure P_0 . For deflagrations, the pressure drop across the flame is usually negligible, so pressure can be assumed constant in the presence of laminar fronts (throughout this thesis it is assumed $P_0 = 1 \text{ atm} = 101325 \text{ Pa}$). If the mixture is initially at rest in the laboratory frame, the combustion wave travels at a velocity called *laminar flame speed*, noted S_L^0 , which depends on the Y_k , T_u , and P_0 . For convenience, laminar flames are usually studied in a steady frame of reference for which the infinite upstream velocity is

equal to S_L^0 . Corresponding equations for gaseous combustion are given in Chapter 2. The canonical situation for a methane-air flame is depicted in Figure 1.12, where the normalized profiles of temperature θ_g , heat release rate (HRR) and progress variables c_{CH_4} and c_{CO_2} are shown in physical space. Note that the transition from fresh to burnt gases is very sharp -

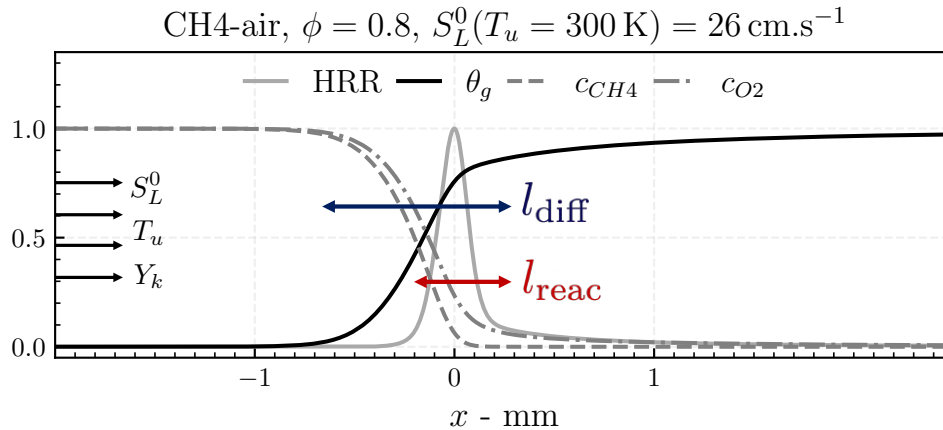


Figure 1.12. – Adiabatic laminar free-flame of methane-air at ambient conditions for an equivalence ratio $\phi = 0.8$, computed with CANTERA [112].

typically of the order of 1 mm. As depicted on Figure 1.12, two length scales are usually defined: one associated to temperature diffusion in the gas l_{diff} , and one describing the reaction zone l_{reac} . It is commonly acknowledged that:

$$l_{\text{diff}} \gg l_{\text{reac}}. \quad (1.1)$$

l_{diff} increases with thermal conductivity but decreases with flame speed. l_{reac} depends also on these parameters but is also governed by the “stiffness” of the mixture, that is, the activation energies E_A of the reactions. Overall, the mechanism for self-sustained combustion is the convective equilibrium between diffusion and reaction: the heat from the burnt gases travels *upstream* by diffusion to preheat the reactants, which themselves diffuse into the reaction zone. When the reactants have reached sufficient energy in sufficient concentration, they react and go rapidly to equilibrium. Note that the equilibrium temperature $\theta_g = 1$ is only partially reached over l_{diff} and l_{reac} . This is due to the longer equilibration of intermediate species. For hydrocarbon flames, the complete oxidation of CO to CO_2 may require more time. For hydrogen flames, it is mostly the OH radical which is usually longer to equilibrate to yield H_2O .

1.2.6.2. Laminar flame speed

Although the computation of a laminar flame appears easy, it requires the simultaneous resolution of S_L^0 , which is an unknown boundary condition of the system, and the physical profiles themselves, which depend in turn upon S_L^0 . As such, the computation of a laminar flame boils down to an *eigenvalue* problem. In general, because the reaction rates are strongly non-linear functions including exponentials, and because the thermo-chemical properties of the gas phase depend a lot upon composition and temperature, it is notoriously difficult to derive analytically a value for S_L^0 so its proper resolution is always done numerically. Yet, there exists many analytical theories that derive values for S_L^0 with simplifying assumptions, unveiling the direct dependencies of flame speed upon the system parameters. Such studies date back to more than 100 years, for instance with the works of Mallard and Le Chatelier [113]. With a simple energy balance, they found that flame speed varies like the square root of gas diffusivity D^{th} and

reaction rate R_r :

$$S_L^0 \propto \sqrt{D^{\text{th}} R_r}. \quad (1.2)$$

More advanced asymptotic analyses - for instance ZFK, Williams, Echehki, Van Kalmthout, see [114, 115] provide more elaborate theoretical prediction for S_L^0 , but these always boil down to a similar dependency. Intrinsically, Equation (1.2) shows that laminar flames are diffusion and reaction-limited systems. It also means that if one wants to increase or decrease the velocity of a laminar flame, one needs to alter somehow D^{th} or R_r . This conceptual viewpoint is particularly relevant for porous media combustion, because as we will see in Chapter 4 heat-recirculation can be viewed as simultaneous alteration of both D^{th} or R_r whose respective intensity depends on the degree of coupling with the wall.

1.2.6.3. Heat loss/gain and multiple flame speeds for laminar flames

“**Adiabatic flame speed**”. In an infinite gaseous medium, there exists a conceptual difficulty concerning adiabatic laminar flames known as the *cold boundary issue* [116]. Mathematically, because the reaction rates do not vanish at the infinite upstream (they are just exponentially small), and because they have an infinite amount of time to react before reaching the reaction front, the classical set of equations governing combustion is ill-posed so the value of S_L^0 does not exist formally-speaking. Nonetheless, by making use of multi-scale asymptotics, or by setting artificially a fixed temperature in a finite domain (it can be done theoretically and is necessary in numerical codes), then a value for S_L^0 is found, even though it requires to modify slightly the formulation of the problem [117, 118]. In that context, S_L^0 can be viewed as the limit value for which this modification is minimal. Interestingly, this modification can be seen as an addition or subtraction of heat from the flame, as if a thermal anchoring artifact were necessary for a flame to exist.

Heat losses. While the cold boundary difficulty brings “unwillingly” non-adiabaticity into the problem, some authors have studied purposefully the influence of heat losses on planar flame fronts, for terms of the form $h(T_g - T_u)$ in the energy equation representing for instance the combustion inside a tube [119, 120]. Those early theories unveiled that for an increasing heat loss intensity, two, one or zero flame speeds S_L^h may co-exist for the same unburnt mixture, temperature and pressure. For small heat losses, two flame speeds are found - one high and one low-velocity regime - as depicted in Figure 1.13. The high-velocity regime is very similar to the

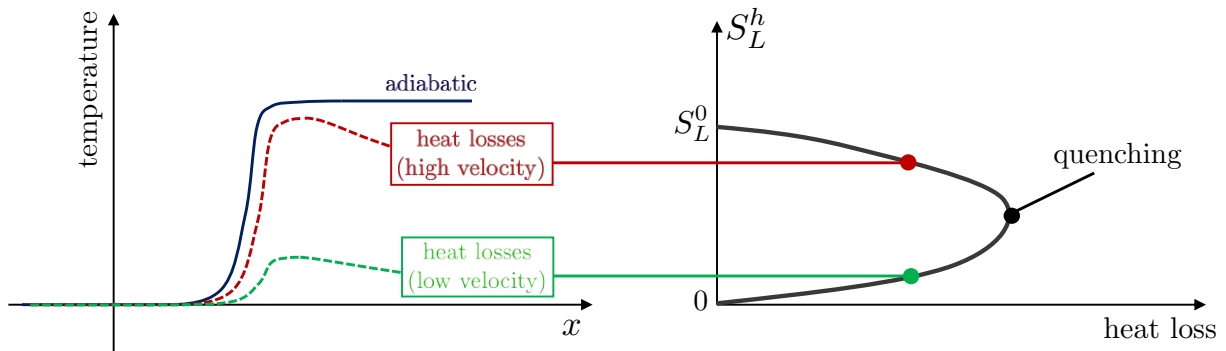


Figure 1.13. – Effect of uniform heat losses on flame structure of laminar flames. Left: for a given heat loss, two solutions may exist, one of high velocity and one of low velocity. Right: influence of heat loss intensity on the multiplicity of solutions.

adiabatic case with a flame speed S_L^h slightly lower than S_L^0 , while the low-velocity regime is very different, with very low temperatures reached in the domain and much smaller values for

S_L^h . In that regime the system is dominated by long-range diffusion and heat losses, as allowed by the lower convective flux, and may lead to partial oxidation of the mixture. The low-velocity regime is often considered *unstable*, meaning that although it enforces the equations it may hardly be observed in experiments. When the heat loss intensity is increased, the two regimes coalesce progressively until reaching a critical value that leads to flame extinction, that is, when the reaction is too weak to overcome the losses. In Figure 1.13, it is seen that when heat losses go to zero, then $S_L^h \rightarrow S_L^0$. Note that the heat losses are necessary to understand the notion of flammability limits otherwise any mixture is theoretically flammable [119] so this conceptual framework has very practical implications.

Heat gains. Interestingly, there seems to be no symmetry between heat loss and gain for laminar flames, either conceptually or in terms of literature abundance. A heating term of the form $h(T_g - T_u)$ with $h < 0$ from the infinite upstream is clearly an ill-posed problem, so heat addition may rather be considered under the form of an increase in unburnt temperature T_u . This is known to increase flame speed, but in the author’s knowledge this does not lead to particular multiplicities. The flame acceleration due to preheating is illustrated in Figure 1.14, which shows the thermal speed-up of 1D *adiabatic* laminar flames in terms of mass flow rate wrt. a reference at 300 K, noted Γ_p , for varying unburnt temperature T_u . Methane-air (a) and hydrogen-air (b) flames are shown for various equivalence ratios. It is observed that the sensitivity of flames to preheating increases with decreasing equivalence ratio, and seems larger for H_2 . This will be discussed further in Chapter 3 because a conceptual difficulty lies here when this sensitivity is linked to the Zel’dovich number. Note that there exists a threshold value for T_u beyond which the notion of laminar flame speed vanishes, leaving its place to auto-ignition of the mixture “everywhere” [121]. This occurs when the notion of diffusion length scale becomes irrelevant, that is, when diffusion does not play its role of step-by-step preheating against convection, and when the reaction zone becomes larger [122].

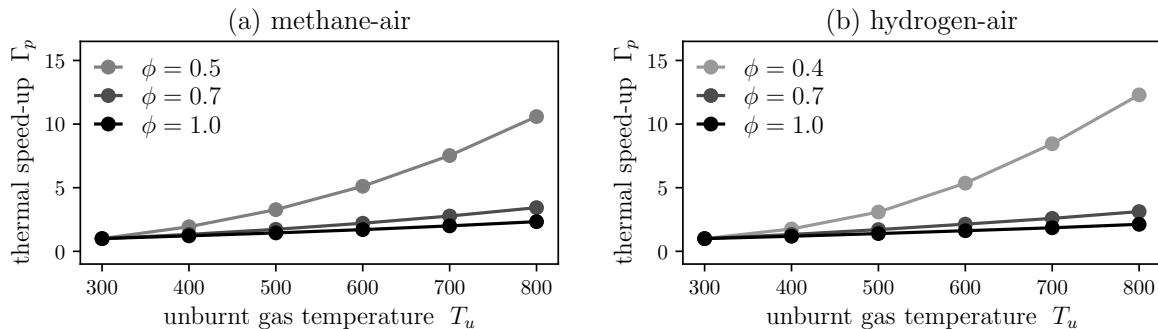


Figure 1.14. – Flame acceleration (speed-up) Γ_p as a function of the unburnt temperature T_u .

More elaborate sources of multiplicities for 1D flames. There exists further subtleties associated with the unicity of the solutions even in the adiabatic case, when the Lewis number is not equal to 1 and when special forms are given for the reaction rates [123, 124]. This illustrates how the multiplicity of solutions for diffusive-reactive equations is far from being an easy topic - which has lost momentum the last two decades given the technical difficulties to answer somewhat theoretical situations, and the extensive use of numerical tools that show excellent agreement with experiments. In addition, there is the question of the influence of complex chemistry on this unicity, but this leads us very far from the objective of this thesis. To some regard, though some exotic flames can be computed theoretically, they may not be found in practice.

In heat-recirculating systems, the coupling with the wall both adds and extracts heat to the flame. Considering the aforementioned influence of non-adiabaticities on flame speed multiplicity, it is expected that porous media burners systems present multiple solutions. These are now reviewed.

1.2.6.4. 1D structure of a flame inside a porous burner

Before discussing the multiplicity of solutions in porous burners, we provide in Figure 1.15 a 1D schematic view of the flame structure inside a porous matrix of finite length. The gas/solid temperature profiles and the heat release rate are drawn respectively in black, dashed grey and red, and the porous burner is drawn in light grey in the background. On each side of the diffusion+reaction region (*i.e.* the flame front) are found the preheating and cooling (relaxation) regions. Overall, the heat transfer from the solid to the gas phase is positive before the flame front and negative afterwards. One can see that flame structure inside the porous medium is very close to the schematic illustration of heat recirculation given in Figure 1.4.

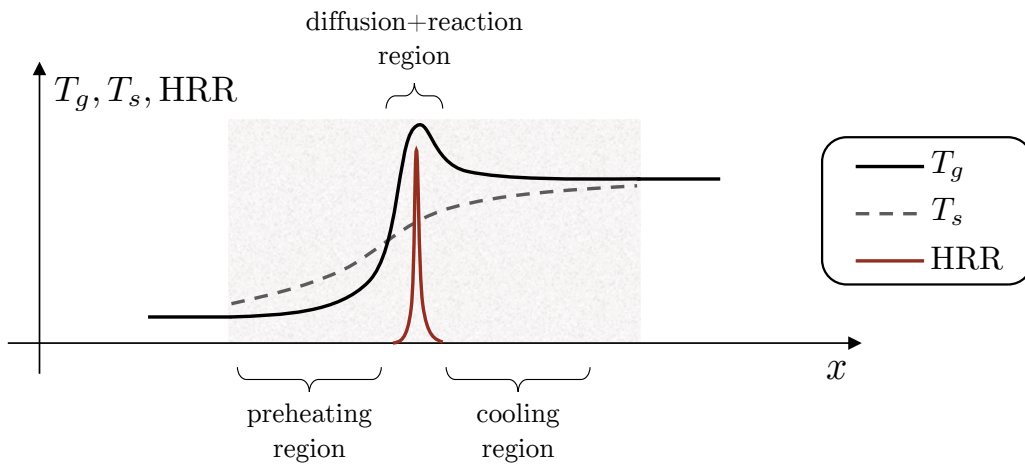


Figure 1.15. – Schematic view of the flame structure inside a porous burner of finite length, illustrating heat recirculation and the various regions of heat transfer, release and diffusion.

1.2.6.5. Heat recirculation, multiple flame speeds and solutions

Conceptually-speaking, the interaction of the flame with a solid provides additional degrees of freedom in the space of possible solutions. Bearing in mind the previous remarks on non-adiabatic combustion and multiple flame speeds, it is therefore reasonable to expect that heat-recirculating devices, which both extract and provide heat to the gas, present operating multiplicities. These can take the form of:

- **Type 1 multiplicity:** different flame locations for the same burning rate ;
- **Type 2 multiplicity:** different burning rates and temperature profiles for a given flame position in the system.

To understand how this occurs, let us move our attention to the specific case of porous burners of finite length. Figure 1.16(a-f) reports qualitatively gas (black) and solid (dashed grey) temperature profiles for multiple steady-state solutions computed numerically by a 1D model of a finite-length porous burner, extracted from the works of Mendes et al. [125]. Figure 1.16(g) reports accordingly the corresponding burning rates \dot{m}_∞ for varying flame positions x . Two types of flames are reported. “Strong” flames of large mass flow rate (bell-shaped curve in

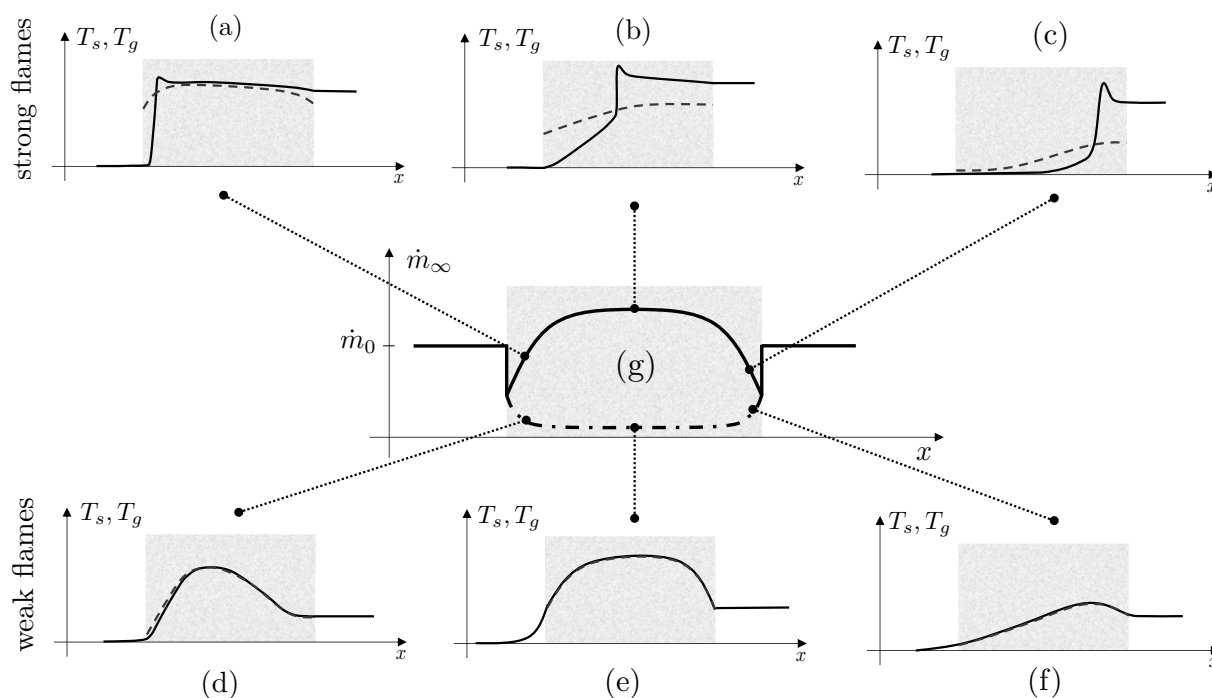


Figure 1.16. – Multiplicities and flame shapes in porous burners of finite length (schematic representation, adapted from the results of [125]). In (a) \rightarrow (f) the gas and solid temperature profiles are shown respectively in solid black and dashed grey, while (g) represents the diagram mass flow rate \dot{m}_∞ vs. position x . The porous medium is represented in light grey. \dot{m}_0 is the mass flow rate of the 1D adiabatic laminar flame.

Figure 1.16(g)) and “weak” flames [126, 127] of lower mass flow rate (U-shaped curve in Figure 1.16(g)). The flame position is pinpointed, say, by the maximum of heat release rate. The mechanisms leading to the bell-shaped curve for strong flames will be described in Chapter 3 [128, 129]. Overall, the flame position in the porous medium in steady state is always characterized by the equilibrium between diffusion, convection, reaction, and heat exchange between the gas and solid phases. Those lead to both Type 1 and Type 2 multiplicities. Strong flames are typically characterized by a stronger non-equilibrium between the gas and solid temperature profiles, whose burning rate is mostly dictated by the preheating (which follows itself a bell-shaped curve). Weak flames are characterized by extensive interphase equilibrium, and they may also be defined as the low-velocity branch in non-adiabatic systems [126]. Overall, weak flames are more difficult to observe in experiments [127, 130]. Their low burning rate may not be beneficial in practical applications [131], and as shown in [125] they may also present partial oxidation of the fuel. Therefore, weak flames are not addressed in this manuscript.

1.2.6.6. Sub-adiabatic combustion

Following Figure 1.13, when the heat extracted from the flame is not recycled properly to enhance combustion kinetics and local temperatures, then the flame may show burning velocities lower than adiabatic. This occurs when the heat losses to the exterior are so large that the heat recirculation is not sufficient to overcome local heat losses in the reaction zone. This situation, - typical of surface combustion [132] where the flame loses energy upstream to the solid - can also be found in porous burners [133].

Because weak flames are rarely observed and of low practical interest, only strong flames are considered throughout this thesis. When radiation and other losses are neglected, subadiabatic combustion is discarded similarly.

1.2.7. Stabilization mechanisms in porous burners

1.2.7.1. Hydrodynamic vs. thermal stabilization

In a classical free-flame burner, flame stability and shape are mostly dictated by the hydrodynamic field. For the canonical case of a bunsen flame, the flow rate determines the angle of the flame cone, and must fall between maximum (blow-off) and minimum (flashback) values. A simple bunsen burner is therefore designed so that, for varying flow rate, the flame remains anchored near a given location. In porous burners, an additional stabilization mechanism intervenes, related to the heat recirculation. Generally-speaking, the flame position is such that the heat budget of the gas+solid system is balanced. This is a *thermal stabilization mechanism*, in contrast with hydrodynamic stabilization. Due to the bell-shaped curve mass flow rate *vs.* position, blow-off is reported to occur near the mid-section of the burner, and flashback occurs near the upstream edge of the burner due to the constriction related to porosity [134, 135].

In real burners, thermal stabilization does not exclude a local anchoring of the flame within the porous structure. At pore scale, it has been recognized through 2/3D numerical simulations, that the flame fronts are not planar and can be stabilized similarly to free-flames at pore scale [136, 137]. For a given flame position, there may be an adaptation mechanism in which the flame surface adapts to keep the same anchored position for a varying mass flow rate. This is illustrated in Figure 1.17, which shows one of our numerical simulations of submerged combustion for a 20% increase in inlet velocity. It is seen that the flame remains attached to the same pores with a different area. Conceptually-speaking, these local augmentations in flame surface may influence the ideal bell-shaped curve of Figure 1.16(g), as illustrated schematically in Figure 1.18. This effect is expectedly further increased in the presence of porous matrix non-homogeneities, and may vanish for stochastic systems on average. However, for lattice-based porous burners this effect may become preponderant. Conditions in which the flame may be planar or not and afferent discussions can be found in Chapters 2 and 6.

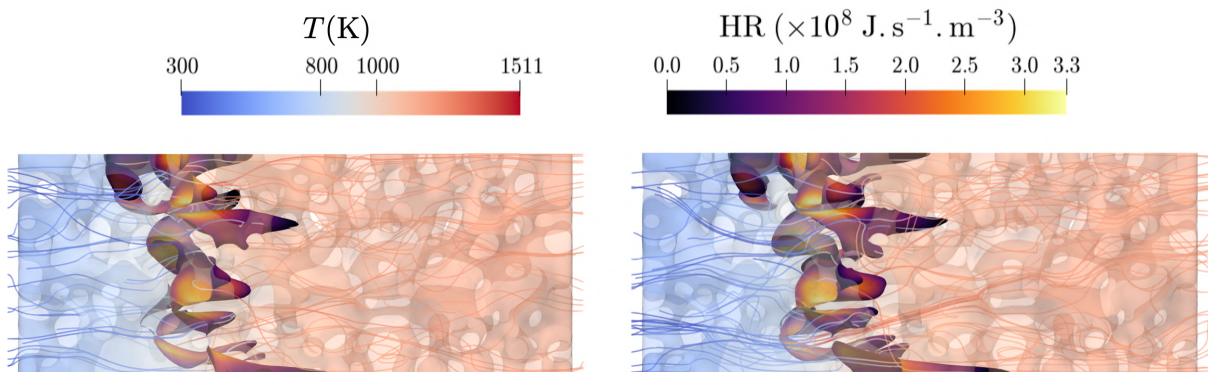


Figure 1.17. – For the same flame anchoring positions within the pores, augmentation of flame surface for an increase in inlet velocity ($1.0 \rightarrow 1.2 \text{ m s}^{-1}$). Hydrogen-air, $\phi = 0.3$, chemical scheme Boivin. The flame surface is defined by 50% of fuel consumption.

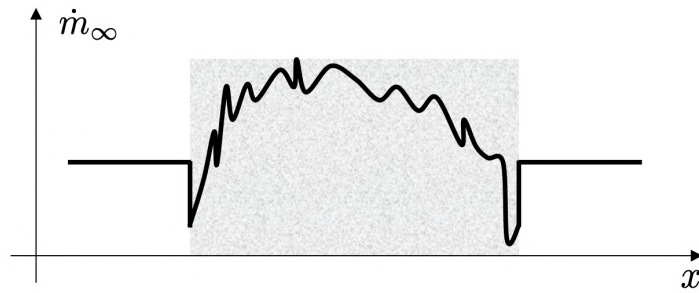


Figure 1.18. – Schematic representation of the pore-level anchoring influence on the stability diagram of a porous burner (strong flames only).

1.2.7.2. Stability of the solutions

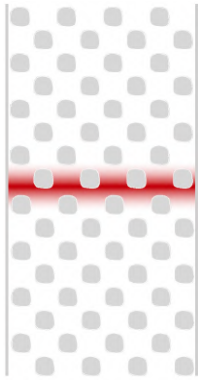
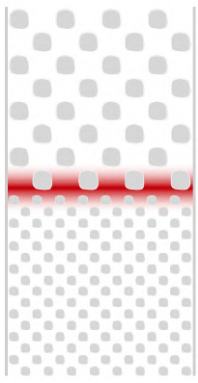
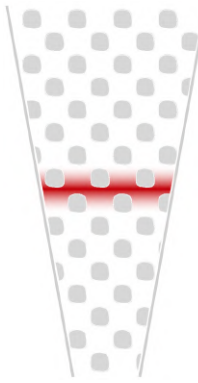
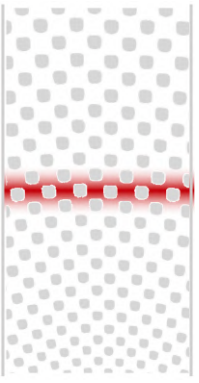
Although the various solutions shown in Figure 1.16 theoretically enforce the governing equations and thermal equilibrium, these are not necessary all stable. In [138] it was first theorized that only flames showing a positive slope of mass flow rate *vs.* position (*i.e.* $\partial\dot{m}_\infty/\partial x > 0$) are stable. The rationale is that, for a small downstream (resp. upstream) disturbance of the flame position for a fixed \dot{m}_∞ , the resulting flame speed is larger (resp. lower), which brings back the flame to its original position. For the regions $\partial\dot{m}_\infty/\partial x < 0$, downstream disturbances lead to blow-off and upstream disturbance to flashback (or, in each case, to another stable point of the burner). This fact was supported experimentally [139] and numerically [34]. So as to compute unstable solutions, it is necessary to fix the position of the flame in the domain: in that case the mass flow rate is an eigenvalue. It is only in [125] that a “rigorous” study of flame stability was achieved by means of Linear Stability Analysis (LSA) on the discretized equations. Although strong flames seem to follow roughly the simple pattern described above, it seems that radiation has a stabilizing role by extending the stable range beyond the mid-section, even when $\partial\dot{m}_\infty/\partial x < 0$. For weak flames, surprisingly the stability criterion is different: regions of negative slope are stable and vice-versa, but since these are found in the upstream section again, one can conclude that flames in porous media should be observed in the upstream regions only. Note that pore-scale anchoring may allow local stabilization, because as shown in Figure 1.18 variations in flame area promote portions of $\partial\dot{m}_\infty/\partial x > 0$ throughout the porous medium. This was observed recently in experiments performed at IMFT by F. Muller (unpublished results).

1.2.7.3. Burner design variations

In the previous sections, the case of homogeneous burners (*i.e.* with uniform pore diameter, material, porosity, etc.) was reviewed. It is illustrated in Table 1.2(a). However, as stressed in [140] and visible on Figure 1.16(g), uniform burners are intrinsically prone to flashback: due to the constriction of the flow near the inlet (porosity effect), the stable mass flow rate in front of the porous matrix is larger than inside: a flame reaching the inlet of the burner will flashback. Also, 1D theory predicts that uniform porous burners present unstable flames in their downstream half. In order to improve burner stability, various designs were proposed in the literature, and shown schematically in Table 1.2(b-d).

- **step burners:** the concept of two-layer porous burner was first proposed by Hsu et al. in [69]. The intention was to fix the position of the flame at the interface between two layers of different physical properties, namely one upstream section with small pores supposedly acting like a flame arrestor, and a downstream section with larger pores used as the combustion zone. The same mechanism was then investigated by Trimis and Durst in [45]. Their results hint towards a propensity of the interface to stabilize the flame.

Table 1.2. – Various designs for porous burners encountered in the literature.

burner type	(a) uniform	(b) step	(c) diverging	(d) graded
design				
primary stabilization mechanism	thermal equilibrium	upstream quenching?	flow divergence	“continuous” quenching?
stability (reported)	+/-	+	+++	++
Refs.	[35, 94, 132] [98, 130, 136] [34, 125, 139]	[45, 69, 141] [34, 142, 143] [30, 144]	[140, 145–152]	[153, 154]

They argued that changes in mass flow rate lead to an augmentation in flame surface locally (multidimensional effect), so that the upstream section acts as a flame holder with the added influence of heat recirculation. From the point of view of the 1D modelling, Diamantis et al. [34] argued that two-layer combustion is governed by a combination of surface combustion from the upstream layer and a submerged mode within the downstream layer, with a reaction zone spanning over the two layers simultaneously. When there is a porosity jump between the two sections, then the stabilization effect is enhanced and somewhat easy to understand: the sudden expansion of the flow creates a local anchoring effect, even from the point of view of the 1D equations (see [142] with 0.1/0.9 porosity jump and for a resulting power range of 1-10). However, for a pore size jump with constant porosity, the anchoring at the interface is not as easy to explain. Indeed, the common argument that there exists a limit Péclet number below which flame propagation in the upstream section is prevented, as found in classical theory of quenching [114, 119, 120, 141, 155, 156] implicitly supposes that the walls are at a fixed (cold) temperature, *which is not the case in the presence of heat recirculation*. This explains why some authors did observe a propagation of the front in the upstream section and flashback, even for very small pores [69, 143, 144]. Since flashback is already observed in surface combustion of single-layer burners [132], it is not surprising that the addition of a downstream layer promotes even more flashback, in the presence of conductive and radiative feedback. Also, it should be mentioned that there are strong shortcomings of 1D models near the interface, because volume-averaged models are known to be less valid near the boundaries. In addition, to date no 3D DNS of two-layer combustion was performed in realistic geometries, so pore-scale mechanisms for flame stabilization remains to be substantiated properly. Incidentally one may note the study of Ellzey and Goel [30] which found step burner to produce less

CO and NO than uniform burner.

- **diverging burners:** starting from the fact that in steady state the local flame speed must be equal to the flow velocity, a diverging design for the porous burner naturally comes to mind. The expansion and progressive deceleration of the flow downstream allows to accommodate a broad range of operating conditions [145]. The very high velocity upstream prevents flashback, while heat recirculation substantially delays blow-off. In that line of thought, Bakry et al. [140] have shown experimentally that the divergent design is helpful in stabilizing flames at elevated pressures and temperatures, which may lead the way to usage in industrial combustion chambers and turbomachinery. Several studies found that using a diverging geometry may be efficient for fuel reforming applications [146–148]. In their hydrogen-air micro-combustion application, Qian et al. [149] found the divergent geometry to yield a 186% increase in blow-out limit and 70% increase in radiation efficiency compared to a straight channel. Dai et al. [150] recently simulated a 2D diverging burner and found an optimal opening angle of 15° for maximum H_2 production. For methane-air combustion, the burner of Hashemi et al. [152] found an optimal angle of 60° . Similar 2D numerical studies may be found in [151]. Voss et al. [157] used a conical burner to compare a 1D numerical model and thermocouple measurements - and found rather good agreement between the two. However, a warning must be raised upon the fact that thanks to the flow expansion, the flame remains near the inlet for large flow rate variations: this may artificially make 1D models and experiments match regardless of modelling issues. Therefore, diverging geometries should not be used to validate fine predictions of 1D models.
- **graded burners:** more recently, Sobhani et al. proposed a novel design based on progressive spatial gradation of the porous matrix properties, either through multiple steps [153] or via continuous additive manufacturing [154]. Their results tend to show that pore-graded topologies (smaller pores upstream) outperform conventional two-step burners, while porosity gradation (lower porosity upstream) is detrimental. The proposed rationale is that a larger range of Stanton numbers reached inside the burner be favorable to burner stability. However, the flame structures and locations inside the porous matrix were not addressed in a comprehensive fashion, and the proposed reasoning is questionable. Notably, no comparison against uniform burners was given. Also, there seems to be an issue with comparing continuous and step burners fundamentally, because the heat transfer at the interface of two stacked porous media is much less than that within a continuous structure. In addition, in [154] pore-size gradation was not achieved independently of an “opposite” porosity gradation (larger porosity upstream), which is a strong confounding factor given the results on porosity gradation. But the biggest issue is probably the absence in the literature of 3D pore-scale simulations which would justify how porosity gradation stabilizes the flame (or not). Overall, as we will show in our 3D pore-level simulations it is possible that the phenomenon observed experimentally be attributed to variable intensity of local quenching effects of the flame front. Upstream (smaller) pores may reduce burning rate, while in larger pores downstream the flame is more independent of the wall (less quenching) and may present larger corrugation (thus larger burning rate). Because these phenomena are absent from current 1D volume-averaged models, this may explain the large discrepancies between 1D simulations and experiments in [153, 154]. Although there seems to be shortcomings in the current understanding of graded burners, it remains a great research topic which shall be addressed in the future, because it leads to the corollary question: how do real flames and volume-averaged models behave for varying pore diameter? This issue is addressed in Chapter 2 and 6.

1.3. Motivations and objectives of the thesis

In this chapter, we have reviewed concepts associated to heat recirculation and flame stabilization inside porous burners, mostly through the prism of 1D assumption. Of course, reactive interstitial flows within porous media are complex 3D objects which present many subtleties at pore scale. Unfortunately, due to the opacity of the solid matrix, there are neither easy and reliable visualisation techniques of the local flame structure within porous burners [158], nor accurate measurements of basic quantities such as local velocities, temperatures and concentrations. This paves the way for detailed numerical simulations, which are hard to set up, computationally-intensive, and therefore limited to small domains and/or simplified geometries.

As we will see in the following, cheap alternatives to 2/3D detailed numerical simulations are *low-order, filtered models*, as used extensively in the literature [34, 159]. Those are typically established from a filtering of the equations in space (*i.e. volume-averaging* [160]) over a certain Representative Elementary Volume (REV). The size of the REV should not be too small, to avoid catching pore-scale non-homogeneities, but not too large to avoid catching macro-scale gradients. Obviously, the filtering process comes with a certain loss in local information - and requires *closure terms* at the macroscopic scale. This yields, from the microscopic conservation equations, macroscale counterparts with *effective modelling terms* of prescribed functional form and associated coefficients. For example, the influence of tortuosity and porosity of the solid matrix may be viewed, at the macroscale, as a modification of the solid conductivity compared to the bulk material.

Unfortunately, this averaging step is intrinsically flawed in the presence of local discontinuities at the scale of the REV, which typically occurs in the presence of combustion flame fronts in the gas phase. As shown schematically in Figure 1.19, when the pore size d_p is larger than the flame thickness δ_L , sharp flame fronts develop and anchor locally: combustion does not occur *in volume* at the scale of the REV, meaning that the standard hypothesis of commutation between reaction rates and volume-averages is not valid. As in LES for turbulent combustion, this is particularly problematic for the determination of macroscopic burning rates [115], which may explain the difficulties of state-of-the-art volume-averaged models to predict stable burner operating ranges with good accuracy. To the best of the author's knowledge, there does not exist combustion models for porous media combustion taking into account these local features.

Accordingly, closing the gap between volume-averaged models and experiments is, as we will see throughout this manuscript, a tremendous task that will take many more years to accomplish (if even possible). Yet, this goal in mind, this Ph.D. work concentrates on various modelling aspects of porous media combustion, both from the point of view of the volume-averaged models and the microscopic equations. The idea is to bring further insights onto the phenomenology of volume-averaged models on the one hand, and unveil realistic pore-scale combustion mechanisms on the other hand:

- first, an in-depth study of the behavior of volume-averaged models is proposed, to complement current knowledge of combustion regimes in porous media, as well as important intrinsic properties of the coupled gas/solid system such as flame speed, which are still lacking in the literature ;
- then, 3D direct pore-level numerical simulations are performed in realistic geometries, so as to unveil the pore-level characteristics of the flame structure and compare quantitatively the resulting fields to state-of-the-art volume-averaged predictions ;
- having understood the phenomenology of the volume-averaged equations and that of a real flame through direct numerical simulations, a first combustion model for reaction rates in porous media is proposed. The intrinsic hurdles and flaws of the volume-averaged are highlighted quantitatively.

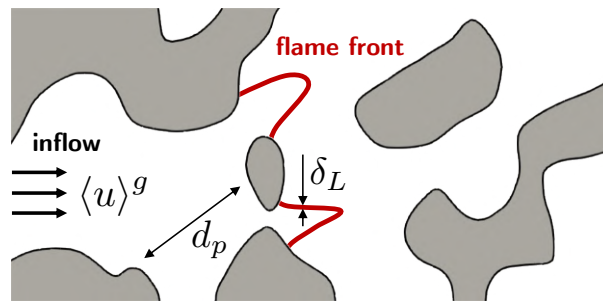


Figure 1.19. – Illustration of typical pore-scale phenomenology: sharp flame fronts anchored locally.

1.4. Outline of the manuscript

- **Chapter 2** is an extension of the literature review presented in Chapter 1, with an emphasis on the physical phenomena related to mass and heat transfer within porous media (dispersion, turbulence, pressure drop, etc.). The importance of the ratio of thermal flame thickness to pore diameter for gaseous flames is underlined. Also, the microscopic governing equations used throughout this thesis are presented, and the upscaling procedure yielding the current macroscopic models is described ;
- **Chapter 3** presents asymptotic analyses of flames within porous media based upon the classical 1D volume-averaged equations, supposing that reaction occurs infinitely fast. For infinitely-long porous media, it is shown that the problem is governed by two dimensionless parameters. In the case of low heat coupling with the wall (decoupled regime), the first fully-explicit formulae for flame speed within porous media are given. This is arguably of academic and practical interest, as the resulting expressions are capable of explaining many previous literature results found in simulations and experiments. Effects of burner finite length are also addressed, and an universal abacus to assess their maximum heat recirculation potential is provided. Also, the case of multi-layered burners is addressed theoretically for the first time, with a notable discussion on the influence of the heat transfer condition between two solid stages ;
- **Chapter 4** extends the results of Chapter 3 by relaxing the hypothesis of infinitely-thin reaction sheet. A wide exploration of the parametrization spectrum allows to unveil the existence of three combustion regimes for increasing interphase heat transfer, named respectively decoupled, intermediate and hyperdiffusive. In addition to Chapter 3, which provided a formula for flame speed in the decoupled regime, the proposed framework provides another formula for the hyperdiffusive regime. The chapter provides also a conceptual vision to reconcile the frameworks of LTNE and LTE (hyperdiffusive regime) through a progressive modification of the superadiabaticity and effective diffusion in the gaseous phase. It is shown that the stiffness of the mixture (related to the Zel’dovich number) explains the influence of chemistry and equivalence ratio on maximum temperatures found in previous studies. Based upon the asymptotic model of Chapter 3, an universal formula for flame speed valid in all regimes is proposed.
- **Chapter 5** presents the pre-processing steps of the 3D numerical simulations - notably the difficult meshing step - from a tomographic X-ray scan to 3D unstructured tetrahedral computational mesh. This chapter is somewhat “technical” and meant to be used by the community as a tutorial, because the meshing of random, reticulated structure poses a technical challenge that must be alleviated to enable more studies to be done in the field ;
- **Chapter 6** presents results of the 3D simulations and links them to the state-of-the-art

1D volume-averaged models. It is suggested that in classical burners, where the flame thickness is smaller than the pore diameter, current models present intrinsic shortcomings which hamper them from predicting quantitatively the burning rates and physical profiles. The validity of macro-scale modelling terms are discussed, and the first closure term for reaction rates is proposed to try and correct the volume-averaged models. It is shown that hydrodynamic dispersion does not account for the burning rate of flames within porous media, and has no reason to have a strong influence at the pore level. We suggest that afferent interpretations found in the literature in terms of extra mixing should be taken with caution ;

- **Chapter 7** presents the specifics of H₂ combustion within porous media. Based upon a literature review, the possible phenomena occurring within porous media, related to the preferential diffusion of species, are listed. Then, the first 3D simulations of hydrogen combustion in porous burners are shown and discussed. It is shown that the structure of hydrogen flames is strongly multi-dimensional and comes with further modelling challenges. The propensity of hydrogen flames to flashback in large pores is also underlined.

Figure 1.20 presents the triptych theory/simulations/experiments and the conceptual positioning of the various chapters.

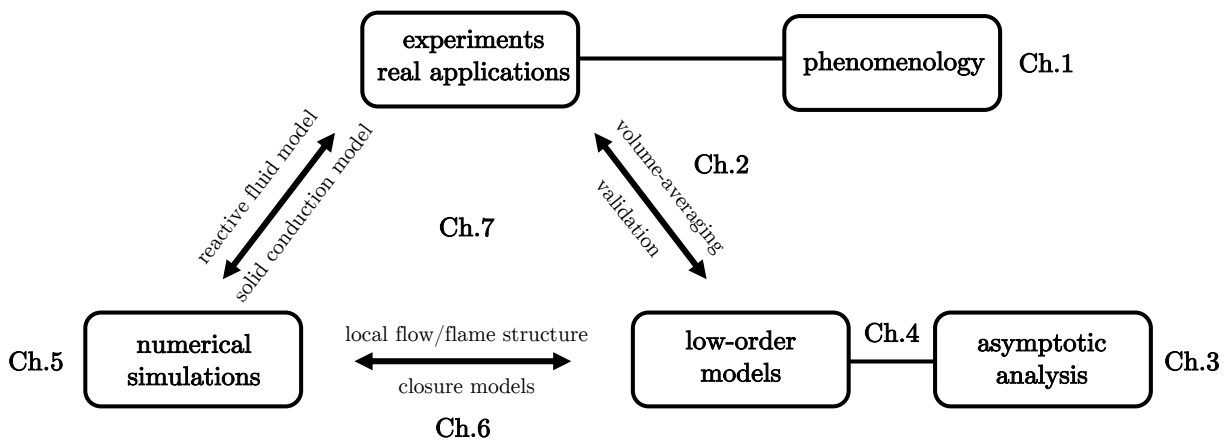


Figure 1.20. – Outline of the manuscript.

1.5. Publications during the thesis

1.5.1. Works related to porous media combustion

- **Masset, P. A.**, Duchaine, F., Pestre, A. & Selle, L. (2022). Modelling challenges of volume-averaged combustion within porous media. *Combustion and Flame, to be submitted*.
- **Masset, P. A.**, Dounia, O., & Selle, L. (2021). Porous media combustion: from decoupled to hyperdiffusive flames. *Combustion and Flame*, 241, 112052.
- **Masset, P. A.**, Dounia, O., & Selle, L. (2021). Fully explicit formulae for flame speed in infinite and finite porous media. *Combustion Theory and Modelling*, 1-28.

1.5.2. Other works

- **Masset, P. A.**, & Wissocq, G. (2020). Linear hydrodynamics and stability of the discrete velocity Boltzmann equations. *Journal of Fluid Mechanics*, 897.
- Mader, A., Born, L., Körner, A., Schieber, G., **Masset, P. A.**, Milwich, M., ... & Knippers, J. (2020). Bio-inspired integrated pneumatic actuation for compliant fiber-reinforced plastics. *Composite Structures*, 233, 111558.

From micro to macroscopic scale

A proper modelling of porous media combustion requires a correct understanding and interpretation of the physical phenomena taking place at both microscopic and macroscopic scales. To that end, this chapter reviews the phenomenology of heat and mass transfer within porous media, including: dispersion, interphase heat exchange, effective thermal conductivities, radiation, turbulence, pressure drop, and of course, chemical reactions. A classification of associated regimes in terms of various dimensionless numbers is given. Then, the volume-averaging mathematical steps from micro to macroscale equations are provided, casting some light on the assumptions underlying volume-averaged equations currently used in the literature.

Overview

2.1. Flow, flames and heat transfer within porous media	28
2.1.1. Physical phenomena at micro and macroscales	28
2.1.2. Flow regimes	29
2.1.3. Pressure drop	29
2.1.4. Turbulence	30
2.1.5. Interphase heat exchange	32
2.1.6. Dispersion in the gas phase	33
2.1.7. Influence of the pore diameter	36
2.1.8. Summary of reduced parameters	38
2.1.9. Heat transfer through the solid matrix	39
2.2. Modelling equations and upscaling hypotheses	41
2.2.1. Classical stationary volume-averaged equations	41
2.2.2. Pointwise governing equations	42
2.2.3. Volume-averaging	44
2.2.4. Conclusions of the chapter	50
2.A. Geometrical proof of the spatial averaging theorem	51
2.B. Deviation terms for products of N quantities	52

“A great deal more is known than has been proved.”

RICHARD FEYNMAN

2.1. Flow, flames and heat transfer within porous media

2.1.1. Physical phenomena at micro and macroscales

Heat and mass transfer within porous media have been the topic of extensive research and excellent reviews on the topic can be found in [161, 162]. Most of the time, research has focused on unveiling the relationship between pore-scale physics and macroscale modelling. In porous burners, this task is particularly difficult, because all the following intertwined phenomena take place simultaneously at the microscopic scale:

- convection of the flow within the interstices ;
- heat and mass diffusion in the gas phase ;
- heat diffusion in solid phase ;
- chemical reactions in the gas phase ;
- radiation (gas↔gas, solid↔solid and gas↔solid) ;
- viscosity-related friction at the core and boundaries of the flow.

Some of these *microscale* phenomena are illustrated directly on Figure 2.1, on a slice extracted from one 3D DNS performed in this thesis. The temperature of the gas and solid are shown in blue/red, heat release in black, and the interphase gas/solid is colored by the wall heat flux intensity in green/purple. The presence of superadiabatic pockets is observed. In the simulation radiation was not considered so it is illustrated only schematically.

Note that chemical reactions near the fluid/solid boundary (such as catalytic combustion) are excluded from the present work. The same goes for gas↔gas and gas↔solid radiation, which are assumed negligible compared to solid↔solid radiation and conduction. At the macroscopic scale, the listed phenomena give rise to “effective” phenomenologies and properties of the flow. For instance, the tortuosity and porosity of the solid matrix lead to the notion of effective thermal conductivity at the macroscale. Other phenomena include pressure drop, turbulence, volume interphase heat exchange, dispersion, etc. Those are reviewed in this section with afferent reduced parameters.

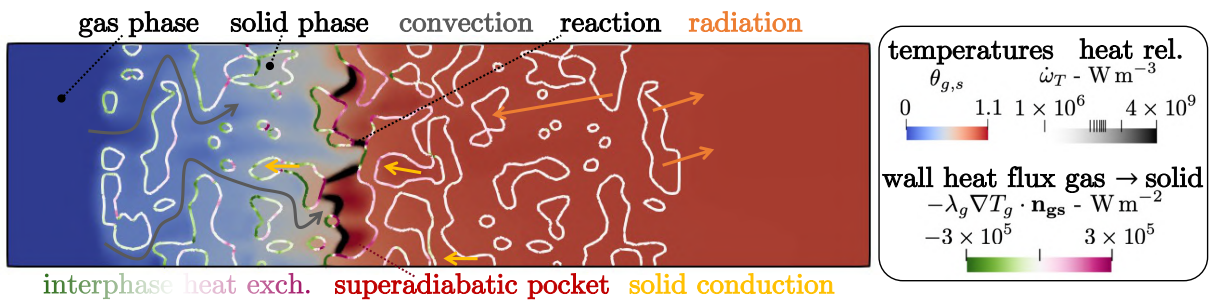


Figure 2.1. – Illustration of various microscale phenomena occurring in porous media combustion on a slice extracted from a 3D DNS. Afferent notations are introduced later in this chapter. Superadiabatic regions correspond to reduced temperatures $\theta_g > 1$.

2.1.2. Flow regimes

Let us begin with some vocabulary specific to flows within porous media. For increasing interstitial velocities, a variety of flow regimes are successively encountered, as summarized in Table 2.1. The so-called Darcy regime corresponds to low-velocities where the Stokes flow approximation applies: the flow is steady and dominated by viscous forces. For larger velocities, the Forchheimer regime encompasses both steady and unsteady states, from laminar to the transition to turbulent: inertial forces become more and more dominant. Note that the Forchheimer and turbulent regimes are sometimes put together under “non-Darcian” denomination.

regime	Darcy	Forchheimer		turbulent	
flow state	laminar			transition	fully-developed turbulent
	steady		unsteady		
	linear	non-linear			

Table 2.1. – Various flow regimes for increasing interstitial velocities inside porous media.

2.1.3. Pressure drop

The porous medium acts obviously as an obstacle to the incoming flow. The no-slip conditions, the internal shear layers, but also the turbulent eddies if present all dissipate kinetic energy through mechanical stresses, which, once averaged at the macroscopic scale, lead to an overall pressure gradient. For low porosities and very small pore sizes, as found in air/water filters [163] and in soil exploration [164], this pressure drop may become substantial [165]. In a 1856 report concerning the water supply system of the French city of Dijon, Henry Darcy proposed an empirical, linear law relating the pressure drop and infiltration velocity in sand filters [166], valid in the Darcy regime. Adapted in more modern notations, it writes:

$$-\frac{\partial P}{\partial x} = \frac{\mu \langle u \rangle^g}{k_p}, \quad (2.1)$$

where P is the (macroscopic) pressure, x the flow direction, μ the dynamic viscosity, k_p a permeability factor and $\langle u \rangle^g$ the intrinsic (interstitial) velocity ($\langle \cdot \rangle^g$ is the intrinsic volume-average in the fluid phase, defined later in the chapter). By viewing the porous medium as a network of small tubes where many laminar Poiseuille flows take place simultaneously, approximate analytical expressions for k_p may be obtained [167–169]. A more general analysis can also be performed through volume-averaging asymptotics [170], yielding the same linear relation for macroscopic pressure gradient at low flow velocities. Of course, deviations from the simplistic Darcy’s law are observed experimentally at larger velocities [171], when inertial forces become predominant. Many correlations were proposed to complement Darcy’s law [172], one of the most famous being the Forchheimer correction [173]:

$$-\frac{\partial P}{\partial x} = \frac{\mu \langle u \rangle^g}{k_p} + \beta_F \rho_g [\langle u \rangle^g]^2, \quad (2.2)$$

where β_F is a non-Darcy (also called Forchheimer) coefficient and ρ_g the fluid density. Physically, the term $\rho_g [\langle u \rangle^g]^2$ corresponds to the well-known dynamic pressure - coherent with the common assumption that deviations from linear are due to increasing inertial effects. The transition from Darcy to non-Darcy being governed by the relative importance of inertial to viscous forces, the Reynolds number is classically used to discriminate the two regimes:

$$\text{Re}_p = \frac{\langle u \rangle^g d_p}{\nu}, \quad (2.3)$$

where d_p is the mean pore diameter, ν is the kinematic viscosity. Other definitions for the Reynolds number, based on the particle diameter (solid phase) or permeability can be found in the literature [171]. That based on the permeability is sometimes termed Forchheimer number. For that reason, but also because there is a very large spectrum of fluids, flow configurations and pore geometries, it is impossible to provide a general criterion to when Darcy's law applies. Most of the time, permeability k_p and Forchheimer coefficient β_F are fitted over experimental data.

For porous media burners, Equation (2.2) was shown to be sufficiently accurate in [174], with typical pressure drops of the order of 0.5-5% [174, 175]. For the sake of illustration, Figure 2.2 presents a typical pressure field obtained in a numerical simulation performed during this thesis, where a typical value of 3% is found for pressure drop. In such proportions, the influence of pressure variations on combustion is negligible, thus low-order models may be considered isobaric. Accordingly, this manuscript does not investigate further macroscopic pressure gradients - their proper prediction and modelling constituting an entire field of investigation alone [172].

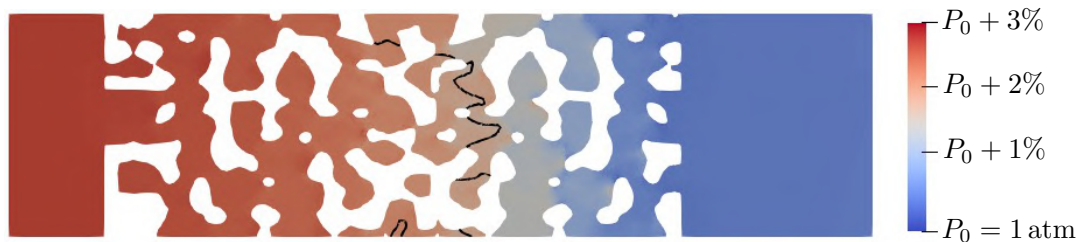


Figure 2.2. – Illustration of pressure drop in porous media combustion. Hydrogen-air flame at equivalence ratio $\phi = 0.3$. The black line marks the isocontour 10% of H₂ consumption. Inlet velocity $U_{\text{in}} = 2.5 \text{ m s}^{-1}$. Mean pore diameter $\bar{d}_p = 1 \text{ mm}$.

2.1.4. Turbulence

Turbulence may be characterized by disorganized, chaotic movement of flow, where eddies of different sizes and speeds are observed. It can be defined in opposition to laminar flows, which appear well-organized, layer-by-layer, and somewhat dominated by viscous forces. From the early works of Osborne Reynolds discussing the onset of turbulence in a simple tube [176], a plethora of research has been conducted in many types of flows (contained flows, free flows, jet flows), and turbulence remains today an active topic of research in fluid dynamics [177, 178]. Although the threshold values leading to turbulence may depend upon the geometry of the system, the fluid properties, the flow configuration and other variables, the Reynolds number remains the relevant reduced parameter describing whether convective or viscous dissipation dominates, and therefore, whether turbulence exists or not. Of course, one should keep in mind that “turbulence” encompasses a variety of spatial and spectral properties of the flow, and the transition from laminar to turbulent is not sharp. For flow in porous media, following [179, 180] one may find approximate thresholds for a series of regimes in terms of the Reynolds number:

- $Re_p < 25$: **linear (Darcy) regime**, where Stokes flow approximation applies ;
- $25 < Re_p < 375$: **inertial regime**, the flow remains steady and the pores are set of large inertial cores. The velocity field is substantially different from the Darcy regime ;
- $375 < Re_p < 750$: **transitional regime**, the flow becomes unsteady and begins to form large vortical structures and/or intermittency ;
- $750 < Re_p < 3500$: **turbulent regime**, the flow resembles more and more conventional free turbulence ;

- $Re_p > 3500$: **asymptotic regime**, the Reynolds number is so large that turbulence may be approximated locally as isotropic over the pore region.

Figure 2.3 shows cold flow simulations performed in this thesis to illustrate these various regimes in a regular geometry. We noted in our simulations that for random structures (such as Figure 2.2), unsteadiness was triggered for lower Reynolds numbers at a given pore size.

Overall, the modelling of turbulence for porous media at the macroscale is not an easy task, and has been the topic of much controversy [181]. While the low-order modelling of steady flows requires “only” an average in space (volume-averaging), unsteady/turbulent flows require a second average in time (Reynolds averaging). Unfortunately, both averages do not commute. Knowing which method should be applied first is still an open question, as it changes the behavior and phenomenology of the resulting macroscale equations. Antohe and Lage pioneered a $k - \epsilon$ formulation for turbulence within porous media starting by space integration [182]. Their analysis was extended by Getachew and co-workers [183] who included non-linear contribution from the Forchheimer term in the time-averaged momentum equation, leading to extra terms in the momentum, turbulent kinetic energy and dissipation rate equations. Nakayama and Kuwahara [184] developed a volume-averaged formalism of the microscopic $k - \epsilon$ equations and found some agreement with 2D numerical simulations over a periodic array of square rods. The approach starting from time integration was proposed by Masuoka and Takatsu in [185].

A third approach consists in using the so-called double-decomposition method pioneered by

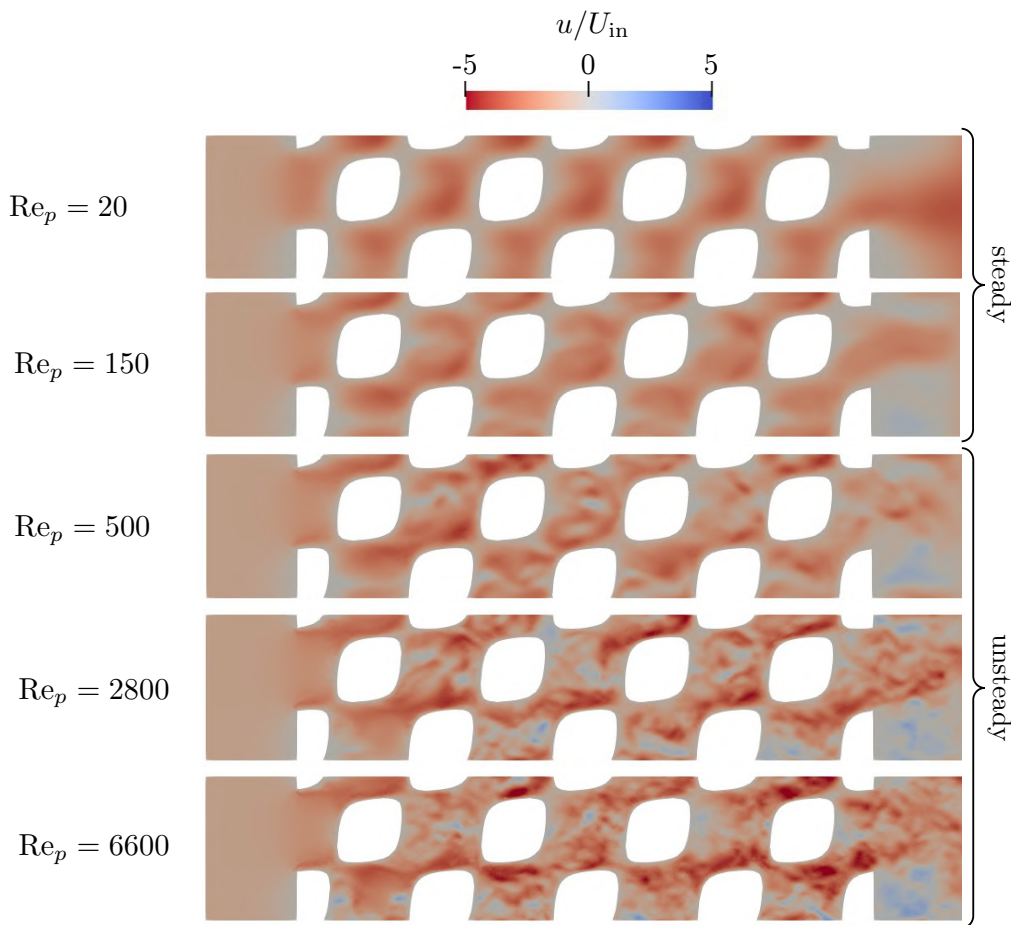


Figure 2.3. – Ratio of longitudinal velocity component u to inlet velocity U_{in} , for increasing pore-based Reynolds numbers Re_p . Each case corresponds to a different listed regime.

de Lemos [186]. This method consists in delaying the final averaging step by writing simultaneously spatial and temporal deviations from the averages and treating the resulting time and space deviation cross-products separately. This modelling was applied for porous media combustion in [187, 188], which compared four different thermo-mechanical models, namely laminar, laminar with radiation, turbulent, and turbulent with radiation. Closure terms for the gas equation involved thermal dispersion, turbulent heat flux, turbulent thermal dispersion and local conduction. Reactions were modelled simply by commuting the reaction rates with the averages (no combustion model). Minor influence of turbulence on the results was found, which may be explained by the low Reynolds numbers found in porous burners, but also by the strong assumptions performed during the volume-averaging procedure. Unfortunately, these modelling aspects remain unsubstantiated by detailed DNS or experiments, so those are still mostly hypothetical. Since there does not even exist a combustion model for reaction rates in steady state, it is not surprising that the addition of fluctuations in time is still not addressed. Another analysis of the influence of turbulence modelling in porous burners is found in [189]: overall only the effect of turbulence on effective diffusivity in the gas energy equation was shown to change the solution by broadening the flame what reduces maximum temperatures. Overall, much more work is required to unveil the specificities of turbulence in porous media combustion. Note that an additional difficulty lies in the fact that due to the presence of the pores, the structure of the flow is largely constrained, and turbulence in each pore is somewhat independent [190], so the classical approaches used in free-flow turbulent combustion might fail without proper handling.

Given the already large complexity of steady combustion within porous media, unsteady/turbulent flows are excluded from the theoretical framework of this thesis.

2.1.5. Interphase heat exchange

When there exists locally a gradient at the gas/solid interface, heat is transferred between the two phases. This typically occurs when the temperatures of the gas $\langle T_g \rangle^g$ and solid $\langle T_s \rangle^s$ are different at the macroscale. Accordingly, a volume interphase heat transfer coefficient h_V (unit $\text{W m}^{-3} \text{K}^{-1}$) is often used to model the heat transfer from the gas to the solid Q_{gs} as:

$$Q_{gs} = h_V [\langle T_g \rangle^g - \langle T_s \rangle^s]. \quad (2.4)$$

In some situations, this heat transfer is so large that the two phases are in thermal equilibrium. This led some authors to consider the framework of Local Thermal Equilibrium (LTE), in which the solid energy equation is discarded and the system gas+solid is viewed as an effective medium [191–193]. This is modelled at the macroscale by an effective heat capacity and conductivity. In porous media combustion however, the large temperature gradients generated by the flame are often incompatible with LTE hypothesis. This is why the Local Thermal Non-Equilibrium hypothesis (LTNE) is rather employed through Equation (2.4), which requires a specific energy equation in the solid phase [194]. In fact, the model of Equation (2.4) is *local*, in the sense that local heat transfer depends only on the local averaged quantities. This is of course overly simplistic to cover all situations, so again keep in mind that this closure term is partly *ad hoc*. In [195], Quintard has shown that a dependency of the heat transfer upon macroscale gas and solid temperature gradients is conceivable - leading to the requirement of additional heat conductivity tensors. In our numerical simulations however, it was found that Equation (2.4) may be sufficient for our application of porous media combustion. This is illustrated in Figure 2.4, which shows a best fit for h_V for an interphase heat transfer per unit volume Q_{gs} given by Equation (2.4). Table 2.2 shows a literature selection of expressions for volume interphase heat transfer coefficient h_V , adapted to the present notations. The correlation of Kuwahara et al. was obtained from 2D DNS on a periodic array of isothermal square rods, implicitly valid for

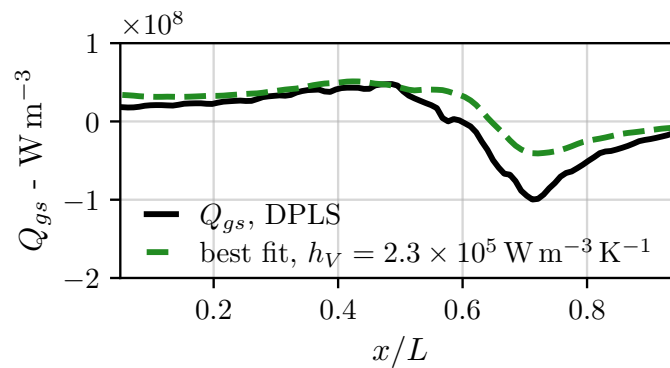


Figure 2.4. – Fit of constant h_V for an interphase heat exchange of the form of Equation (6.26) in a reactive coupled gas/solid 3D DNS performed in this thesis.

solid thermal conductivities much larger than the gas [196]. Their work somewhat catches the experimental values obtained by Wakao and Kaguei for packed beds [197]. Very similar studies were performed by Saito and de Lemos [198, 199] with and without turbulence. Another correlation can be found in the work of Vzukauskas [200]. It is argued from numerical simulations that similar trends are valid for laminar and turbulent flows.

Ref.	Heat transfer coefficient
Kuwahara et al. [196]	$h_V = \frac{\lambda_g \mathcal{S}_V}{d_p \sqrt{1-\epsilon}} \left[\left(1 + 4 \frac{1-\epsilon}{\epsilon} \right) + \frac{1}{2} \sqrt{1-\epsilon} \left(\frac{\text{Re}_p}{\sqrt{1-\epsilon}} \right)^{0.6} \text{Pr}^{1/3} \right]$
Wakao and Kaguei [197]	$h_V = \frac{\lambda_g \mathcal{S}_V}{d_p \sqrt{1-\epsilon}} \left[2 + 1.1 \left(\frac{\text{Re}_p}{\sqrt{1-\epsilon}} \right)^{0.6} \text{Pr}^{1/3} \right]$
Vzukauskas [200]	$h_V = \frac{\lambda_g \mathcal{S}_V}{d_p \sqrt{1-\epsilon}} \left[0.022 \left(\frac{\text{Re}_p}{\sqrt{1-\epsilon}} \right)^{0.84} \text{Pr}^{0.36} \right]$
Saito and de Lemos [199]	$h_V = \frac{\lambda_g \mathcal{S}_V}{d_p \sqrt{1-\epsilon}} \left[0.08 \left(\frac{\text{Re}_p}{\epsilon \sqrt{1-\epsilon}} \right)^{0.8} \text{Pr}^{1/3} \right]$

Table 2.2. – Various expressions for interphase heat transfer found in the literature. Pr is the Prandtl number, \mathcal{S}_V is the surface density, ϵ the porosity, and λ_g the gas thermal conductivity.

2.1.6. Dispersion in the gas phase

We now investigate the phenomenon of dispersion within porous media, which refers to the notion of effective diffusivity at the macroscale related to the meandering nature of the interstitial flow. Because our application cases are 1D burners, the emphasis is put on the longitudinal dispersion coefficient. Transverse dispersion is not considered.

2.1.6.1. Phenomenology of dispersion

Consider the uniform convection of a gaseous free flow as shown in Figure 2.5(a). A thin pulse of a scalar quantity ψ (say for instance, temperature or species concentration) is imposed at time $t = 0$. It is common knowledge that, due to the intrinsic diffusivity within the gas D_ψ^{intr} , after some time Δt the pulse is broadened: this is diffusion. A 1D simplistic conservation equation

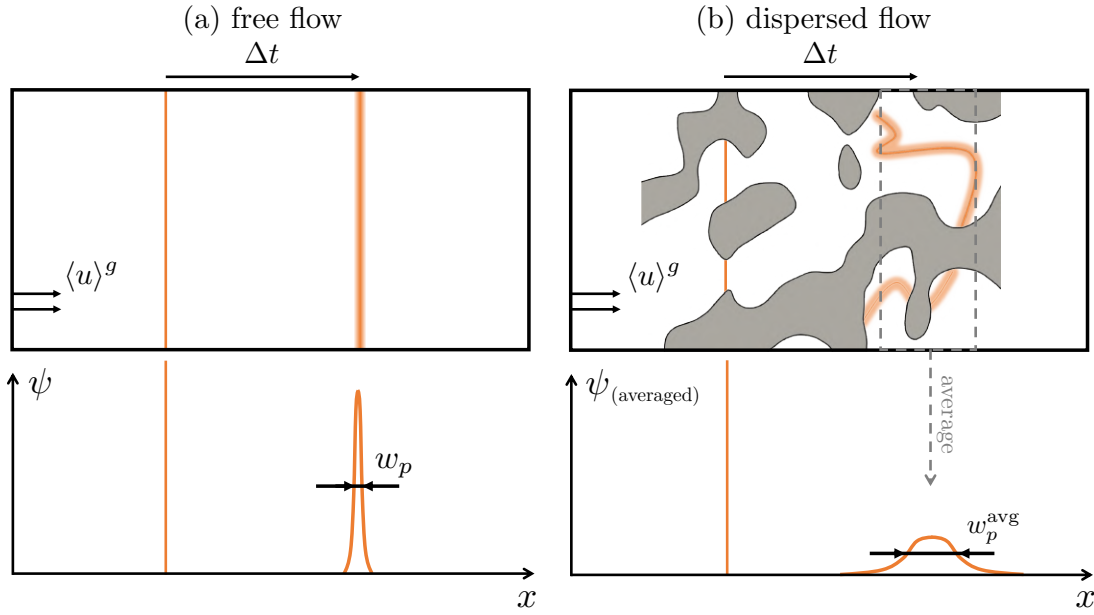


Figure 2.5. – Illustration of dispersion.

for ψ depicting this situation is:

$$\frac{\partial \psi}{\partial t} + \frac{\partial \langle u \rangle^g \psi}{\partial x} - \frac{\partial}{\partial x} \left[D_\psi^{\text{intr}} \frac{\partial \psi}{\partial x} \right] = 0, \quad (2.5)$$

where $\langle u \rangle^g$ is the local flow velocity (bulk in free-flow, intrinsic volume-average in the porous media). In the moving frame of the initial pulse, this yields a length scale for pulse width w_p given by:

$$w_p^2 \sim D_\psi^{\text{intr}} \Delta t. \quad (2.6)$$

Now if the same experiment is done inside a stationary flow within a porous medium as in Figure 2.5(b), the 1D structure of the pulse is destroyed due to the meandering nature of the interstitial flow (effects of velocity gradients, tortuosity, no-slip conditions, transverse diffusion, recirculation zones, etc.). Yet, by *averaging* the resulting ψ field in volume, then a 1D gaussian-like structure may be recovered, reminiscent of the evolution described by Equation (2.5). Of course, the afferent pulse width w_p^{avg} for the same time Δt will be different from w_p . But at the macroscopic scale, one may introduce an *effective diffusivity* D_ψ^{eff} to model the situation of Figure 2.5(b) - a vision valid from a phenomenological point of view. By considering the scaling law of Equation (2.6), this effective diffusivity can be approximated by:

$$D_\psi^{\text{eff}} \sim D_\psi^{\text{intr}} \left[\frac{w_p^{\text{avg}}}{w_p} \right]^2. \quad (2.7)$$

The values of D_ψ^{eff} depend on the relative intensities of diffusion and convection. At pore scale, the dimensionless number discerning their relative importance is the Péclet number:

$$\text{Pe}_{p,\psi} = \frac{\langle u \rangle^g d_p}{D_\psi^{\text{intr}}}, \quad (2.8)$$

where d_p is the pore diameter.

2.1.6.2. Case $Pe_{p,\psi} \ll 1$

When the bulk velocity is very small ($\langle u \rangle^g \rightarrow 0$), then the flow is almost immobile within the porous medium and the diffusion is hampered by the presence of obstacles, which increase the path lengths of the particles wrt. the longitudinal direction. In that situation the final pulse in the porous medium width may be lower than in the free flow. This gives rise to the notion of tortuosity in the gas phase τ_g which may be defined accordingly by:

$$D_\psi^{\text{eff}}(\langle u \rangle^g \rightarrow 0) \sim \frac{D_\psi^{\text{intr}}}{\tau_g} < D_\psi^{\text{intr}}. \quad (2.9)$$

In that regime, advection effects are negligible compared to diffusion, and τ_g is independent upon $\langle u \rangle^g$. The interested reader may find further information on the multiple definitions and ways to determine tortuosity in [201–204]. As advocated in [205], if tortuosity is indeed viewed as the relative extra length required by the particles to travel in the longitudinal direction, then a simple yet insightful estimation of tortuosity computed from the velocity field \mathbf{u} in the flow direction \mathbf{x} is:

$$\tau_g = \left[\frac{\int \mathbf{u} \cdot \mathbf{x} dV}{\int \|\mathbf{u}\| dV} \right]^{N_{\tau_g}}, \quad (2.10)$$

where N_{τ_g} may not be equal to unity [205]. It should be further noted that tortuosity is often recognized in the literature as a “fudge” factor, symptomatic of the difficulties arising with volume-averaging. Typically in this thesis it was found that $\tau_g \sim 1.1 - 1.2$.

2.1.6.3. Case $Pe_{p,\psi} \gg 1$

When, on the contrary, the bulk velocity is large, then advective effects are predominant over diffusion and the effective diffusivity is related to the velocity fluctuations, themselves related to the bulk velocity of the flow:

$$D_\psi^{\text{eff}} \propto \langle u \rangle^g. \quad (2.11)$$

This simplistic view is of course not representative of the plethora of literature developments describing dispersive effects in porous media from experimental, numerical and theoretical viewpoints. And from the early works of Taylor and Aris [206, 207] which modelled the dispersion of a solute in capillary tubes, much experimental [208], numerical [209] and theoretical derivations [210, 211] were performed to predict values for D_ψ^{eff} . It was found again that the Péclet number is the proper reduced parameter governing the regimes of dispersion and its quantitative magnitude. Figure 2.6, adapted from [208], compiles reported literature values of dispersion intensity $D_\psi^{\text{eff}}/D_\psi^{\text{intr}}$ in the case of the mass transport of a solute, for various Schmidt numbers. Although there is some “dispersion” of the results depending on the type of porous medium, geometry, fluid, Schmidt numbers, etc., the highlighted trend is quite unequivocal. It presents the aforementioned tortuosity regime for very low Péclet numbers, and a linear regime for larger Péclet numbers, with a transition near $Pe_p = 1$. The simple asymptotic fit shown in Figure 2.6 is typically used in the literature of porous media combustion - and the author is not aware of any usage of more elaborate models in the field. Although a simple linear trend may appear to be simplistic there is quite robust theoretical evidence that the dispersion coefficients may be simple polynomial functions of the Péclet number [210]. In this thesis it will be assumed that:

$$\tau_g = 1 \quad \text{and therefore} \quad D_\psi^{\text{eff}} = D_\psi^{\text{intr}} + 0.5 \cdot A^{\text{dis}} \cdot \langle u \rangle^g, \quad (2.12)$$

where A^{dis} will be fitted to a given geometry and is related to the pore size (and topology). Incidentally, readers familiar with turbulent combustion may find a direct analogy between dispersion in porous media and turbulent diffusion in free flows [212, 213].

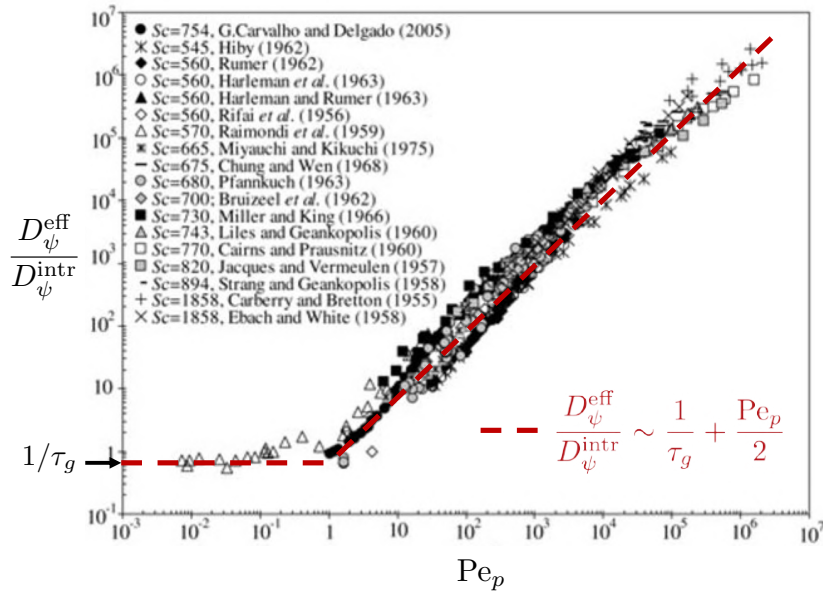


Figure 2.6. – Adapted from [208]: correlation of dispersion as a function of the Péclet number.

2.1.6.4. Interpretation of dispersion at the microscale

Anticipating on the results of Chapter 6, it is important to note that dispersion should *a priori* only make sense at the averaged scale, *i.e.* that of the REV. Conceptually-speaking, this implies that pore-scale physical phenomena do not “see” and should not be governed by the large-scale effective diffusivity D_{ψ}^{eff} . This constitutes a major concern regarding porous media combustion, because as shown in Equation (1.2) from Chapter 1, diffusion of heat is directly related to the burning rate of flames. So if D_{ψ}^{eff} is used in the macroscale equations, the burning rate will be modified. Yet, if the flame fronts are thin compared to the pore diameter (flamelet approach), then their local burning rate has no reason to be related to the macroscale diffusivity - but rather to the local intrinsic diffusivity of the gas. In the thin flame front regime, there is therefore an apparent contradiction between the phenomenology of macroscale effective diffusivity at the averaged scale - to pore-scale diffusion which may be more relevant to the flame fronts. This contradiction is directly related to the large pore-scale deviations with gradients smaller than the REV - and constitutes a direct illustration of the difficulties arising when aggregating together several macroscale models. So, in the low-order equations, one may wonder whether D_{ψ}^{eff} or D_{ψ}^{intr} should be used. Certainly, the modelling will be sensitive to the inclusion of dispersion, and to the author’s viewpoint it is one of the reasons why state-of-the-art volume-averaged models still fail to predict with sufficient precision burning rates within porous media. Dispersion is usually appreciated in the literature because by construction it smoothes out the temperature and species concentration profiles - something which is observed in the experiments. However, this broadening may have different origins (see Chapters 4 and 6), so overall one should consider dispersion in porous media combustion with great caution.

2.1.7. Influence of the pore diameter

In an effort to shed light on the physics of flames embedded in porous media, we now investigate the importance of the pore diameter. The length scale relevant for combustion processes is the flame thickness δ_L , which can be identified in the gas phase as the diffusion length scale l_{diff}

[115]:

$$\delta_L \sim l_{\text{diff}} = \frac{D_{th}}{\langle u \rangle^g}, \quad (2.13)$$

where D_{th} is the intrinsic thermal diffusivity in the gas phase. It follows that the ratio pore diameter to (thermal) flame thickness is:

$$\frac{d_p}{\delta_L} = \frac{\langle u \rangle^g d_p}{D_{th}} = \text{Pe}_{p,th}, \quad (2.14)$$

that is, the definition of the thermal Péclet number $\text{Pe}_{p,th}$. From here, one can discern two distinct regimes:

- The regime $\text{Pe}_{p,th} \ll 1$ (see Figure 2.7(a)), *i.e.* pore sizes smaller than the flame thickness $d_p \ll \delta_L$. In this case the flame does not constitute a discontinuity at the scale of the REV. Accordingly, the combustion can be considered to occur “in volume” at the scale of the REV *i.e.* there is no need *a priori* for a combustion model for reaction rates: their average at the scale of the REV should be close to the reaction rate of the dependent averaged quantities (temperatures, concentrations, density). This occurs because local deviations are very small.
- The regime $\text{Pe}_{p,th} \gg 1$ (see Figure 2.7(b)), *i.e.* pore sizes larger than the flame thickness $d_p \gg \delta_L$. In that case there is a large discontinuity at the scale of the REV, in opposition to the underlying principles of the separation of length scales for volume-averaging. There is no combustion in volume at REV scale, *i.e.* no commutation between the reaction rates and their average. Therefore, the macroscale reaction rates must be modelled. This situation is very similar to the case of the flamelets regime in turbulent combustion [212].

A comparison between Figures 2.6 and 2.7 suggests that **the classical framework of volume-averaging may be violated whenever dispersion is dominant**. This is a further but coherent warning on the inclusion of dispersion in the volume-averaged equations. Although dispersion undeniably occurs within porous burners, its significance wrt. the local flame fronts may be lost in the macroscale equations, which may require a dedicated modelling of the reaction rates. Unfortunately, up to date in the literature this view is not addressed and no combustion models other than a simple commutation (“no model”) has been used.

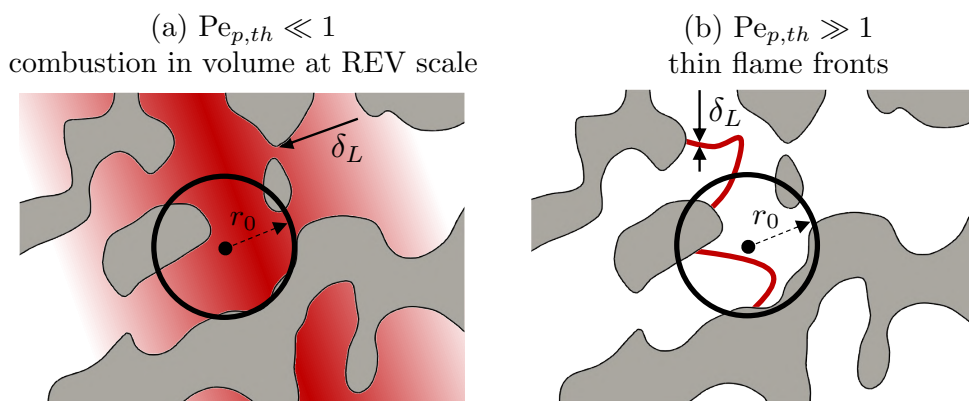


Figure 2.7. – Illustration: smaller and larger d_p/δ_L ratios.

The ratio d_p/δ_L may be interpreted differently through a Damkholer number Da , defined as the ratio of the time scales of convection τ_u and chemical reaction τ_c :

$$\text{Da} = \frac{\tau_u}{\tau_c} \sim \frac{d_p/\langle u \rangle^g}{\delta_L/\langle u \rangle^g} = \frac{d_p}{\delta_L}. \quad (2.15)$$

When $Da \gg 1$ chemical reactions occur infinitely-fast compared to the time scales of the flow, in agreement with the “flamelets regime” viewpoint. On the other hand, when $Da \ll 1$ reactions are the limiting phenomena and any mixing induced by the flow at pore scale is readily homogenized: this is the “well-stirred reactor regime”, and the reaction rates may be estimated at the reaction rates obtained by using the mean values. Interestingly, this view is again very consistent with the phenomenology of turbulent flames (see Section 5.2.2 of [115]). Pushing further the analogy, the steady interstitial porous flow may be viewed as “stationary turbulence”, where the characteristic velocity fluctuation u' is defined in space, not in time, and where the fluctuation length scale l'_t is directly related to the pore diameter d_p . Furthermore, the fact that the flow is constrained within the solid matrix may relate together $u' \propto l'_t \propto d_p$ (see notations in [115]), such that the classification could be more independent to other reduced groups than in turbulent combustion (Reynolds and Karlovitz numbers). Equations (2.14) and (2.15) show that $Da = Pe_{p,th} = d_p/\delta_L$, so again the pore diameter certainly plays a part in the physics of porous media combustion.

The careful reader may argue that length scales other than δ_L intervene for laminar flames, for example the diffusion length scales of the species k , which are at first order given by $\delta_L Le_k^{-1}$, and the reaction length scale given respectively by $\delta_L \beta^{-1}$ where β is the Zel'dovich number. A similar argument could have been made upon the definition of the Damkholer number, in which the chemical time scale could have been similarly scaled by β^{-1} . These considerations do not invalidate the previous conclusions but may shift the threshold value of d_p/δ_L leading from flamelets to combustion in volume (considering the most stringent constraint on the reaction length scale, towards β^{-1} *i.e.* is smaller values).

Also, it is worth pointing out that the above rationale is not common in the community of porous media combustion. In fact, to the best of the author's knowledge there is no elaborate combustion model in the literature for porous burners to date, especially regarding the closure of the reaction rates and its relationship to the pore diameter (or related dimensionless parameters) and other physical phenomena at stake (dispersion, local heat transfer, etc.). Therefore, the above arguments may be viewed as a first attempt to classify the phenomenology of porous combustion from a physicist point of view.

2.1.8. Summary of reduced parameters

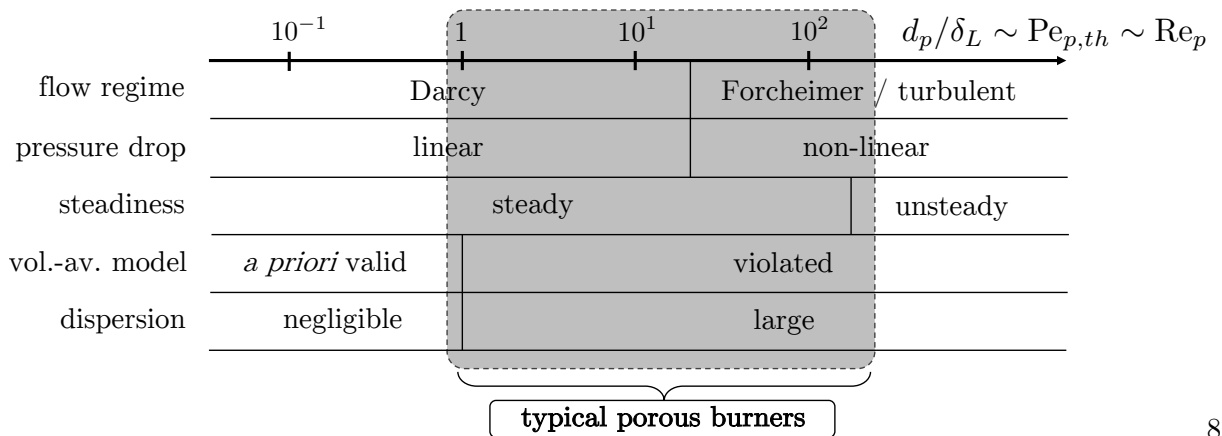
In gases, the local transfer of momentum and thermal energy is governed by the collisions between molecules. A consequence is that Prandtl number Pr , being the ratio of momentum diffusivity (*i.e.* kinematic viscosity) to thermal diffusivity, is of order unity in gases. In the numerical combustion solver AVBP used in this thesis, the Prandtl number is intrinsically assumed constant (approximately $Pr = 0.7$ with our chemical scheme). Therefore, due to the relation:

$$Pe_{p,th} = Re_p \cdot Pr, \quad (2.16)$$

we can conclude the important relation valid for gases:

$$Pe_{p,th} \sim Re_p. \quad (2.17)$$

Putting together the results of previous sections, this allows us to attempt a generalized classification of flow regimes for porous media combustion, only in terms of $d_p/\delta_L \sim Pe_{p,th} \sim Re_p$, as shown in Figure 2.8. The typical range for porous burners found in the literature is also highlighted. This summarized vision may seem simplistic to many regards, but has important conceptual consequences that deserve some attention, such as the apparent mutual exclusion between the validity of the volume-averaged equations and the influence of hydrodynamic dispersion, or the interactions between each macroscopic phenomenon. Also, note that it is not excluded that the flow be unsteady for large pore sizes or mass flow rates, where the classical steady-state formalism is not adapted.



8

Figure 2.8. – Generalized classification of flow regimes within porous media, adapted to porous media combustion, based on the notion of thermal flame thickness.

2.1.9. Heat transfer through the solid matrix

This subsection addresses the energy transfers taking place from and to the solid porous matrix. These include heat conduction within the walls and solid \leftrightarrow solid radiation.

2.1.9.1. Heat conduction - effective conductivity

Due to the tortuosity and porosity of the solid matrix, heat conduction at the macroscopic scale is lower than if the material were uniform, *i.e.* composed only of the bulk material. By noting λ_s the conductivity of the bulk material and λ_s^{eff} the macroscale effective conductivity, it simply means that in general, $\lambda_s^{\text{eff}} < \lambda_s$. If one neglects deviations from the average during the upscaling procedure, one finds exactly $\lambda_s^{\text{eff}} = (1 - \epsilon)\lambda_s$ where ϵ is the porosity. This approximation is largely used in the literature [174, 214] and may be interpreted easily, since ϵ represents the fraction of “missing” surface to conduct the heat in the direction of the macroscale temperature gradient. Note that this notion is different from an effective global conductivity also taking into account heat transfer throughout the fluid phase, as found under LTE framework [191]. This effective conductivity can be computed multiple ways. In 3D direct numerical simulations performed during this thesis, one may check directly whether the macroscopic gradient of intrinsic volume-averaged solid temperature $-\nabla \langle T_s \rangle^s$ is proportional to the slice-averaged longitudinal heat flux Q_x^{DNS} , the constant of proportionality (to fit) being λ_s^{eff} :

$$Q_x^{\text{DNS}} = -\lambda_s^{\text{eff}} \cdot \nabla \langle T_s \rangle^s. \quad (2.18)$$

This is done in Figure 2.9(a), where an excellent functional agreement is found at the macroscale (*i.e.* for the shape of the curve). It indicates that in a real burner, the notion of effective conductivity to represent the heat transfer within the solid phase has the correct phenomenology, even in the presence of interphase heat transfer. An independent simulation can be performed for the solid phase only (without fluid) and is shown in Figure 2.9(b). Again, excellent functional agreement is found. The fact that λ_s^{eff} has very close optimal values in (a) and (b) suggests that the value of effective conductivity may be evaluated somewhat *independently*. This notion of independent estimation is related to the possible confusion of microscopic deviations into different macroscale terms, and this topic is addressed at the end of this chapter and in Chapter 6. Note that these observations may be less valid when the Biot number is very large, because there would be larger deviations due to a less uniform solid temperature field - but this is not typical of porous burners which show large solid thermal conductivities and small pore sizes.

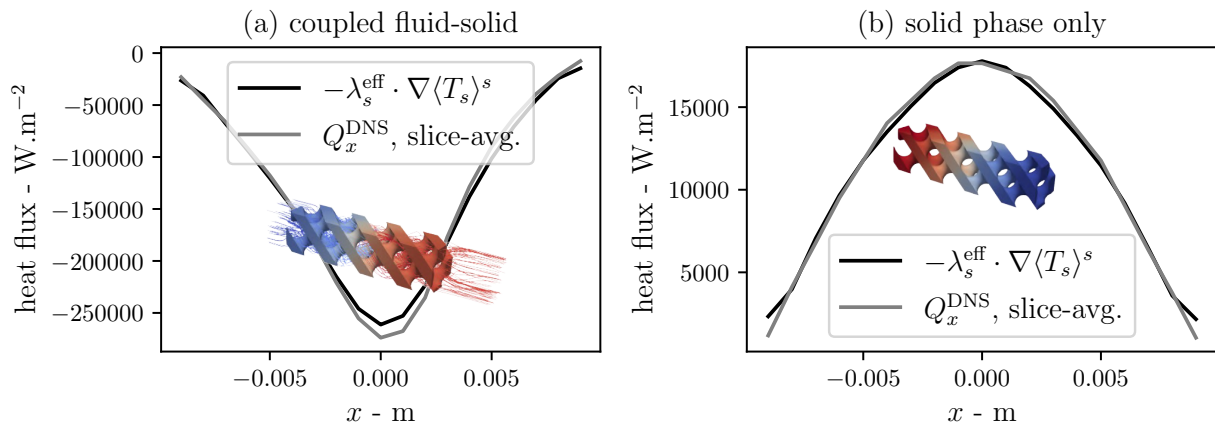


Figure 2.9. – Best fit of effective conductivity in (a) a steady reactive coupled gas-solid simulation, yielding $\lambda_s^{\text{eff}} = 2.09 \text{ W m}^{-1} \text{ K}^{-1}$ and (b) a transient solid-only heat transfer simulation, yielding $\lambda_s^{\text{eff}} = 1.98 \text{ W m}^{-1} \text{ K}^{-1}$. A 3D view is provided for visualisation of the shape of the fields.

2.1.9.2. Radiation

Radiation within porous media is a vast literature topic on its own, which may present different modelling strategies as a function of particle sizes, geometry and distribution, spectral properties of the material, surface characteristics, temperature range, and many other parameters [215]. In porous media burners, it is classically assumed that geometrical optics apply, and the Radiative Transfer Equation (RTE) integrated over all wavelengths is classically used. It implicitly assumes that the porous matrix can be viewed as an equivalent, homogeneous medium of effective radiative properties - *i.e.* there simply exists effective extinction, absorption and scattering coefficients at the macroscale. The determination of these effective properties, and the conditions under which this modelling is valid remains an open question, and is largely out of the scope of the present work. Yet, we note that in volume-averaged models, it has now become standard to resolve numerically the RTE or its various approximations, what allows to retrieve with more or less accuracy experimental temperature profiles [34, 159, 216].

Physically-speaking, the influence of radiation on burner stability is two-sided: while it increases the intensity of internal heat recirculation - and in turn burner operating range, subsequent radiative losses on the boundaries may on the contrary have a detrimental effect regarding blow-off. In burners of small length or of large scattering albedo, heat losses might become dominant. More generally, Sathe et al. [217] have shown numerically that, from the point of view of the 1D volume-averaged equations, the internal stability of the flame is governed by the optical thickness and scattering albedo. For a fixed scattering albedo, larger optical thicknesses lead to larger heat recirculation thus better resistance to blow-off, while for a fixed optical thickness, larger scattering albedo lead to lower heat recirculation thus lower burner stability.

Overall, radiation does not qualitatively change the pore-scale phenomenology of combustion within porous media. At the macroscopic scale, it may be viewed as a separate topic, being a source term in the solid energy equation. To some extent, it may also be modelled by increasing artificially the solid thermal conductivity. In the limit of large optical thickness (typically small pores), the Roseland approximation may be used. The results in [125, 218] indicate that although quantitatively invalid, the shape of the curves burning rate *vs.* position, as shown in Figure 1.16 of Chapter 1, remain qualitatively the same with and without radiation, and whether an effective conductivity model is chosen or not.

Because the present work is aimed at developing asymptotic analyses on the equations on the one hand, and to compare as closely as possible the relations between 3D simulations and 1D volume-averaged models on the other hand, including radiation is an unnecessary complication to our goals. The strong non-linearity of radiation does not allow to handle the equations in an analytical fashion, and the comparison between micro and macroscale models would suffer from an additional confounding factor, that is, the validity of the volume-averaged radiation. Therefore, radiation is discarded from the present work without altering the conclusions regarding combustion modelling.

2.2. Modelling equations and upscaling hypotheses

This section first presents the modelling hypotheses for the flow and solid matrix used throughout this manuscript. These are based upon the governing equations found in the CFD software AVBP and AVTP developed by CERFACS [219]. Then, the methodology of volume-averaging is presented - this allows us to introduce properly definitions and hypotheses made during the upscaling process yielding the canonical volume-averaged equations used for porous media combustion.

2.2.1. Classical stationary volume-averaged equations

With the intention to stress the hypotheses made during upscaling, let us begin by stating the classical, isotropic, stationary, volume-averaged equations of porous media combustion, as found classically in the literature [29, 30, 34, 191, 220, 221]:

$$\nabla \cdot (\epsilon \rho_{g,k} \mathbf{u}) + \nabla \cdot (\epsilon \mathbf{J}_k^{\text{eff}}) - \epsilon \dot{\omega}_k = 0, \quad (2.19)$$

$$\rho_g c_{p_g} \epsilon \mathbf{u} \cdot \nabla T_g - \nabla \cdot [\epsilon \rho_g c_{p_g} D_{th}^{\text{eff}} \nabla T_g] + \epsilon \left[\sum_k c_{p_g,k} \mathbf{J}_k^{\text{eff}} \right] \cdot \nabla T_g - \epsilon \dot{\omega}_T + h_V (T_g - T_s) = 0, \quad (2.20)$$

$$\nabla \cdot [\lambda_s^{\text{eff}} \nabla T_s] + h_V (T_g - T_s) = 0. \quad (2.21)$$

For better readability, all the macroscale quantities are here implicitly expressed as their intrinsic volume-average $\langle \cdot \rangle^{g,s}$. T_g and T_s denote gas and solid temperatures, ϵ local porosity, ρ_g and $\rho_{g,k}$ global and partial densities, \mathbf{u} velocity field, $\dot{\omega}_k$ mass reaction rates and $\dot{\omega}_T$ resulting heat release rate per unit volume, $\mathbf{J}_k^{\text{eff}}$ effective macroscale diffusion flux of species k , c_{p_g} and $c_{p_g,k}$ the global and partial mass heat capacities, D_{th}^{eff} effective macroscale diffusivity, h_V volume heat transfer coefficient and λ_s^{eff} the effective macroscale heat conductivity in the solid phase. We now provide some theoretical elements stressing how these equations can be obtained and under which hypotheses, starting from the pointwise (microscopic) governing equations. Note that classically and implicitly, it is assumed that the reaction rates commute with the average, which is a strong hypothesis.

2.2.2. Pointwise governing equations

2.2.2.1. Equations in the gas phase - AVBP

The microscopic modelling of the gas phase is based upon the following compressible-reactive Navier-Stokes equations, as resolved in AVBP:

$$\frac{\partial \rho_{g,k}}{\partial t} + \nabla \cdot (\rho_{g,k} \mathbf{u}) + \nabla \cdot \mathbf{J}_k - \dot{\omega}_k = 0, \quad (2.22)$$

$$\frac{\partial \rho_g \mathbf{u}}{\partial t} + \nabla \cdot (\rho_g \mathbf{u} \mathbf{u}) + \nabla \cdot [P \underline{\mathbf{I}} - \underline{\boldsymbol{\tau}}] = 0, \quad (2.23)$$

$$\frac{\partial \rho_g E}{\partial t} + \nabla \cdot (\rho_g E \mathbf{u}) + \nabla \cdot [\mathbf{u} \cdot (P \underline{\mathbf{I}} - \underline{\boldsymbol{\tau}}) + \mathbf{q}] - \dot{\omega}_T^0 = 0. \quad (2.24)$$

- the fluid is Newtonian ;
- volume forces such as gravitation and radiation in the gas phase are neglected ;
- E is the total (non-chemical) energy per mass unit, ρ_g the gas density, \mathbf{u} the velocity field, $\underline{\boldsymbol{\tau}}$ the viscous stress tensor ;
- the gas temperature T_g is defined implicitly through the species sensible enthalpies $h_{s,k}$ by integrating the species heat capacities $c_{p_g,k}$:

$$h_{s,k} = \int_{T_{\text{ref},h}}^{T_g} c_{p_g,k}(T) dT. \quad (2.25)$$

- the total enthalpy is obtained by adding the formation enthalpies $h_k = h_{s,k} + \Delta h_k^{f,0}(T_{\text{ref},h})$, with $T_{\text{ref},h} = 0$ K is the reference temperature ;
- the law of perfect gases applies, the partial pressures P_k being given by:

$$P_k = \rho_{g,k} \frac{R_g}{W_k} T_g \quad \text{so that} \quad P = \sum_k P_k, \quad (2.26)$$

where $\rho_{g,k} = \rho_g Y_k$ and W_k are respectively the partial density and the molecular mass of species k , and R_g is the universal gas constant. Since by definition $\rho_g = \sum_k \rho_{g,k}$, the global equation of state is:

$$P = \rho_g \frac{R_g}{W} T_g \quad \text{where} \quad \frac{1}{W} = \sum_k \frac{Y_k}{W_k}. \quad (2.27)$$

- diffusion is computed by using the Hirschfelder and Curtis approximation:

$$\mathbf{J}_k = -\rho_g \left(D_k \frac{W_k}{W} \nabla X_k - Y_k \mathbf{V}^c \right), \quad (2.28)$$

where the correction velocity \mathbf{V}^c ensures mass conservation:

$$\mathbf{V}^c = \sum_{k=1}^N D_k \frac{W_k}{W} \nabla X_k. \quad (2.29)$$

- the heat flux \mathbf{q} is composed of the Fourier heat flux with a conductivity λ_g , plus the flux related to preferential diffusion of the sensible species enthalpies $h_{s,k}$:

$$\mathbf{q} = -\lambda_g \nabla T_g + \sum_k \mathbf{J}_k h_{s,k}, \quad (2.30)$$

- transport is simplified assuming constant Prandtl ($\text{Pr} = 0.7$) and species Schmidt numbers (Sc_k):

$$\text{Sc}_k = \text{Pr} \cdot \text{Le}_k, \quad (2.31)$$

so that the Lewis numbers are also constants.

- the heat release per unit volume $\dot{\omega}_T^0$ is given by the formation enthalpies (see Equation (1.68) in [115]):

$$\dot{\omega}_T^0 = - \sum_k \Delta h_k^{f,0}(T_{\text{ref},h}) \dot{\omega}_k \quad (2.32)$$

- viscosity is computed using a power law:

$$\mu = \mu_{\text{ref}} \left(\frac{T_g}{T_{\text{ref},\mu}} \right)^{n_\mu}. \quad (2.33)$$

Adapted to the present mixtures, the reference values used are $\mu_{\text{ref}} = 7.05 \times 10^{-5} \text{ kg m}^{-1} \text{ s}^{-1}$ for the reference viscosity at a temperature $T_{\text{ref},\mu} = 2205 \text{ K}$ and $n_\mu = 0.64$ for the temperature exponent.

2.2.2.2. Stationary version with temperature

Because a vast majority of volume-averaged models for porous media combustion are based upon the temperature form of the gas energy equation, let us re-write Equation (2.24) as:

$$\nabla \cdot (\rho_{g,k} \mathbf{u}) + \nabla \cdot \mathbf{J}_k - \dot{\omega}_k = 0, \quad (2.34)$$

$$\nabla \cdot (\rho_g \mathbf{u} \mathbf{u}) + \nabla \cdot [P \underline{\mathbf{I}} - \underline{\boldsymbol{\tau}}] = 0, \quad (2.35)$$

$$\begin{aligned} \rho_g c_{p_g} \mathbf{u} \cdot \nabla T_g - \nabla \cdot [\lambda_g \nabla T_g] + \left[\sum_k c_{p_g,k} \mathbf{J}_k \right] \cdot \nabla T_g - \mathbf{u} \cdot \nabla P \\ - \nabla \mathbf{u} : \underline{\boldsymbol{\tau}} - \dot{\omega}_T = 0. \end{aligned} \quad (2.36)$$

This time the heat release rate per unit volume $\dot{\omega}_T$ is defined using the enthalpies (see Equation (1.68) in [115]):

$$\dot{\omega}_T = - \sum_k h_k \dot{\omega}_k, \quad (2.37)$$

but since $\dot{\omega}_T$ and $\dot{\omega}_T^0$ from Equation (2.32) differ only by a negligible amount, they are confounded in the following:

$$\dot{\omega}_T \equiv \dot{\omega}_T^0. \quad (2.38)$$

2.2.2.3. Stationary isobaric version for low Mach numbers

For low Mach number flows, the approximation $P = \text{constant}$ is valid and the momentum equation can be discarded. Also, we assume that the internal heat production by viscous stresses $\nabla \mathbf{u} : \underline{\boldsymbol{\tau}}$ is negligible in the low-Mach regime, especially when compared to the exothermic chemical reactions of combustion. This leaves us, for the gas phase, with the following microscopic equations:

$$\nabla \cdot (\rho_{g,k} \mathbf{u}) + \nabla \cdot \mathbf{J}_k - \dot{\omega}_k = 0, \quad (2.39)$$

$$\rho_g c_{p_g} \mathbf{u} \cdot \nabla T_g - \nabla \cdot [\lambda_g \nabla T_g] + \left[\sum_k c_{p_g,k} \mathbf{J}_k \right] \cdot \nabla T_g - \dot{\omega}_T = 0. \quad (2.40)$$

2.2.2.4. Heat equation in the solid phase - AVTP

The transient pointwise heat equation solved by AVTP is simply:

$$\rho_s c_{p_s} \frac{\partial T_s}{\partial t} - \nabla \cdot [\lambda_s \nabla T_s] = 0, \quad (2.41)$$

so that in steady state, one simply has:

$$\nabla \cdot [\lambda_s \nabla T_s] = 0. \quad (2.42)$$

Note that even when the conductivity λ_s is constant, the solid temperature field T_s still depends on λ_s through the boundary conditions.

2.2.2.5. Boundary conditions

Since we neglect heterogeneous reactions at the interface between the gas and the solid \mathcal{A}_{gs} , we write the continuity of heat fluxes and temperatures as:

$$\lambda_g \nabla T_g \cdot \mathbf{n}_{gs} = \lambda_s \nabla T_s \cdot \mathbf{n}_{gs} \quad \text{and} \quad T_s = T_g \quad \text{on } \mathcal{A}_{gs}. \quad (2.43)$$

The no-slip and non-permeable-inert conditions at the gas/solid interface read:

$$\mathbf{u} = 0 \quad \text{and} \quad \mathbf{J}_{\mathbf{k}} \cdot \mathbf{n}_{gs} = 0 \quad \text{on } \mathcal{A}_{gs}. \quad (2.44)$$

2.2.3. Volume-averaging

2.2.3.1. Notations

The principle of volume-averaging is illustrated in Figure 2.10. The integration volume \mathcal{V} can be either a centroid of radius r_0 centered on the position \mathbf{x} , or, assuming a preferential direction x , a slice encompassing the entire domain in the y and z -directions and of thickness $2r_0$. For a given control volume \mathcal{V} , we define the volume-averaging operator $\langle \cdot \rangle$ of a quantity ψ as:

$$\langle \psi \rangle = \frac{1}{\mathcal{V}} \int_{\mathcal{V}} \psi \, dV. \quad (2.45)$$

$\langle \psi \rangle$ is called the *superficial* average of ψ . Note that the integration is done, technically, through the variable \mathbf{y} for a fixed value of \mathbf{x} (the differential dV may be re-written $d\mathbf{y}^3$). Since ψ may not be defined in the entire integration volume \mathcal{V} and because in experiments $\langle \psi \rangle$ is typically not measurable, we also introduce the convenient *intrinsic* averages $\langle \cdot \rangle^{g,s}$ for the gas and solid phases respectively as:

$$\langle \psi \rangle^g = \frac{1}{\mathcal{V}_g} \int_{\mathcal{V}_g} \psi \, dV \quad \text{and} \quad \langle \psi \rangle^s = \frac{1}{\mathcal{V}_s} \int_{\mathcal{V}_s} \psi \, dV \quad (2.46)$$

A formal definition of porosity may be given accordingly:

$$\epsilon = \frac{\mathcal{V}_g}{\mathcal{V}_g + \mathcal{V}_s} = \frac{\mathcal{V}_g}{\mathcal{V}}. \quad (2.47)$$

The volume \mathcal{V} shall be large enough to smooth the local variations at the pore-level, yet small enough to model the large-scale gradients. In practice, this occurs when the value of $\langle \psi \rangle$ reaches a plateau for increasing r_0 , and \mathcal{V} is then called Representative Elementary Volume (REV). This hypothesis can be recast more rigorously in terms of length scales: for a quantity ψ defined

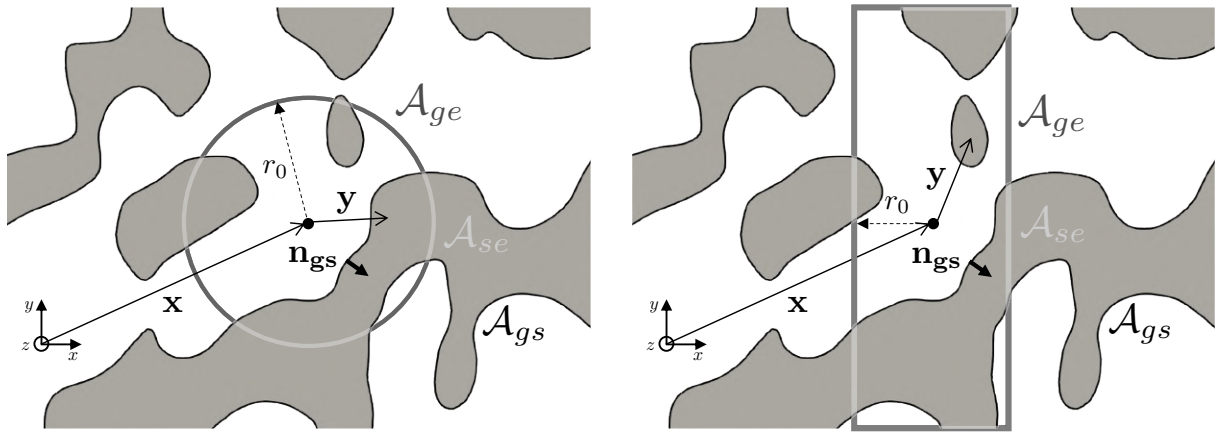


Figure 2.10. – Principle of volume-averaging over a Representative Elementary Volume (REV) with (a) a centroid of radius r_0 and (b) a slice infinite in the y and z directions of thickness r_0 .

either in the gas or solid phase, one can define $l_{g,s}$ the length scale microscopic variations and $L_{g,s}$ that of the macroscopic ones, as:

$$l_{g,s} = \frac{\psi}{|\nabla\psi|} \quad \text{and} \quad L_{g,s} = \frac{\langle\psi\rangle^{g,s}}{|\nabla\langle\psi\rangle^{g,s}|}. \quad (2.48)$$

A correct value of r_0 for the volume-averaging procedure should comply to:

$$l_{g,s} \ll r_0 \ll L_{g,s}. \quad (2.49)$$

Also, the variations of the average quantities should occur over a distance smaller than the total length of the domain, leading to a further restriction *a priori*:

$$l_{g,s} \ll r_0 \ll L_{g,s} < L_{\text{domain}}. \quad (2.50)$$

Note that the restriction (2.50) concerns both the *geometrical* domain (through L_{domain}), but also the *spectral* domain through Equation (2.48). This can be viewed simply by considering a periodic signal $\psi \propto e^{i\mathbf{k}\cdot\mathbf{x}}$ giving $\psi/|\nabla\psi| = 1/|\mathbf{k}|$. In the simulations performed in this thesis the value of $r_0 = d_p/2$ was found to avoid both micro-variations and macroscale gradients, so that the size of the REV is set to a pore diameter.

2.2.3.2. Deviations from the average

The purpose of this work is not to propose a novel upscaling procedure leading to macroscale models derived *a priori*. Rather, in the following we perform some volume-averaging steps so as to identify where are the subtleties and strong modelling assumptions, what will be useful in the comparison 1D low-order model *vs.* 3D DNS of Chapter 6. This will allow notably to address the fidelity of the macro-scale models, the quality of the functional modelling of closure terms, and the ability to unveil which microscopic terms end up in which macroscopic ones. For that, we can begin by introducing the notion of deviations from the averaged quantities:

$$\psi = \langle\psi\rangle^{g,s} + \psi'. \quad (2.51)$$

Fundamentally, this decomposition may be defined differently following the formal dependencies upon \mathbf{x} and/or \mathbf{y} . There are two main approaches regarding this issue. A dependence of $\langle\psi\rangle^{g,s}$ on

\mathbf{y} is classically supposed and is called Gray's decomposition. On the other hand, here we chose to consider $\langle \psi \rangle^{g,s}$ constant over \mathcal{V} , so that ψ' represents the pointwise microscopic deviation from the \mathbf{x} -centered volume-averaged value. This viewpoint implies that:

$$\langle \psi' \rangle^{g,s} = 0 \quad \text{and} \quad \langle \langle \psi \rangle^{g,s} \rangle^{g,s} = \langle \psi \rangle^{g,s}. \quad (2.52)$$

In general, the terms in the pointwise equations are functions f of N pointwise variables, of the form $f(\psi_{i \in [1,N]})$, whose averaged value $\langle f(\psi_{i \in [1,N]}) \rangle^{g,s}$ is not equal to the value of f at the averages $f(\langle \psi_{i \in [1,N]} \rangle^{g,s})$. In other words, the microscopic terms do not commute *a priori* with their averages. Here lies precisely the difficulty of low-order filtered models, requiring macroscopic closure terms to "correct" the commutation errors. In combustion, we will see that this is particularly critical for the reaction rates $\dot{\omega}_k(\rho_g, T_g, Y_k)$ or complex products involving many variables and their gradients. To compare the difference between $\langle f(\psi_{i \in [1,N]}) \rangle^{g,s}$ and $f(\langle \psi_{i \in [1,N]} \rangle^{g,s})$, one may introduce two formal operators. One for the pure commutation \mathcal{A} :

$$\mathcal{A}\left(f\left(\psi_{i \in [1,N]}\right)\right) = f\left(\langle \psi_{i \in [1,N]} \rangle^{g,s}\right), \quad (2.53)$$

and one for the deviations \mathcal{D} :

$$\mathcal{D}\left(f\left(\psi_{i \in [1,N]}\right)\right) = \langle f\left(\psi_{i \in [1,N]}\right) \rangle^{g,s} - f\left(\langle \psi_{i \in [1,N]} \rangle^{g,s}\right). \quad (2.54)$$

When the expression of f is lengthy, the formal dependencies upon the ψ_i may be discarded and one writes:

$$f = \mathcal{A}(f) + \mathcal{D}(f). \quad (2.55)$$

In the simple case of a product of two variables ψ and ζ , thanks to the lack of dependency of the averages upon \mathbf{y} the deviations are:

$$\langle \psi \zeta \rangle^{g,s} = \underbrace{\langle \psi \rangle^{g,s} \langle \zeta \rangle^{g,s}}_{\mathcal{A}(\psi \zeta)} + \underbrace{\langle \psi' \zeta' \rangle^{g,s}}_{\mathcal{D}(\psi \zeta)}. \quad (2.56)$$

The decomposition of Equation (2.55) is used thoroughly in the following, because the terms $\mathcal{A}(f)$ are strongly related to the terms in common between the microscopic and macroscopic equations, whilst the terms $\mathcal{D}(f)$ are strongly related to the closure terms/effective properties of the media.

2.2.3.3. Spatial averaging theorem

For microscopic terms showing the form of a gradient or a divergence, the relation linking the spatial derivative of the average and the average of the spatial derivative is called the *spatial averaging theorem*. Based upon intrinsic averages, this theorem writes:

$$\langle \nabla \psi \rangle^g = \epsilon^{-1} \nabla [\epsilon \langle \psi \rangle^g] + \frac{1}{\mathcal{V}_g} \int_{\mathcal{A}_{gs}} \psi \mathbf{n}_{gs} \, dS \quad (2.57)$$

for ψ defined in the gas phase, and:

$$\langle \nabla \psi \rangle^s = (1 - \epsilon)^{-1} \nabla [(1 - \epsilon) \langle \psi \rangle^s] - \frac{1}{\mathcal{V}_s} \int_{\mathcal{A}_{gs}} \psi \mathbf{n}_{gs} \, dS. \quad (2.58)$$

for its solid counterpart, where normals were simply reversed. A geometrical proof of the theorem is given in Appendix 2.A. Though presented here with gradients, this theorem is also valid under divergence form.

2.2.3.4. Volume-averaging in the solid phase

Starting back from the pointwise equation:

$$\nabla \cdot (\lambda_s \nabla T_s) = 0. \quad (2.59)$$

By applying the intrinsic volume-average $\langle \cdot \rangle^s$ and the spatial averaging theorem, one has:

$$(1 - \epsilon)^{-1} \nabla \cdot [(1 - \epsilon) \langle \lambda_s \nabla T_s \rangle^s] - \frac{1}{\mathcal{V}_s} \int_{\mathcal{A}_{gs}} \lambda_s \nabla T_s \cdot \mathbf{n}_{gs} \, dS = 0, \quad (2.60)$$

which allows, when multiplied by $(1 - \epsilon)$, to come back to energy balance terms defined per unit volume of space (not just the of solid phase):

$$\nabla \cdot [(1 - \epsilon) \langle \lambda_s \nabla T_s \rangle^s] + \underbrace{\frac{1}{\mathcal{V}} \int_{\mathcal{A}_{gs}} -\lambda_s \nabla T_s \cdot \mathbf{n}_{gs} \, dS}_{Q_{gs}} = 0. \quad (2.61)$$

By definition the rightmost term is the macroscopic volume interphase heat transfer Q_{gs} , that is, the total heat flux exchanged from the gas to the solid per unit volume. By applying the average-deviation decomposition as defined by Equation (2.55), one obtains:

$$\nabla \cdot [(1 - \epsilon) \mathcal{A}(\lambda_s \nabla T_s)] + \nabla \cdot [(1 - \epsilon) \mathcal{D}(\lambda_s \nabla T_s)] + Q_{gs} = 0. \quad (2.62)$$

In this form Equation (2.64) is substantially different from the classical volume-averaged Equation (2.21). However, a term-by-term identification suggests that:

$$Q_{gs} = h_V [\langle T_g \rangle^g - \langle T_s \rangle^s], \quad (2.63)$$

$$\underbrace{\nabla \cdot [(1 - \epsilon) \mathcal{A}(\lambda_s \nabla T_s)]}_{\chi_1} + \nabla \cdot [(1 - \epsilon) \mathcal{D}(\lambda_s \nabla T_s)] = \underbrace{\nabla \cdot [\lambda_s^{\text{eff}} \nabla \langle T_s \rangle^s]}_{\chi_2}. \quad (2.64)$$

The formal denomination of the terms χ_1 and χ_2 is introduced for later use in Chapter 6. The proposed identification supposes that the macroscopic, phenomenologically-based terms in the volume-averaged equations are equal to rigorous integrals of microscopic counterparts. This is of course an approximation. For instance, a difference between the rigorous expression of Q_{gs} and the functional form $h_V [\langle T_g \rangle^g - \langle T_s \rangle^s]$ was visible in Figure 2.4.

If the deviations in the solid phase are assumed negligible, then it comes that:

$$\lambda_s^{\text{eff}} = (1 - \epsilon) \lambda_s, \quad (2.65)$$

which is often used in the literature, because it only requires the knowledge of the bulk thermal conductivity and contains the leading-order influence of porosity. Note also that more elaborate, anisotropic models can be developed by introducing an effective conductivity tensor $\underline{\underline{\Lambda}}_s^{\text{eff}}$ such that Equation (2.21) becomes:

$$\nabla \cdot [\underline{\underline{\Lambda}}_s^{\text{eff}} \nabla \langle T_s \rangle^s] + h_V [\langle T_g \rangle^g - \langle T_s \rangle^s] = 0. \quad (2.66)$$

This tensor contains more accurately the microscale information from the deviations, but requires much more work to determine the numerous coefficients. In this work it is assumed implicitly that:

$$\underline{\underline{\Lambda}}_s^{\text{eff}} = \lambda_s^{\text{eff}} \mathbf{Id}, \quad (2.67)$$

so that the closure of the macroscale equation boils down to determining only one effective conductivity coefficient.

2.2.3.5. Volume-averaging in the gas phase

Species equation: by applying the intrinsic volume-average in the gas phase $\langle \cdot \rangle^g$, one obtains the following species conservation equation:

$$\nabla \cdot (\epsilon \langle \rho_{g,k} \mathbf{u} \rangle^g) + \nabla \cdot (\epsilon \langle \mathbf{J}_k \rangle^g) - \epsilon \langle \dot{\omega}_k \rangle^g = 0. \quad (2.68)$$

The commutation between the average operator and the divergence is obtained by making use of the spatial averaging theorem and the boundary conditions at the inert, non-permeable gas-solid interface \mathcal{A}_{gs} , where: $\mathbf{u} \cdot \mathbf{n}_{gs} = 0$ and $\mathbf{J}_k \cdot \mathbf{n}_{gs} = 0$. Then again, by using the average-deviation decomposition as defined by Equation (2.55), one obtains:

$$\begin{aligned} \nabla \cdot [\epsilon \mathcal{A}(\rho_{g,k} \mathbf{u})] + \nabla \cdot [\epsilon \mathcal{D}(\rho_{g,k} \mathbf{u})] + \nabla \cdot [\epsilon \mathcal{A}(\mathbf{J}_k)] \\ + \nabla \cdot [\epsilon \mathcal{D}(\mathbf{J}_k)] - \epsilon \mathcal{A}(\dot{\omega}_k) - \epsilon \mathcal{D}(\dot{\omega}_k) = 0. \end{aligned} \quad (2.69)$$

From here, retrieving the classical volume-averaged Equation (2.19) from Equation (2.69) is not straightforward. Rigorously, only the terms $\nabla \cdot [\epsilon \mathcal{A}(\rho_{g,k} \mathbf{u})]$ and $\epsilon \mathcal{A}(\dot{\omega}_k)$ are in common, so the direct identification of the remaining terms imposes:

$$\underbrace{\nabla \cdot [\epsilon \mathcal{D}(\rho_{g,k} \mathbf{u})] + \nabla \cdot [\epsilon \mathcal{A}(\mathbf{J}_k)] + \nabla \cdot [\epsilon \mathcal{D}(\mathbf{J}_k)]}_{\Upsilon_1} = \nabla \cdot \underbrace{(\epsilon \mathbf{J}_k^{\text{eff}})}_{\Upsilon_2}, \quad (2.70)$$

$$-\epsilon \mathcal{D}(\dot{\omega}_k) = 0. \quad (2.71)$$

The formal denomination of the terms Υ_1 and Υ_2 is introduced for later use in Chapter 6. In the absence of trivial alternatives, the effective macroscopic species diffusion flux $\mathbf{J}_k^{\text{eff}}$ is classically provided in an *ad hoc* fashion, by invoking a macroscopic closure term of functional form very similar to its microscopic counterpart:

$$\mathbf{J}_k^{\text{eff}} = -\langle \rho_g \rangle^g \left(D_k^{\text{eff}} \frac{W_k}{\langle W \rangle^g} \nabla \langle X_k \rangle^g - Y_k \langle \mathbf{V}^{\text{c,eff}} \rangle^g \right), \quad (2.72)$$

with a macroscopic diffusivity, following Equation (2.12), given by:

$$D_k^{\text{eff}} = D_k + 0.5 \cdot A^{\text{dis}} \cdot \langle u \rangle^g. \quad (2.73)$$

The macroscale correction velocity is given by:

$$\langle \mathbf{V}^{\text{c,eff}} \rangle^g = \sum_{k=1}^N D_k^{\text{eff}} \frac{W_k}{\langle W \rangle^g} \nabla \langle X_k \rangle^g. \quad (2.74)$$

Again, knowing whether Equation (2.70) is a good modelling functional can be verified *a priori* using the 3D fields from numerical simulations, and this will be investigated in Chapter 6. Concerning the macroscopic modelling of dispersion, more elaborate models may be devised by introducing additional fitting terms through an effective diffusivity tensor $\underline{\underline{\mathbf{D}}}_k^{\text{eff}}$, which again boils down to a scalar D_k^{eff} in isotropic and 1D cases:

$$\underline{\underline{\mathbf{D}}}_k^{\text{eff}} = \left[D_k + 0.5 \cdot A^{\text{dis}} \cdot \langle u \rangle^g \right] \underline{\underline{\mathbf{Id}}}. \quad (2.75)$$

In the literature, some authors have formally compensated the errors associated with the non-commutation of reaction rates by considering Equation (2.71) valid and assigning the remaining errors (*i.e.* deviations) to the macroscopic dispersion coefficient. It is not an evident choice, because it is hard to know, when macroscopic modelling errors are made, what should be done

to compensate them in the models (modification of the effective diffusivity? relaxation of the commutation assumption for the reaction rates? new model for the reaction rates?). Following the first idea, the dependency of dispersion coefficient upon reaction was identified theoretically in an academic case in [222]. It was argued, however, that the corresponding upscaling procedure itself loses validity in the presence of large reaction intensities. This is reminiscent of previous warnings that dispersion and reaction may be dissociated and possibly conflicting at the macroscale. Note that Equation (2.71) is typically wrong due to the large non-linearity of reaction rates, especially when the pore sizes are large and the flame fronts sharp wrt. the REV.

Gas temperature equation: by taking the intrinsic volume-averaging operator in the gas phase, one obtains after making use of the spatial averaging theorem and by multiplying by ϵ :

$$\begin{aligned} \epsilon \mathcal{A}(\rho_g c_{p_g} \mathbf{u} \cdot \nabla T_g) + \epsilon \mathcal{D}(\rho_g c_{p_g} \mathbf{u} \cdot \nabla T_g) - \nabla \cdot [\epsilon \mathcal{A}(\lambda_g \nabla T_g)] \\ - \nabla \cdot [\epsilon \mathcal{D}(\lambda_g \nabla T_g)] + Q_{gs} + \epsilon \mathcal{A} \left(\left[\sum_k c_{p_g, k} \mathbf{J}_k \right] \cdot \nabla T_g \right) \\ + \epsilon \mathcal{D} \left(\left[\sum_k c_{p_g, k} \mathbf{J}_k \right] \cdot \nabla T_g \right) - \epsilon \mathcal{A}(\dot{\omega}'_T) - \epsilon \mathcal{D}(\dot{\omega}'_T) = 0. \end{aligned} \quad (2.76)$$

where the spatial averaging theorem was used to obtain one more time the macroscopic inter-phase heat exchange Q_{gs} :

$$Q_{gs} = \frac{1}{\mathcal{V}} \int_{\mathcal{A}_{gs}} -\lambda_g \nabla T_g \cdot \mathbf{n}_{gs} \, dS. \quad (2.77)$$

Here the difference between the terms of Equations (2.20) and (2.76) is still very pronounced. In addition to the term Q_{gs} which is the same than Equation (2.63), the following identifications may be proposed:

$$\underbrace{\epsilon \mathcal{D}(\rho_g c_{p_g} \mathbf{u} \cdot \nabla T_g) - \nabla \cdot [\epsilon \mathcal{A}(\lambda_g \nabla T_g)] - \nabla \cdot [\epsilon \mathcal{D}(\lambda_g \nabla T_g)]}_{\Xi_1} = \underbrace{-\nabla \cdot [\epsilon \rho_g c_{p_g} D_{th}^{\text{eff}} \nabla \langle T_g \rangle^g]}_{\Xi_2} \quad (2.78)$$

$$\underbrace{\epsilon \mathcal{A} \left(\left[\sum_k c_{p_g, k} \mathbf{J}_k \right] \cdot \nabla T_g \right) + \epsilon \mathcal{D} \left(\left[\sum_k c_{p_g, k} \mathbf{J}_k \right] \cdot \nabla T_g \right)}_{\Psi_1} = \underbrace{\epsilon \left[\sum_k c_{p_g, k} \mathbf{J}_k^{\text{eff}} \right] \cdot \nabla \langle T_g \rangle^g}_{\Psi_2} \quad (2.79)$$

$$-\epsilon \mathcal{D}(\dot{\omega}'_T) = 0 \quad (2.80)$$

The formal denomination of the terms Ξ_1 , Ξ_2 , Ψ_1 and Ψ_2 is introduced for later use in Chapter 6. The effective macroscale diffusion fluxes are given by the general empirical relation proposed in Equation (2.12):

$$D_{th}^{\text{eff}} = D_{th} + 0.5 \cdot A^{\text{dis}} \cdot \langle u \rangle^g = \frac{\langle \lambda_g \rangle^g}{\langle \rho_g \rangle^g \langle c_{p_g} \rangle^g} + 0.5 \cdot A^{\text{dis}} \cdot \langle u \rangle^g. \quad (2.81)$$

On the difficulty of upscaling: identifications such as Equations (2.78-2.80) and the assignment of *ad hoc* macroscopic models are not free of errors. In general there is no bijectivity between micro and macroscopic terms (filtering comes necessarily with a loss in local information). Especially in the presence of sharp flame fronts, it is not excluded that this loss of information puts a damper on the possibility to retrieve with sufficient accuracy intrinsic properties of the system such as burning rates, because a large susceptibility upon diffusive and reactive models is expected.

2.2.4. Conclusions of the chapter

In a first part, this chapter listed and investigated the various microscopic phenomena occurring at pore scale in submerged combustion, followed by a review of their modelling strategies at the macroscopic scale. This included effects of convection (steadiness, dispersion), heat transfer at the gas/solid interphase (volume interphase heat exchange), heat transfer within each phase (effective solid conductivity) and chemical reactions (macroscopic heat production). It was shown that the ratio of pore diameter to thermal flame thickness, equal to the thermal Péclet number, has a value very close to the Reynolds number for gaseous combustion in air and governs simultaneously many of the aforementioned macroscopic flow phenomena. This led to the conclusion that there may be a mutual exclusion between the validity of the commutation of reaction rates with the volume-average at the macroscale and the presence of hydrodynamic dispersion. Also, one should keep in mind that unsteadiness may arise in porous media for relatively low Reynolds number, to which the current, widespread steady-state volume-averaged models are unadapted.

In a second part, the upscaling procedure yielding the classical volume-averaged models from the microscopic conservation equations was pursued. By associating systematically the microscopic integrals to the classical macroscopic volume-averaged terms, we could obtain a rigorous theoretical framework to assess the quality of state-of-the-art volume-averaged models. This will be useful to comment upon the predictability of volume-averaged models in terms of burning rates and physical profiles in Chapters 6 and 7. Generally-speaking, one should keep in mind that the derivation of a valid closed set of macroscopic equations from an upscaling procedure is a notoriously difficult task - even when the microscopic equations are simplified (*e.g.* constant density, constant diffusion coefficients, fixed velocity field, etc.). And although macroscopic effects such as dispersion, interphase heat transfer and effective conductivities seem to have some value *independently*, nothing proves that their *aggregation* yields correct phenomenologies and quantitatively valid results. For instance, we have stressed theoretical and phenomenological contradictions between macroscale reaction terms and dispersion, and more are expected to arise (*e.g.* the interaction of dispersion or reaction with the interphase heat exchange, see again Chapter 6). These issues are expected to be particularly problematic in the presence of sharp flame fronts at the scale of a Representative Elementary Volume, a situation which is typical of porous burners found in the literature. From the point of view of combustion, the present issues resemble questions arising with the volume-averaged modelling of turbulent combustion (LES), and strong analogies between the two domains have been proposed. Certainly, a model for the reaction rates within porous media is required. Unfortunately, to date these are absent from the literature. This is why this thesis work focuses on the behavior of the volume-averaged models, which are then compared to 3D DNS - with the hope of stressing the most important problems and proposing improvements. The approach of this manuscript resembles, for instance, that used to derive the Charlette model for wrinkled turbulent flames, for which understanding (1) the asymptotic response of flames to modifications of the diffusion coefficient and Arrhenius pre-exponentials and (2) the structure of a wrinkled turbulent flame, allows to represent at first order the complex convoluted flames at a filtered scale. The asymptotic study of flames in porous media is precisely the topic of Chapters 3 and 4, and in-depth study of the intertwined flame front is done in Chapters 5, 6 and 7.

2.A. Geometrical proof of the spatial averaging theorem

We now present a simple, physicist-like proof of the spatial averaging theorem with modern notations, originating from early works in the literature [223–225]. An illustration of the proof and notations are given in Figure 2.11. We begin by recalling the relations of the spatial averaging theorem for the gas phase:

$$\langle \nabla \psi \rangle^g = \epsilon^{-1} \nabla [\epsilon \langle \psi \rangle^g] + \frac{1}{\mathcal{V}_g} \int_{\mathcal{A}_{gs}} \psi \mathbf{n}_{gs} dS. \quad (2.82)$$

and for the solid phase:

$$\langle \nabla \psi \rangle^s = (1 - \epsilon)^{-1} \nabla [(1 - \epsilon) \langle \psi \rangle^s] - \frac{1}{\mathcal{V}_s} \int_{\mathcal{A}_{gs}} \psi \mathbf{n}_{gs} dS. \quad (2.83)$$

These two relations are exactly the same conceptually-speaking. From the point of view of the solid phase its “porosity” is $(1 - \epsilon)$ and the exterior normals are $-\mathbf{n}_{gs}$, so only the proof of the relation in the gas phase is necessary. The first ingredient is to make use of the traditional Green-Ostrogradski’s theorem:

$$\langle \nabla \psi \rangle^g = \frac{1}{\mathcal{V}_g} \int_{\mathcal{V}_g} \nabla \psi dV = \frac{1}{\mathcal{V}_g} \int_{\mathcal{A}_{ge}} \psi \mathbf{n}_{ge} dS + \frac{1}{\mathcal{V}_g} \int_{\mathcal{A}_{gs}} \psi \mathbf{n}_{gs} dS. \quad (2.84)$$

A comparison between Equations (2.57) and (2.84) suggests that the spatial averaging theorem is equivalent to the following equality:

$$\frac{1}{\mathcal{V}_g} \int_{\mathcal{A}_{ge}} \psi \mathbf{n}_{ge} dS = \epsilon^{-1} \nabla \left[\epsilon \frac{1}{\mathcal{V}_g} \int_{\mathcal{V}_g} \psi dV \right]. \quad (2.85)$$

By enforcing constant volume \mathcal{V} for the REV, the porosity $\epsilon = \mathcal{V}_g/\mathcal{V}$ can in fact be discarded in the rightmost term which is re-written as:

$$\epsilon^{-1} \nabla \left[\epsilon \frac{1}{\mathcal{V}_g} \int_{\mathcal{V}_g} \psi dV \right] = \frac{1}{\mathcal{V}_g} \nabla \int_{\mathcal{V}_g} \psi dV. \quad (2.86)$$

By making use of the result that for any two vectors $\mathbf{A} \in \mathbb{R}^3$ and $\mathbf{B} \in \mathbb{R}^3$, $\mathbf{A} = \mathbf{B} \iff \forall \boldsymbol{\pi} \in \mathbb{R}^3, \boldsymbol{\pi} \cdot \mathbf{A} = \boldsymbol{\pi} \cdot \mathbf{B}$, we recast Equation (2.85) after simplifying by $1/\mathcal{V}_g$ into:

$$\forall \boldsymbol{\pi} \in \mathbb{R}^3, \quad \boldsymbol{\pi} \cdot \int_{\mathcal{A}_{ge}} \psi \mathbf{n}_{ge} dS = \boldsymbol{\pi} \cdot \nabla \int_{\mathcal{V}_g} \psi dV, \quad (2.87)$$

where the operator $\boldsymbol{\pi} \cdot \nabla$ defines the derivation along the axis defined by $\boldsymbol{\pi}$. To evaluate it, let us take a look Figure 2.11 and consider an arbitrary axis directed along $\boldsymbol{\pi}$, whose abscissa s defines the center of a spherical REV noted $\mathcal{V}(s)$. We recall that the REV comprises both fluid and solid domains: $\mathcal{V}(s) = \mathcal{V}_g(s) \cup \mathcal{V}_s(s)$. For an infinitely small displacement ds along $\boldsymbol{\pi}$, the REV engulfs a new region of space in the fluid $\Delta \mathcal{V}_g^+$ (red in Figure 2.11), while receding over another region $\Delta \mathcal{V}_g^-$ (blue). These regions may be used to calculate the derivative along the axis $\boldsymbol{\pi} \cdot \nabla = d/ds$ as such:

$$\boldsymbol{\pi} \cdot \nabla \int_{\mathcal{V}_g} \psi dV = \frac{d}{ds} \int_{\mathcal{V}_g(s)} \psi dV \quad (2.88)$$

$$= \lim_{ds \rightarrow 0} \left(\frac{\int_{\mathcal{V}_g(s+ds)} \psi dV - \int_{\mathcal{V}_g(s)} \psi dV}{ds} \right) \quad (2.89)$$

$$= \lim_{ds \rightarrow 0} \left(\frac{\int_{\Delta \mathcal{V}_g^+} \psi dV - \int_{\Delta \mathcal{V}_g^-} \psi dV}{ds} \right). \quad (2.90)$$

Because the volumes $\Delta\mathcal{V}_g^+$ and $\Delta\mathcal{V}_g^-$ are infinitesimal and generated respectively by the fluid-fluid interfaces \mathcal{A}_{gs}^+ and \mathcal{A}_{gs}^- , it is possible to replace, at the first order in ds , their volume integration by a local surface integration:

$$\int_{\Delta\mathcal{V}_g^\pm} \psi dV = \pm \int_{\mathcal{A}_{ge}^\pm} \psi dS \mathbf{n}_{ge} \cdot \boldsymbol{\pi} ds + \mathcal{O}(ds^2). \quad (2.91)$$

By recalling that $\mathcal{A}_{ge} = \mathcal{A}_{gs}^+ \cup \mathcal{A}_{gs}^-$, Equations (2.88-2.90) yield then:

$$\boldsymbol{\pi} \cdot \nabla \int_{\mathcal{V}_g} \psi dV = \boldsymbol{\pi} \cdot \int_{\mathcal{A}_{ge}} \psi \mathbf{n}_{ge} dS, \quad (2.92)$$

which is the expected result. This demonstration is only valid in cases where the interfaces and spatial function ψ are smooth enough. This excludes very particular configurations but such mathematical concerns are out of the scope of the present work. This demonstration can be viewed as the ‘‘physicist’’ proof of the spatial averaging theorem.

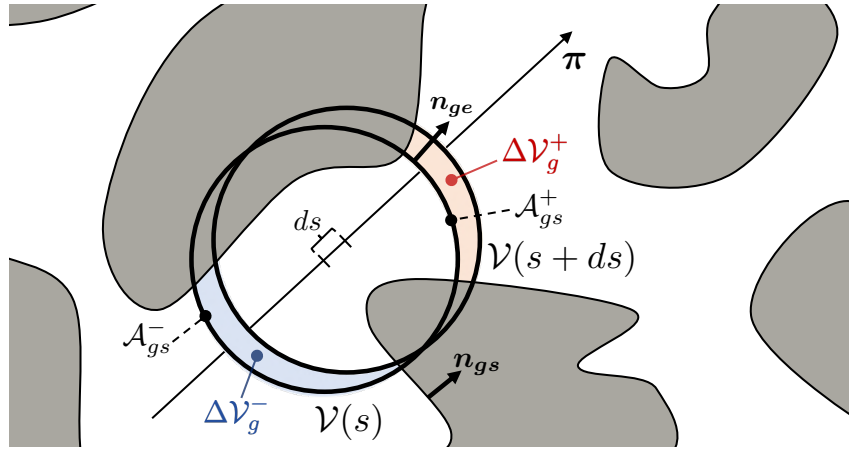


Figure 2.11. – Geometrical proof of the spatial averaging theorem.

2.B. Deviation terms for products of N quantities

For any general product of N quantities $\psi_{i \in [1, N]}$, we have the following (somewhat useless yet entertaining) relation:

$$\langle \prod_{i=1}^N \psi_i \rangle^{g,s} = \underbrace{\prod_{i=1}^N \langle \psi_i \rangle^{g,s}}_{\mathcal{A}(\prod_{i=1}^N \psi_i)} + \underbrace{\sum_{k=0}^{N-1} \sum_{\substack{I \subset [1, N], \#I=k \\ J=[1, N] \setminus I}} \prod_{i \in I} \langle \psi_i \rangle^{g,s} \langle \prod_{j \in J} \psi'_j \rangle^{g,s}}_{\mathcal{D}(\prod_{i=1}^N \psi_i)}. \quad (2.93)$$

Note that in the rightmost term, when $k = N - 1$ then $\#J = 1$ and $\langle \prod_{j \in J} \psi'_j \rangle^{g,s} = \langle \psi'_j \rangle^{g,s} = 0$, thus the sum running over k can be stopped at $k = N - 2$, thus:

$$\mathcal{D} \left(\prod_{i=1}^N \psi_i \right) = \sum_{k=0}^{N-2} \sum_{\substack{I \subset [1, N], \#I=k \\ J=[1, N] \setminus I}} \prod_{i \in I} \langle \psi_i \rangle^{g,s} \langle \prod_{j \in J} \psi'_j \rangle^{g,s} \quad (2.94)$$

Asymptotic analysis of flames in infinite, finite and multi-staged porous burners

This chapter is based on the article **Masset, P. A., Dounia, O., & Selle, L. (2021). Fully explicit formulae for flame speed in infinite and finite porous media. Combustion Theory and Modelling, 1-28** published during this thesis, augmented by new results.

Based upon simplified, constant-coefficient volume-averaged equations and assuming infinitely-thin reaction sheet, this chapter proposes analytical studies of gaseous flames in inert porous media. The central hypothesis is that interphase heat transfer has negligible impact on the local flame structure. This requires a gradual separation between the length scales of chemical reactions, gas diffusion, and interphase thermal re-equilibration. By resolving the gas and solid equations without reaction on each side of the reaction sheet, the preheating of the fresh gases ahead of the flame front is analytically computed at leading order. Combustion kinetics are solved separately, assuming the consumption rate to be a sole function of this preheating. Two kinetic models are considered, namely single-step Arrhenius and power law fits from experiments or detailed computations. Several fully-explicit formulae for flame speed in porous media are given accordingly. A universal abacus provides the maximum flame speed attainable in finite porous media. The explicit, ready-to-use nature of the present theory is particularly suitable for practical designs. The proposed results are consistent with previous theoretical, numerical and experimental trends of the literature. Notably, the fully-explicit nature of flame speed allows to explain previous trends observed in experiments and numerical simulations. In addition, the presented framework is directly applicable to 1D multi-staged burners, and allows to study their stability - what has seemingly not been done before in the literature.

Overview

3.1. Chapter introduction	54
3.2. Fully explicit formulae for flame speed in infinite porous media	57
3.2.1. Configuration	57
3.2.2. Modelling assumptions and decoupled methodology	57
3.2.3. Thermal problem \mathcal{T}	58
3.2.4. Length scales separation and approximation of η_{rec}	63
3.2.5. Chemical problem - model closure	64
3.2.6. Discussion and validation	67
3.3. Effects of flame wrinkling	68
3.3.1. Taking into account flame wrinkling	68
3.3.2. Theoretical influence of the wrinkling factor Γ_w	68
3.4. Effects of finite length & multi-staged burners	70
3.4.1. Single-staged burner: problem formulation	70

3.4.2. Influence of flame position	73
3.4.3. Universal behavior of finite-length effects in the decoupled regime . . .	74
3.4.4. Multi-staged burners: problem formulation	75
3.4.5. Boundary conditions	76
3.4.6. Interest of the present modelling for stability discussions	76
3.4.7. Influence of the thermal resistance	77
3.4.8. Porosity step	79
3.4.9. Interphase heat transfer & solid conductivity step	79
3.4.10. A “realistic” two-step burner?	80
3.4.11. Case $N \rightarrow \infty$: topology gradation	81
3.5. Conclusions of the chapter	83
3.A. Gas temperature continuity	84
3.B. Maximum of gas temperature at $x = 0$	84
3.C. Characteristic polynomial	86
3.D. Description of the coupled solver	87
3.E. Matrix for resolution of the single-layer finite porous	88

“Life is and will ever remain an equation incapable of solution, but it contains certain known factors.”

NIKOLA TESLA

3.1. Chapter introduction

Some key advantages of combustion in inert porous media are the increased flammability limits and stability, allowing a significant reduction in pollutant emissions (e.g. CO and NOx) [29, 102, 226]. The underlying mechanism is the preheating of the fresh gases, whose increased chemical reactivity allows to burn very lean mixtures [49, 62, 227]. This preheating is achieved by harvesting energy from the burnt gases through interphase heat exchange, which is then recirculated upstream by conduction and radiation in the porous matrix. Conceptually-speaking, the solid porous matrix is a supplementary path for upstream energy transfer to sustain combustion processes. Due to this preheating, the peak temperature in the gas domain may locally exceed the adiabatic temperature. This feature, characteristic of heat-recirculating burners, is often referred to as *superadiabatic* or *excess enthalpy* combustion.

Experimental investigations of flames submerged within porous media are intricate, mainly because of the opacity of the solid matrix and its small characteristic length scales. Measurements of temperature profiles, especially in the gas phase, are not trivial and may require advanced diagnostics [158, 228]. For example, to the author’s knowledge, a standard and essential quantity such as the local gas velocity has not been measured in these configurations. Regarding numerical simulations, there are many levels of approximation and corresponding modelling strategies. The most widespread may be the volume-averaged equations including reaction terms. This requires the determination of equivalent properties, such as a volume heat transfer coefficient, equivalent mixing diffusion or thermal conductivity, which may not be constant and cannot always be measured. The seminal works of Takeno et al. [134, 135] laid down the concept of excess enthalpy combustion, proposing numerical solutions in semi-infinite and finite geometries. Their one-dimensional model assumed constant solid temperature and single-step Arrhenius kinetics. Unlike classical gaseous combustion, mass flow rate and flame position were shown to be linked. A single branch was found in the semi-infinite case, while two branches were found in the finite

case - meaning that for a given inlet velocity, two flame positions are possible. A critical mass flow rate defining blow-off was identified. A similar model was used by Yoshizawa et al. [229] to predict the temperature profile in the solid and the relative importance of diffusion, conduction, and reaction terms along the flow direction was discussed. Later, it was shown in [230] that the classical shortcomings of single-step kinetics were more limiting for configurations with strong heat recirculation, where slow chemical reactions may drive the global behavior. This motivated the extension of traditional, one-dimensional combustion codes such as PREMIX or CANTERA to account for complex kinetics [69, 159, 231, 232]. Albeit improving accuracy, general trends remain the same. Some authors also considered two-dimensional simulations, again with volume-averaged equations. Notably, the recent work of Li et al. [98] on a porous microcombustor may be highlighted for its careful choice of modelling constants. Given the importance of proper radiation modelling to enhance predictability, many authors also resolved the Radiative Transfer Equation or one of its various approximations [34, 159, 218, 232–234]. At the other side of the numerical spectrum, Direct Pore Level Simulations (DPLS) were undertaken by some researchers, looking for insights on the corrugated flame structure intertwined in the porous medium [136, 235].

In parallel to numerical simulations, analytical works were carried out. By means of asymptotic theory, Dehaies and Joulin [236] studied the semi-infinite case of Takeno and Sato [134]. They also found one branch of solutions for inlet speed versus flame position. Buckmaster and Takeno [138] followed through to account for the finite case. They found two or more distinct branches, depending on flame position and heat losses to ambient (the apparition of a third or fourth branch stems from the consideration of *local* heat losses). Later on, Escobedo and Viljoen [237] were the first to propose an analytical approximation following a linearized Roseland hypothesis. They discussed features of radiant efficiency and also found two distinct flame positions for a given inlet speed. Soon afterwards, Boshoff-Mostert and Viljoen [238] published an Arrhenius-based model which always led to superadiabatic temperatures, but their work did not catch the downstream branch found by most other authors. More recently, Pereira et al. [239–241] published a series of articles on the structure of a flame within infinite porous media. Unique feature of the literature, they treated in [240] the case of ultra-lean mixtures, where interphase heat exchange plays a role at the scale of gas diffusion. In the rest of the literature where interphase equilibrium is not assumed, authors considered diffusion and reaction zones to be exempt of interphase heat transfer. It means that apart from the matching conditions on each side of the reaction-diffusion region, the flame was often implicitly assumed to behave locally as an adiabatic free-flame.

It is worth mentioning that the formalism of flames submerged within porous media shares many traits with the study of combustion in micro and mesoscale tubes [126, 127, 242–246]. Conceptually, small tubes can be seen as a straightened porous structure also featuring substantial thermal coupling with the wall. Lee and Maruta [126] have described many stationary propagation regimes of the flame front through a theoretical one-dimensional, single-step Arrhenius model. They have shown that superadiabatic combustion with high wall temperatures occurs only for slowly-moving, almost stationary flames. This feature is coherent with the results of the vast literature on filtration combustion, where thermal and reaction waves should be superimposed to achieve maximum superadiabatic effect [41, 247–251]. Unlike the present work, which considers stationary flames with substantial interphase non-equilibrium, filtration combustion focuses mainly on flame front propagation, assuming strong interphase equilibrium.

Despite the fact that many aspects of combustion in porous media have already been explored, it seems that a simple, fully-explicit formula for flame speed as a function of basic porous matrix and mixture properties is yet to be proposed. For instance, the formula proposed by Pereira [239] requires to solve an implicit problem involving recirculation efficiency to obtain the flame speed. In addition, analytical models suffer from the single-step approximation, which may hide the

actual sensitivity of the flame to preheating. Eventually, little practical design rules and universal relationships between infinite and finite porous media have been explored. The purpose of the present chapter is to cover these issues, by proposing a ready-to-use analytical model in both infinite and finite cases. Assuming the flame to behave locally as an adiabatic free-flame, it is possible to 1) solve the thermal problem on each side of the reaction sheet so as to compute the preheating of the flame, and then 2) solve the chemical problem separately, so as to know how the flame responds to this preheating. The modelling of each phase allows to predict when gas diffusion and interphase re-equilibration length scales are well separated, assessing whether the local adiabaticity hypothesis is valid. Analytical approximations provide fully-explicit forms for the flame speed. The proposed decoupled methodology allows to consider complex chemistry through correlations of free-flames consumption rates as a function of preheating, thus offering alternatives to single-step. The present work is also meant to retrieve and discuss many key features of combustion within porous media from the literature, which can be summarised as follows:

- the flame structure consists of a macroscale preheating region, followed by a thin reaction-diffusion zone, then by another macroscale thermal relaxation region (counterpart of the preheating region, of comparable length) ;
- recirculation efficiency decreases with equivalence ratio and porosity, and increases with solid conductivity and volume heat transfer coefficient ;
- for finite-length porous media, two or more solutions may be found for a given inlet speed.

In addition, as mentioned in Chapter 1, practical designs of porous burners may differ significantly from the configurations studied in simplified asymptotic analyses in infinite and even finite burners. Design variations may include flow divergence [140], varying pore size [153], but the most widely used strategy to stabilize flames inside porous burners is the so-called *multi-staged* or *multi-step* approach [34, 69], which consists in stacking together porous media of different pore sizes, porosities and materials. This may enforce an hydrodynamic stabilization at the interfaces through porosity jumps, and a thermal stabilization effect through pore size/material variations. It was notably suggested that the upstream solid matrix sections should have small pores, lower thermal conductivity and lower porosity [159]. Usually, two-staged burners are considered, with a fine-pored structure upstream supposedly acting as a flame arrestor (quenching). However, many authors did notice flashback even when the pore size was smaller than the predicted quenching distance, indicating that the notion of quenching is not completely relevant in the presence of strong heat recirculation. Also, there has been no comments in the literature upon a possible solid temperature discontinuity between two successive solid layers, given their very low contact points. More generally, to the best of the author's knowledge there does not seem to exist any asymptotic theory of multi-staged burners, nor theoretical considerations regarding their stability for varying solid matrix properties. As we will see, the asymptotic framework developed for infinite and finite porous media directly applies to multi-staged burners, provided jump conditions are prescribed between the layers.

The chapter is organised as follows. Section 3.2 treats the case of the infinite porous medium, and several fully-analytical expressions for flame speed-up are provided. Section 3.3 considers theoretical implications of flame wrinkling. Section 3.4 is dedicated to the influence of finite length on flame stabilization and recirculation efficiency, and to some results on multi-staged burners are given.

Note: in Chapters 3 and 4 the quantities are implicitly expressed as their volume average $\langle \cdot \rangle^{g,s}$, whose notation is dropped for better readability.

3.2. Fully explicit formulae for flame speed in infinite porous media

3.2.1. Configuration

The configuration sketched in Figure 3.1 represents a steady flame submerged in an infinite, inert and homogeneous porous medium, characterised by its porosity ϵ , surface density \mathcal{S}_V and thermal conductivity λ_s . This thermal conductivity may include the effects of tortuosity and a rough modelling of radiation, which is not considered due to its highly non-linear nature. The problem is assumed to be one-dimensional along the space coordinate x , and the steady flame is localized at the arbitrary position $x = 0$ by its reaction zone, assumed infinitely thin. Gas and solid properties are assumed constant. The gas phase is characterised by its thermal

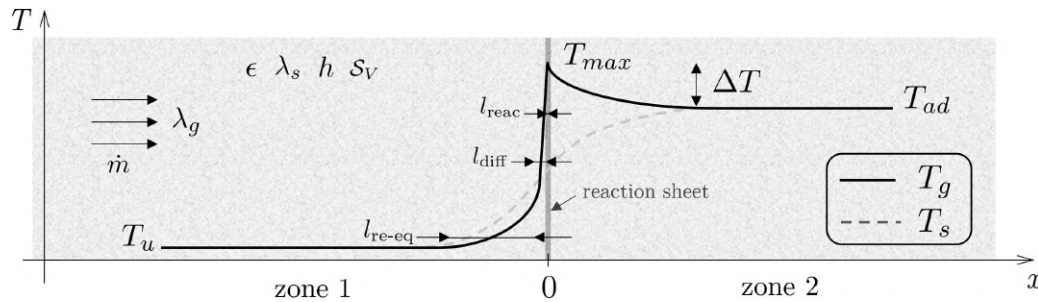


Figure 3.1. – Principle: flame submerged within infinite porous medium.

conductivity λ_g and heat capacity per mass unit c_{pg} . A perfect gas model is assumed. The solid and gas temperatures are noted T_s and T_g respectively and the heat flux between the two phases is modelled via a classical transfer coefficient h . The phase-averaged mass flow rate \dot{m} (with the notations of Chapter 2 it is $\langle \rho_g \rangle^g \langle u \rangle^g$) is imposed upstream at a temperature T_u . Note that mass conservation for constant porosity yields $\dot{m} = \text{constant}$. The system is assumed to be globally adiabatic so that far downstream both solid and gas temperatures equal the adiabatic equilibrium temperature T_{ad} . Due to the presence of the solid matrix, the gas is preheated before reaching the flame front. This may lead to a maximum gas temperature T_{max} above the adiabatic temperature, which is shown in Appendix 3.B to be reached at the origin in the reaction zone. This classical behavior of combustion in inert porous media is quantified via the so-called excess temperature ΔT , defined as:

$$\Delta T = T_{max} - T_{ad}. \quad (3.1)$$

If the reactive-diffusive flame structure is not affected by interphase heat transfer, then ΔT is also the preheating temperature perceived upstream the flame front. We now discuss this hypothesis, and see how it corresponds to what we call the *decoupled* methodology.

3.2.2. Modelling assumptions and decoupled methodology

An adiabatic free-flame front comprises two gaseous length scales [114]:

- a non-reactive, diffusion zone of length l_{diff} , where the heat from the reaction zone is diffused upstream through a steep temperature gradient ;
- a reactive zone of length l_{reac} where the chemical energy of the mixture is released. Classically, one finds $l_{reac} \ll l_{diff}$.

For flames embedded in porous media, a third length scale l_{re-eq} intervenes in the gas phase, related to the interphase re-equilibrium zones on each side of the flame front, as shown in Figure 3.1. Under the assumption of length scale separation, that is:

$$l_{re-eq} \gg l_{diff} \gg l_{reac}, \quad (3.2)$$

the flame in the porous medium can be considered *locally adiabatic* and interphase heat exchange plays a minor role at the scale of diffusion and reaction. This hypothesis, corresponding to (3.2) is adopted in the present work. It notably allows for decoupling the analysis into two distinct, independent problems:

- a thermal problem \mathcal{T} , which provides the preheating temperature ΔT as a function of the inlet mass flux \dot{m} . It is obtained by solving the non-reactive, coupled gas and solid equations on each side of the reaction sheet;
- a chemical problem \mathcal{C} , which describes the sensitivity the consumption rate \dot{m} to the preheating ΔT .

Formally, these two problems can be written:

$$\Delta T = \mathcal{T}(\dot{m}) \quad \text{and} \quad \dot{m} = \mathcal{C}(\Delta T). \quad (3.3)$$

Combining them leads to an implicit formulation:

$$\dot{m} = (\mathcal{C} \circ \mathcal{T})(\dot{m}), \quad (3.4)$$

whose resolution provides the value of \dot{m} consistent with both the non-reactive equations outside the reaction sheet and the local sensitivity of the flame to preheating. The benefits of the methodology are the following. Solving the non-reactive equations boils down to simple linear algebra. Under the some hypotheses, notably Equation (3.2), the preheating/excess temperature finds a simplified expression. Also, both single-step and more complex chemistry can be considered for the resolution of Equation (3.4).

3.2.3. Thermal problem \mathcal{T}

In this section, the thermal problem \mathcal{T} is solved both numerically and analytically.

3.2.3.1. Equations and boundary conditions

On each side of the flame, no reaction occurs. Consequently, the steady-state, isobaric, volume averaged one-dimensional energy equations for the solid and gas phase read [252]:

$$\lambda_s \partial_x^2 T_s + \frac{h_V}{1-\epsilon} (T_g - T_s) = 0 \quad (\text{solid}), \quad (3.5)$$

$$-\dot{m} c_{p_g} \partial_x T_g + \lambda_g \partial_x^2 T_g - \frac{h_V}{\epsilon} (T_g - T_s) = 0 \quad (\text{gas}), \quad (3.6)$$

where $h_V = h \mathcal{S}_V$ is the heat exchange coefficient per unit volume. The porous medium is assumed globally adiabatic, thus there are no heat losses in the equations. This justifies the boundary conditions for the gas and solid phases, which must reach thermal equilibrium far upstream and downstream:

$$T_s \xrightarrow{x \rightarrow -\infty} T_u \quad \text{and} \quad T_g \xrightarrow{x \rightarrow -\infty} T_u, \quad (3.7)$$

$$T_s \xrightarrow{x \rightarrow +\infty} T_{ad} \quad \text{and} \quad T_g \xrightarrow{x \rightarrow +\infty} T_{ad}. \quad (3.8)$$

3.2.3.2. Dimensionless equations

The coordinates and temperatures are normalized as:

$$x^* = x / \sqrt{\frac{(1-\epsilon)\lambda_s}{h_V}}, \quad \theta_s = \frac{T_s - T_u}{T_{ad} - T_u}, \quad \theta_g = \frac{T_g - T_u}{T_{ad} - T_u} \quad \text{and} \quad \theta_{max} = \frac{T_{max} - T_u}{T_{ad} - T_u}. \quad (3.9)$$

It follows that the reduced adiabatic temperature is, by definition: $\theta_{ad} = 1$. Also, since $T_{ad} - T_u$ represents the thermal load, it is found that the dimensionless preheating temperature ΔT identifies to the recirculation efficiency:

$$\eta_{rec} = \frac{\Delta T}{T_{ad} - T_u} = \frac{T_{max} - T_{ad}}{T_{ad} - T_u} = \theta_{max} - \theta_{ad} = \theta_{max} - 1. \quad (3.10)$$

For a given mixture, the knowledge of η_{rec} is thus directly equivalent to that of ΔT :

$$\Delta T = \alpha T_{ad} \eta_{rec}, \quad (3.11)$$

where $\alpha = (T_{ad} - T_u)/T_{ad}$. Equations (3.5-3.6) can be normalised using (3.9), yielding:

$$\partial^2 \theta_s + \theta_g - \theta_s = 0, \quad (3.12)$$

$$-r_{\dot{m}} \partial \theta_g + r_\lambda \partial^2 \theta_g + \theta_s - \theta_g = 0, \quad (3.13)$$

where $\partial \equiv \partial_{x^*}$ and the constants $r_{\dot{m}}$ and r_λ are defined by:

$$r_{\dot{m}} = \frac{\dot{m} \epsilon c_{pg}}{\sqrt{h_V(1-\epsilon)\lambda_s}} \quad \text{and} \quad r_\lambda = \frac{\epsilon \lambda_g}{(1-\epsilon)\lambda_s}. \quad (3.14)$$

The product $h_V(1-\epsilon)\lambda_s$ can be interpreted as a conductance for the recirculated heat, first harvested via h_V , then conducted upstream through the solid matrix via $(1-\epsilon)\lambda_s$. As such, the quantity $r_{\dot{m}}$ can be seen as a ratio between the thermal load, proportional to $\dot{m}c_{pg}$, and the energy recirculated upstream by the solid. Thus, the inverse of $r_{\dot{m}}$ is expected to be closely related to the recirculation efficiency. The other ratio, r_λ , represents the ability of the system to conduct energy, either in the gas with the term $\epsilon \lambda_g$, or through the solid with the term $(1-\epsilon)\lambda_s$. The solutions for the solid and gas temperatures are respectively noted θ_s^1, θ_g^1 in zone 1, and θ_s^2, θ_g^2 in zone 2. Following Equations (3.7-3.8), the normalised boundary conditions are:

$$\theta_s^1 \xrightarrow{x^* \rightarrow -\infty} 0 \quad \text{and} \quad \theta_g^1 \xrightarrow{x^* \rightarrow -\infty} 0 \quad (3.15)$$

$$\theta_s^2 \xrightarrow{x^* \rightarrow +\infty} 1 \quad \text{and} \quad \theta_g^2 \xrightarrow{x^* \rightarrow +\infty} 1 \quad (3.16)$$

Combining Equations (3.12-3.13), the problem reduces to a single linear differential equation for θ_s with constant coefficients, valid in both zones:

$$\partial \left[r_\lambda \partial^3 - r_{\dot{m}} \partial^2 - (r_\lambda + 1) \partial + r_{\dot{m}} \right] \theta_s = 0. \quad (3.17)$$

By integrating Equation (3.17) once and applying the boundary conditions (3.15-3.16), the governing equation in each zone becomes:

$$\left[r_\lambda \partial^3 - r_{\dot{m}} \partial^2 - (r_\lambda + 1) \partial + r_{\dot{m}} \right] \theta_s^1 = 0 \quad \text{in zone 1,} \quad (3.18)$$

$$\left[r_\lambda \partial^3 - r_{\dot{m}} \partial^2 - (r_\lambda + 1) \partial + r_{\dot{m}} \right] (\theta_s^2 - 1) = 0 \quad \text{in zone 2.} \quad (3.19)$$

The general solutions of Equations (3.18-3.19) are linear combinations of exponentials, whose eigenvalues are given by the roots of the same characteristic polynomial:

$$r_\lambda \lambda^3 - r_{\dot{m}} \lambda^2 - (r_\lambda + 1) \lambda + r_{\dot{m}} = 0. \quad (3.20)$$

For $\dot{m} > 0$, the roots are necessarily two positive reals and a negative one, ordered $\lambda_1 < 0 < \lambda_2 < \lambda_3$. A proof and further details are provided in Appendix 3.C. Since the boundary conditions

require boundedness at $x \rightarrow \pm\infty$, the solutions of Equations (3.18) and (3.19) for the solid temperature take the following form:

$$\theta_s^1(x^*) = A_2 e^{\lambda_2 x^*} + A_3 e^{\lambda_3 x^*}, \quad (3.21)$$

$$\theta_s^2(x^*) = 1 + A_1 e^{\lambda_1 x^*}. \quad (3.22)$$

Using Equation (3.12), the gas temperature is also found:

$$\theta_g^1(x^*) = A_2(1 - \lambda_2^2) e^{\lambda_2 x^*} + A_3(1 - \lambda_3^2) e^{\lambda_3 x^*}, \quad (3.23)$$

$$\theta_g^2(x^*) = 1 + A_1(1 - \lambda_1^2) e^{\lambda_1 x^*}. \quad (3.24)$$

The determination of the three unknowns A_1 , A_2 and A_3 requires three jump conditions between zones 1 and 2, at $x = 0$. Assuming negligible interphase heat exchange at the scale of the reaction zone, the temperature of the solid and its derivative are necessarily continuous across the flame:

$$T_s(x = 0^-) = T_s(x = 0^+), \quad (3.25)$$

$$\partial_x T_s(x = 0^-) = \partial_x T_s(x = 0^+). \quad (3.26)$$

For the gas, the conservation of enthalpy across the flame reads:

$$\lambda_g \partial_x T_g(x = 0^-) = \dot{m} c_{p_g} (T_{ad} - T_u) + \lambda_g \partial_x T_g(x = 0^+). \quad (3.27)$$

It is shown in Appendix 3.A that Equation (3.27), together with Equation (3.26) and the boundary conditions (3.15-3.16) is in fact equivalent to imposing gas temperature continuity. The three jump conditions are thus:

$$\theta_s^1(x^* = 0^-) = \theta_s^2(x^* = 0^+) \quad \text{continuity of solid temperature,} \quad (3.28)$$

$$\partial \theta_s^1(x^* = 0^-) = \partial \theta_s^2(x^* = 0^+) \quad \text{continuity of solid heat flux,} \quad (3.29)$$

$$\theta_g^1(x^* = 0^-) = \theta_g^2(x^* = 0^+) \quad \text{continuity of gas temperature.} \quad (3.30)$$

Applying the boundary conditions (3.28-3.30) to Equations (3.21-3.22), one gets a linear system:

$$A_2 + A_3 - A_1 = 1, \quad (3.31)$$

$$\lambda_2 A_2 + \lambda_3 A_3 - \lambda_1 A_1 = 0, \quad (3.32)$$

$$A_2(1 - \lambda_2^2) + A_3(1 - \lambda_3^2) - A_1(1 - \lambda_1^2) = 1, \quad (3.33)$$

whose resolution gives the coefficients A_i , thus the temperature profiles. The formal solution is provided in Appendix 3.B. As explained in Section 3.2.1, the temperature of interest is the maximum temperature found at the origin:

$$\theta_{max} = \theta_g^1(x^* = 0^-) = \theta_g^2(x^* = 0^+). \quad (3.34)$$

Using Equations (3.10) and (3.24) yields:

$$\eta_{rec} = \theta_g^2(x^* = 0^+) - 1 = A_1(1 - \lambda_1^2), \quad (3.35)$$

proving that heat recirculation depends only on the smallest (negative) solution of Equation (3.20), which depends *a priori* on both $r_{\dot{m}}$ and r_λ . Formally, using (3.10) the solution of the thermal problem \mathcal{T} writes:

$$\Delta T = (T_{ad} - T_u) \eta_{rec}(r_{\dot{m}}, r_\lambda). \quad (3.36)$$

3.2.3.3. Numerical solutions of the thermal problem

Before providing an analytical solution for η_{rec} , let us take a look at particular solutions to gain physical insight on the model and the range of validity of its underlying assumptions. Examples of temperature profiles are shown in Figure 3.2 for four different inlet mass fluxes and given porous/mixture properties, *i.e.* four different values of $r_{\dot{m}}$ for a given value of r_λ . It is observed that the solid temperature does not exceed the adiabatic temperature, which is coherent with most findings in the literature. A graphical representation of the recirculation efficiency η_{rec} , as defined in Equation (3.35), is shown in Figure 3.2(a).

In Figures 3.2(a) and 3.2(b), the temperature increase in the gas by diffusion is very sharp, and a clear distinction between the length scales of preheating and gas diffusion is observed. On the contrary, Figures 3.2(c) and 3.2(d) show $\theta_s \sim \theta_g$ because of the much stronger interphase equilibrium - except in the vicinity of the reaction sheet. This suggests that there are lower

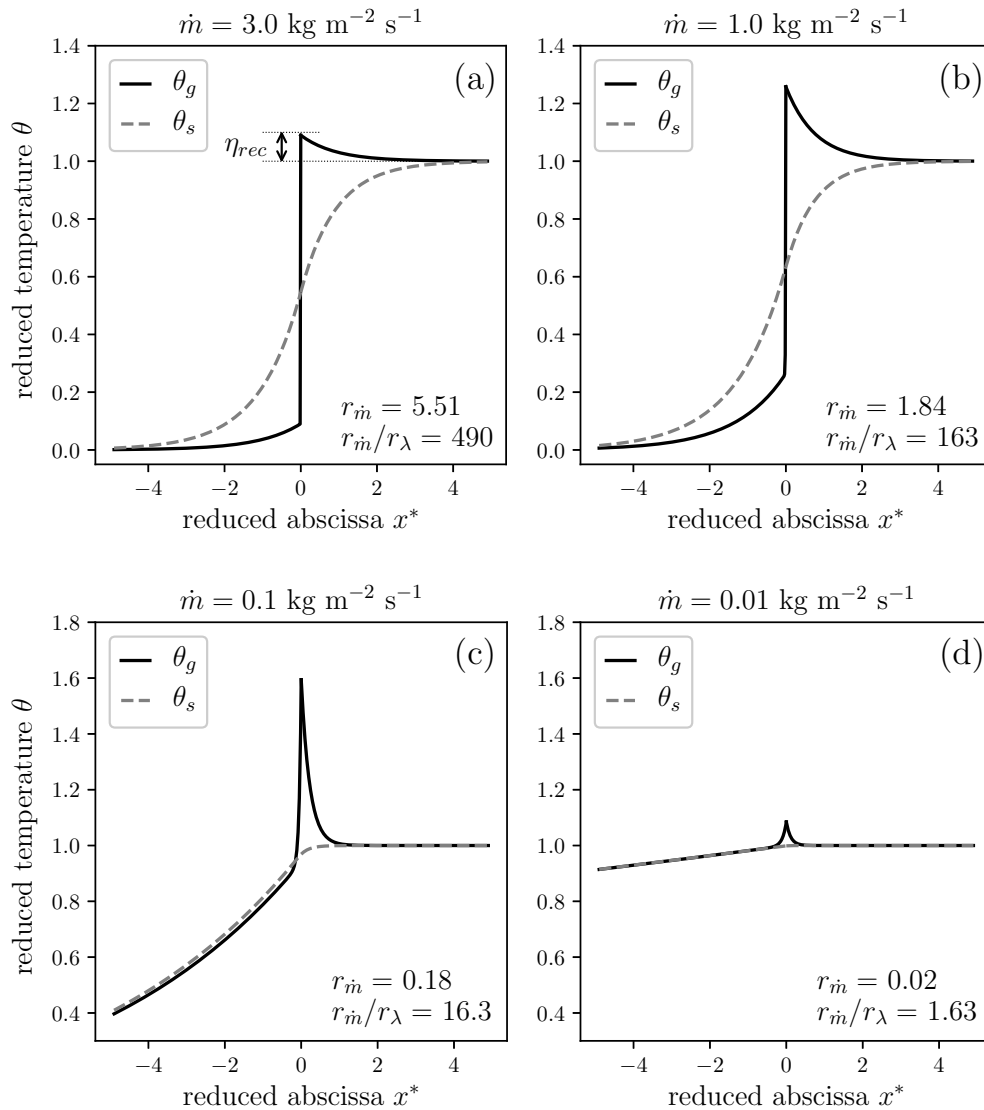


Figure 3.2. – Temperature profiles for four different inlet mass flow rates and $r_\lambda = 0.01$. The parameters used are: $\epsilon = 0.8$, $\lambda_s = 20 \text{ W m}^{-1} \text{ K}^{-1}$, $\lambda_g = 0.025 \text{ W m}^{-1} \text{ K}^{-1}$, $h_V = 1.2 \times 10^5 \text{ W m}^{-3} \text{ K}^{-1}$, and $c_{pg} = 1 \times 10^3 \text{ J kg}^{-1} \text{ K}^{-1}$.

bounds for both $r_{\dot{m}}$ and $r_{\dot{m}}/r_\lambda$ below which the scale-separation hypothesis (3.2) is not valid. It is nevertheless pointed out that the temperature profiles in Figures 3.2(c) and 3.2(d) are quite similar to those of so-called weak flames. The analysis of this similarity is beyond the scope of the present work. Using this preliminary observation, a necessary condition for the validity of the model (decoupled regime) is proposed:

$$r_{\dot{m}} \gg 0.1 \quad \text{and} \quad r_{\dot{m}}/r_\lambda \gg 10. \quad (3.37)$$

In order to investigate these limitations in a more systematic way, the numerical solutions of η_{rec} are plotted versus $r_{\dot{m}}$ for different values of r_λ in Figure 3.3. The four cases of Figure 3.2 are also displayed. Typical values representative of combustion in porous media can be found in [239], where $r_{\dot{m}} = 1.78$ and $r_\lambda = 0.07$. By covering two orders of magnitude above and below these values, the proposed range should cover most porous media and mixtures. The solutions verifying $r_{\dot{m}} > 0.5$ and $r_{\dot{m}}/r_\lambda > 50$, consistent with assumptions (3.37), are drawn in solid lines, while the others are drawn in dotted lines. Interestingly, these solid lines seem to collapse the dashed curve whose equation is $1/2r_{\dot{m}}$, with little influence of the parameter r_λ . In summary, it seems that under the assumptions (3.37):

- the length scales of preheating and gas diffusion are well separated (*cf.* Figure 3.2), which is consistent with the modelling assumptions;
- the solution of the thermal problem can be approximated by $\eta_{rec} \simeq 1/2r_{\dot{m}}$.

Similar ranges were explored in previous studies. For example, the case $r_\lambda \ll 1$ was considered by Lee and Maruta for mesoscale tubes [126]. The limits considered by Pereira [239] were 1) $r_\lambda \ll 1$ if $\epsilon/(1-\epsilon) = O(1)$ and 2) $r_{\dot{m}}^2/r_\lambda \gg 1$ if $\epsilon = O(1)$. By combining $r_{\dot{m}} \gg 0.1$ and $r_{\dot{m}}/r_\lambda \gg 10$, this latter limit is retrieved, without the influence of porosity which is not considered in [239] to discriminate asymptotic regimes.

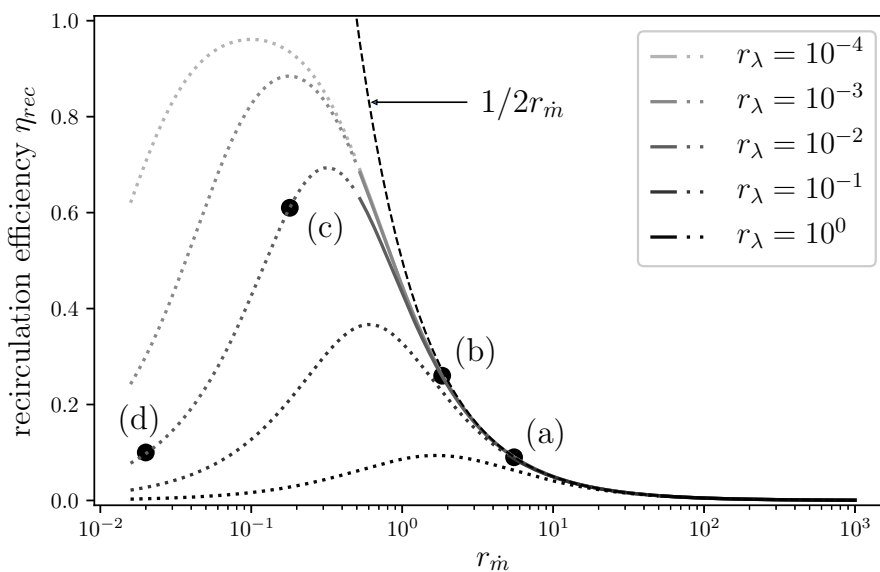


Figure 3.3. – Recirculation efficiency η_{rec} for various values of the dimensionless parameters $r_{\dot{m}}$ and r_λ . Solid lines: $r_{\dot{m}} > 0.5$ and $r_{\dot{m}}/r_\lambda > 50$. Dotted lines: $r_{\dot{m}} < 0.5$ or $r_{\dot{m}}/r_\lambda < 50$. The points (a-d) correspond to Figure 3.2.

3.2.4. Length scales separation and approximation of η_{rec}

3.2.4.1. Length scales separation

In this Section, mathematical developments and physical interpretation are provided under the assumption (3.37). First, let us recall that since $\sqrt{(1-\epsilon)\lambda_s/h_V}$ is the length used to normalize the equations, each root λ_i of (3.20) found in the exponentials of Equations (3.23-3.24) provides a dimensional length scale l_i given by:

$$l_i = \frac{\sqrt{(1-\epsilon)\lambda_s/h_V}}{|\lambda_i|}. \quad (3.38)$$

It is thus of interest to find the expression of the roots λ_i in the regime (3.37). Their rigorous, general forms and Taylor expansions in the regime (3.37) are given in Appendix 3.C. At the leading order, it is found that:

$$\lambda_1 \simeq -1, \quad \lambda_2 \simeq 1 \quad \text{and} \quad \lambda_3 \simeq \frac{r_{\dot{m}}}{r_\lambda}, \quad (3.39)$$

so that:

$$l_1 \simeq l_2 \simeq \sqrt{\frac{(1-\epsilon)\lambda_s}{h_V}} \quad \text{and} \quad l_3 \simeq \frac{\lambda_g}{\dot{m} c_{p_g}}. \quad (3.40)$$

l_3 is the well-known gas diffusion length scale, denoted l_{diff} , while l_1 and l_2 define the typical length of interphase thermal re-equilibration, denoted $l_{\text{re-eq}}$:

$$l_{\text{re-eq}} = \sqrt{\frac{(1-\epsilon)\lambda_s}{h_V}}. \quad (3.41)$$

This scale characterises the preheating and interphase relaxation regions before and after the flame front, as can be seen on Figures 3.2(a) and (b). This analysis gives an interpretation of $r_{\dot{m}}/r_\lambda$ as a ratio of length scales:

$$\frac{r_{\dot{m}}}{r_\lambda} = \sqrt{\frac{(1-\epsilon)\lambda_s}{h_V}} / \left(\frac{\lambda_g}{\dot{m} c_{p_g}} \right) = \frac{l_{\text{re-eq}}}{l_{\text{diff}}}. \quad (3.42)$$

The condition $r_{\dot{m}}/r_\lambda \gg 10$ is thus consistent with the separation of length scales of Equation (3.2) underlying the decoupled hypothesis of the present modelling.

3.2.4.2. Approximation of η_{rec}

Combining Equations (3.108) and (3.129-3.131) into Equation (3.35), the leading-order analytical solution for the heat recirculation is:

$$\eta_{rec} \simeq \frac{1}{2r_{\dot{m}}}, \quad (3.43)$$

which is exactly the asymptote plotted in Figure 3.3. In this regime, the thermal problem does not depend on r_λ , which is coherent with the collapse of the curves in Figure 3.3. Equation (3.43) supports further the discussion of Section 3.2.3.2 on the physical significance of $r_{\dot{m}}$ and that of Section 3.2.3.3 on the condition $r_{\dot{m}} \gg 0.1$, showing that the approximate solution is valid when heat recirculation is not overly intense. In dimensional terms, the solution for \mathcal{T} in Equation (3.3) is therefore:

$$\Delta T = (T_{ad} - T_u) \frac{\sqrt{h_V(1-\epsilon)\lambda_s}}{2\dot{m}\epsilon c_{p_g}}. \quad (3.44)$$

It is insightful to understand which physical properties are likely to play a significant part in validating the regime (3.37) or not. These are:

- the mass flow rate \dot{m} : very slow flames might show a strong interphase equilibrium. This regime was studied thoroughly by Pereira et al. [240];
- the solid thermal conductivity λ_s : its decrease leads to a lower separation of length scales. Note that the tortuosity of the solid matrix may be considered by altering the value of λ_s ;
- the volume heat transfer coefficient h_V is also a key parameter which is often difficult to assess [29]. It is typically affected by the material surface state, the geometry, the Reynolds number, etc.

3.2.5. Chemical problem - model closure

In the present section, two paths for the resolution of the chemical problem \mathcal{C} are proposed. Each time, the principle is to find a kinetic relation between the inlet mass flux \dot{m} and the preheating of the fresh gases ΔT . First, a single-step Arrhenius estimation based on the work of Pereira et al. [239] is investigated. Then, a power law approximation of the consumption rate increase with preheating is identified through numerical simulations of adiabatic free-flames. For the sake of the example, two typical mixtures are considered: one methane-air and one hydrogen-air, whose descriptive values are given in Table 3.1. The parameter β is the so-called

mixture	ϕ	α	β	T_{ad} (K)
methane-air	0.80	0.85	9.07	1996
hydrogen-air	0.52	0.82	8.27	1683

Table 3.1. – Relevant thermodynamic and chemical properties for two reacting mixtures used as examples.

Zel'dovich number, related to the activation temperature T_a through:

$$\beta = \frac{T_a(T_{ad} - T_u)}{T_{ad}^2}. \quad (3.45)$$

Values for β in Table 3.1 are found in [239] for methane and [253] for hydrogen. In what follows, S_L^P denotes the global consumption speed (*i.e.* the gas velocity at the infinite upstream), and $S_L^0(T)$ the speed of the corresponding adiabatic free-flame of fresh gases at a temperature T . The flame speed-up is defined as the ratio $S_L^P/S_L^0(T_u)$. It quantifies the acceleration of combustion due to the heat recirculation in the porous matrix. This speed-up is also that of the mass fluxes and is directly related to \dot{m} , thus $\mathcal{C}(\Delta T)$, through:

$$\frac{S_L^P}{S_L^0(T_u)} = \frac{\dot{m}}{\dot{m}_0} = \frac{\mathcal{C}(\Delta T)}{\dot{m}_0}. \quad (3.46)$$

where $\dot{m}_0 = \rho_u S_L^0(T_u)$ is the mass flux of the adiabatic free-flame without porous medium and ρ_u is the density at the infinite upstream. Note that \dot{m}_0 is an input of the model in the sense that ρ_u and $S_L^0(T_u)$ are known *a priori*.

3.2.5.1. Single-step kinetics

The first kinetic model is based indirectly on theoretical work of Peireira et al. [239]. They analyzed the asymptotic structure of a flame submerged in a porous medium. Alike the present model, their methodology consisted in neglecting interphase heat exchange at the scale of reaction and diffusion. They made use of a single-step Arrhenius law, and matched the preheating and flame exit gas temperature gradients - something not caught by the present model, but of

negligible importance in the regime (3.2). For a null temperature exponent in the Arrhenius term, they found the following expression for flame speed-up:

$$\frac{S_L^P}{S_L^0(T_u)} = (1 + \alpha\eta_{rec}) \exp\left(\frac{1}{2} \frac{\beta\eta_{rec}}{1 + \alpha\eta_{rec}}\right). \quad (3.47)$$

In coherence with the regime (3.37), assuming $\alpha\eta_{rec}$ small enough yields a simplified expression for Equation (3.47):

$$\frac{S_L^P}{S_L^0(T_u)} = \exp\left(\frac{\beta\eta_{rec}}{2}\right). \quad (3.48)$$

The relative error between Equations (3.47) and (3.48) is plotted in Figure 3.4 for representative values of α and β . This shows that (3.48) is a fair approximation of (3.47) only for recirculation efficiencies below 0.3. Using this simplification, the derivation is pursued and we define:

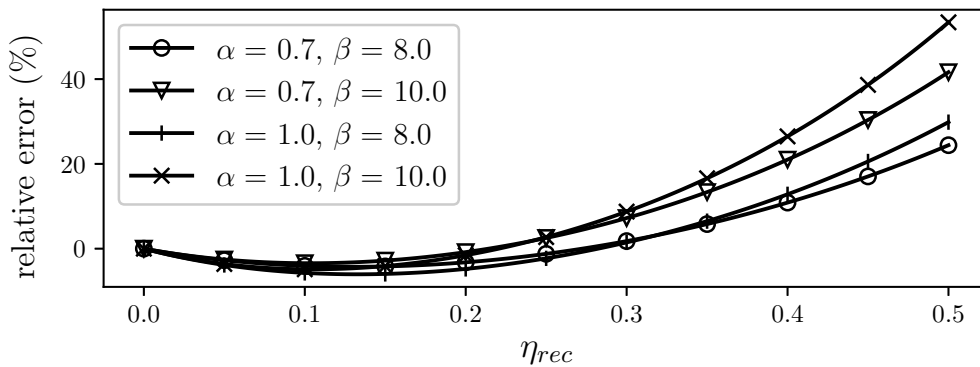


Figure 3.4. – Relative error between Equations (3.47) and (3.48).

$$\eta_{rec}^0 = \eta_{rec} \frac{\dot{m}}{\dot{m}_0}, \quad (3.49)$$

which, using Equation (3.43), yields:

$$\eta_{rec}^0 = \frac{\sqrt{h_V(1-\epsilon)\lambda_s}}{2\dot{m}_0\epsilon c_{pg}}. \quad (3.50)$$

This shows that η_{rec}^0 is a constant related to the physical properties of the mixture and the porous medium. Then using Equations (3.46) and (3.49), Equation (3.48) becomes:

$$Z = W \exp(W), \quad (3.51)$$

where:

$$Z = \frac{\beta\eta_{rec}^0}{2} \quad \text{and} \quad W = \frac{\beta\eta_{rec}^0}{2} \frac{\dot{m}_0}{\dot{m}}. \quad (3.52)$$

The solution of Equation (3.51) is given by the the first branch of the Lambert function \mathcal{W} [254]. Recalling Equation (3.46), this yields a fully-explicit formula for flame speed-up:

$$\frac{S_L^P}{S_L^0(T_u)} = \frac{\beta\eta_{rec}^0}{2\mathcal{W}(\beta\eta_{rec}^0/2)}. \quad (3.53)$$

In order to discuss trends, Equation (3.53) is further simplified in the limit of small η_{rec}^0 using the Taylor expansion of $\mathcal{W}(Z)$ at the origin:

$$\mathcal{W}(Z) = Z - Z^2 + O(Z^3), \quad (3.54)$$

which simplifies Equation (3.53) to:

$$\frac{S_L^P}{S_L^0(T_u)} \simeq 1 + \frac{\beta}{2} \eta_{rec}^0. \quad (3.55)$$

3.2.5.2. Power law approximation

In this study, it is assumed that preheating and combustion are decoupled meaning that the local flame velocity is that of a preheated laminar adiabatic flat flame, *i.e.* $S_L^0(T_u + \Delta T)$. Mass conservation in steady state reads:

$$\rho(T_u)S_L^P = \rho(T_u + \Delta T)S_L^0(T_u + \Delta T), \quad (3.56)$$

which, following the isobaric hypothesis, yields:

$$\frac{S_L^P}{S_L^0(T_u)} = \left(\frac{T_u}{T_u + \Delta T} \right) \frac{S_L^0(T_u + \Delta T)}{S_L^0(T_u)}. \quad (3.57)$$

Consequently, the determination of the flame speed-up only requires the knowledge of the adiabatic flame speed S_L^0 at T_u and $T_u + \Delta T$. Within a given temperature range it is common practice to fit experimental or numerical results via a power law. In order to simplify the algebra, one can choose a power of $(1 + \Delta T/T_u)$ in which case equation (3.57) reduces to:

$$\frac{S_L^P}{S_L^0(T_u)} = \left(1 + \frac{\Delta T}{T_u} \right)^{n_T} = \left(1 + \frac{T_{ad}}{T_u} \alpha \eta_{rec} \right)^{n_T}. \quad (3.58)$$

Examples corresponding to the two mixtures of Table 3.1 are shown in Figure 3.5, where the reference flame speeds have been computed with CANTERA [112] using GRIMECH 3.0. In both cases, the power law approximation is quite accurate. Note that since overly large preheating temperatures lead to auto-ignition and a lack of numerical convergence of the adiabatic flames,

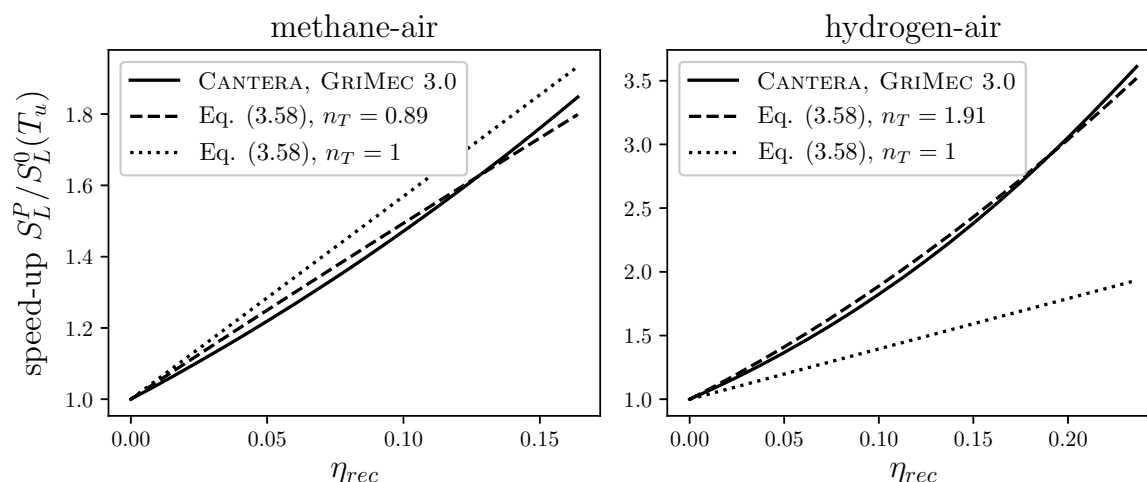


Figure 3.5. – Speed-up of the porous medium system: numerical simulations and power law correlations.

the maximal preheating temperature is set to 300 K, which leads to different bounds in terms of η_{rec} between the two plots. The specific case $n_T = 1$, particularly convenient analytically, is also shown for comparison. Following this approximation, an analytical formulation for the chemical problem is obtained by feeding Equations (3.46) and (3.49) into (3.58):

$$\left(\frac{S_L^P}{S_L^0(T_u)}\right)^{\frac{1}{n_T}+1} - \frac{S_L^P}{S_L^0(T_u)} = \frac{T_{ad}}{T_u} \alpha \eta_{rec}^0. \quad (3.59)$$

Because this equation is not amenable to a general analytical solution, two special cases are considered. First in the limit of small η_{rec}^0 , a first-order Taylor expansion yields:

$$\frac{S_L^P}{S_L^0(T_u)} \simeq 1 + n_T \frac{T_{ad}}{T_u} \alpha \eta_{rec}^0. \quad (3.60)$$

Then in the special case $n_T = 1$:

$$\frac{S_L^P}{S_L^0(T_u)} = \frac{1}{2} \left[1 + \sqrt{1 + 4 \frac{T_{ad}}{T_u} \alpha \eta_{rec}^0} \right]. \quad (3.61)$$

3.2.6. Discussion and validation

Several fully-explicit formulae for flame speed-up were derived in Section 3.2.5: Equation (3.55) for single-step Arrhenius; Equations (3.60) and (3.61) assuming a power-law sensitivity to temperature for the adiabatic free-flame speed. Both Equations (3.55) and (3.60) are first-order approximations where the speed-up is proportional to η_{rec}^0 , with a slope depending on the sensitivity of their respective chemical model. These are useful to analyse general trends of flames with heat recirculation. As already discussed in the literature: recirculation efficiency decreases with porosity, and increases with solid conductivity and volume heat transfer coefficient. In addition, it is found here that recirculation efficiency increases with the adiabatic temperature T_{ad} and decreases with the fresh gases temperature T_u and adiabatic free-flame speed. Furthermore, the previously-observed decrease in recirculation efficiency with equivalence ratio can be explained as resulting from the larger impact of equivalence ratio on \dot{m}_0 than T_{ad} .

Equations (3.53) and (3.59) are more general solutions of the chemical problem but because they respectively require the knowledge of the Lambert function and a numerical integration, they are less useful for interpretation.

These analytical solutions are now compared to a numerical resolution using the software CANTERA with GRIMECH 3.0 as chemical scheme (the infinitely-thin reaction sheet is relaxed). For this validation, CANTERA was coupled to an in-house code solving the thermal problem in the solid matrix. This procedure is described more thoroughly in Appendix 3.D. The two mixtures of Table 3.1 are considered with the following properties for the porous medium: $\epsilon = 0.9$, $\lambda_s = 10 \text{ W m}^{-1} \text{ K}^{-1}$, and $h_V = 1 \times 10^4 \text{ W m}^{-3} \text{ K}^{-1}$. This leads to the values $r_{\dot{m}} = 5.29$, $r_{\dot{m}}/r_\lambda = 70.5$ for the methane-air mixture and $r_{\dot{m}} = 8.06$, $r_{\dot{m}}/r_\lambda = 109.7$ for hydrogen-air, all falling within the regime (3.37). Results are shown on Figure 3.6. As expected, Equations (3.53) and (3.59) are more accurate than their corresponding first-order approximation, namely Equations (3.55) and (3.60). Thanks to its non-linear behavior, Equation (3.61) is quite close to the reference simulation, albeit assuming $n_T = 1$. The two main sources of error between the fully-resolved simulations and the various analytical formulae result respectively from the thermal and chemical modellings. In Figure 3.6, the parameters $r_{\dot{m}}$ and r_λ fall largely within the validity range (3.37) so that primarily the performance of the chemical modelling is assessed. Further investigations showed similar errors throughout the regime (3.37).

As a concluding remark, it is important to stress the implications of the choice of β . Equations (3.55) and (3.60) show that speed-up is given, at the first-order, by η_{rec}^0 times a certain

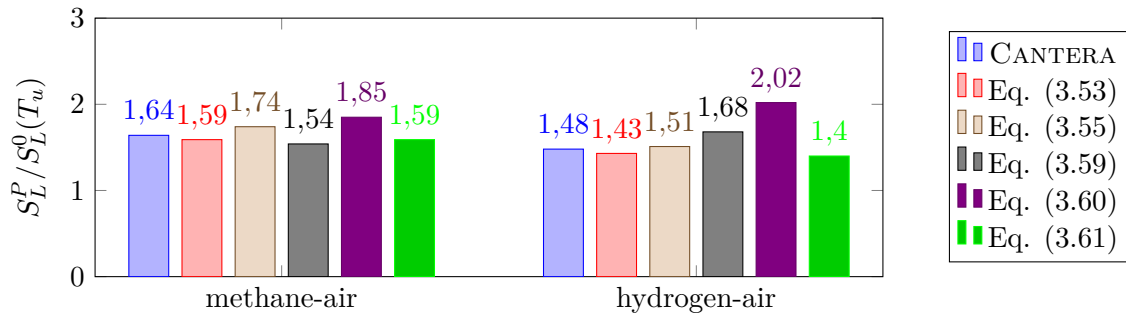


Figure 3.6. – Validation of the speed-up $S_L^P/S_L^0(T_u)$: comparison between a reference numerical simulation with CANTERA + GRIMECH 3.0 and the various formulae derived in this chapter.

coefficient expressing the chemical sensitivity of the mixture to preheating. It is $\beta/2$ for single-step and $\alpha T_{ad}/T_u n_T$ for power law. Classically, hydrogen-air mixtures have lower activation energies compared to methane-air, as can be seen in Table 3.1. This apparently contradicts the fact that n_T is much larger for hydrogen-air, as shown in Figure 3.5. The reason is β is usually fitted for given structural properties at reference conditions, such as auto-ignition delay, laminar flame speed, or flame thickness. This does not guarantee a correct response to preheating. It is of course possible to tailor β to make its value coherent with n_T , but it comes at the expense of other structural parameters. Since this procedure is not standard in the literature, traditional values of β were used in this manuscript.

3.3. Effects of flame wrinkling

3.3.1. Taking into account flame wrinkling

In simulations and experiments, it is observed that the flame front is not planar:

- First, because the flame anchors at discrete locations related to the local pore geometry, leading to a longitudinal distribution of the flame front (see illustration of Figure 3.7(a), and more details in Chapter 6). Though this contradicts a particular localisation of the reaction sheet as in the model, the jump condition may remain accurate if the spatial distribution is sufficiently narrow (in general, assuming error cancellation the mean location of heat release may be chosen as a reference). Unfortunately, by construction this effect cannot be considered in the model ;
- Also, at the pore level, the flame front may present a certain corrugation (see Figure 3.7(b)). In other words, the pores may act locally as flame holders, whose ratio of bulk velocity to local flame speed may be greater than one. Consequently, the local burning rate increases of a certain *wrinkling factor* $\Gamma_w > 1$, which is related to the local flame surface density. This factor may depend upon the pore topology and dimensions. Note that this view assumes pore diameters larger than the flame thickness $d_p \gg \delta_L$.

3.3.2. Theoretical influence of the wrinkling factor Γ_w

The factor Γ_w shall not influence the thermal problem, because the latter only depends upon the fixed mass flux \dot{m} which is an eigenvalue of the coupled thermal-chemical system. However, it influences the local burning rate of the chemical closure problem. We now provide the alternative forms for Arrhenius single-step and power law approximations.

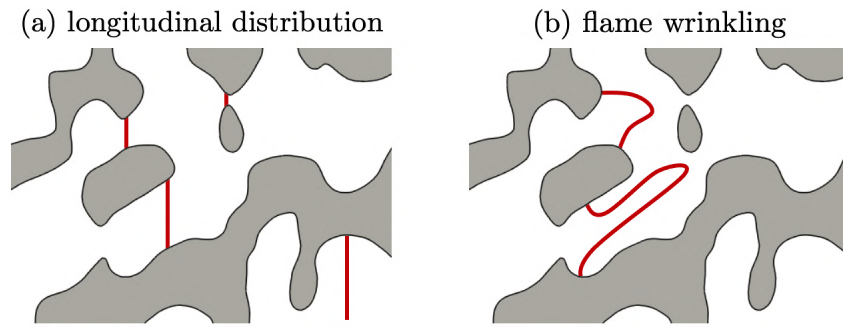


Figure 3.7. – Illustration of flame distribution and wrinkling inside porous media.

3.3.2.1. Single-step Arrhenius

The chemical closure becomes:

$$\frac{S_L^P}{S_L^0(T_u)} = \Gamma_w \exp\left(\frac{\beta\eta_{rec}}{2}\right), \quad (3.62)$$

leading to:

$$\frac{S_L^P}{S_L^0(T_u)} = \frac{\beta\eta_{rec}^0}{2\mathcal{W}(\beta\eta_{rec}^0/2\Gamma_w)}, \quad (3.63)$$

and eventually:

$$\frac{S_L^P}{S_L^0(T_u)} \simeq 1 + (\Gamma_w - 1) + \frac{\beta\eta_{rec}^0}{2}. \quad (3.64)$$

Note that in Equation (3.64) the factor Γ_w has no influence at the first order in η_{rec}^0 . This results from the fact that \dot{m} increases in proportion of Γ_w , while recirculation efficiency decreases in inverse proportion of Γ_w .

3.3.2.2. Power law

The chemical closure becomes:

$$\frac{S_L^P}{S_L^0(T_u)} = \Gamma_w \left(1 + \frac{\Delta T}{T_u}\right)^{n_T}, \quad (3.65)$$

so that:

$$\frac{S_L^P}{S_L^0(T_u)} \left(\frac{S_L^P}{\Gamma_w S_L^0(T_u)}\right)^{1/n_T} - \frac{S_L^P}{S_L^0(T_u)} = \frac{T_{ad}}{T_u} \alpha \eta_{rec}^0, \quad (3.66)$$

which gives, at the first order in η_{rec}^0 :

$$\frac{S_L^P}{S_L^0(T_u)} \simeq 1 + (\Gamma_w - 1) + n_T \frac{T_{ad}}{T_u} \alpha \eta_{rec}^0. \quad (3.67)$$

Similar to Equation (3.64), Equation (3.67) does not show any dependency upon Γ_w on its first-order term in η_{rec}^0 , for the same reasons of proportionality. Overall, one should keep in mind the counter-intuitive fact that, for a fixed h_V , recirculation efficiency decreases with inlet mass flux, that is, the preheating temperature decreases with mass flow, leading to a lower local acceleration “compensated” by Γ_w . This would not be the case if h_V is assumed to vary with \dot{m} .

3.3.2.3. Conclusion on flame wrinkling

At the first order in η_{rec}^0 , the local wrinkling of the flame front does not affect the extent of flame acceleration due to heat recirculation, and the influence of Γ_w is purely geometrical. Note also that from Equation (3.65) an increase in local flame surface can be interpreted, from the point of view of the 1D equations, as an increase in adiabatic flame speed S_L^0 .

3.4. Effects of finite length & multi-staged burners

In this section, we investigate the role of finite length on superadiabatic properties and recirculation efficiency. The influence of radiant heat losses at the extremities of the porous medium is also studied. It is shown that the maximum recirculation efficiency in a porous medium of finite length converges towards that of its infinite counterpart in a universal manner. Then we introduce a theoretical model for multi-staged burners and study the influence of parameter variations on their stability and performance.

3.4.1. Single-staged burner: problem formulation

A flame submerged in a finite porous medium is now considered, as depicted in Figure 3.8. Due to the constriction of the flow, the mass flux per surface unit of gas now depends on the axial coordinate x and is not the same within and outside the solid matrix. In order to keep the same notations than in the infinite case, \dot{m} still denotes the intrinsic mass flux inside the porous structure, so that:

$$\text{intrinsic mass flux} = \begin{cases} \dot{m} & \text{if } x \in [-x_p, L - x_p] \text{ inside the porous medium,} \\ \dot{m}\epsilon & \text{outside the porous medium.} \end{cases} \quad (3.68)$$

In addition to the parameters defined in Section 3.2, both the length of the porous medium L and the distance of the reaction sheet from the inlet $x_p \in [0, L]$ are specified. For the flame to be submerged, only porous media much longer than the diffusion length scale are considered:

$$L \gg l_{\text{diff}}. \quad (3.69)$$

Using (3.41) and (3.42), this condition becomes:

$$L^* \gg \frac{r_\lambda}{r_{\dot{m}}}. \quad (3.70)$$

Four regions are distinguished: G1 and G2 are the gaseous zones before and after the porous medium, while S1 and S2 are the two-phase zones before and after the reaction sheet. The solid inlet is located at $x = -x_p$ and the outlet at $x = L - x_p$. Heat losses via radiation are noted J_{left} at the inlet and J_{right} at the outlet. All corresponding dimensionless quantities are noted with the * superscript.

Alike the infinite case, the principle here is to find the flame speed-up in function of an implicit formulation (3.4), but this time, there is one distinct problem for each prescribed flame position x_p . Since this position changes the temperature profiles, thus heat recirculation, the flame speed-up is expected to be a function of x_p . One can anticipate that when the flame is close to the inlet or the outlet heat exchange with the solid is limited, thus reducing the speed-up. A maximum speed-up is therefore expected for a flame around the mid-section of the porous medium. The objectives of this section are to predict the speed-up for a given flame position and quantify the influence of the finite solid length.

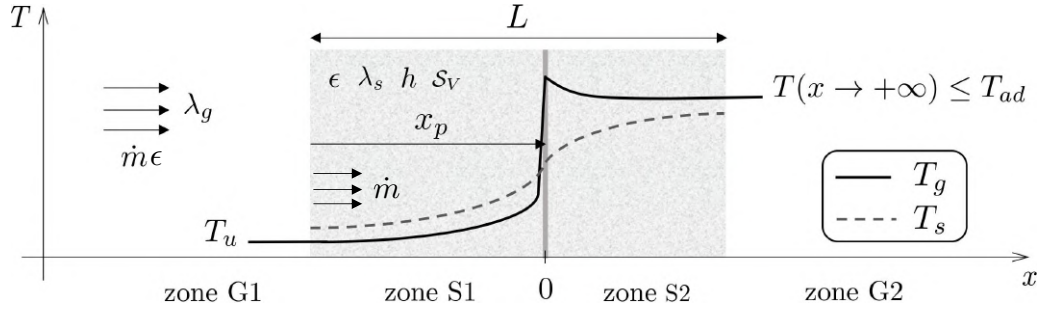


Figure 3.8. – Principle: flame submerged in a finite porous medium.

For zones S1 and S2, the governing equations remain those of the infinite case (3.5-3.6), whose general solutions are:

$$\theta_s^{S1}(x^*) = A_0^{S1} + \sum_{i=1}^3 A_i^{S1} e^{\lambda_i x^*} \quad \text{and} \quad \theta_s^{S2}(x^*) = A_0^{S2} + \sum_{i=1}^3 A_i^{S2} e^{\lambda_i x^*}. \quad (3.71)$$

Again, λ_i are the roots of the polynomial (3.20) for which $\lambda_1 < 0 < \lambda_2 < \lambda_3$. This time, the two constants A_0^{S1} and A_0^{S2} must be determined using the conditions all over the domain, not just the boundary conditions. For the zones G1 and G2, the modelling reduces to a single gas equation without coupling with the solid:

$$-\epsilon \dot{m} c_{pg} \partial_x T_g + \lambda_g \partial_x^2 T_g = 0, \quad (3.72)$$

where ϵ intervenes due to mass conservation and the present definition of \dot{m} as the mass flux per surface unit of gas. Normalisation yields:

$$\partial [-\epsilon r \dot{m} \theta_g + r \lambda \partial \theta_g] = 0, \quad (3.73)$$

whose solutions compatible with the boundary conditions are respectively:

$$\theta_g^{G1}(x^*) = A_0^{G1} e^{\frac{r \dot{m}}{r \lambda} x^*} \quad \text{and} \quad \theta_g^{G2}(x^*) = A_0^{G2}. \quad (3.74)$$

In zone G2, the temperature $\theta_g^{G2}(x^*)$ is a constant, whose value is determined by the gas temperature continuity at the exit of the solid. It is as such an output of the problem, not an unknown:

$$A_0^{S2} = \theta_g^{G2}(x^*) = \theta_g^{S2}(x^* = L^* - x_p^*). \quad (3.75)$$

This leaves 9 unknowns for 9 jump conditions: the A_i^{S1} , the A_i^{S2} and A_0^{G1} are to be determined. At the flame front, we have:

$$\theta_s^{S1}(x^* = 0^-) = \theta_s^{S2}(x^* = 0^+) \quad \text{continuity of solid temperature,} \quad (3.76)$$

$$\partial \theta_s^{S1}(x^* = 0^-) = \partial \theta_s^{S2}(x^* = 0^+) \quad \text{continuity of solid heat flux,} \quad (3.77)$$

$$\theta_g^{S1}(x^* = 0^-) = \theta_g^{S2}(x^* = 0^+) \quad \text{continuity of gas temperature,} \quad (3.78)$$

$$\partial \theta_g^{S1}(x^* = 0^-) = \frac{r \dot{m}}{r \lambda} + \partial \theta_g^{S2}(x^* = 0^+) \quad \text{discontinuity of gas heat flux.} \quad (3.79)$$

This time, both gas continuity and the energy release from reaction must be prescribed. This is due to the indirect relation of the constants A_0^{S1} and A_0^{S2} to the boundary conditions at

the infinite upstream and downstream. Then, at the solid inlet, possible heat losses must be accounted for, as well as the effect of porosity on gas heat flux continuity:

$$\partial\theta_s^{S1}(x^* = -x_p^*) = J_{\text{left}}^* \quad \text{inlet heat loss,} \quad (3.80)$$

$$\partial\theta_g^{G1}(x^* = -x_p^*) = \epsilon \partial\theta_g^{S1}(x^* = -x_p^*) \quad \text{continuity of gas heat flux,} \quad (3.81)$$

$$\theta_g^{G1}(x^* = -x_p^*) = \theta_g^{S1}(x^* = -x_p^*) \quad \text{continuity of gas temperature.} \quad (3.82)$$

At the outlet, the gas temperature gradient must go to zero because the gas temperature in region G2 is constant, so that:

$$\partial\theta_s^{S2}(x^* = L^* - x_p^*) = -J_{\text{right}}^* \quad \text{outlet heat loss,} \quad (3.83)$$

$$\partial\theta_g^{S2}(x^* = L^* - x_p^*) = 0 \quad \text{continuity of gas heat flux.} \quad (3.84)$$

In the adiabatic case, it is trivial that $J_{\text{left}}^* = 0$ and $J_{\text{right}}^* = 0$. Heat losses to the exterior may be considered, for instance radiant heat losses using a Stephan model, for which it is found that:

$$J_{\text{left}}^* = \sqrt{\frac{1-\epsilon}{h_V \lambda_s}} \sigma T_u^4 \left(1 + \alpha \frac{T_{ad}}{T_u} \theta_s^{S1}(x^* = -x_p^*) \right)^4, \quad (3.85)$$

$$J_{\text{right}}^* = \sqrt{\frac{1-\epsilon}{h_V \lambda_s}} \sigma T_u^4 \left(1 + \alpha \frac{T_{ad}}{T_u} \theta_s^{S2}(x^* = L^* - x_p^*) \right)^4. \quad (3.86)$$

Note that in Equations (3.85-3.86) the background radiation is omitted. This is an approximation, though this does not change qualitatively the influence of heat losses, especially on the hot (right) side where the outward radiation is largely dominant. For the typically colder (left) boundary this influence can be considered negligible. The jump conditions (3.76-3.84) can be recast under matrix formalism as:

$$\underline{\mathbf{M}} \cdot \mathbf{A} = \mathbf{B}, \quad (3.87)$$

where \mathbf{A} is the column matrix of unknowns:

$$\mathbf{A} = \left[A_0^{S1} \quad A_1^{S1} \quad A_2^{S1} \quad A_3^{S1} \quad A_0^{S2} \quad A_1^{S2} \quad A_2^{S2} \quad A_3^{S2} e^{\lambda_3(L^* - x_p^*)} \quad A_0^{G1} e^{-\epsilon \frac{r_{in}}{r_\lambda} x_p^*} \right]^T, \quad (3.88)$$

and \mathbf{B} the second member:

$$\mathbf{B} = \left[0 \quad 0 \quad 0 \quad r_{in}/r_\lambda \quad J_{\text{left}}^* \quad 0 \quad 0 \quad -J_{\text{right}}^* \quad 0 \right]^T. \quad (3.89)$$

The matrix $\underline{\mathbf{M}}$ is provided in Appendix 3.E. Note that in Equation (3.88), the coefficient A_3^{S2} is lumped together with $e^{\lambda_3(L^* - x_p^*)}$ and A_0^{G1} with $e^{-\epsilon \frac{r_{in}}{r_\lambda} x_p^*}$. This allows for a well-conditioned numerical inversion of Equation (3.87). A close look at Equations (3.89) and (3.135) reveals that η_{rec} depends this time on more than r_{in} and r_λ . In the adiabatic case, the solution is a function of L and x_p , but also of ϵ through the inlet jump condition (3.81). This latter dependency is very small for flames several gas diffusion length scales away from the solid inlet. This motivated some authors to discard the influence of porosity at the inlet and use directly a Dirichlet condition instead. When considering radiant heat losses, the non-linearity of J_{left}^* and J_{right}^* brings supplementary dependencies, namely of T_{ad} , T_u and the parameter $\sqrt{(1-\epsilon)/h_V \lambda_s}$. Numerically, this non-linearity is treated using a basic recursive method.

Examples of gas and solid temperature profiles are shown in Figure 3.9, without and with radiant heat losses, together with those of the same porous medium of infinite length. As expected, the reduction of the preheating length leads to a lower superadiabaticity compared to the infinite case. Since interphase non-equilibrium (*i.e.* $\theta_g - \theta_s$) is higher, the preheating rate is also higher and the preheating temperature gradient steeper. Regarding radiant heat losses, one can see in Figure 3.9 that they lead to a reduction in both gas and solid temperatures at the outlet of the porous medium.

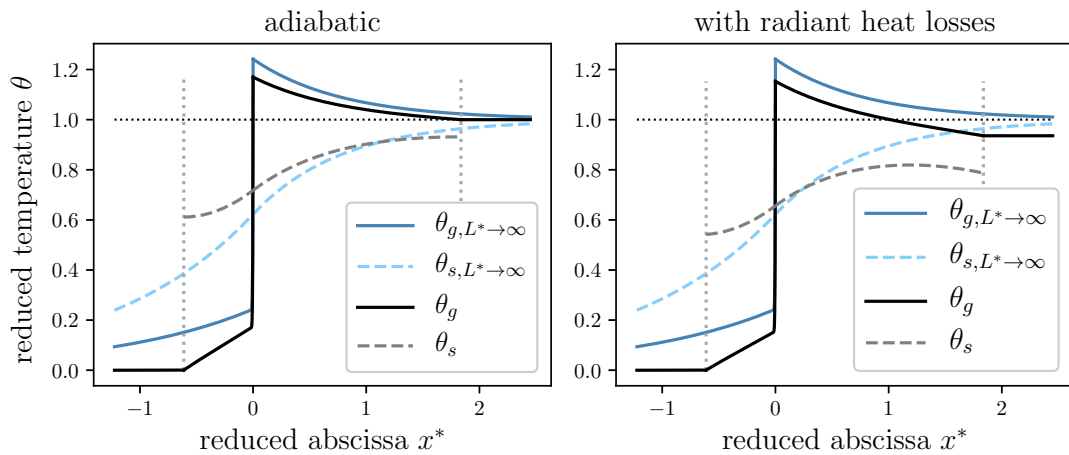


Figure 3.9. – Example of temperature profiles: adiabatic and radiant heat losses cases. The solution of the equivalent infinite porous medium is superimposed for comparison. The parameters used are: $T_u = 300$ K, $T_{ad} = 2000$ K, $\epsilon = 0.8$, $\lambda_s = 20$ W m⁻¹ K⁻¹, $\lambda_g = 0.025$ W m⁻¹ K⁻¹, $h_V = 6 \times 10^4$ W m⁻³ K⁻¹, $c_{p_g} = 1 \times 10^3$ J kg⁻¹ K⁻¹, $L = 2$ cm, $\dot{m} = 1.2$ kg m⁻² s⁻¹, and $x_p = L/4$.

3.4.2. Influence of flame position

As anticipated, finite porous media lengths reduce heat recirculation and therefore superadiabaticity. For a more detailed analysis of this effect, Figure 3.10 presents the recirculation efficiency η_{rec} versus the reduced flame position x_p^* for various reduced porous media lengths L^* , at a given arbitrary inlet mass flux. It is observed that the maximum superadiabatic effect

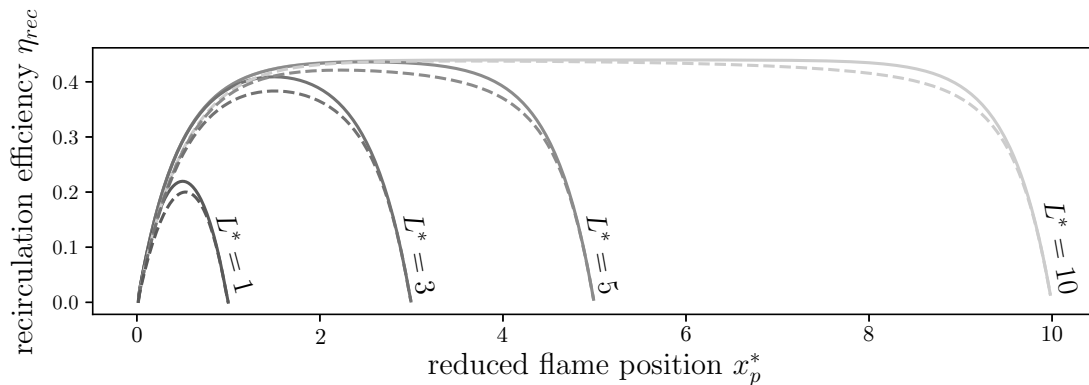


Figure 3.10. – Recirculation efficiency versus flame position for various lengths of porous media. Solid line: adiabatic case. Dashed line: with radiant heat losses. Parameters used: $T_u = 300$ K, $T_{ad} = 2000$ K, $\epsilon = 0.8$ and $\sqrt{(1 - \epsilon)/h_V \lambda_s} = 2 \times 10^{-4}$ m² K W⁻¹ for the radiant heat losses case.

in the porous medium increases with solid length until $L^* \sim 5$. In these situations, the effects of finite length are not perceivable for a flame deep inside the porous medium. In parallel, it is observed that radiant heat losses lead to lower recirculation efficiencies. Overall, Figure 3.10 indicates that recirculation efficiency is a concave, direct function of flame position. And since speed-up is a monotonous function of η_{rec} , a similar trend is expected for the flame speed-up. This is indeed observed in Figure 3.11, where $S_L^P/S_L^0(T_u)$ is plotted versus flame position x_p^* (a chemical model is now prescribed, see caption). It appears that the flame speed is also a

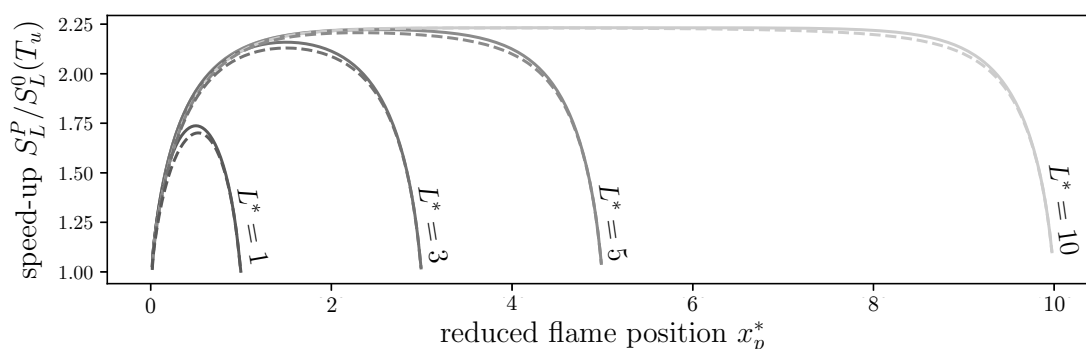


Figure 3.11. – Speed-up ratio versus flame position for various lengths of porous media. Solid line: adiabatic case. Dashed line: with radiant heat losses. The parameters used are: $T_u = 300$ K, $T_{ad} = 2000$ K, $\epsilon = 0.8$, $\lambda_s = 20$ W m⁻¹ K⁻¹, $\lambda_g = 0.025$ W m⁻¹ K⁻¹, $h_V = 2.4 \times 10^5$ W m⁻³ K⁻¹, $c_{p_g} = 1 \times 10^3$ J kg⁻¹ K⁻¹, $\dot{m}_0 = 1.2$ kg m⁻² s⁻¹, and $n_T = 1$.

function of flame position, with an upstream and a downstream branch: for a given inlet mass flux, two solutions are possible, on each side of the porous. Following the rationale of other authors, notably that of Diamantis [34], only the upstream branch is expected to be stable. A graphical explanation for the stability is that close to the inlet, the speed-up increases if the flame is pushed back while near the outlet, the speed-up decreases with x^* .

3.4.3. Universal behavior of finite-length effects in the decoupled regime

As discussed above, Figures 3.10 and 3.11 show a convergence of the maximum superadiabaticity, typically when $L^* > 5$. We now investigate the universality in this convergence. Figure 3.12 shows ratios of the maximum recirculation efficiency obtained in a finite porous medium

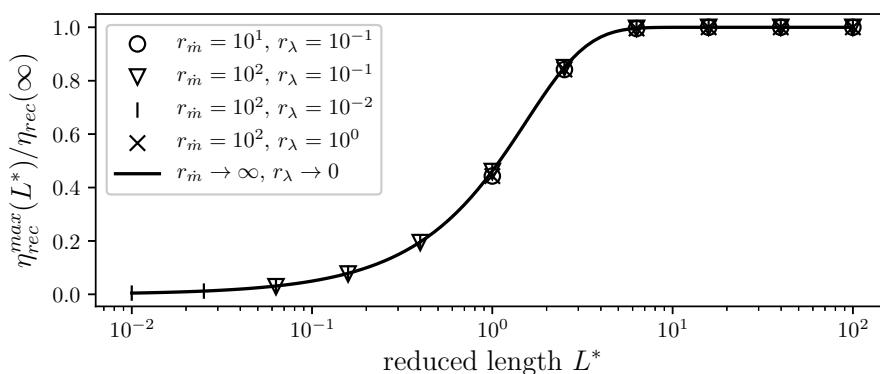


Figure 3.12. – Convergence towards the infinite porous medium case - universal curve in the conditions (3.37) and (3.70).

$\eta_{rec}^{max}(L^*)$ and the one found in its infinite counterpart $\eta_{rec}(\infty)$, for various values of $r_{\dot{m}}$, r_λ and L^* . The chosen values satisfy the decoupled regime (3.37) and submerged flame (3.70) conditions. All these cases are very close to the limit case $r_{\dot{m}} \rightarrow \infty$, $r_\lambda \rightarrow 0$ with relative differences below 5%. For the sake of clarity, only a few cases are presented in Figure 3.12 but they cover all the solid line regions of Figure 3.3. This is a strong indication that finite-length effects only depend on the normalised length L^* and confirms that for $L^* > 5$, a porous matrix can be treated as infinite from the perspective of heat recirculation.

This is arguably of great practical interest. Using the model presented in Section 3.2 (either numerical integration or analytical approximations), one can compute $\eta_{rec}(\infty)$. Then with Figure 3.12, one can estimate finite-length effects and obtain the numerical value for $\eta_{rec}^{max}(L^*)$. This means that heat recirculation and flame speed-up can be anticipated at the design stage of a porous burner using intrinsic properties of the gaseous and solid phases. In other words, it is possible to use the speed-up formulae proposed in the infinite case, by multiplying η_{rec}^0 by the value of the ratio reported from Figure 3.12.

3.4.4. Multi-staged burners: problem formulation

The case of multi-staged (also called multi-step, multi-layered) burners is now considered, as depicted in Figure 3.13. A series of N porous layers are stacked together, each having its own length L_n , porosity ϵ_n , thermal conductivity $\lambda_{s,n}$ and volume heat transfer coefficient $h_{V,n}$, for $n \in [1, N]$. A reference mass flux \dot{m}_∞ is imposed at the infinite upstream, so that the interstitial mass flux in the n^{th} layer is:

$$\frac{\dot{m}_\infty}{\epsilon_n}. \quad (3.90)$$

The position of the interfaces are noted $x^n = \sum_{j \in [1, n]} L_j$ for $n \in [1, N - 1]$. The thermal

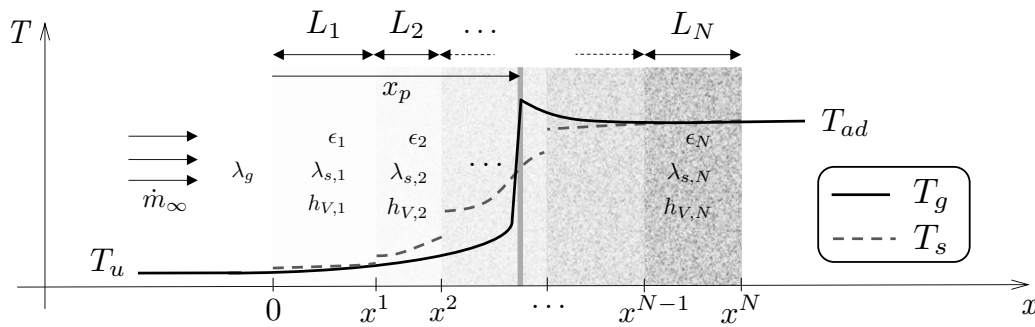


Figure 3.13. – Principle: theoretical modelling of multi-step burners.

conductivity λ_g is supposed constant. We also introduce a reduced mass flux different in each layer:

$$r_{\dot{m},n} = \frac{\dot{m}_\infty c_{p_g}}{\sqrt{(1 - \epsilon_n) \lambda_{s,n} h_{V,n}}}, \quad (3.91)$$

and the second reduced parameter linked to the ratio of conductivities:

$$r_{\lambda,n} = \frac{\epsilon_n \lambda_g}{(1 - \epsilon_n) \lambda_{s,n}}, \quad (3.92)$$

so that the governing energy equation valid in each region becomes:

$$\partial_n \left[r_{\lambda,n} \partial_n^3 - r_{\dot{m},n} \partial_n^2 - (r_{\lambda,n} + 1) \partial_n + r_{\dot{m},n} \right] \theta_s = 0. \quad (3.93)$$

where formally the reduced derivative depends also on the layer considered through:

$$x_n^* = x / \sqrt{\frac{(1 - \epsilon_n) \lambda_{s,n}}{h_{V,n}}} \quad \text{and} \quad \partial_n \equiv \frac{\partial}{\partial x_n^*}. \quad (3.94)$$

The solution of Equation (3.93) in each region (noted arbitrarily X) is:

$$\theta_s^X(x_n^*) = A_0^X + \sum_{i=1}^3 A_i^X e^{\lambda_{i,n} x_n^*}. \quad (3.95)$$

where the $\lambda_{i,n}$ are again the roots of the n^{th} characteristic polynomial:

$$r_{\lambda,n} \lambda^3 - r_{\dot{m},n} \lambda^2 - (r_{\lambda,n} + 1) \lambda + r_{\dot{m},n} = 0. \quad (3.96)$$

When the flame is stabilized in the n^{th} layer, then formally there exists two sub-regions to be resolved because the flame sheet presents a jump condition on its own within the layer. For the sake of brevity and simplicity to the reader, further technical details regarding indices and names for the different regions are omitted. Instead, we focus mainly on the boundary conditions at the porous interfaces, since those at the infinite upstream/downstream, at the inlet/outlet and at the flame sheet are the same than with the single-layered finite case.

3.4.5. Boundary conditions

Between two porous layers, continuity of gas temperature and energy fluxes through both gas and solid phases are still ensured. However, due to the very low contact points between two porous layers, it is expected that a temperature discontinuity arises - a notion known as contact surface resistance [255]. Interestingly, to the author's knowledge the presence of this thermal resistance seems to have been omitted in the literature. With dimensions, the jump condition in $x = x^n$ may be written as:

$$\lambda_{s,n} \left. \frac{\partial T_s}{\partial x} \right|_{x=x^n} = \frac{1}{R_n} [T_s(x^{n,+}) - T_s(x^{n,-})], \quad (3.97)$$

where R_n is the thermal resistance between the two layers, which can be viewed conceptually as a ratio of a thickness to a conductivity of a resistive material $e_{\text{res}}/\lambda_{\text{res}}$. Without dimensions, we get:

$$\frac{\lambda_{s,n}}{\sqrt{\frac{(1-\epsilon_n)\lambda_{s,n}}{h_{V,n}}}} \left. \frac{\partial \theta_s}{\partial x_n^*} \right|_{x_n^*=x_n^{n,*}} = \frac{1}{R_n} [\theta_s(x^{n,+}) - \theta_s(x^{n,-})]. \quad (3.98)$$

The set of equations may be resolved by a method similar to the single-layered case, namely through a linear system which may readily be inverted (and again, the thermal problem is completed by a chemical closure). However, due to the complexity of the general matrix system, it is not provided here. In fact, thanks to symbolic representations of linear systems through the Python library SYMPY, it was not even necessary to write it down at all. Note also that the case $N = 1$ encompasses the single-layered case and the numerical code was written in a way to handle it properly. It was the occasion to verify that the results were the same by the two different methods.

Note that by taking $N \rightarrow \infty$ for a given total stacking length, *we can easily introduce spatially-varying, arbitrary profiles* for the physical parameters, in a fully-analytical fashion. Nonetheless computational cost increases substantially for very large values of N so the generation of solution curves for varying flame positions becomes rapidly costly. A parallelization of of the script may be necessary in the future.

3.4.6. Interest of the present modelling for stability discussions

As discussed earlier, under 1D framework the stability of porous burners may be investigated by looking at the slope of the curve of mass flow rate *vs.* position (which we call hereafter stability curves). For single-step burners, the theoretical stability as predicted by 1D theory is shown in Figure 3.14(a). It is classically found that only portions of positive slope are stable. This leads to the prediction (well-verified experimentally) that only flames in the upstream portion of the porous medium should be stable, that flashback may occur for flames near the inlet due to the constriction of the flow, and that surface combustion is also intrinsically stable.

In the case of multi-layered porous burners, as depicted in Figure 3.14(b) one may wonder under which circumstances property variations and interfaces help for the burner stability and flame anchoring. Notably, it is not excluded that some configurations tend to destabilize the porous medium and the stacking be detrimental. Also, there may be a strong influence of the thermal resistance between the layers on the stability of these curves, which is now investigated.

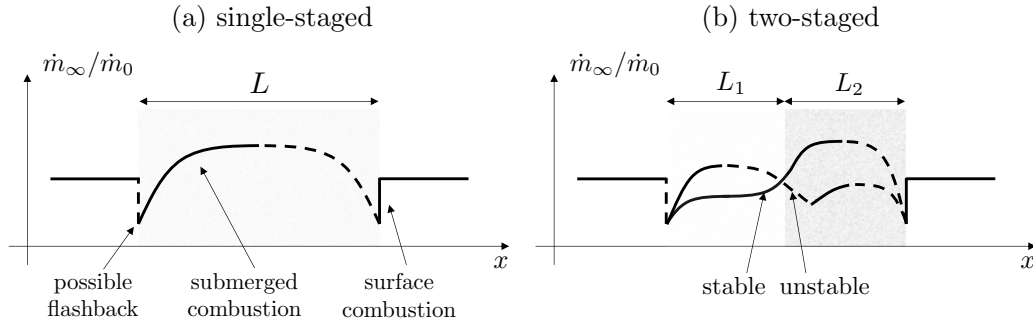


Figure 3.14. – Illustration of the stability of single and multi-layered porous burners as predicted by 1D asymptotic theory.

3.4.7. Influence of the thermal resistance

We begin our investigation of multi-step burners by considering the influence of the thermal resistance between two identical layers, as well as its conceptual implications. On Figure 3.15 are shown three stability curves for a two-step porous burner composed of two layers of same macroscopic properties, for increasing thermal resistance R_1 . Solid lines correspond to regions of positive slope and dashed regions to negative slope. When the $R_1 = 0$, one obtains the previous stability curve found in Figure 3.11. On the contrary, when $R_1 = 10$ (very high resistance), then the two layers become thermally independent, **the recirculation efficiency at the interface is zero, and each layer shows an independent bell-shaped curve**. For intermediate R_1 values, the recirculation efficiency at the interface is not zero, yielding a M-shaped curve. **Overall, it seems that the introduction of a thermal resistance provides an additional**

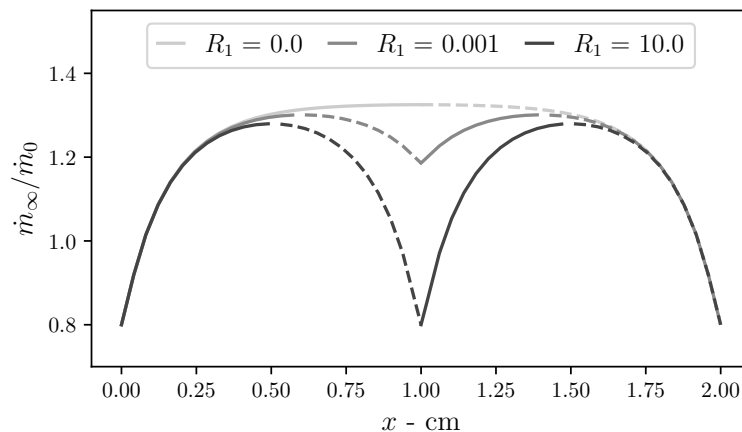


Figure 3.15. – Two-step burner for increasing thermal resistance between the two layers. Thermo-physical properties: $\lambda_{s,1} = \lambda_{s,2} = 3.0 \text{ W m}^{-1} \text{ K}^{-1}$, $h_{V,1} = h_{V,2} = 5 \times 10^4 \text{ W m}^{-3} \text{ K}^{-1}$, $\epsilon_1 = \epsilon_2 = 0.8$, $c_{p_g} = \text{J kg}^{-1} \text{ K}^{-1}$, $L_1 = L_2 = 1 \text{ cm}$, $\dot{m}_0 = 0.5 \text{ kg m}^{-2} \text{ s}^{-1}$, $\beta = 8.0$, $\lambda_g = 0.025 \text{ W m}^{-1} \text{ K}^{-1}$. Unit for R_1 is $\text{W m}^{-2} \text{ K}^{-1}$.

flame anchoring capability, through a second stable region near the interface between the two layers.

Assessing *a priori* the value of R_1 may be quite hard - if ever possible. Therefore, without further information, one may simply state that the stable flames may be found within the envelope formed by the curves ranging from $R_1 = 0$ to $R_1 \rightarrow \infty$, as shown schematically in Figure 3.16. This directly illustrates how a thermal resistance may allow a “wider” stability range, at least near the mid-section of the burner. Experimentally, this resistance might be tuned by hand: in [256], a small gap was introduced between two porous layers, what turned out beneficial for the operating range of the burner. Of course, in practical devices radiation cannot be neglected, so that even between two layers separated by a physical gap there exists non-zero heat exchange. A consequence is that, conceptually-speaking, there may exist an upper bound for R_1 . Yet, the present theory and the experimental findings of [256] suggest that reducing the back-propagation of heat from the downstream layer may be beneficial for an internal stabilization of a flame between two porous layers.

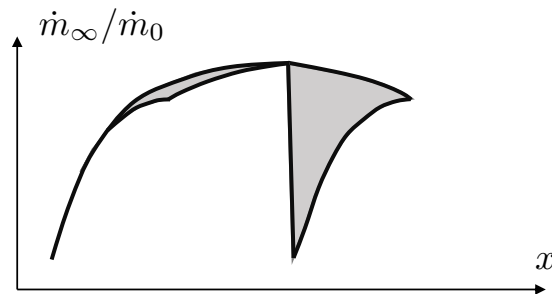


Figure 3.16. – Stability envelope for all values of resistances.

Physical profiles of gas and solid temperature profiles are illustrated in Figure 3.17, for two values of the surface contact resistance. It is observed that for larger values of R_1 , the temperature gap between the solid layers increases, so that each layer becomes more and more thermally independent.

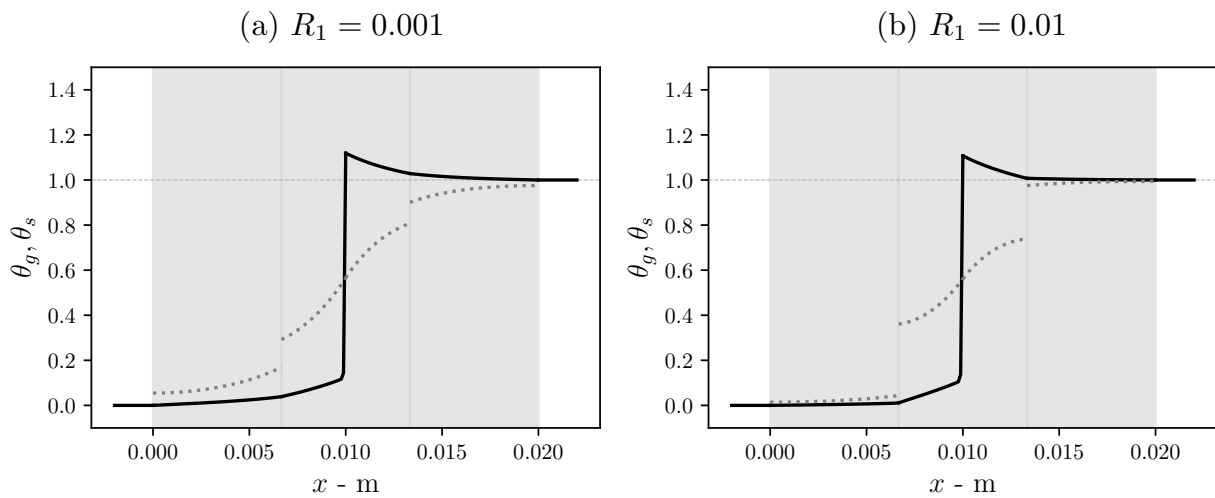


Figure 3.17. – Profiles in the physical space for lower (a) and larger (b) surface contact resistance values, same thermo-physical properties than Figure 3.15 but this time $N = 3$ and $L_1 = L_2 = L_3 = 2/3\text{cm}$. Unit for R_1 is $\text{W m}^{-2} \text{K}^{-1}$.

3.4.8. Porosity step

The influence of a porosity step between two porous layers of otherwise identical macroscopic properties is now investigated. Figure 3.18 presents a two-step burner for a positive ($\epsilon_1 < \epsilon_2$) and negative ($\epsilon_1 > \epsilon_2$) porosity step, assuming perfect thermal contact ($R_1 = 0$). Although a negative porosity step seems to favor the stabilization of the flame in the upstream layer, it seems completely detrimental regarding interface stability. This duality is explained by the existence of conflicting influence of the porosity step on stability. The first is the hydrodynamic effect related to the constriction of the flow at the interface. The second is related to the recirculation efficiency: coming back to the analytical expression of Equation (3.44), one finds that sections of lower porosities show larger recirculation efficiencies. Therefore, in the case $\epsilon_1 < \epsilon_2$ the flame is more preheated in the upstream layer but less preheated downstream (which is why the second part of the M-curve is lower), while in the case $\epsilon_1 > \epsilon_2$ the flame is less preheated but there is a range of burning rates for which the flame is stable at the interface - related to the porosity jump. This was observed in [142], where a 1-10 power range was observed with a flame seemingly stabilized at the interface.

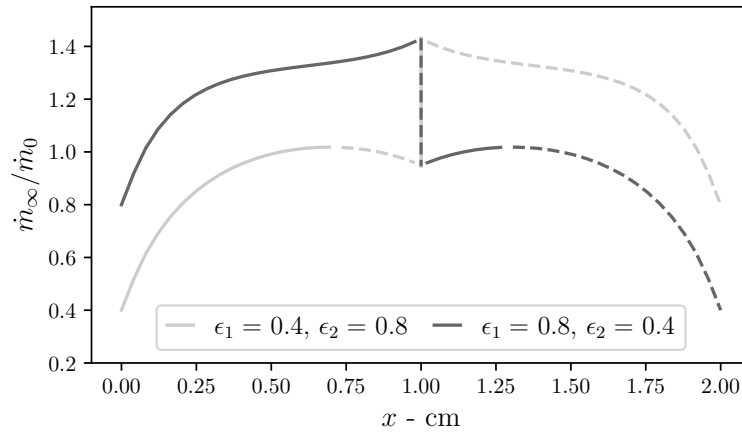


Figure 3.18. – Influence of porosity step. $R_1 = 0$, same other thermo-physical properties than Figure 3.15.

3.4.9. Interphase heat transfer & solid conductivity step

Figures 3.19 and 3.20 illustrate both positive and negative steps in heat transfer coefficient and solid conductivity, by a factor of 5, for two layers of same length and otherwise same macroscopic properties, assuming $R_1 = 0$. In Figure 3.19 the flame acceleration is larger (resp. lower) in the region of larger (resp. lower) heat transfer coefficient. In Figure 3.20 the flame acceleration is larger (resp. lower) in the region of larger (resp. lower) solid conductivity. These effects may be explained again by considering the analytical expression for recirculation efficiency of Equation (3.44). Increasing the heat recirculation downstream seems to have, from the point of view of the 1D equations, a positive influence on flame stabilization, though these do not trigger an interface stabilization such as found with the porosity step. Interestingly, there seems to be a discontinuity in the slope burning rate *vs.* position for a step of h_V coefficient at the interface, whilst the transition is seemingly smooth for a step of λ_s . Note also that for the same reference macroscopic parameters, the increase in maximum mass flow rate is larger through a modification of the interphase heat transfer coefficient than the solid thermal conductivity, although their influence in Equation (3.44) seems equivalent. This can be explained by the finite

nature of the setup and its implications on recirculation efficiency. As shown in Figure 3.12, the larger the quantity $L/\sqrt{(1-\epsilon)\lambda_s/h_V}$, the larger the maximum recirculation efficiency found in a finite-length porous medium.

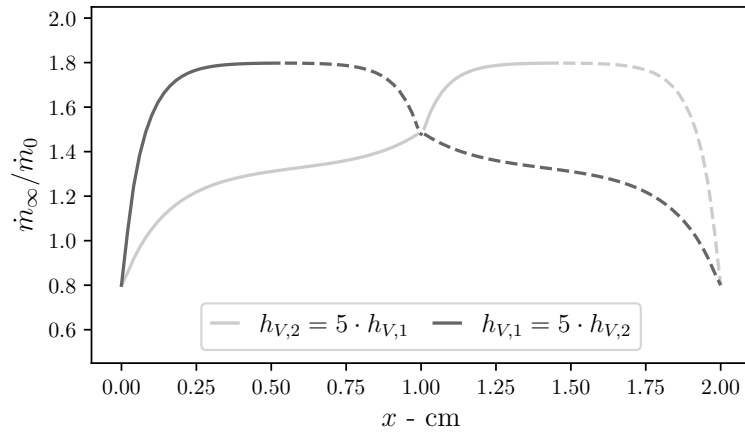


Figure 3.19. – Influence of interphase heat coefficient step, from a reference $h_V = 5 \times 10^4 \text{ W m}^{-3} \text{ K}^{-1}$. $R_1 = 0$, same other thermo-physical properties than Figure 3.15.

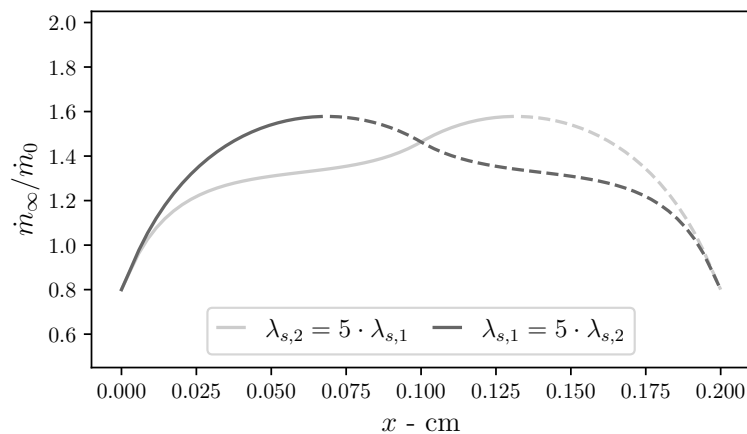


Figure 3.20. – Influence of thermal conductivity step, from a reference $\lambda_s = 3.0 \text{ W m}^{-1} \text{ K}^{-1}$. $R_1 = 0$, same other thermo-physical properties than Figure 3.15.

3.4.10. A “realistic” two-step burner?

The present analytical model seems to agree with design trends for two-step burners found previously in the literature, such as in the works of Barra et al. [221] suggesting that the upstream section should have lower conductivity and lower interphase heat exchange coefficient. Nonetheless, these results seem contradictory with the choice of smaller pores upstream, because smaller pores yield larger h_V values. Unfortunately, due to the constraint related to the decoupled regime, beyond which the assumptions of a simple chemical closure and coupling with the thermal problem fail, the present 1D toy model is unable to predict adequately the burning rate found in regions of large interphase heat transfer, typical of burners found in the literature. What is more, although in the decoupled approximation there always exists solutions for burning rate, we have encountered situations where the coupling between the thermal and chemical

problems would not possess any solution point. For instance, we have tried to reproduce the two-layer burner studied in [34] but no solution points were obtained in the upstream section (not shown).

Generally, the choice of very small pores upstream is motivated by a quenching argument - even though it was shown experimentally that these are insufficient to prevent flashback in the upstream layer. Following other arguments intuited by Trimis and Durst in [45], the stabilization at the interface may be alternatively explained by a local modification of the flame area near the pore size discontinuity. This seems coherent with the findings of Gauthier et al. [32] in heat-recirculating 2D channels, where flame front wrinkling was shown to increase largely for increasing channel height. So even without a change in porosity, a pore size step may induce an interface stabilization. This is illustrated in Figure 3.21, showing the influence of a zero flame wrinkling in the upstream layer ($\Gamma_w = 1$), followed by a two-fold increase in flame surface ($\Gamma_w = 2$). It is observed, as expected, that the opening of the flame has a strong stabilizing effect at the interface, and allows much larger mass flow rates.

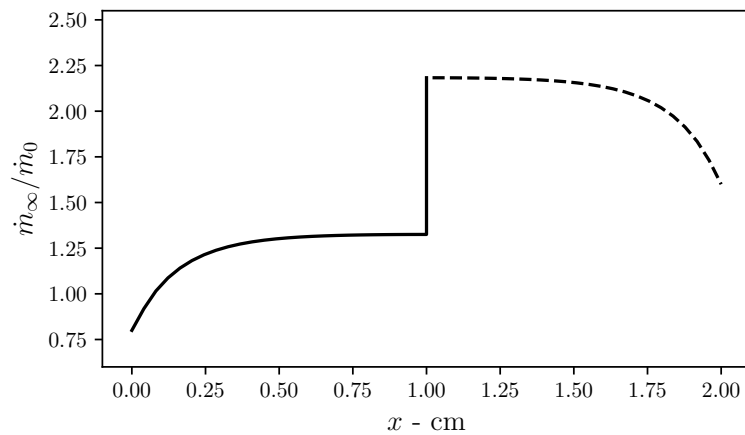


Figure 3.21. – Influence of flame wrinkling, with $\Gamma_w = 1$ upstream and $\Gamma_w = 2$ downstream, $R_1 = 0$, same other thermo-physical properties than Figure 3.15.

3.4.11. Case $N \rightarrow \infty$: topology gradation

One other strength of the present model is the ability to approach cases of topological gradation, that is, when the macroscopic properties are varied continuously along the axial coordinate. This is achieved by taking large values of N for a fixed total porous length. In [153, 154], it was shown experimentally and numerically that the operating range of porous burners could be substantially affected by making use of topological gradation. Notably, it was argued that a continuous increase in pore size downstream could have a stabilizing effect, whilst a continuous increase in porosity downstream has on the contrary a detrimental influence. Because we cannot illustrate directly pore-size variations in the toy model, we illustrate in Figure 3.22 the increase in the number of layers N for progressive porosity variations from 0.4 to 0.8. In the case $N = 1$ the intermediate value of 0.6 is used. It is observed that, compared to the reference case $N = 1$, porosity variations have little influence on the overall burner stability, which seems to disagree with the experimental observations of [154]. However, keep in mind that in [154] porosity could not be varied independently of heat transfer coefficient, effective conductivity, flame anchoring and wrinkling, etc. So it is difficult to draw definite conclusions.

To conclude, we discuss briefly the potential influence of radiation with porosity and pore size variations. Concerning radiation, as discussed in [221] the radiative extinction coefficient κ_{rad}

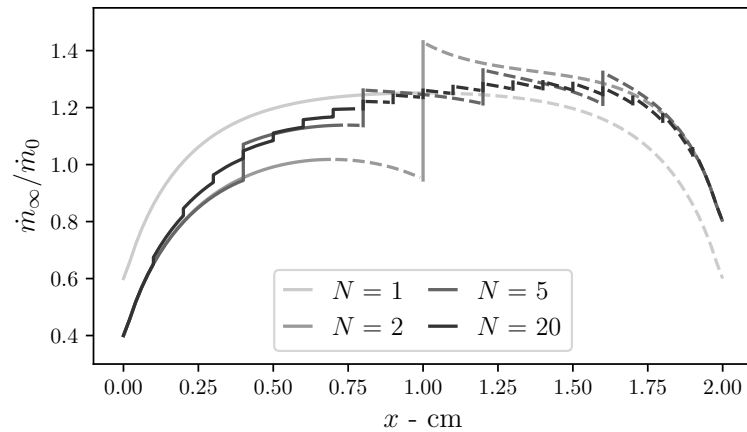


Figure 3.22. – Influence of the number of layers N , for a fixed length L , $R_i = 0$, same other thermo-physical properties than Figure 3.22.

scales as:

$$\kappa_{\text{rad}} \propto \frac{(1 - \epsilon)}{d_p}. \quad (3.99)$$

This means that a gradual increase in porosity/pore size reduces κ_{rad} may be viewed as an increase in solid thermal conductivity. Following Figure 3.20 this should have a stabilizing effect. So again, a progressive increase in porosity should not be overly detrimental to burner stability: the explanation must be found somewhere else. Overall, the very large discrepancies between the present model, the 1D numerical model and experiments in [153, 154] urge for further conceptual work and 3D DNS to unveil the true stabilization mechanisms within graded porous burners.

3.5. Conclusions of the chapter

- In this chapter, a one-dimensional framework was considered for the modelling of combustion in porous media. Heat losses are neglected in the sense that the domain is globally adiabatic and the case of an infinite porous media is considered first. Under the assumption of scale-separation for interphase heat exchange, gas diffusion and combustion, several analytical, fully explicit formulae were derived for the heat recirculation efficiency and flame acceleration. Major trends were spelled out, namely: a decrease with equivalence ratio, porosity and ambient temperature, and an increase with solid conductivity, volume heat transfer coefficient and adiabatic temperature. Two dimensionless numbers denoted $r_{\dot{m}}$ and r_{λ} drive this phenomena and the present study is valid for $r_{\dot{m}} \gg 0.1$ and $r_{\dot{m}}/r_{\lambda} \gg 10$, which is the transcription of the scale-separation hypothesis.
- The analysis was then extended to finite-length porous burners. Numerical resolution of the problem showed the existence of two solutions near the extremities of the porous, the one upstream being stable and the other one being unstable. This feature has already been discussed in the literature but variations in the length of the porous burner showed a convergence of the heat recirculation for normalised lengths $L^* > 5$. A parametric investigation pointed out that this convergence is independent of the porous flame parameters and solely determined by L^* , which is of practical interest for the design of porous burners.
- The general case of multi-step burners was finally studied. The theoretical modelling of thermal contact resistance between two porous layers revealed that limitations in upstream heat propagation could be beneficial to stabilize the flame near the interface between two layers. Also, it was found that sudden increases in porosity have beneficial influence on burner stability. In two-step burners, in coherence with previous literature findings, lower upstream interphase heat transfer coefficient and solid thermal conductivity were found to improve stability - which seems however contradictory to the choice of smaller pore upstream. This contradiction may be resolved by considering the local wrinkling of the flame, which may be linked to pore size. In addition, we stress the fact that the present toy model is unable to model very small pore sizes, which typically fall outside of the decoupled analysis. Further research is therefore required to unveil the true interface stabilization mechanisms in multi-staged layers, notably through 3D DNS and more detailed 1D numerical models. Due to the thermal contact resistance radiation may be a very important point to consider in such burners.

3.A. Gas temperature continuity

In this appendix, we prove the equivalence of gas temperature continuity and energy conservation from reaction (3.27), provided the continuity of the solid heat flux (3.26) and consistent boundary conditions (3.15-3.16):

$$T_g(x = 0^-) = T_g(x = 0^+) \iff (3.15) + (3.16) + (3.26) + (3.27). \quad (3.100)$$

We reason without dimensions. Equations (3.12) and (3.13) can be rearranged as follows, by substituting the term $\theta_s - \theta_g$:

$$r_\lambda \partial^2 \theta_g + \partial^2 \theta_s = r_{\dot{m}} \partial \theta_g. \quad (3.101)$$

By integrating Equation (3.101) from $-\infty$ to 0^- in zone 1 and 0^+ to $+\infty$ in zone 2 and taking into account the boundary conditions (3.15-3.16), we find respectively:

$$r_\lambda \partial \theta_g^1(x^* = 0^-) + \partial \theta_s^1(x^* = 0^-) = r_{\dot{m}} \theta_g^1(x^* = 0^-), \quad (3.102)$$

$$r_\lambda \partial \theta_g^2(x^* = 0^+) + \partial \theta_s^2(x^* = 0^+) = r_{\dot{m}} [\theta_g^2(x^* = 0^+) - 1]. \quad (3.103)$$

Subtracting Equation (3.102) to Equation (3.103) and using solid heat flux continuity (3.26) yields:

$$\partial \theta_g^1(x^* = 0^-) - \partial \theta_g^2(x^* = 0^+) = \frac{r_{\dot{m}}}{r_\lambda} + \frac{r_{\dot{m}}}{r_\lambda} [\theta_g^1(x^* = 0^-) - \theta_g^2(x^* = 0^+)]. \quad (3.104)$$

When the gas temperature is continuous at the origin, Equation (3.104) simplifies to:

$$\partial \theta_g^1(x^* = 0^-) = \frac{r_{\dot{m}}}{r_\lambda} + \partial \theta_g^2(x^* = 0^+), \quad (3.105)$$

which is the dimensionless form of Equation (3.27). This proves the equivalence (3.100). The gas temperature is continuous over the entire gas domain.

3.B. Maximum of gas temperature at $x = 0$

We now show that the gas temperature is maximal at the origin:

$$\theta_{max} = \theta_g^1(x^* = 0^-) = \theta_g^2(x^* = 0^+). \quad (3.34)$$

Since the gas temperature is continuous over the entire domain, it is sufficient to show its strict increase in zone 1 and its strict decrease in zone 2. Recalling the sign of each root of Equation (3.20):

$$\lambda_1 < 0 < \lambda_2 < \lambda_3, \quad (3.106)$$

and looking at Equations (3.23-3.24), it is clear that if:

$$A_i(1 - \lambda_i^2) > 0, \quad (3.107)$$

then the variations meet the researched property. To move forward, it is necessary to resolve formally the system (3.31-3.33). This gives:

$$A_1 = \frac{-\lambda_2 \lambda_3}{(\lambda_2 - \lambda_1)(\lambda_3 - \lambda_1)}, \quad (3.108)$$

$$A_2 = \frac{-\lambda_1 \lambda_3}{(\lambda_2 - \lambda_1)(\lambda_3 - \lambda_2)}, \quad (3.109)$$

$$A_3 = \frac{+\lambda_1 \lambda_2}{(\lambda_3 - \lambda_1)(\lambda_3 - \lambda_2)}. \quad (3.110)$$

By using Equation (3.106), it is clear that the denominators in Equations (3.108-3.110) are positive. Then, taking into account the signs in front of the numerators, the condition (3.107) breaks down into:

$$\lambda_2\lambda_3(1 - \lambda_1^2) < 0, \quad \lambda_1\lambda_3(1 - \lambda_2^2) < 0 \quad \text{and} \quad \lambda_1\lambda_2(1 - \lambda_3^2) > 0. \quad (3.111)$$

This requires studying the sign of:

$$\lambda_i\lambda_j(1 - \lambda_k^2), \quad (3.112)$$

for the circular permutations $i, j, k \in \{1, 2, 3\}$. For that, we make use of the relations between the roots and the coefficients of the polynomial of Equation (3.20):

$$\lambda_1 + \lambda_2 + \lambda_3 = \frac{r\dot{m}}{r_\lambda}, \quad (3.113)$$

$$\lambda_1\lambda_2 + \lambda_2\lambda_3 + \lambda_1\lambda_3 = -\frac{1 + r_\lambda}{r_\lambda}, \quad (3.114)$$

$$\lambda_1\lambda_2\lambda_3 = -\frac{r\dot{m}}{r_\lambda}. \quad (3.115)$$

Using Equation (3.115), the term (3.112) becomes:

$$\lambda_i\lambda_j - (\lambda_i\lambda_j\lambda_k)\lambda_k = \lambda_i\lambda_j + \lambda_k\frac{r\dot{m}}{r_\lambda}. \quad (3.116)$$

Then, by using Equation (3.114), it becomes:

$$-\frac{1 + r_\lambda}{r_\lambda} - \lambda_j\lambda_k - \lambda_i\lambda_k + \lambda_k\frac{r\dot{m}}{r_\lambda} = -\frac{1 + r_\lambda}{r_\lambda} - \left(\lambda_j + \lambda_i - \frac{r\dot{m}}{r_\lambda}\right)\lambda_k. \quad (3.117)$$

And then thanks to Equation (3.113), we find a compact form for (3.112):

$$-\frac{1 + r_\lambda}{r_\lambda} + \lambda_k^2, \quad (3.118)$$

so that (3.111) is equivalent to:

$$-\frac{1 + r_\lambda}{r_\lambda} + \lambda_1^2 < 0, \quad -\frac{1 + r_\lambda}{r_\lambda} + \lambda_2^2 < 0, \quad \text{and} \quad -\frac{1 + r_\lambda}{r_\lambda} + \lambda_3^2 > 0. \quad (3.119)$$

One way to prove (3.119) is to use the continuity and monotony of the roots with regard to $r\dot{m}$. The monotony can be seen by considering the form (3.127) given in Appendix 3.C. Keeping in mind the ordering $\lambda_1 < 0 < \lambda_2 < \lambda_3$, let us study the roots of (3.20) when $r\dot{m} \rightarrow 0$ and $r\dot{m} \rightarrow +\infty$. We find:

$$r\dot{m} \rightarrow 0 \quad \Longrightarrow \quad \lambda_1 \rightarrow -\frac{1 + r_\lambda}{r_\lambda}, \quad \lambda_2 \rightarrow 0 \quad \text{and} \quad \lambda_3 \rightarrow \frac{1 + r_\lambda}{r_\lambda}, \quad (3.120)$$

$$r\dot{m} \rightarrow +\infty \quad \Longrightarrow \quad \lambda_1 \rightarrow -1, \quad \lambda_2 \rightarrow 1 \quad \text{and} \quad \lambda_3 \rightarrow +\infty. \quad (3.121)$$

Since $(1 + r_\lambda)/r_\lambda > 1$, it is found that:

$$\lambda_1 \in \left] -\frac{1 + r_\lambda}{r_\lambda}, -1 \right[, \quad \lambda_2 \in]0, 1[\quad \text{and} \quad \lambda_3 \in \left] \frac{1 + r_\lambda}{r_\lambda}, +\infty \right[, \quad (3.122)$$

what leads to (3.119). This proves that the maximum temperature is reached at $x = 0$.

3.C. Characteristic polynomial

In this appendix, the characteristic polynomial of Equation (3.20) is scrutinized. The general forms of its roots and their respective Taylor developments in the regime (3.37) are given. So as to simplify further calculations, the following notations are introduced:

$$\zeta = \frac{r_\lambda}{r_{\dot{m}}} \quad \text{and} \quad \chi = \frac{1 + r_\lambda}{r_\lambda} > 1. \quad (3.123)$$

Equation (3.20) becomes:

$$\lambda^3 - \zeta^{-1}\lambda^2 - \chi\lambda + \zeta^{-1} = 0. \quad (3.124)$$

Following Cardano's general theory, the canonical variables are introduced:

$$p = -\left(\frac{1}{3\zeta^2} + \chi\right) \quad \text{and} \quad q = -\frac{1}{3\zeta} \left(\frac{2}{9\zeta^2} + \chi - 3\right). \quad (3.125)$$

The discriminant of Equation (3.124) is:

$$\Delta = -(4p^3 + 9q^2) = \frac{4}{\zeta^4} + \frac{9(2\chi - 1)}{\zeta^2} + 4\chi^2 > 0, \quad (3.126)$$

whose positivity comes from $\chi > 1$. This confirms that Equation (3.20) has three real solutions $(\lambda_1, \lambda_2, \lambda_3) \in \mathbb{R}^3$. Using the relations (3.113-3.115), namely the negativity of their product and the positivity of their sum, it is deduced that their sign follows (3.106).

The general solutions take the following form:

$$\lambda_k = \frac{1}{3\zeta} + 2\sqrt{\frac{-p}{3}} \cos \left[\frac{1}{3} \arccos \left(\frac{3q}{2p} \sqrt{\frac{3}{-p}} \right) + \frac{2k\pi}{3} \right] \quad \text{for } k \in \{1, 2, 3\}. \quad (3.127)$$

The regime (3.37) can be recast in terms of ζ and χ as:

$$r_{\dot{m}}^{-1} = (\chi - 1)\zeta \ll 10 \quad \text{and} \quad \left(\frac{r_{\dot{m}}}{r_\lambda}\right)^{-1} = \zeta \ll 0.1, \quad (3.128)$$

which means that a Taylor development in ζ near the origin is conceivable. After some calculations, this gives:

$$\lambda_1 = -1 - \frac{(\chi - 1)}{2}\zeta - \frac{(\chi - 5)(\chi - 1)}{8}\zeta^2 + O(\zeta^3), \quad (3.129)$$

$$\lambda_2 = 1 - \frac{(\chi - 1)}{2}\zeta + \frac{(\chi - 5)(\chi - 1)}{8}\zeta^2 + O(\zeta^3), \quad (3.130)$$

$$\lambda_3 = \frac{1}{\zeta} + (\chi - 1)\zeta + O(\zeta^3). \quad (3.131)$$

It is worth noting that often, terms similar to $(\chi - 1)\zeta$ appear in the expansions. This is the translation that roughly, the regime (3.37) corresponds to $r_{\dot{m}} \rightarrow +\infty$ for a fixed r_λ . These developments show that the approximated roots found in Section 3.2.4 are dominant-order approximations in ζ . The roots λ_1 and λ_2 tend to be symmetric, of norm close to unity, while λ_3 has a propensity to be large.

3.D. Description of the coupled solver

The software CANTERA is coupled to a solid solver based on finite differences, implicit in time and second-order in space. The two codes exchange respectively constant solid and gaseous temperature profiles, until convergence is reached. The relative tolerances are 1×10^{-7} for CANTERA and 1×10^{-10} for the solid solver. The initial condition is set using the present analytical derivation. The adaptative mesh refinement from CANTERA is used. The resolved steady, volume-averaged equations are:

$$\dot{m} \partial_x Y_k + \partial_x J_k - \dot{\omega}_k = 0, \quad (3.132)$$

$$\dot{m} c_{p_g} \partial_x T_g - \partial_x (\lambda_g \partial_x T_g) + \sum_k c_{p_g,k} J_k \partial_x T_g + \sum_k h_k \dot{\omega}_k + \frac{h_V}{\epsilon} (T_g - T_s) = 0, \quad (3.133)$$

$$\lambda_s \partial_x^2 T_s + \frac{h_V}{1 - \epsilon} (T_g - T_s) = 0. \quad (3.134)$$

c_{p_g} and λ_g denote respectively the heat mass capacity of the mixture and the gas thermal conductivity, which here both depend locally on the temperature and composition. For each species k , Y_k denotes the mass fraction, J_k the diffusive flux, $c_{p_g,k}$ the heat mass capacity, h_k^0 the mass formation enthalpy and $\dot{\omega}_k$ the mass production rate per unit volume. The chemical scheme used is GRIMECH3.0, which comprises 53 reactions and 325 species.

3.E. Matrix for resolution of the single-layer finite porous

$$\underline{\underline{\mathbf{M}}} = \begin{bmatrix} 1 & 1 & 1 \\ 0 & \lambda_1 & \lambda_2 \\ 1 & 1 - \lambda_1^2 & 1 - \lambda_2^2 \\ 0 & \lambda_1(1 - \lambda_1^2) & \lambda_2(1 - \lambda_2^2) \\ 0 & \lambda_1 e^{-\lambda_1 x_p^*} & \lambda_2 e^{-\lambda_2 x_p^*} \\ 0 & \epsilon \lambda_1 (1 - \lambda_1^2) e^{-\lambda_1 x_p^*} & \epsilon \lambda_2 (1 - \lambda_2^2) e^{-\lambda_2 x_p^*} \\ 1 & (1 - \lambda_1^2) e^{-\lambda_1 x_p^*} & (1 - \lambda_2^2) e^{-\lambda_2 x_p^*} \\ 0 & 0 & 0 \\ 0 & 0 & 0 \end{bmatrix}$$

$$\begin{bmatrix} 1 & -1 & -1 \\ \lambda_3 & 0 & -\lambda_1 \\ 1 - \lambda_3^2 & -1 & -(1 - \lambda_1^2) \\ \lambda_3(1 - \lambda_3^2) & 0 & -\lambda_1(1 - \lambda_1^2) \\ \lambda_3 e^{-\lambda_3 x_p^*} & 0 & 0 \\ \epsilon \lambda_3 (1 - \lambda_3^2) e^{-\lambda_3 x_p^*} & 0 & 0 \\ (1 - \lambda_3^2) e^{-\lambda_3 x_p^*} & 0 & 0 \\ 0 & 0 & \lambda_1 e^{\lambda_1(L^* - x_p^*)} \\ 0 & 0 & \lambda_1(1 - \lambda_1^2) e^{\lambda_1(L^* - x_p^*)} \end{bmatrix}$$

$$\left. \begin{bmatrix} -1 & -e^{-\lambda_3(L^* - x_p^*)} & 0 \\ -\lambda_2 & -\lambda_3 e^{-\lambda_3(L^* - x_p^*)} & 0 \\ -(1 - \lambda_2^2) & -(1 - \lambda_3^2) e^{-\lambda_3(L^* - x_p^*)} & 0 \\ -\lambda_2(1 - \lambda_2^2) & -\lambda_3(1 - \lambda_3^2) e^{-\lambda_3(L^* - x_p^*)} & 0 \\ 0 & 0 & 0 \\ 0 & 0 & -\epsilon r_{\dot{m}}/r\lambda \\ 0 & 0 & -1 \\ \lambda_2 e^{\lambda_2(L^* - x_p^*)} & \lambda_3 & 0 \\ \lambda_2(1 - \lambda_2^2) e^{\lambda_2(L^* - x_p^*)} & \lambda_3(1 - \lambda_3^2) & 0 \end{bmatrix} \right\} \quad (3.135)$$

Combustion regimes of the 1D volume-averaged equations

This chapter is based on the article Masset, P. A., Dounia, O., & Selle, L. (2021). **Porous media combustion: from decoupled to hyperdiffusive flames.** *Combustion and Flame*, 241, 112052. published during this thesis, augmented by new results.

By relaxing the assumption of infinitely-fast chemistry of Chapter 3, this chapter proposes a classification of volume-averaged porous media combustion in three distinct regimes for increasing interphase heat transfer, namely: decoupled, intermediate and hyperdiffusive. In the decoupled regime, flames behave as preheated free-flames. In the intermediate regime, large superadiabaticities are found. In the hyperdiffusive regime, flames are governed solely by an increase in thermal conductivity. The transition between these regimes is shown to be driven by two dimensionless parameters. The extent of the intermediate regime and the maximal superadiabaticity are proven to be related to the ratio between the diffusive and reactive length scales of the reference free-flame. Eventually, it is emphasized how the heat-recirculating system acts locally as a Lewis-changing device, whose effect harmonizes in the hyperdiffusive regime.

Overview

4.1. Chapter introduction	90
4.2. Methodology	91
4.2.1. Simplified analytical model (AM)	92
4.2.2. Dimensionless parametrization	93
4.2.3. 1D numerical simulations (SIM)	94
4.2.4. Relations between (AM) and (SIM)	94
4.2.5. Exploration of the parametric space	95
4.3. From decoupled to hyperdiffusive regimes	95
4.3.1. General description of the regimes	95
4.3.2. Transitions between the regimes	97
4.4. Detailed structure of the various regimes	101
4.4.1. Porous media as Lewis-changing devices	101
4.4.2. Broadening effects in porous media	103
4.4.3. Effects of equivalence ratio, fuel and complex chemistry	105
4.5. Generalized formulae for flame speed in all regimes	107
4.5.1. Flame acceleration due to preheating - F	107
4.5.2. Flame acceleration due to hyperdiffusion - G	107
4.5.3. Validation of the formula	108
4.6. Conclusions of the chapter	109
4.A. Approximations of the analytical model (AM)	110
4.A.1. Decoupled regime	110
4.A.2. Hyperdiffusive regime	110

4.B. Criterium for regime discrimination of Figure 4.3	110
4.C. Flame structure in the space (\mathbf{Y}_F, θ_g)	111

“How can you govern a country which has 246 varieties of cheese?”

CHARLES DE GAULLE

4.1. Chapter introduction

Flames within porous media present unique properties such as increased burning rate and broadened flammability limits, allowing stable combustion of very lean mixtures for minimal CO/NO_x emissions [49, 102, 226]. The main mechanism underpinning this performance is commonly identified as the preheating of the fresh gases before the flame front, due to an upstream recirculation of combustion heat through the solid matrix [62, 227]. Heat recirculation may lead to a localized accumulation of enthalpy and temperatures above the equilibrium temperature - a feature often called superadiabatic or excess enthalpy combustion. It is well-known that porous combustion systems present many challenges, either experimentally, conceptually, or numerically. Notably, non-intrusive experimental measurements require advanced apparatus [158, 228, 257] which, still today, do not provide reliably basic physical quantities such as local gas velocity at the pore level. Many coupled, multi-scale phenomena take place simultaneously, such as conduction, convection, interphase heat exchange, radiation and chemical reactions. This leads to a vast number of design possibilities and applications, but renders modelling generalizations more intricate.

Numerous approaches were followed in the modelling of porous media combustion, from phenomenological models [49, 258] to more recent 3D pore-level simulations [136, 235, 259]. Among them, substantial effort was dedicated into finding predictive volume-averaged models of reduced computational cost. Although such theories are unlikely to catch all the subtleties occurring at the pore level, some agreement for superadiabatic properties [134, 135], burning velocity [231, 260], temperature profiles [158, 216, 261] and emissions [192, 262] was obtained against experimental data.

The first important modelling feature in porous media combustion is of course the heat coupling between the gas and the solid matrix. To model it, some authors have tried a single-phase approach with an artificial increase in the gas thermal conductivity, which increases burning rate. For example, Mohamad et al. [191] considered a 2D numerical model with no solid equation. A similar approach was followed by Brenner et al. [192] with complex chemistry and experimentally-fitted values for the effective thermal conductivity. Li et al. [263] found this effective thermal conductivity to increase with decreasing porosity. Chua [193] postulated a form for conductivity enhancement and found reasonable agreement with experimental data. Intrinsically, this modelling choice is based on the idea that the porous matrix can be seen as a supplementary pathway to sustain combustion processes and, more generally, to diffuse heat in the coupled system. A consequence is that enhanced gas diffusion by heat coupling may artificially increase the Lewis number of the mixture, changing considerably the internal flame structure. Interestingly, interpreting porous media as Lewis-changing devices was proposed in a brief communication of Jones [264], who called upon researchers to consider this conceptual approach. Up to date, this call remains unanswered: the keyword “Lewis” is not even stated in the most reknown reviews on the topic [29, 102, 227, 265]. One of the aims of this chapter is to rehabilitate this intuition, and show how this Lewis-changing capability is conceptually intrinsic of volume-averaged porous media combustion.

From the point of view of the volume-averaged equations, the effective thermal diffusivity in the gas phase may also be enhanced by forced convection through the porous medium. This phenomenon, called hydrodynamic dispersion, was considered by previous authors by increasing the thermal and mass diffusivities in the same proportions [231, 266, 267]. Note that contrary to heat coupling, this does not change much the effective Lewis number. However, this effect is discarded in this chapter, since the phenomenology linking dispersion (large-scale phenomenon) to enhanced burning rate at the flame front (pore-scale phenomenon) has not yet been supported properly by pore-scale experiments or numerical simulations. Hence, it is not excluded that dispersion is still used today as a “stuff” parameter, mirror of the single-phase modelling based on effective diffusivities. This aspect will be discussed in detail in Chapter 6.

Instead of increasing artificially the thermal conductivity to model the heat coupling between the gas and the solid, a more general methodology consists in modelling the two phases separately, and couple them through a volume heat transfer coefficient. The studies of Sahraoui and Kaviany underlined the importance of this approach [194, 268]. Interestingly, single-phase and two-phase modellings present *a priori* different mechanisms for the increase in burning rate. Single-phase models tend to show a flame acceleration through increased diffusion, while two-phase models tend to view flame acceleration as a preheating effect over larger length scales. To the best of the author’s knowledge, a framework reconciling these two approaches is yet to be proposed. This requires a thorough understanding of the transition between the various combustion regimes for increasing interphase heat transfer, with a large and systematic exploration of the gas/solid parametric space. Unfortunately, it appears that the parametric explorations in the literature are numerous but rather narrow [159, 263, 267], due to the strong motivation of most researchers to fit specific experimental/numerical conditions. Nevertheless, this analysis is of critical importance, given the fact that “local” analyses may hide non-monotonous influences of parameters. For instance, we show in this chapter that large heat transfer coefficients suppress superadiabaticity, possibly leading to a local maximum in burning velocity. Eventually, with the exception of the works of Pereira et al. [239, 240], no simple dimensionless characteristic parameters were introduced to distinguish asymptotic regimes of flames within porous media. In Chapter 1, we have shown that when the reactive-diffusive and interphase non-equilibrium length scales are separated, the combustion regime is determined via an analytical derivation based on two independent parameters. Can these two be exploited further?

In the present chapter, a very large parametric space of the volume-averaged coupled gas/solid 1D equations is explored. Each numerical solution is analyzed and compared to the simplified analytical model of Chapter 3, which assumed infinitely-thin reaction sheet and constant gas properties (Section 4.2). From very low to very large interphase heat transfer, three successive combustion regimes are distinguished, namely: **decoupled, intermediate and hyperdiffusive**. By using the two aforementioned parameters, the transitions between these regimes are studied analytically (Section 4.3). To conclude, important details on the flame structure are provided: first through the relation between the heat coupling and the effective Lewis number, then with a study of the so-called broadening of flames within porous media, and eventually by addressing mathematically the effects of fuel, complex chemistry and equivalence ratio (Section 4.4).

4.2. Methodology

This section addresses the relation between two modelling approaches of porous media combustion. One fully analytical solution assuming a thin reaction sheet with constant properties (AM), and numerical simulations with a detailed modelling of thermochemistry (SIM). It is shown that the two dimensionless parameters of (AM) are relevant to study the various combustion regimes observed in (SIM). Radiative transfer is not included in this chapter, which means

that it can not be quantitatively accurate. This has already been modelled at the macroscopic scale through an increase in solid thermal conductivity (*e.g.* Chap. 5.11 in [161]). The associated non-linearity prevents the derivation of analytical solutions but to our knowledge does not affect the qualitative behaviour of combustion in porous media.

4.2.1. Simplified analytical model (AM)

The one-dimensional theoretical modelling of flames in porous media developed in Chapter 3 is now briefly recalled, and referred to in this chapter under the denomination (AM) for Analytical Model. Again, the reaction zone is assumed infinitely-thin, as depicted in Figure 4.1. The model consists of a steady isobaric flame submerged in an infinite, inert and homogeneous porous medium, characterised by its porosity ϵ , thermal conductivity λ_s and volume heat transfer coefficient h_V . The system is assumed to be globally adiabatic, which neglects heat losses to the exterior, either by conduction, convection or radiation. This chapter is therefore in the same spirit as fundamental studies on adiabatic free flames: those are rarely encountered in practical applications but their study reveals fundamental properties of great importance. T_s and T_g denote the solid and gas temperatures respectively. At the infinite upstream, the phase-averaged mass flow rate is $\dot{m} = \rho_u S_L^P$, equal to the product of the inlet density ρ_u and burning velocity S_L^P . The fresh mixture enters the domain at a temperature T_u and leaves at the equilibrium temperature T_{ad} . The corresponding volume-averaged equations, valid on each side of the reaction sheet, are [252]:

$$\lambda_s \partial_x^2 T_s + \frac{h_V}{1-\epsilon} (T_g - T_s) = 0 \quad (\text{solid}), \quad (4.1)$$

$$-\dot{m} c_{p_g}^{(AM)} \partial_x T_g + \lambda_g^{(AM)} \partial_x^2 T_g - \frac{h_V}{\epsilon} (T_g - T_s) = 0 \quad (\text{gas}), \quad (4.2)$$

with $c_{p_g}^{(AM)}$ the heat capacity per mass unit and $\lambda_g^{(AM)}$ the thermal conductivity of the mixture - the superscript (AM) being used to avoid the confusion with the composition and temperature-dependent parameters in the model resolved numerically (SIM). In addition to assuming all properties constant, the other strong hypothesis of the present modelling resides in the lumping of the reaction zone into a jump condition:

$$\lambda_g^{(AM)} \partial_x T_g(x=0^-) = \dot{m} c_{p_g}^{(AM)} (T_{ad} - T_u) + \lambda_g^{(AM)} \partial_x T_g(x=0^+). \quad (4.3)$$

Although strict adiabaticity is never achieved in practical combustion systems, this chapter assumes global adiabaticity. In that case, equilibrium is reached far upstream and downstream, leading to the following boundary conditions:

$$T_s \xrightarrow{x \rightarrow -\infty} T_u \quad \text{and} \quad T_g \xrightarrow{x \rightarrow -\infty} T_u, \quad (4.4)$$

$$T_s \xrightarrow{x \rightarrow +\infty} T_{ad} \quad \text{and} \quad T_g \xrightarrow{x \rightarrow +\infty} T_{ad}. \quad (4.5)$$

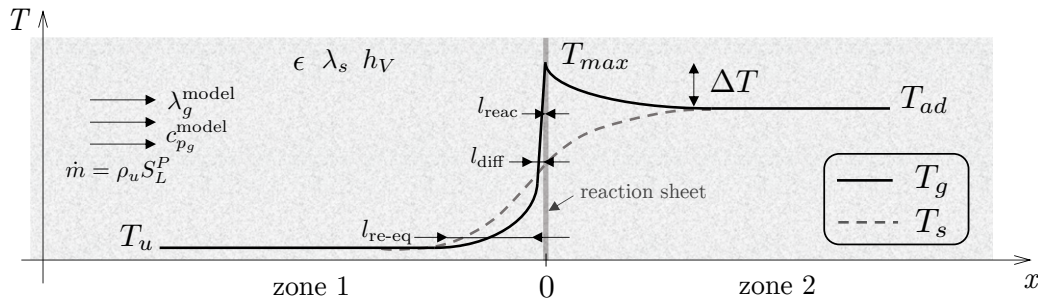


Figure 4.1. – Representation of a submerged flame in infinite porous media.

This modelling always yields a maximum temperature $T_{max} > T_{ad}$, larger than the equilibrium temperature. Supposing interphase heat exchange to play a minor role at the scale of reaction and diffusion (decoupled regime), the flame can be considered locally as an adiabatic free-flame preheated by the temperature:

$$\Delta T = T_{max} - T_{ad}. \quad (4.6)$$

On Figure 4.1 are also depicted the three characteristic length scales of porous media combustion, namely:

- l_{re-eq} , defining the interphase re-equilibration regions before and after the flame front. It represents the gas/solid out-of-equilibrium zone;
- l_{diff} , related to heat diffusion in the gas phase;
- l_{reac} , defining the thickness of the reaction zone. In the analytical model (AM), it is assumed $l_{reac} = 0$.

Eventually, so as to account for the flame acceleration due to the presence of the porous matrix, the “speed-up” is defined as the ratio between the burning velocity S_L^P and the laminar adiabatic free-flame speed without porous medium S_L^0 :

$$\text{speed-up} = \frac{S_L^P}{S_L^0}. \quad (4.7)$$

In chapters 6 and 7, this quantity will be noted Γ .

4.2.2. Dimensionless parametrization

By normalizing the coordinates and temperatures as:

$$x^* = x / \sqrt{\frac{(1-\epsilon)\lambda_s}{h_V}}, \quad \theta_s = \frac{T_s - T_u}{T_{ad} - T_u}, \quad \theta_g = \frac{T_g - T_u}{T_{ad} - T_u} \quad \text{and} \quad \theta_{max} = \frac{T_{max} - T_u}{T_{ad} - T_u}, \quad (4.8)$$

Equations (4.1) and (4.2) become:

$$\partial^2 \theta_s + \theta_g - \theta_s = 0, \quad (4.9)$$

$$-r_{\dot{m}} \partial \theta_g + r_\lambda \partial^2 \theta_g + \theta_s - \theta_g = 0, \quad (4.10)$$

where $\partial \equiv \partial_{x^*}$, and

$$r_{\dot{m}} = \frac{\dot{m} \epsilon c_{p_g}^{(AM)}}{\sqrt{h_V (1-\epsilon)\lambda_s}} \quad \text{and} \quad r_\lambda = \frac{\epsilon \lambda_g^{(AM)}}{(1-\epsilon)\lambda_s}. \quad (4.11)$$

Note that $r_{\dot{m}}$ and r_λ fully determine the solutions of the problem. We also introduce the following useful notation:

$$\chi = 1 + \frac{1}{r_\lambda}. \quad (4.12)$$

Eventually, recirculation efficiency is defined as the dimensionless superadiabaticity as:

$$\eta_{rec} = \frac{\Delta T}{T_{ad} - T_u} = \theta_{max} - 1. \quad (4.13)$$

The fully analytical resolution of this analytical model (AM) was performed in Chapter 3.

4.2.3. 1D numerical simulations (SIM)

A more complete description of the gas phase is considered. Without dispersion, the volume-averaged equations of Chapter 2 become:

$$\dot{m} \partial_x Y_k + \partial_x J_k - \dot{\omega}_k = 0, \quad (4.14)$$

$$\dot{m} c_{p_g} \partial_x T_g - \partial_x (\lambda_g \partial_x T_g) + \sum_k c_{p_g,k} J_k \partial_x T_g + \sum_k h_k \dot{\omega}_k + \frac{h_V}{\epsilon} (T_g - T_s) = 0, \quad (4.15)$$

$$\lambda_s \partial_x^2 T_s + \frac{h_V}{1 - \epsilon} (T_g - T_s) = 0, \quad (4.16)$$

where c_{p_g} and λ_g denote respectively the heat mass capacity of the mixture and the gas thermal conductivity, which both depend locally on the temperature and composition. For each species k , Y_k denotes the mass fraction, J_k the diffusive flux, $c_{p_g,k}$ the heat mass capacity, h_k the mass enthalpy and $\dot{\omega}_k$ the mass production rate per unit volume.

To resolve these equations, the software CANTERA is coupled to an external, implicit centered finite differences solver to resolve the energy equation in the solid phase. The two codes are run successively. Mesh refinement is managed by CANTERA (slope parameter 0.05, curve 0.02), and the solid solver uses the same mesh. The relative tolerances are set to 1×10^{-7} for CANTERA and 1×10^{-10} for the solid solver. The convergence of the coupling strategy is checked by imposing a relative difference in L2 norm on gas and solid temperature profiles below 1×10^{-6} . The profiles are initialized by using the solutions of the analytical model (AM). Convergence was always obtained.

Concerning chemistry, both complex and single-step reaction schemes are considered, namely the well-established mechanism GRIMECH3.0 with 53 reactions and 325 species, and single-step approximations for methane and hydrogen combustion in air whose parameters are given in Table 4.1. In all cases, transport and thermodynamic properties are that of GRIMECH3.0.

Arrhenius parameter	A	T _A (K)	n _F	n _O
1S methane-air	10 ¹²	17500	1	0.5
1S hydrogen-air	10 ¹⁴	10500	1	1

Table 4.1. – Arrhenius pre-exponential factors A , activation temperatures T_A and fuel/oxidizer orders n_F/n_O used in the single-step approximations, for a molar production rate

$$\text{of the form } A \left[\frac{\rho_g Y_F}{W_F} \right]^{n_F} \left[\frac{\rho_g Y_O}{W_O} \right]^{n_O} \exp \left(-\frac{T_A}{T_g} \right).$$

For what follows we introduce a notation for reduced mass fraction of fuel F :

$$\mathbb{Y}_F = Y_F / \max(Y_F). \quad (4.17)$$

where F can be either methane or hydrogen. \mathbb{Y}_F is linked to the progress variable of the fuel c_F through $c_F = 1 - \mathbb{Y}_F$.

4.2.4. Relations between (AM) and (SIM)

4.2.4.1. Choice of constant properties for (AM)

Obviously, Equations (4.14-4.16) and (4.9-4.10) are not equivalent. The analytical model (AM) assumes constant gaseous properties, whilst the numerical simulations (SIM) present a much larger parametric space. This implies that the values $c_{p_g}^{(AM)}$ and $\lambda_g^{(AM)}$ fed into the two

parameters $r_{\dot{m}}$ and r_λ must be chosen carefully for comparison. Preliminary analyses showed that picking the effective thermal conductivity and heat mass capacity in the fresh gases:

$$\lambda_g^{(\text{AM})} = \lambda_g(x \rightarrow -\infty) = \lambda_g^u, \quad (4.18)$$

$$c_{p_g}^{(\text{AM})} = c_{p_g}(x \rightarrow -\infty) = c_{p_g}^u, \quad (4.19)$$

allows to retrieve the physical phenomena at stake, such as preheating values and flame speed in the hyperdiffusive regime. Other choices do not alter qualitatively the conclusions.

4.2.5. Exploration of the parametric space

4.2.5.1. Definition of the parametric space

The parametric space of the numerical simulations (SIM) is composed of (1) the inlet mixture properties, namely pressure, temperature and composition, (2) a reaction scheme with its thermochemistry and (3) the porous media properties, namely porosity ϵ , conductivity λ_s , and heat transfer coefficient h_V . For a fixed inlet mixture and reaction scheme, the three parameters $(\epsilon, \lambda_s, h_V)$ determine $r_{\dot{m}}$ and r_λ . Yet it is remarked that multiplying Equation (4.16) by $(1-\epsilon)/\epsilon$, we can reduce this parametrization to only two parameters:

$$\frac{1-\epsilon}{\epsilon} \lambda_s \quad \text{and} \quad \frac{h_V}{\epsilon}, \quad (4.20)$$

so that for a given ϵ , there is a bijection between the sets $(r_{\dot{m}}, r_\lambda)$ and (λ_s, h_V) . Therefore, porosity can be viewed as an arbitrary dummy parameter in the dimensionless space and without any loss of generality, the choice is made to set $\epsilon = 0.9$.

4.2.5.2. Numerical strategy (SIM)

Numerical simulations are run as follows. A value of r_λ is fixed for a given inlet mixture by prescribing λ_s . The heat exchange coefficient h_V is then increased exponentially, what tends to yield uniformly-distributed values for $r_{\dot{m}}$. Note that $r_{\dot{m}}$ is an output of the simulations, since it requires the eigenvalue \dot{m} . Typical values (in $\text{W m}^{-1} \cdot \text{K}^{-1}$) being 10^{-2} - 10^{-1} for λ_g and 10^0 - 10^3 for λ_s , it is chosen to pick r_λ within 10^{-3} - 10^0 , yielding representative flames. The heat transfer coefficient h_V is varied typically between 10^3 and $10^9 \text{ W m}^{-3} \cdot \text{K}^{-1}$ to encompass extreme asymptotic regimes (typical values lie well between these two limits [34]). The present strategy is therefore meant to be as systematic and complete as possible.

4.2.5.3. Baseline case

The chosen baseline case is single-step methane-air at atmospheric pressure for an equivalence ratio $\phi = 0.5$. It will serve as a reference to discuss the influence of reaction scheme, equivalence ratio and fuel on the burning regimes and their properties. Although $\phi = 0.5$ lies slightly below the experimental lean flammability of methane, a flame speed can be computed with CANTERA because there are no heat losses. Using such a low equivalence ratio as a reference will allow to emphasize clearly the influence of equivalence ratio and complex chemistry.

4.3. From decoupled to hyperdiffusive regimes

4.3.1. General description of the regimes

Before showing the many solution points of the baseline case described in Section 4.2.5.3, we consider three individual solutions for different values of h_V and fixed $r_\lambda = 0.1$. In Figure 4.2(a-d) are plotted gas and solid temperature profiles and in Figure 4.2(e-h) those of reduced heat

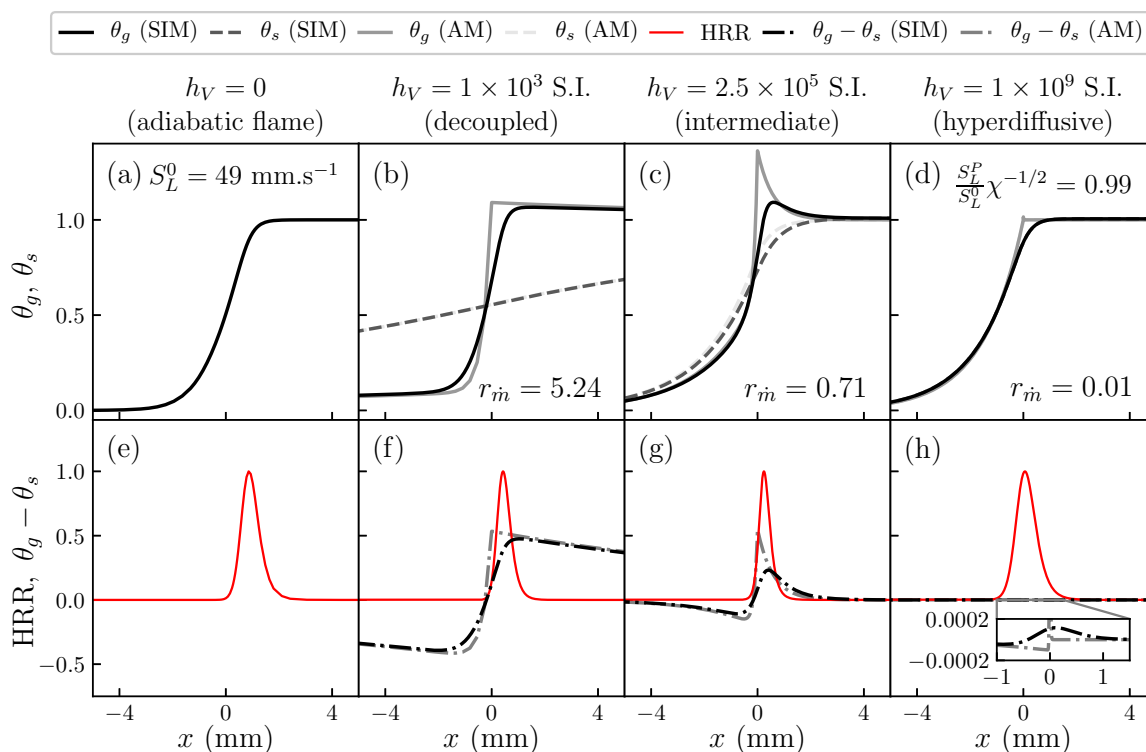


Figure 4.2. – Solid/gas temperatures, heat release rate and interphase out-of-equilibrium temperatures from the numerical simulations (SIM) and the analytical model (AM). Methane-air, single-step, $\phi = 0.5$. The unit for h_V is $\text{W.m}^{-3}.\text{K}^{-1}$. In case (b), θ_s for (AM) and (SIM) are superimposed. In case (d), $\theta_s \sim \theta_g$ both for (AM) and (SIM).

release rate (HRR) with the difference between gas and solid temperatures. The extent of the term $\theta_g - \theta_s$ allows to estimate the length scale $l_{\text{re-eq}}$, the HRR profile that of l_{reac} . The profiles obtained from the analytical model (AM) are also shown for comparison. The reference case $h_V = 0$ corresponds to the adiabatic free-flame. The resulting values of $r_{\dot{m}}$ are given accordingly in each case. Overall, it is observed that temperature profiles are retrieved correctly by (AM), apart from the peak temperature which is overestimated. This is due to the extension of the reaction zone, an effect well-known in the field of asymptotic theory and was already observed in [239]. This indicates that the parameters $r_{\dot{m}}$ and r_λ suffice to characterize important traits of the solutions of (SIM), such as preheating, solid temperature profile and, at least qualitatively, superadiabatic behavior. As h_V is increased, the flame structure changes dramatically. Three distinct regimes are progressively observed, named respectively **decoupled**, **intermediate** and **hyperdiffusive**. They are now described individually.

4.3.1.1. Decoupled regime - Figure 4.2(b) and (f)

The decoupled regime was studied thoroughly in [214, 239]. It is characterized by large interphase non-equilibrium and small solid-temperature gradients, with extended re-equilibration zones before and after the flame front. Locally, the flame structure is very close to an adiabatic flame, shifted by a certain preheating temperature. This preheating leads to an increase in flame speed, which can be predicted by computing the corresponding “preheated” adiabatic laminar free-flame. In that regime, the increase in flame speed is dominated by the increase in

the temperature of the reaction zone, which is visibly shortened by a decrease in chemical time scale (Arrhenius effect). In that case, it is clear that interphase heat transfer does not impact locally the flame structure:

$$l_{\text{re-eq}} \gg l_{\text{diff}} \gg l_{\text{reac}}. \quad (4.21)$$

4.3.1.2. Hyperdiffusive regime - Figure 4.2(d) and (h)

On the other side of the spectrum, the hyperdiffusive regime is characterized by large inter-phase heat transfer. In this regime, solid and gas temperatures are almost equal, which means that a single-phase modelling is adequate. Little or no superadiabatic behavior is observed. The flame has a structure similar to an adiabatic flame, yet showing a smaller temperature gradient, indicating a larger effective diffusivity all across the flame front. This is the first hint towards the denomination ‘‘hyperdiffusive’’. Anticipating on future results, as shown on Figure 4.2(d) speed-up appears to have converged towards $\chi^{1/2}$, an asymptotic value independent of h_V . This observation will be justified in Section 4.3.2. As shows the zoomed-in subplot of Figure 4.2(h), in that situation the re-equilibrium length scale is of the same order or smaller than the reaction length scale, indicating that interphase heat transfer plays a major role at the very heart of the flame front:

$$l_{\text{diff}} \gg l_{\text{reac}} \sim l_{\text{re-eq}}. \quad (4.22)$$

4.3.1.3. Intermediate regime - Figure 4.2(c) and (g)

The intermediate regime covers a range of solutions for which the length scale of interphase re-equilibration $l_{\text{re-eq}}$ meddles with the classical length scale of diffusion in the gas phase l_{diff} , yet remaining larger than that of reaction:

$$l_{\text{diff}} \sim l_{\text{re-eq}} \gg l_{\text{reac}}. \quad (4.23)$$

This intermediate regime is governed by both superadiabatic and hyperdiffusive effects, where the maximal temperatures are found. Incidentally, the interested reader shall relate this regime to the ‘‘ultra-lean limit’’ studied by Pereira et al. in [240] with asymptotic theory.

4.3.1.4. Summary of observations

It is observed that the relative size of the re-equilibration length scale versus that of diffusion and reaction is characteristic of the various burning regimes. It is expected that, the larger the ratio $l_{\text{diff}}/l_{\text{reac}}$, the broader the intermediate regime. Moreover, it appears that the burning regimes are progressively characterized from preheating/superadiabatic to hyperdiffusive effects. These observations are investigated and supported mathematically in the following Section 4.3.2.

4.3.2. Transitions between the regimes

So as to propose a taxonomy of burning regimes with a minimal set of parameters, we attempt in this section to locate their transition by using only $r_{\dot{m}}$ and r_λ . Two methodologies to classify the regimes are compared. The first makes use of the speed-up and preheating values, the second an equivalent resistive model.

4.3.2.1. Classification using speed-up convergence and preheating

Following Section 4.2.5, numerical simulations (SIM) are run for given values of r_λ . The heat exchange coefficient h_V is varied continuously and the resulting values of $r_{\dot{m}}$ are reported. For

the baseline case (single-step, methane-air, $\phi = 0.5$), Figure 4.3 shows the speed-up values obtained in (SIM) versus the speed-up of adiabatic flames with the same amount of preheating. Four values of r_λ are reported. The three specific points from Figure 4.2 are shown specifically. Figure 4.3 is interpreted as follows. Data located close to the first bisector correspond to points whose speed-up is dominated by preheating effects, characteristic of the decoupled regime, and are colored in black. The points that appear to converge on the left, without preheating/superadiabatic effects, indicate the hyperdiffusive regime and are colored in light grey. The intermediate regime is defined by complementary, colored in medium grey. The exact quantitative criteria used to discriminate the regimes is given in Appendix 4.B. Symbols and colors are common for all figures throughout the chapter, to facilitate cross-examinations and understanding. Overall, it is observed that speed-up values vary greatly with r_λ in a seemingly auto-similar fashion.

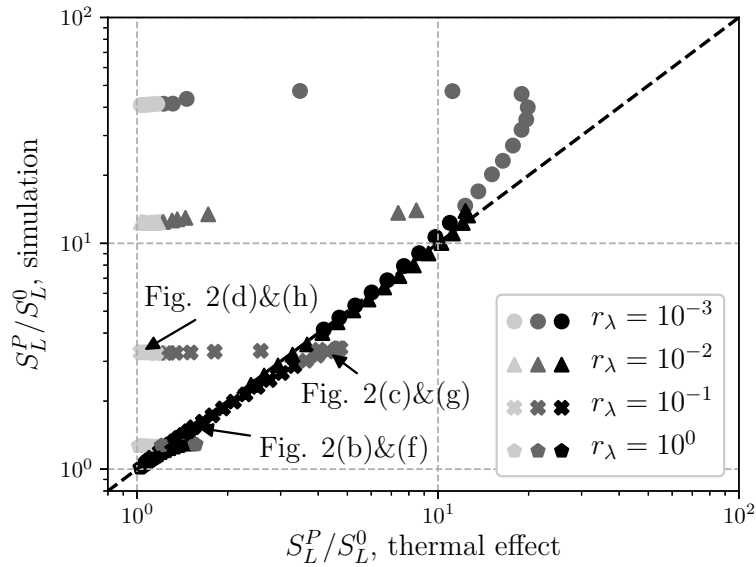


Figure 4.3. – Computed speed-up versus speed-up related to preheating. Methane-air, $\phi = 0.5$, single-step. Symbols: simulations (black: decoupled, medium grey: intermediate, light grey: hyperdiffusive).

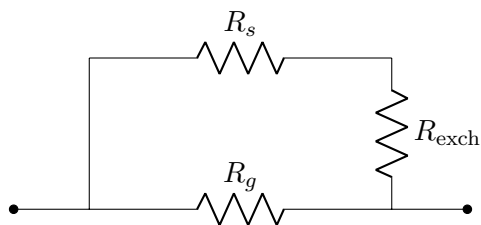


Figure 4.4. – Simplified resistive model.

where:

$$R_s = \frac{1}{(1 - \epsilon)\lambda_s}$$

$$R_g = \frac{1}{\epsilon\lambda_g}$$

$$R_{\text{exch}} = \frac{1}{h_V l_{\text{re-eq}}^2}$$

4.3.2.2. Classification using an equivalent resistive model

Regimes distinction can be approached differently by considering the simple resistive model of Figure 4.4, which presents the two pathways for upstream energy transfer: through the gas

(R_g) and through the solid after interphase exchange ($R_s + R_{\text{exch}}$). This model resembles that developed by Leach et al. for microcombustors [258], and represents the equivalent conductivity of the coupled gas/solid system. Since heat recirculation has an influence over the length scale of thermal interphase non-equilibrium, the relevant length scale for R_{exch} is $l_{\text{re-eq}}$. By using classical Kirchoff's laws and picking the constant gaseous properties to their value in the fresh gases, the equivalent resistance R_{eq} is shown to be:

$$R_{\text{eq}} = R_g \delta^{-1} \quad \text{where} \quad \delta = 1 + \frac{1}{r_\lambda} \left(\frac{1}{1 + \left[\frac{r_{\dot{m}} l_{\text{diff}}}{r_\lambda l_{\text{re-eq}}} \right]^2} \right), \quad (4.24)$$

where the classical diffusive length scale $l_{\text{diff}} = \lambda_g / \dot{m} c_{p_g}$ appears naturally thanks to $r_{\dot{m}}$ and r_λ . In the decoupled regime $r_{\dot{m}} \rightarrow +\infty$ thus $\delta \rightarrow 1$: the flame front does not “see” the porous medium because the effective thermal conductivity remains related only to λ_g . In the hyperdiffusive regime, $r_{\dot{m}} \rightarrow 0$ thus $\delta \rightarrow 1 + 1/r_\lambda = \chi$: the flame front is governed by an increased thermal conductivity, of a factor χ . This result is of major importance, since (1) it substantiates further the denomination “hyperdiffusive”, (2) it seemingly implies that flames in this regime can be interpreted as free-flames of increased thermal conductivity, which have no reason to show any superadiabatic behavior and (3) given that asymptotic theory predicts a laminar flame speed proportional to the square root of the thermal conductivity, the observation $S_L^P/S_L^0 \rightarrow \sqrt{\chi}$ is retrieved. By considering closely Equation (4.24), it is observed that $1/r_\lambda$ is a measure of the superadiabatic/hyperdiffusive intensity, while the ratio $r_{\dot{m}} l_{\text{diff}} / r_\lambda l_{\text{re-eq}}$ seems to govern the transition between the regimes. This supports the observation of auto-similar behavior for speed-up values observed in Figure 4.3. Based upon these considerations, it is now possible to study more precisely regime transitions.

Between the decoupled and intermediate regimes: as explained in Section 4.3.1.3, the re-equilibration length scale is in this case of the order of the diffusive length scale, so that $l_{\text{re-eq}} \sim l_{\text{diff}}$. This gives:

$$\frac{r_{\dot{m}} l_{\text{diff}}}{r_\lambda l_{\text{re-eq}}} \sim \frac{r_{\dot{m}}}{r_\lambda} \quad (\text{decoupled} \rightarrow \text{intermediate}), \quad (4.25)$$

thus the ratio $r_{\dot{m}}/r_\lambda$ is expected to intervene directly in this first transition, as a measure of deviations of δ from unity in proportion of $1/r_\lambda$. Incidentally, smaller deviations from δ to unity can be caught by rearranging differently the denominator of Equation (4.24), which verifies $r_\lambda(1 + [r_{\dot{m}}/r_\lambda]^2) \sim r_{\dot{m}}^2/r_\lambda$. The latter can be viewed equivalently in terms of $r_{\dot{m}}/r_\lambda^{1/2}$. Both measures will be tested in what follows.

Between the intermediate and hyperdiffusive regimes: as explained in Section 4.3.1.2, in this case a further influence of heat recirculation on the internal flame structure is observed with $l_{\text{re-eq}} \sim l_{\text{reac}}$, leading to $r_{\dot{m}} l_{\text{diff}} / r_\lambda l_{\text{re-eq}} \sim r_{\dot{m}} l_{\text{diff}} / r_\lambda l_{\text{reac}}$. Contrary to the transition decoupled \rightarrow intermediate, there is no direct simplification so the ratio $l_{\text{diff}}/l_{\text{reac}}$ must be expressed differently. First, let us study the evolution of the diffusive length scale: since by definition $l_{\text{diff}} = \lambda_g / \dot{m} c_{p_g} = \lambda_g / \rho_u S_L^P c_{p_g}$, the product $S_L^P l_{\text{diff}}$ can be considered almost constant. By taking its value in the case of the reference free-flame, denoted by the superscript 0 , we obtain $l_{\text{diff}} = l_{\text{diff}}^0 S_L^0 / S_L^P$. Concerning the reaction length scale, Equation (4.41) gives $l_{\text{reac}} \sim l_{\text{reac}}^0 S_L^P / S_L^0$ as shown later in Section 4.4.2. The last ingredient is to recall the speed-up convergence in the hyperdiffusive regime $S_L^P/S_L^0 \rightarrow \sqrt{\chi}$, so that:

$$\frac{r_{\dot{m}} l_{\text{diff}}}{r_\lambda l_{\text{re-eq}}} \sim \gamma \frac{r_{\dot{m}}}{r_\lambda} \chi^{-1} \quad (\text{intermediate} \rightarrow \text{hyperdiffusive}). \quad (4.26)$$

where γ is the ratio between the diffusion and reaction length scales of the free-flame:

$$\gamma = \frac{l_{\text{diff}}^0}{l_{\text{reac}}^0}. \quad (4.27)$$

This ratio represents the “stiffness” of the reaction-diffusion equation. Classical asymptotic theory predicts that γ is of the order of the Zel’dovich number β [115]:

$$\gamma = O(\beta) \quad \text{where} \quad \beta = \frac{T_a(T_{ad} - T_u)}{T_{ad}^2}. \quad (4.28)$$

Equation (4.26) is the mathematical translation of what was anticipated in Section 4.3.1.4: the larger γ , the larger the intermediate regime. A further remark is that for typically-small values of r_λ , $\chi \sim 1/r_\lambda$ thus $\chi^{-1}/r_\lambda \sim 1$, meaning that the transition between these two regimes will occur at almost constant $r_{\dot{m}}$. At the limit, we have:

$$\gamma \frac{r_{\dot{m}}}{r_\lambda} \chi^{-1} = O(1) \quad \iff \quad \frac{r_{\dot{m}}}{r_\lambda} \chi^{-1} = O(1/\gamma), \quad (4.29)$$

where classically $1/\gamma \sim 1/\beta \sim 0.1$.

4.3.2.3. Comparison between the two classifications

The mathematical predictions of the resistive model from Section 4.3.2.2 are now compared to the classification of simulation points from Section 4.3.2.1. On Figure 4.5 are plotted the same data from Figure 4.3 in the space $(r_{\dot{m}}, r_\lambda)$ with various limit curves. The decoupled \rightarrow

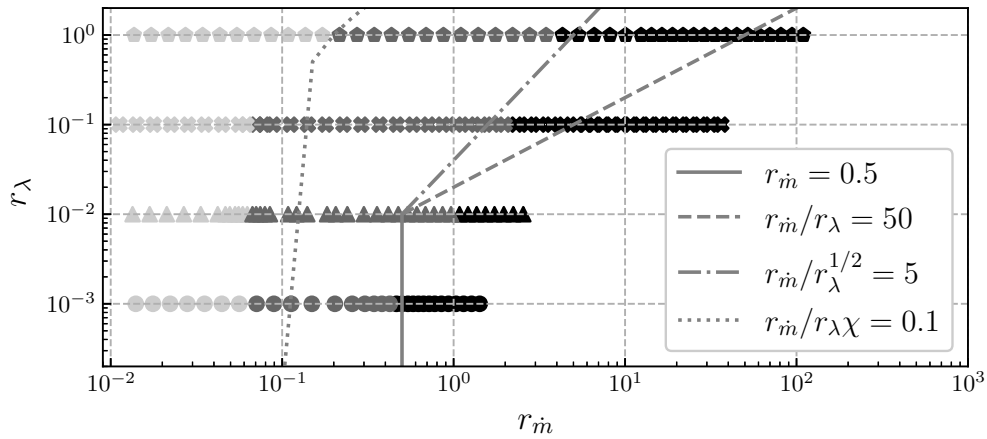


Figure 4.5. – Points of Figure 4.3 in the space $(r_{\dot{m}}, r_\lambda)$ and various mathematical predictions. Symbols: simulations (black: decoupled, medium grey: intermediate, light grey: hyperdiffusive). Methane-air, $\phi = 0.5$, single-step.

intermediate limit found in Chapter 1, shown on Figure 4.5, is recalled:

$$r_{\dot{m}} > 0.5 \quad \text{and} \quad \frac{r_{\dot{m}}}{r_\lambda} > 50. \quad (4.30)$$

The ratio $r_{\dot{m}}/r_\lambda$ was shown in Chapter 3 to be equal to $l_{\text{re-eq}}/l_{\text{diff}}$ in the decoupled regime, what governs directly the length scale separation of Equation (4.21). The raw limitation $r_{\dot{m}} > 0.5$ is more complicated to account for precisely using the resistive model. In Chapter 3 it constituted a

cut-off because (1) very small values of r_λ corresponds to very large preheating/superadiabaticity, which is not always attainable physically and might lead to other phenomena such as auto-ignition and (2) deviations from the asymptote at leading order in the decoupled regime are more pronounced. Interestingly, this cut-off is perceivable on Figure 4.5, further supporting the analysis performed in Chapter 3. Yet, by looking at Figure 4.5, it appears that the limit in $r_{\dot{m}}/r_\lambda$ tends to be overly restrictive. An observatory, alternative limit can be proposed:

$$\frac{r_{\dot{m}}}{r_\lambda^{1/2}} = 5. \quad (4.31)$$

The term $r_{\dot{m}}/r_\lambda^{1/2}$ was predicted by the resistive model, and also appears in the asymptotic developments of Appendix 4.A in Equations (4.45-4.47) through the product $(\chi - 1)\epsilon^2$. Since it corresponds to higher-order corrections of the decoupled regime, it is reasonable to think that it intervenes in the fine-tuning of regime discriminations. On the other hand, the transition to the hyperdiffusive regime seems to be reasonably caught by Equation (4.29), that is:

$$\frac{r_{\dot{m}}}{r_\lambda} \chi^{-1} = 0.1. \quad (4.32)$$

Notably, the predicted small dependency upon r_λ for small values is well observed. Although the limit curves do not perfectly match the numerical simulations (SIM), it can be argued that $r_{\dot{m}}$ and r_λ are good candidates to locate the transition between the regimes. Some of the reasons explaining the differences are (1) the classification of each solution point was fixed by a different method, namely through Figure 4.3, (2) the scaling laws used are not completely valid at the transition between regimes, and (3) the resistive model suffers from many assumptions, such as constant properties taken in the fresh gases. Note that the proposed classification, being based on dimensionless numbers, is assumed to be universal.

4.4. Detailed structure of the various regimes

More details on the flame structure in the different regimes are now provided. First, we investigate the idea that the presence of the porous matrix has an impact similar to a change in effective Lewis number. For that, internal flame structures are described for various interphase heat transfer intensities. Then, we attempt to clarify the so-called ‘‘broadening’’ of flames within porous media. Eventually, effects of equivalence ratio, fuel and complex chemistry are shown to have predictable influence on the flame structure and the transition between the regimes through the parameter γ .

4.4.1. Porous media as Lewis-changing devices

4.4.1.1. Equivalent gaseous equation

By using Equation (4.16) to replace the term $h_V(T_g - T_s)$ in Equation (4.15), we get:

$$\dot{m}c_{p_g} \partial_x T_g - \partial_x \left[\left(\lambda_g + \frac{1 - \epsilon}{\epsilon} \lambda_s \frac{\partial T_s}{\partial T_g} \right) \partial_x T_g \right] + \sum_k c_{p_{g,k}} J_k \partial_x T_g + \sum_k h_k \dot{\omega}_k = 0. \quad (4.33)$$

It is equivalent to a gaseous model of effective thermal conductivity:

$$\lambda_g^{\text{eff}} = \lambda_g + \frac{1 - \epsilon}{\epsilon} \lambda_s \frac{\partial \theta_s}{\partial \theta_g}. \quad (4.34)$$

Interphase coupling can therefore be interpreted in terms of additional thermal diffusion, proportional to the ratio of solid and temperature gradients $\partial \theta_s / \partial \theta_g$.

4.4.1.2. Effective Lewis number

In the gaseous phase, the traditional definition of the Lewis number for the fuel is:

$$\text{Le}_F = \frac{\lambda_g}{\rho_g c_{p_g} \mathcal{D}_F}, \quad (4.35)$$

where \mathcal{D}_F is the mass diffusivity of the fuel in the mixture. From Equations (4.33-4.35), we define the effective Lewis number of the coupled system, Le_F^{eff} , which depends on the temperature profiles θ_g and θ_s , so that:

$$\frac{\text{Le}_F^{\text{eff}}}{\text{Le}_F} = 1 + \frac{(1 - \epsilon)\lambda_s}{\epsilon\lambda_g} \frac{\partial\theta_s}{\partial\theta_g} = 1 + \frac{1}{r\lambda} \frac{\partial\theta_s}{\partial\theta_g}. \quad (4.36)$$

In the case $r_m \rightarrow 0$ (hyperdiffusive regime), $\theta_s \sim \theta_g$ thus $\partial\theta_s/\partial\theta_g \sim 1$: the change in Lewis number harmonizes spatially, and the equations boil down to an adiabatic laminar free-flame of increased thermal conductivity $\lambda_g + (1 - \epsilon)\lambda_s/\epsilon$. This equivalent flame, named Limit Hyperdiffusive Free-Flame (LHFF), is compared in Figure 4.6 to that of Figure 4.2(d). It is observed that the profiles match very well, confirming that the hyperdiffusive regime can be viewed as a flame of increased thermal conductivity.

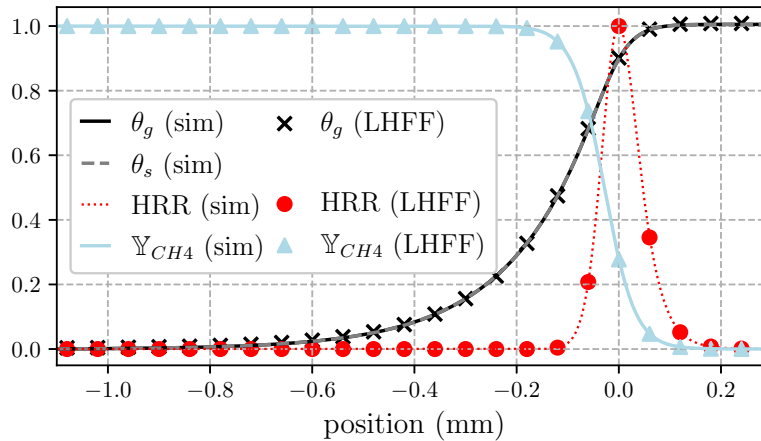


Figure 4.6. – Comparison between the hyperdiffusive flame of Figure 4.2(d) and its free-flame counterpart of increased thermal conductivity. Methane-air, single-step, $\phi = 0.5$.

Also, the effect of the effective Lewis number can be viewed directly in the space (\mathbb{Y}_F, θ_g) , in which only unity-Lewis number flames present straight lines. For the sake of brevity, this study is carried out in Appendix 4.C.

4.4.1.3. Lewis-changing effect at the flame front - (\mathbb{Y}_F, θ_g) space

The Lewis-changing effect is further illustrated in Figure 4.7, which shows structures of the adiabatic, LHFF, decoupled, intermediate and hyperdiffusive flames in the space (\mathbb{Y}_F, θ_g) . In this graph, it is textbook knowledge that unity Lewis numbers lead to similar fuel and energy equations, thus to unity slopes. In the decoupled regime, the flame structure is only shifted by a certain preheating temperature, showing a superadiabatic behavior. This confirms further that decoupled flames in porous media are simply preheated laminar flames. In the intermediate regime, the superadiabatic behavior is still visible, and a non-unity Lewis number effect

is perceived. In the hyperdiffusive regime, the flame structure is very close to the LHFF. In conclusion: with increasing heat transfer, the flame structure is first shifted upwards (preheating/superadiabatic effects) and then “rotated” anti-clockwise (Lewis-changing effect). Note that the smoothing after the preheating on the right of the plot is directly related to the transition to the hyperdiffusive regime, when interphase heat exchange meddles with the internal thermal-diffusive flame structure.

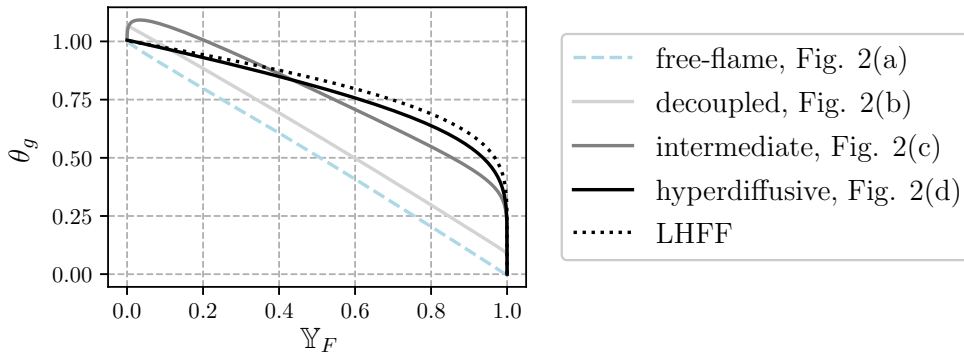


Figure 4.7. – Structure of the flames of Figure 4.2(a-d).

4.4.2. Broadening effects in porous media

There is apparent consensus in the literature [159, 191, 192, 231] that porous media combustion leads to broader profiles for gas temperature and reaction rate, compared to the adiabatic laminar free-flame. Put simply, profiles appear to be “smoothed” compared to the reference adiabatic laminar free-flame. Experimental measurements and 2-3D averaged numerical simulations also showed temperature profiles and reaction zones significantly broadened [235]. While the presents results, which concern 1D volume-averaged simulations, show a certain broadening in the hyperdiffusive regime (see Figure 4.2(d) and (h)), a shortening is rather visible in the decoupled regime (see Figure 4.2(b) and (f)). This indicates that broadening effects mostly have a multidimensional origin, not caught by the volume-averaging method. To the author’s understanding, the observed broadening should be carefully attributed to different, possibly concomitant phenomena: (1) the averaging of a convoluted flame front (geometry, hydrodynamics, dispersion), (2) the struggle of experimental apparatus to measure each phase individually and in a small region of space, (3) the gas/solid harmonization of length scales in the intermediate and hyperdiffusive regimes, and (4) concerning the reaction zone only, the increase in burning rate. While effects (1) and (2) are likely to be dominant in practice, effects (3) and (4) are the only ones caught by the present analysis.

4.4.2.1. Reaction length scale

We can try to understand effect (4) by studying the evolution of l_{reac} with integral properties of the solution. By integrating Equation (4.15), one finds:

$$\rho_u S_L^P \int_{\mathbb{R}^+} c_{p_g} \partial_x T_g dx + \int_{\mathbb{R}^+} \sum_k h_k \dot{\omega}_k dx = 0. \quad (4.37)$$

The reaction length scale can be retrieved by estimating roughly the integral of heat release for single-step as:

$$\int_{\mathbb{R}^+} \sum_k h_k \dot{\omega}_k dx \sim \text{cst.} \times l_{\text{reac}} e^{\beta(\theta_{\text{max,HRR}} - \theta_{\text{max,HRR}}^0)}, \quad (4.38)$$

where $\theta_{max,HRR}$ defines the gas temperature at the maximum of heat release. Intrinsically, Equation (4.38) can be viewed as the influence of superadiabaticity on the chemical time scale for a given convective flux. The arbitrary reference $\theta_{max,HRR}^0$ was chosen for convenience, since $\theta_{max,HRR} \rightarrow \theta_{max,HRR}^0$ for both the free-flame and the hyperdiffusive limit. This is supported by Figure 4.8(a), which shows the evolution of $\theta_{max,HRR}$ as a function of $1/r_{\dot{m}}$ for the different solution points. By combining Equations (4.37) and (4.38) and supposing the term $\int_{\mathbb{R}^+} c_{p_g} \partial_x T_g$ constant, we have:

$$l_{\text{reac}} \propto S_L^P e^{-\beta(\theta_{max,HRR} - \theta_{max,HRR}^0)}, \quad (4.39)$$

which, considered with and without porous medium (*i.e.* a free-flame where $S_L^P = S_L^0$), leads to the following relation:

$$l_{\text{reac}} = l_{\text{reac}}^0 \frac{S_L^P}{S_L^0} e^{-\beta(\theta_{max,HRR} - \theta_{max,HRR}^0)}. \quad (4.40)$$

Equation (4.40) can be ultimately simplified in the hyperdiffusive limit to the relation used in Section 4.3.2.2:

$$l_{\text{reac}} = l_{\text{reac}}^0 \frac{S_L^P}{S_L^0}. \quad (4.41)$$

Accordingly, Figure 4.8(b) shows the evolution of l_{reac} , flanked by the theoretical prediction of Equation (4.40). The behavior of the reaction zone thickness is qualitatively predicted. It is clear that a shortening of the reaction zone is predicted in the decoupled regime, while a broadening is visible in the hyperdiffusive regime.

4.4.2.2. Conclusion on broadening effects

Overall, it is only in the hyperdiffusive regime that a broadening of the reaction and diffusion length scales is predictable can be anticipated with the 1D volume-averaged equations. In the decoupled and intermediate cases, it depends on the predominance of either superadiabaticity, hyperdiffusion or flame acceleration. This stresses the necessity to discriminate properly between potential causes leading to a broadening of the flame front inside porous media.

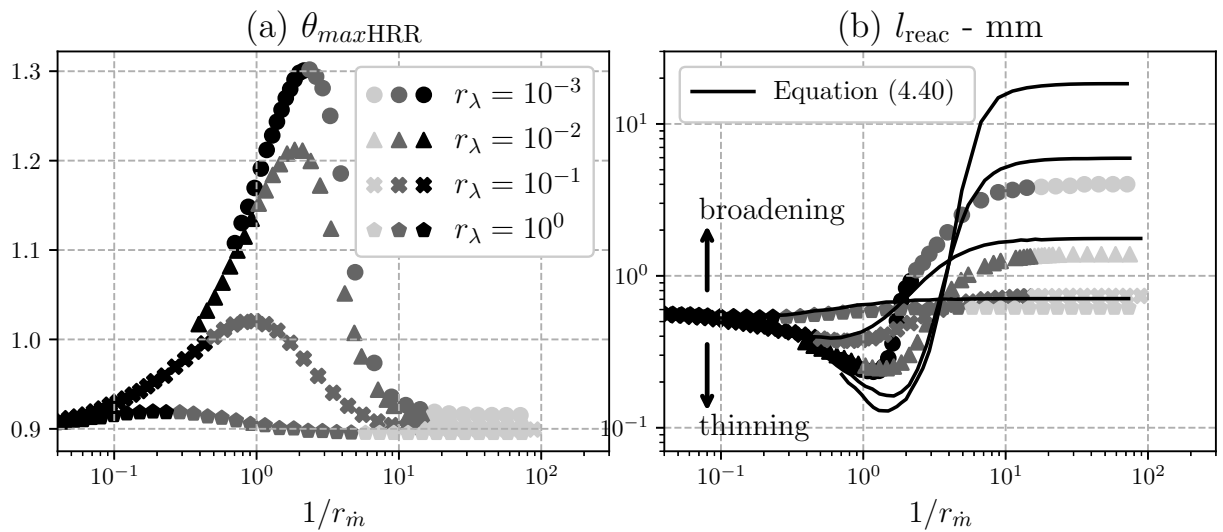


Figure 4.8. – (a) Temperature at the maximum of heat release rate. (b) Length of the reaction zone defined as the centered segment covering 80% of the integral of heat release rate. Large symbols: simulations. Small symbols: theoretical prediction.

4.4.3. Effects of equivalence ratio, fuel and complex chemistry

In the following, we explain how changes in equivalence ratio, fuel and chemical scheme influence (1) the extent of the intermediate regime and (2) the maximal superadiabatic temperature reached in the domain, both through the chemical stiffness of the mixture γ .

4.4.3.1. Effects of equivalence ratio

Figure 4.9 shows the maximum temperature obtained in the numerical solutions θ_{max} as a function of $1/r_{\dot{m}}$ for two equivalence ratios $\phi = 0.5$ and $\phi = 1.0$. The ratio of γ values for the two mixtures is also given in the caption. It is observed that a larger equivalence ratio leads to smaller superadiabatic values and a smaller γ . This effect can be understood by recalling the stiffer the mixture, that is, the larger γ , the more peaked the temperature profiles. This is because large values of γ correspond to the large activation energy limit, where a jump condition is valid at the scale of reaction: $\beta \sim \gamma = l_{diff}^0/l_{reac}^0 \rightarrow +\infty$. Since on the lean side (*i.e.* $\phi < 1$), β decreases with ϕ , it is therefore normal to find larger superadiabatic values for $\phi = 0.5$ than for $\phi = 1.0$. In general, maximal superadiabatic effects are expected at both ends of the flammability limits. At the same time, it is observed that the size of the intermediate regime increases with ϕ . Again it is directly related to the value of γ through Equation (4.29).

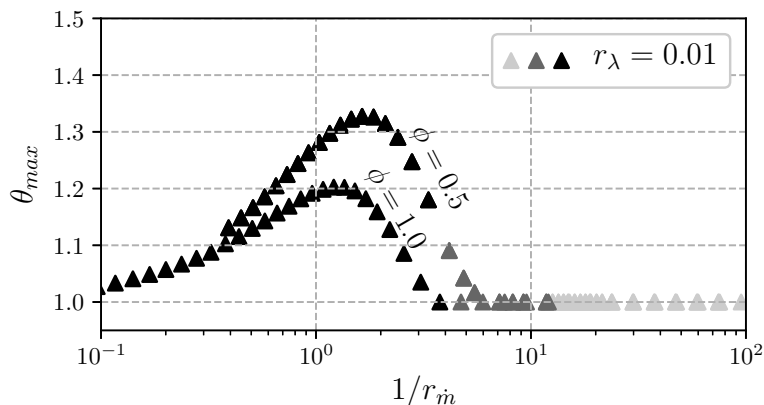


Figure 4.9. – Effect of equivalence ratio on the maximum temperature. Single-step, methane-air. The ratio of stiffnesses reads: $\gamma_{1S,\phi=1.0,CH_4}/\gamma_{1S,\phi=0.5,CH_4} = 0.61$.

4.4.3.2. Effects of fuel

Similarly, the effect of fuel can be understood by considering the relative values of γ . For a given equivalence ratio, different fuels present different activation energies (see Table 4.1) and different equilibrium temperatures. In turn, it influences directly β , therefore γ . This is illustrated in Figure 4.10, which compares θ_{max} for methane-air and hydrogen-air combustion. Again, the ratio of stiffnesses given in the caption shows that the larger γ , the smaller the superadiabaticity and the shorter the intermediate regime.

4.4.3.3. Effects of detailed chemistry

Detailed chemistry comes with an increased level of complexity. The local production and consumption of intermediate species can distribute heat release over larger length scales - sometimes so large that the flame in the porous medium does not present superadiabaticity. This feature was observed in the early work of Hsu and Matthews [230], and is particularly pronounced near

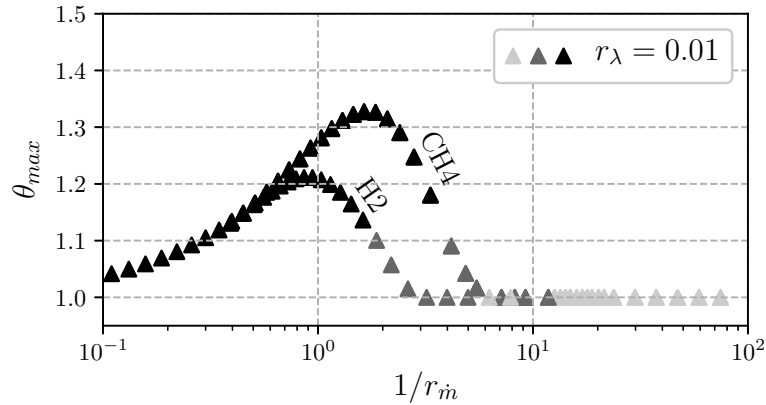


Figure 4.10. – Effect of fuel on the maximum temperature. Single-step, $\phi = 0.5$. The ratio of stiffness reads: $\gamma_{1S,\phi=0.5,H2}/\gamma_{1S,\phi=0.5,CH4} = 0.59$.

stoichiometry, for which the value of $\beta \sim \gamma$ is minimal [269]. Coherently, our investigations showed almost zero superadiabaticity for $\phi = 1.0$, methane-air and GRIMECH3.0 (not shown). Interestingly, a somewhat opposite phenomenon might appear on the rich side of hydrocarbon flames. For methane-air and $\phi > 1.4$, a successive combination of exothermic and endothermic reactions take place so that the adiabatic laminar free-flame presents a local superadiabaticity even without a porous medium [270]. This means that for a given γ , the maximal temperature might be slightly higher than its equilibrium value.

Yet, γ remains the major parameter driving superadiabatic properties. It is illustrated in Figure 4.11, which compares θ_{max} for single-step and complex chemistry (GRIMECH3.0). Again, the ratio of stiffnesses is provided in the caption. It confirms the trend concerning superadiabaticity. However, contrary to what is expected, the intermediate regime appears to be slightly broader. This is due to the fact that, albeit the existence of large length scales in the reaction zone, the majority of heat is released over a shorter one, delaying the full transition to the hyperdiffusive regime.

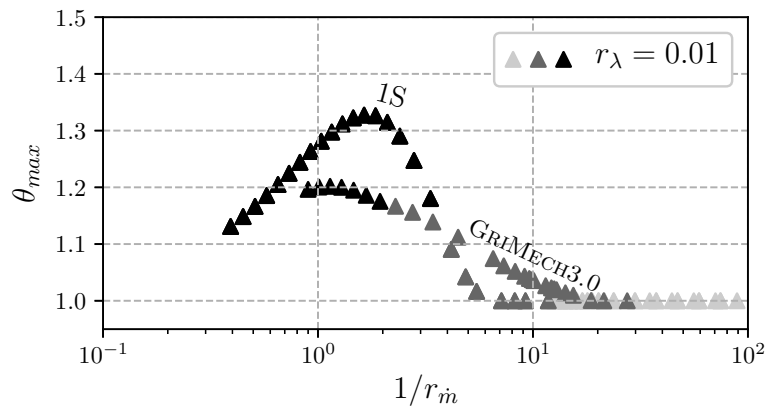


Figure 4.11. – Effect of reaction scheme on the maximum temperature. Methane-air, $\phi = 0.5$. The ratio of stiffness reads: $\gamma_{GRIMECH3.0,\phi=0.5,CH4}/\gamma_{1S,\phi=0.5,CH4} = 0.84$.

4.4.3.4. Conclusions on γ and further remark

The stiffness γ , related to the Zel'dovich number β , appears to be a useful parameter to assess the level of superadiabaticity of the solutions, and at least for single-step, the transition intermediate \rightarrow hyperdiffusive and thus the size of the intermediate regime. For detailed chemistry, due to the successive individual reactions (exothermic or endothermic, and to which extent), the parameter γ seems insufficient to characterize the fine transition intermediate \rightarrow hyperdiffusive and a case-by-case analysis is necessary. Note that γ is a concept more general than β , because β is not directly defined for detailed chemistry.

4.5. Generalized formulae for flame speed in all regimes

In this final section, we propose a formula for flame speed within porous media, based on the thermal model, which depends only upon $(r_{\dot{m}}, r_\lambda)$. It is intended to be valid in all burning regimes. It is based on the mathematical product between the acceleration due to preheating, denoted $F(r_{\dot{m}}, r_\lambda)$, and the acceleration due to hyperdiffusive effects, denoted $G(r_{\dot{m}}, r_\lambda)$, so that:

$$\frac{S_L^P}{S_L^0} = F(r_{\dot{m}}, r_\lambda) \cdot G(r_{\dot{m}}, r_\lambda). \quad (4.42)$$

In the decoupled regime, it is required that $G \rightarrow 1$ and similarly in the hyperdiffusive regime $F \rightarrow 1$. We now provide the forms for the functions F and G .

4.5.1. Flame acceleration due to preheating - F

The value of η_{rec} in the thermal model proved to be a very good sensor of preheating effects. As proposed in Chapter 3 the resulting flame acceleration can be modelled through an Arrhenius-like or exponent-like form:

$$F(r_{\dot{m}}, r_\lambda) = \exp\left[\frac{\beta \eta_{rec}}{2}\right] \quad \text{or} \quad F(r_{\dot{m}}, r_\lambda) = \left[1 + \frac{T_{ad}}{T_u} \alpha \eta_{rec}\right]^{n_T}, \quad (4.43)$$

where $\alpha = (T_{ad} - T_u)/T_{ad}$ and n_T is the exponent of temperature (typically $n_T \sim 1$).

4.5.2. Flame acceleration due to hyperdiffusion - G

Since the thermal model supposes $l_{reac} = 0$, it is intrinsically unable to catch the transition intermediate \rightarrow hyperdiffusive. It is therefore more complicated to obtain a good sensor of flame acceleration due to hyperdiffusion. A way around this problem is to consider the evolution of length scales within the solutions of the thermal model. The latter are carried by two positive eigenvalues λ_2, λ_3 for $x < 0$ and one negative λ_1 for $x > 0$, whose inverse moduli are related to the characteristic length scales of the flame structure through $l_i = \sqrt{(1 - \epsilon)\lambda_s/h_V/|\lambda_i|}$. As shows Appendix 4.A, the eigenvalues λ_i converge towards constants in the hyperdiffusive regime, which are fortuitously related to the theoretical prediction of speed-up $\sqrt{\chi}$. This invites to consider the following form for flame acceleration due to hyperdiffusion:

$$G(r_{\dot{m}}, r_\lambda) = \frac{\lambda_2 + \lambda_3}{\lambda_2^\infty + \lambda_3^\infty} = \frac{\lambda_2 + \lambda_3}{1 + r_{\dot{m}}/r_\lambda}, \quad (4.44)$$

where $\lambda_2^\infty = 1$, $\lambda_3^\infty = r_{\dot{m}}/r_\lambda$ are the eigenvalues in the decoupled limit $r_{\dot{m}} \rightarrow \infty$. As required, $G \rightarrow 1$ for $r_{\dot{m}} \rightarrow +\infty$ and $G \rightarrow \sqrt{\chi}$ for $r_{\dot{m}} \rightarrow 0$ with a transition occurring in the vicinity of $r_{\dot{m}} \sim 0.1$, typical of the hyperdiffusive regime. Albeit imperfect, the proposed form for G somewhat catches the convergence $\theta_g \sim \theta_s$, characteristic of the hyperdiffusive regime.

4.5.3. Validation of the formula

The analytical prediction of Equation (4.42) is plotted in Figure 4.12, along with the numerical simulations of the base case (methane-air, single-step, $\phi = 0.5$), for an exponent form for F with $\beta = 8$. The speed-up value of the LHFF flame computed with CANTERA is shown for comparison. It is observed that the formula gives correct results for rather large values of $r_\lambda > 0.1$, but is unable to catch properly the subtleties of the transition intermediate \rightarrow hyperdiffusive for smaller values. It is mostly related to the absence of a reaction length scale in the thermal model. Although imperfect, Equation (4.42) constitutes the first attempt to give a formula for flame speed in porous media valid in all regimes. Enhancing this prediction could be the topic of further work in the community.

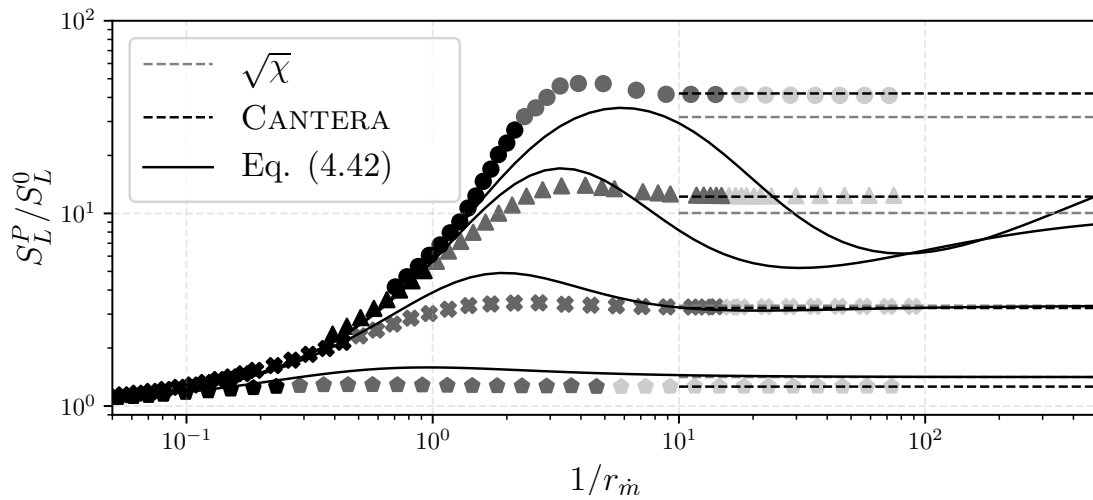


Figure 4.12. – Theoretical prediction of Equation (4.42) versus numerical simulations of methane-air, single-step, $\phi = 0.5$.

4.6. Conclusions of the chapter

By means of 1D numerical simulations and a simplified analytical model, a systematic study of the volume-averaged equations for flames in porous media was carried out for a very large spectrum of the dimensionless parameters $r_{\dot{m}}$ and r_{λ} . This analysis allowed to draw the following general conclusions:

- for increasing interphase heat transfer, flames in porous media present three distinct burning regimes, namely decoupled, intermediate and hyperdiffusive (Figure 4.2). They are defined by the increasing penetration of the length scale of interphase heat transfer into the flame front (diffusion then reaction). The decoupled regime presents simply preheated flames. The intermediate regimes shows strong superadiabaticity. The hyperdiffusive regime can be seen as flames of increased thermal conductivity, where a single-phase modelling is valid ;
- these regimes can be distinguished and characterized by using only the two parameters $r_{\dot{m}}$ and r_{λ} ;
- the heat recirculation via the solid matrix can be interpreted in terms of additional gas diffusion, which in turn changes radically the effective Lewis number;
- in the decoupled regime a thinning of the reaction length scale is observed, while a broadening is visible in the hyperdiffusive regime ;
- the ratio of diffusion to reaction length scales in the free-flame γ is a good indicator of the maximum superadiabaticity attainable in the domain and the extent of the intermediate regime. Note that for single-step, γ is typically of the order of the Zel'dovich number β .

Together with the conclusions of Chapter 3, it is worth emphasizing how remarkable are $r_{\dot{m}}$ and r_{λ} with regard to porous media combustion. Not only are they capable of predicting the transition between the various burning regimes, but they also contain information about flame speed: through $r_{\dot{m}}$ in the decoupled regime [214] and through r_{λ} in the hyperdiffusive regime. As a main limitation, this work supposes the volume-averaged equations valid as a starting point. Therefore, it cannot discuss directly when the presented regimes can be found in experiments. This stresses once more the need to conduct pore-level simulations to unveil the behavior of the flame near the reaction front. A phenomenological rule is that larger pores lead to lower interphase heat transfer and clear flame fronts lowly coupled to the wall, hence a decoupled regime, while smaller pores will lead to much greater interphase equilibrium and a hyperdiffusive regime. Since surface density increases exponentially with smaller pores, the transition between the two behaviors is expected to be sharp. Also, because the present framework is one-dimensional and adiabatic, it intrinsically cannot catch the 2/3D and non-adiabatic effects observed in some experiments. In such situations, $r_{\dot{m}}$ and r_{λ} obviously do not fully characterize the solutions: spatial anisotropies and affected temperature profiles are expected.

4.A. Approximations of the analytical model (AM)

4.A.1. Decoupled regime

We recall the definitions: $\varepsilon = r_\lambda/r_m$ and $\chi = 1 + 1/r_\lambda$. Asymptotically, the decoupled regime corresponds to the limit $\varepsilon \rightarrow 0$. This yields:

$$\lambda_1 = -1 - \frac{(\chi - 1)}{2}\varepsilon - \frac{(\chi - 5)(\chi - 1)}{8}\varepsilon^2 + O(\varepsilon^3), \quad (4.45)$$

$$\lambda_2 = 1 - \frac{(\chi - 1)}{2}\varepsilon + \frac{(\chi - 5)(\chi - 1)}{8}\varepsilon^2 + O(\varepsilon^3), \quad (4.46)$$

$$\lambda_3 = \frac{1}{\varepsilon} + (\chi - 1)\varepsilon + O(\varepsilon^3). \quad (4.47)$$

4.A.2. Hyperdiffusive regime

The hyperdiffusive regime corresponds to the limit $\varepsilon^{-1} \rightarrow 0$. This leads to:

$$\lambda_1 = -\sqrt{\chi} + \frac{\chi + 1}{4\chi}\varepsilon^{-1} - \frac{(\chi - 1)(\chi + 3)}{16\chi^{5/2}}\varepsilon^{-2} + O(\varepsilon^{-3}) \quad (4.48)$$

$$\lambda_2 = 0 + \frac{\chi + 1}{4\chi}\varepsilon^{-1} + \frac{(\chi - 1)(\chi + 3)}{16\chi^{5/2}}\varepsilon^{-2} + O(\varepsilon^{-3}) \quad (4.49)$$

$$\lambda_3 = \sqrt{\chi} + \frac{\chi - 1}{2\chi}\varepsilon^{-1} + 0 + O(\varepsilon^{-3}) \quad (4.50)$$

4.B. Criterium for regime discrimination of Figure 4.3

In this chapter, each regime is attributed a color through Figure 4.3. By noting speed-up values in a compact form as:

$$\Gamma_s = \frac{S_L^P}{S_L^0}, \text{ simulation} \quad \text{and} \quad \Gamma_t = \frac{S_L^P}{S_L^0}, \text{ thermal effect}, \quad (4.51)$$

as well as their converged value in the hyperdiffusive limit $h_V \rightarrow +\infty$:

$$\Gamma_s^\infty = \Gamma_s(h_V \rightarrow +\infty) \quad \text{and} \quad \Gamma_t^\infty = \Gamma_t(h_V \rightarrow +\infty), \quad (4.52)$$

we define geometrically simulation points in the decoupled regime by the first values for increasing interphase heat transfer verifying:

$$\left| \frac{\Gamma_s}{\Gamma_t} - 1 \right| < c_1. \quad (4.53)$$

Similarly the hyperdiffusive regime is given for points verifying:

$$\sqrt{\left(\frac{\Gamma_s}{\Gamma_s^\infty}\right)^2 + \left(\frac{\Gamma_t}{\Gamma_t^\infty}\right)^2} - 1 < c_2. \quad (4.54)$$

The constants used: $c_1 = 0.17$ and $c_2 = 0.55$ are necessary arbitrary, because providing objective boundaries for asymptotic regimes is not possible.

4.C. Flame structure in the space (\mathbf{Y}_F, θ_g)

Further insight on the internal flame structure can be gained by considering Figure 4.13, which shows the progressive flame structures from the decoupled to hyperdiffusive regime in the space (\mathbf{Y}_F, θ_g) , colored with reduced heat release rate (HRR). Three additional orientated curves monitor the first 20% and 80% of the integrated heat release rate, as well as its maximum, showing the progressive extension of the reaction zone. It is seen that the increase in diffusion in the flame front induced by hyperdiffusion shifts and extends the reaction zone towards the fresh gases. In the decoupled regime, the orientated curves travel upwards, showing that superadiabaticity is the leading-order phenomenon.

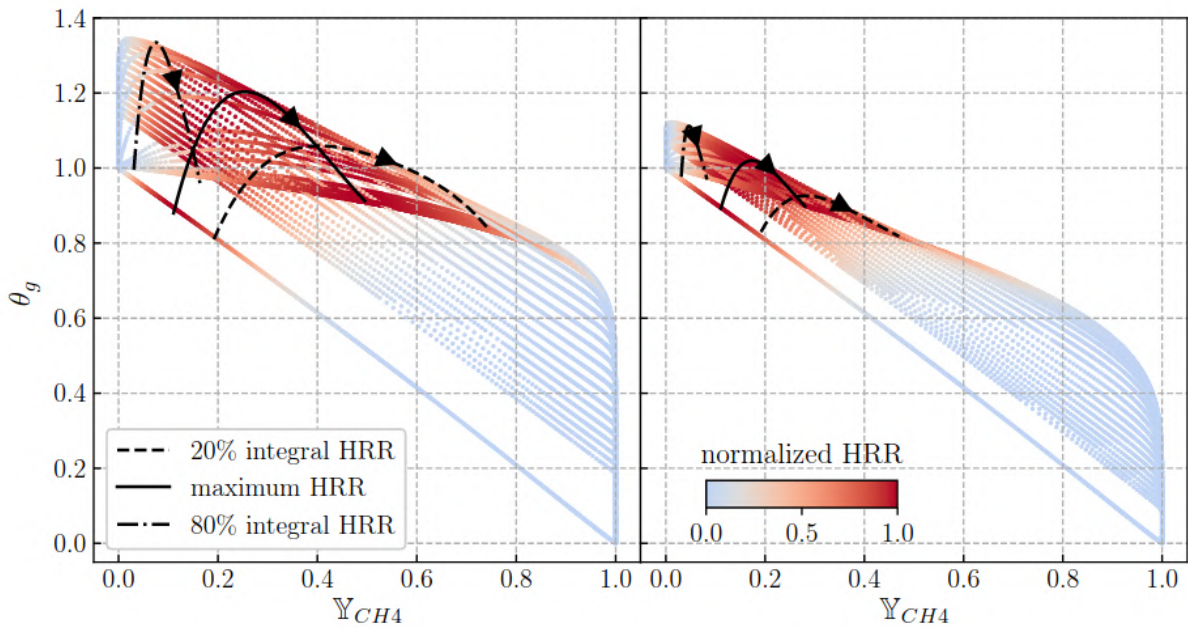


Figure 4.13. – Structures of flames including normalized HRR, methane-air, $\phi = 0.5$, single step, $r_\lambda = 0.1$.

It is also interesting to see the influence of the Lewis number of the mixture on such graphs, for which the free-flame does not present a straight line in the space (\mathbf{Y}_F, θ_g) . Notably, lean hydrogen-air flames are known to present strong below-unity Lewis effects (typically 0.3-0.4). In Section 4.4.1, we underlined the Lewis-changing capability of porous media through heat coupling. In the hyperdiffusive regime, *i.e.* for intense interphase heat transfer, the Lewis number of the mixture is multiplied by a factor close to χ , which can take very large values for small r_λ . This effect is illustrated in Figure 4.14, which shows the evolving structure of a single-step, hydrogen-air flame for increasing interphase heat transfer, with an equivalence ratio $\phi = 0.5$ and $r_\lambda = 0.01$ (*i.e.* $\chi = 101$). This yields a flame of effective Lewis number 30-40 in the hyperdiffusive regime. The decoupled regime with preheating is still visible (shift of the structure upwards) followed by a rotation which translates the harmonization of the Lewis increase across the flame front. In a word, Figure 4.14 shows how porous media modifies flames from below to well beyond unity Lewis number.

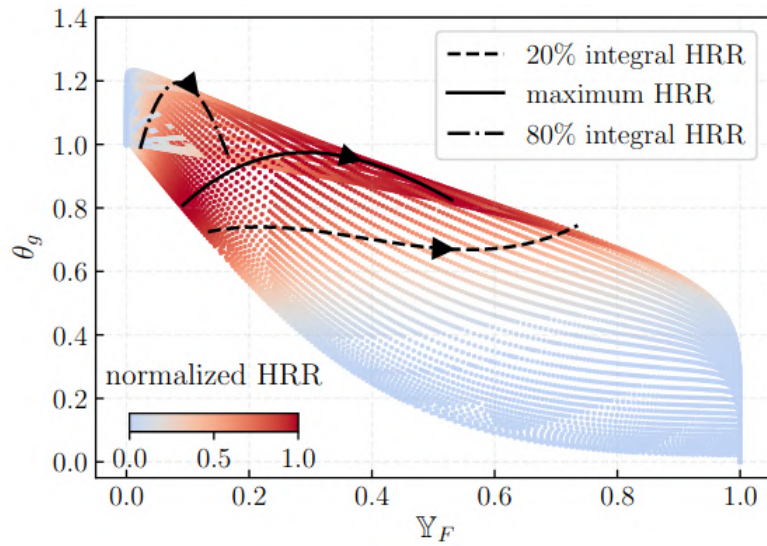


Figure 4.14. – Progressive structure of a lean hydrogen-air flame for increased heat transfer, including normalized HRR. Single-step, $\phi = 0.5$, $r_\lambda = 0.01$.

Towards high fidelity simulations of reacting fronts within porous media

In addition to the very large computational resources required to simulate porous media combustion at the pore level, the generation of both gas and solid meshes poses by itself a certain technical challenge. Notably, the non-analytical or implicit nature of the topology defining the gas/solid interface prevents the simple use of CAD and meshing commercial softwares, either because it is not possible to provide the geometry as an input or because the meshing algorithms often fail. In this section, we describe the general challenges associated to the simulation of flows within porous media, and describe technical solutions yielding working computational meshes. The geometries are obtained either from X-ray tomography of real silicon carbide foams used as porous burners, or generated analytically through Triply Periodic Minimal Surfaces (TPMS).

Overview

5.1. Meshing challenges	114
5.1.1. An issue common to the field of porous media	114
5.1.2. Specificities of porous media combustion	114
5.1.3. Specific case of this thesis	115
5.2. From porous foam to computational mesh	118
5.2.1. Constraints on the computational mesh	118
5.2.2. Step 1: scanning of an actual burner	118
5.2.3. Step 2: 3D voxels filtering	118
5.2.4. Step 3: STL generation and meshing strategies	120
5.3. Generation of lattice-based porous media	124
5.4. Conclusions of the chapter	125

“Not all of us can do great things. But we can do small things with great love.”

MOTHER TERESA

5.1. Meshing challenges

5.1.1. An issue common to the field of porous media

Among the plethora of literature addressing general physics in porous media, published studies on pore-level direct numerical simulations remain rather scarce. This can be explained by several independent reasons:

- first is that most systems of interest are simply too large to be simulated on a machine with sufficiently good resolution - even on very large clusters. For instance, the domain of interest for the study of soil infiltration (aquifers, oil reservoirs) may reach several kilometers in size with pore sizes remaining centi-to-millimetric [271, 272]. In such situations, even low-order models may require heavy parallel computations [273] ;
- second is that even for smaller systems being a few pores wide, the presence of high levels of turbulence or stiff chemical reactions may require cell sizes so small (in combustion, typically 10-100 μm), that the resolution of systems beyond a few centimeters wide becomes prohibitive ;
- the geometrical representation of the interstitial gas/solid interface requires exponentially large information for decreasing pore size. In this thesis even relatively moderate geometries could weight several Gb. on a hard drive just for the surface representation - so one can easily imagine that for fibrous porous media a computation over sufficiently large macroscopic length scales is still out of reach - unless the geometry be viewed in terms of 3D voxels, as adapted to LBM simulations ;
- simultaneously, a good representation of the fluid/solid interface may require very small edges sizes locally. This issue is typically exacerbated for packed beds of individual elements which necessarily show infinitely sharp contact angles (tengencies) and must be handled, regarding numerical stability issues and direct influence on the time step which is governed by the smallest element in the domain. As illustrated in Figure 5.1, extracted from the works of Yakovlev and co-workers [137], the contact angle between two spheres requires special treatment, and special wrap algorithm was developed on purpose for their simulation of combustion within the porous medium. Such operations are not free of physical implications, since they show that the geometrical modification has significant influence on the porosity thus velocity profiles, and radiative heat fluxes.

5.1.2. Specificities of porous media combustion

Due to the stiff chemical reactions occurring in the gaseous phase, a very small edge size is required in the reaction zone. Typically, since flame thicknesses at ambient conditions are of the order of 0.2-2 mm, supposing at least 10 points throughout the flame requires edge sizes between 20 and 200 μm . In addition, since it is not possible to know *a priori* where the flame will stabilize, a large portion of the fluid must be sufficiently refined. An adaptative mesh refinement technique may be used, but it would also require substantial computational cost. What is more, it is not always possible to choose the cell size locally, partly due to the mesh generation process itself but also due to the small features of the gas/solid regions and their interface which cannot

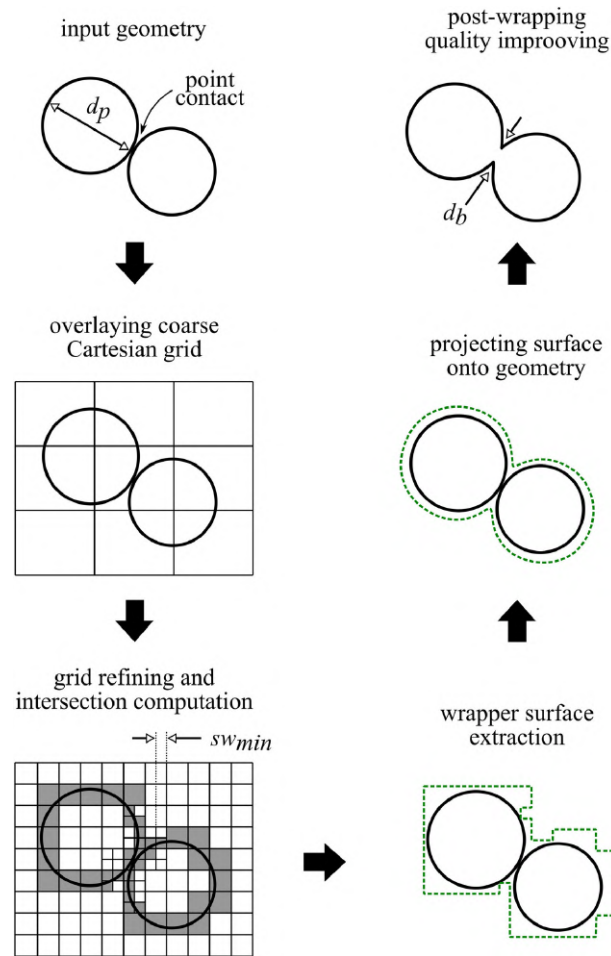


Figure 5.1. – From [137]: illustration of the pre-processing wrap algorithm used to manage the contact point problem for a finite-volume numerical simulation of porous media combustion, in the case of packed bed of spheres.

be easily avoided nor removed. Also, a correct computation of the interphase heat transfer at the wall and within the interstitial flow requires rather small cell sizes anyways (typically $100\ \mu\text{m}$, as observed in the literature and in some initial test in heated 2D channels).

5.1.3. Specific case of this thesis

In this thesis, both combustion of methane and hydrogen in air are addressed. The two reference equivalence ratios considered for mesh convergence study are $\phi = 0.72$ for methane and $\phi = 0.38$ for hydrogen. We may use leaner mixtures for hydrogen in Chapter 7, but since leaner flames present a larger spatial extension, the presented reference cases are sufficient to assess which mesh size is required to compute properly the flame fronts in our simulations. Figure 5.2 presents a 1D convergence study performed with CANTERA and AVBP softwares, based upon adiabatic laminar flame speed computations on a regular grid of spacing Δx . The same transport properties are used in both codes so that they resolve the same equations, with the exception of isobaric and no viscous heat production hypotheses in CANTERA. Note that the discrete operators are different in the two codes, and in the instationary code AVBP the flame speed is computed by following the flame front in a long 1D domain. In porous burners, since the flame is preheated, two unburnt temperatures are considered: $T_u = 300\ \text{K}$ and $T_u = 600\ \text{K}$. Overall, it is observed that a resolution of $80\ \mu\text{m}$ is sufficient to get an error on flame

speed below 3%. It is checked *a posteriori* that at least in each case the species, temperature and heat release profiles sufficiently sampled. In 3D, due to the effect of dimensionality of the elements, it is common to assume that the chosen resolution should be sufficient for DNS. In Table 5.1 are listed a series of DNS related to porous media combustion found in the literature, with afferent modelling assumptions and typical edge sizes. Most of the time, no study of convergence of the burning rate of the flame fronts are carried out and only integral properties such as volume-averaged velocity profiles, or maximum temperature in the domain are assessed to check convergence. In the author's viewpoint this is partly insufficient, because combustion fronts require low edge sizes. Also, often there are lots of points near the boundaries and fewer at the core of the pores. This is problematic because this may hamper the resolution of the fronts and perform, unknowingly, a filtration on the equations so that some studies presented as DNS may in fact be hidden LES (see some studies of mesh sizes larger than 200 μm . Other comments may be given upon the various studies performed in the literature, but these will be commented upon in Chapter 6.

To conclude, in this thesis work, the baseline resolution adopted is uniform, 80 μm .

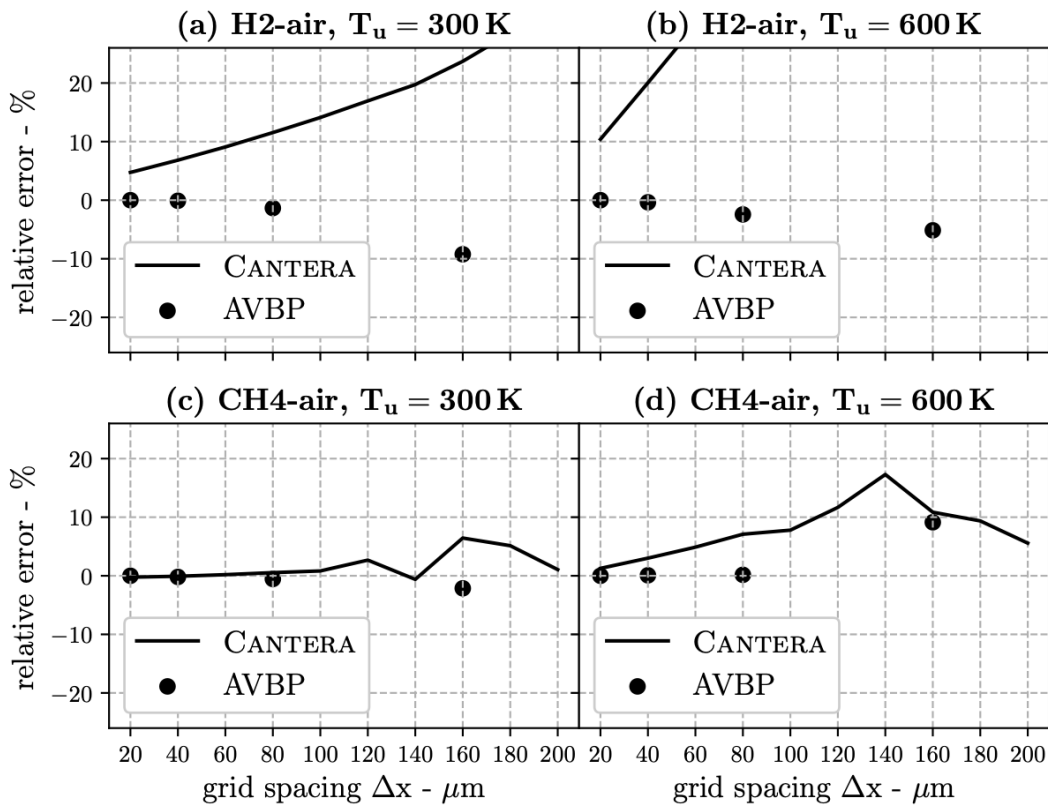


Figure 5.2. – Mesh convergence study for methane-air ($\phi = 0.72$) and hydrogen-air ($\phi = 0.38$) flames, with CANTERA and AVBP.

Table 5.1. – Literature review of 3D DNS for porous media combustion.

Ref.	Study	Fuel	Complex kinetics	Cell size	Domain size (mm)	Agreement with VAM	Radiation
Yakovlev et al. [137]	Unsteady packed-bed combustion	CH4	Yes	< 500 μm	35x35x100 (4.4 pores wide)	Not compared	Yes (gray)
Bedoya et al. [136]	1D models vs. 3D DPLS	CH4	No	160 μm	divergent 65x(inlet: 1.125x9 – outlet: 28x9)	No	No
Billerot et al. [274]	Steady combustion of lattice-based porous media	CH4	No	40 μm	42.5x1.2x1.2	No	Yes (gray)
Liu et al. [275]	2D two-layered packed-bed combustion	CH4	No	> 200 μm	5x140	Not compared	Yes (gray)
Dixon [276]	3D packed-bed steam reforming homog./heterog. rea.	CH4	No	>1200 μm	cylinder 650x150	No (underlined)	No
Hackert et al. [277]	2D bundle of tubes + discrete plates with/out heat losses	CH4	No	40 μm	20x10	Reasonable	Yes
Yamamoto et al. [278]	3D particle-laden medium regeneration process of diesel particulate filter	soot	No	250 μm	50x10x10	Not compared	No
Jouybari et al. [279]	2D RANS study staggered arrangement of square rods	CH4	No	N.A.	100x2.5	No	No
Sarhaoui and Kaviany [194]	1D VAM vs. 2D DNS staggered arrangement of square rods	CH4	No	N.A.	5x1.5	Reasonable	No
Shi et al. [280]	1D VAM and 3D DNS packed bed reactor filtration combustion	CH4	No	\sim 500 μm	cylinder 353x38	Yes (filtration)	Yes
Sirotkin et al. [281]	2D packed bed SPH method filtration combustion	CH4	No	160 μm	40x20	Not compared	No
Ferguson et al. [282]	2D packed bed Delaunay network for solid heat transport	CH4	Yes	<100 μm	40x20	Not compared	No

5.2. From porous foam to computational mesh

Obtaining a computational mesh for a reticulated foam is not a straightforward task. The associated technical difficulties may partly explain why only a few 3D numerical simulation were performed in such geometries. In this work, it is chosen to start from the X-ray tomography of a silicon carbide foam used in a real porous burner for experiments at IMFT. Figure 5.3 presents the main steps yielding a computational mesh, which are now described in detail.

5.2.1. Constraints on the computational mesh

The wanted computational mesh is composed of two distinct and complimentary meshes: one for the fluid region and one for the solid region. They must follow a series of constraints:

- **C1:** they must present plane outer boundaries, one for the inlet, one for the outlet, and sides on which symmetry conditions will be applied (the side symmetries are meant to simulate an infinite medium, so the boundaries of the scanned domain must be cropped) ;
- **C2:** the cropping procedure must not yield too small or sharp regions which would result in tiny elements. In general, the fluid and solid phases must not present features of the order or smaller than the edge size ;
- **C3:** the solid and fluid regions must both be related fields (*i.e.* each phase must consist of a single body), so as to avoid lonely regions ;
- **C4:** the gas and solid meshes must be coincident thus of similar edge sizes locally at the gas/solid interface.

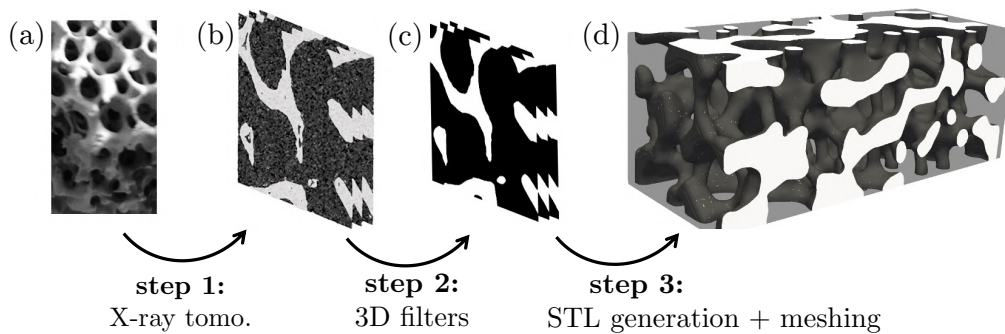


Figure 5.3. – From porous foam to computational mesh.

5.2.2. Step 1: scanning of an actual burner

Because the numerical generation of a reticulated topology is a challenge on its own, it was chosen to make use of an existing porous burner. A sample of silicon carbide reticulated foam (see Figure 5.3(a)) was scanned by X-ray tomography with the device EasyTom XL at IMFT. The samples measured approximately $20\text{ mm} \times 20\text{ mm} \times 20\text{ mm}$. A maximal resolution of $17\mu\text{m}$ was achieved, what is largely sufficient to catch the finest details of the porous matrices for typical pores densities of 30 and 60 PPI. The scanning procedure yields a 3D table of voxels in absorption levels (see Figure 5.3(b) and a typical example in Figure 5.4).

5.2.3. Step 2: 3D voxels filtering

General properties of the scans: as shown in Figure 5.4, the voxels array in absorption levels seemingly presents two main phases, one in grey identified as the solid region (strong

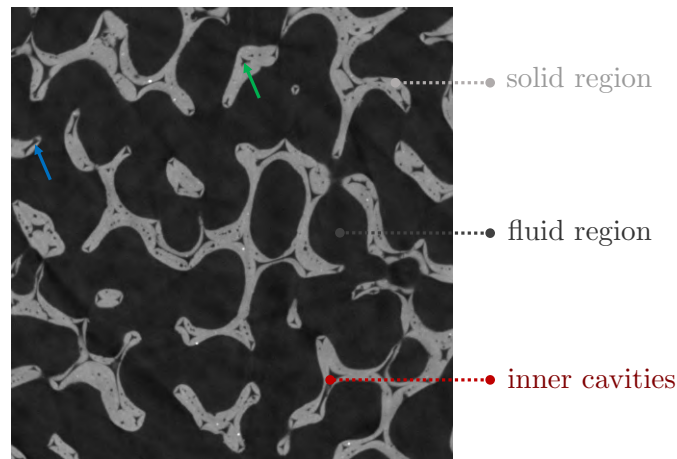


Figure 5.4. – Example of tomographic image of a 30 PPI foam. Note the presence of inner cavities inside the solid. Green arrow: closed cavity. Blue arrow: open cavity

absorption) and one in dark grey/black which corresponds to the fluid region (weak absorption of air). Due to the manufacturing process, the solid region is not perfectly homogeneous and presents small, lighter inclusions. Also, the fluid region is not perfectly homogeneous - due to some reconstruction artifacts (internal diffusion, numerical inversion errors, etc.). Increasing the number of scanning angles may reduce them, but here they are sufficiently low.

The problem of internal cavities: due to the sintering process, the solid matrix presents sharp-cornered holes throughout its mid-sections. Since the shape of these inner cavities would require overly small mesh size and mainly contain inert fluid, they must be removed. Of course, this operation changes the final porosity of the matrix (approximately -10%). Also, one should keep in mind that these inclusions do play a role in the real behavior of the burner. Heat conduction through the solid matrix is modified by these cavities, because heat has to travel through small gaseous layers which act locally as thermal insulation. Concerning radiation, it is expected that more inclusions increase optical thickness.

3D filters: constraints C2 and C3 may be fulfilled by applying a series of filters on the 3D voxel array obtained by X-ray tomography. Ready-to-use filters may be found in the libraries `NDIMAGE` [283] and `SCIKIT-IMAGE` [284]. In order to illustrate the methodology used in 3D, Figure 5.5 shows the intermediate steps after each of these filters on a slice. Starting from the initial scanning array (a), the image is first binarized to differentiate the fluid and solid regions. The resulting image (b) presents the spurious internal cavities, which can be partly removed by finding the largest fluid region and defining the solid as the complementary region. Note that in 2D, this step makes no sense so the 3D information is required. Finding the regions is easily achieved by a flood-fill algorithm. This procedure yields (c), which still presents some inclusions that are connected to the fluid region. To remove them, it is chosen to apply a binary closing filter of a given size that allows to fill the small passages near the solid boundaries. The closing filter may be viewed in terms of a successive dilatation then erosion of the given size¹. This step yields (d), where inner cavities of size larger than the closing filter are still found. Supposing that all the passages at the boundaries were properly closed (in practice they are very small), then the procedure (b) \rightarrow (c) can be repeated to yield the final image (e), thereby enforcing constraint C3. A comparison between the initial scan (a) and (e) is given in (f), and shows a very good modelling of the actual geometry of the burner. However, the series of filters and

1. see [https://en.wikipedia.org/wiki/Closing_\(morphology\)](https://en.wikipedia.org/wiki/Closing_(morphology))

operations (a) \rightarrow (e) do not prevent from small features in both phases (constraint C2). This can be fixed by making case-by-case use of gaussian/median filters + re-binarization to discard small features within the phases, but also by applying successive use of closing filters until the local thicknesses fall above a prescribed threshold. In such cases constraint C3 is again enforced afterwards. Although it was possible to write a general script encompassing all those steps the variety of meshes geometries suffers from some degree of hand-tuning.

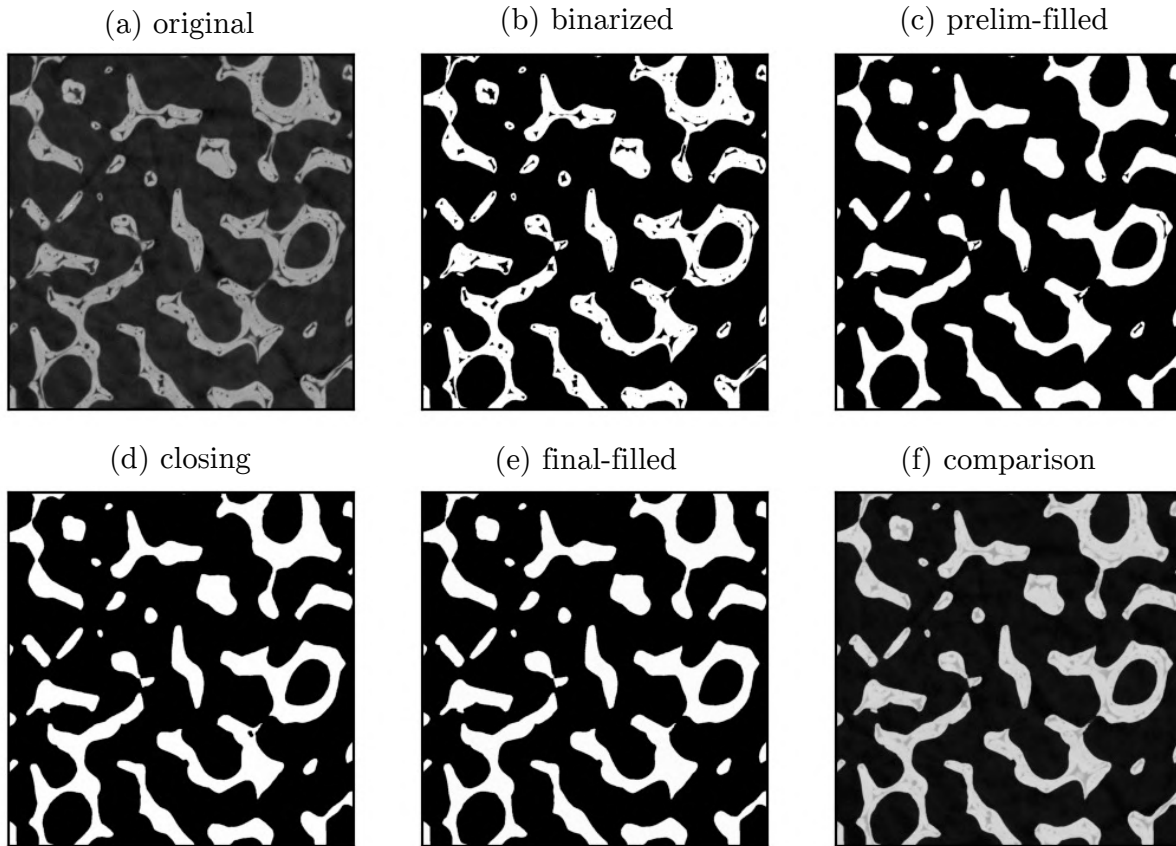


Figure 5.5. – Voxel treatment. From tomographic slice to final domains (a) \rightarrow (e). Comparison between (a) and (e) shown in (f).

5.2.4. Step 3: STL generation and meshing strategies

5.2.4.1. STL generation

From the filtered, binarized 3D voxel array, a “smooth” surface geometry must be generated, yet with plane boundaries on the sides and inlet/outlet regions (constraint C1). The very common STL format is used for surface representation (triangle-based). It is chosen to generate the surface of the fluid region first. Because the development of a specific surface generation tool may be in itself a vast field of research, it is chosen to make use of existing tools in that area. Fortunately, it turns out that in medical science the rendering of voxelized 3D images from MRI/X-ray scans into 3D surface models for visualisation, diagnosis and simulation is common practice. In this line of thought, the tool DICOM2STL [285] from the National Institute of Allergy & Infectious Diseases (NIAID) is used. It is based on a *marching cubes* algorithm, *i.e.* a program which first meshes the (embattled) threshold region between the two phases at the scale of the voxel. Then, various local smoothing filters and simplifications are applied in a tailorable fashion, yielding a smooth representation of the fluid-solid interface. This tool,

however, does not provide plane surfaces as an output on the sides and at the inlet/outlet, because the smoothing is homogeneous. **This means that the STL must be cropped afterwards** to ensure constraint C1. So as to retain the integrity of the initial geometry as well as possible, and to follow constraints C2+C3, an artificial (reflecting) padding on the 3D voxel array is applied on the side boundaries before the STL generation. Also, so as to create inlet and outlet fluid regions, some paddings are also applied longitudinally. Figure 5.6(a) illustrates this padding (sides: green arrows, inlet/outlet: red arrows). Figure 5.6(b) illustrates the geometry after the final cropping, applied using the famous software BLENDER (*object mode* \rightarrow *boolean operation* \rightarrow *difference*). Though the differences between Figures 5.6(a) and (b) are not visually obvious, only (b) is suitable for meshing and numerical simulations. The complimentary solid phase may be defined formally by another boolean operation, but unfortunately in BLENDER for technical reasons it does not work. So the method used in this thesis was to remove the plane boundaries from Figure 5.6(b) and then fill manually the complimentary boundaries. The procedure is illustrated in Figure 5.7.

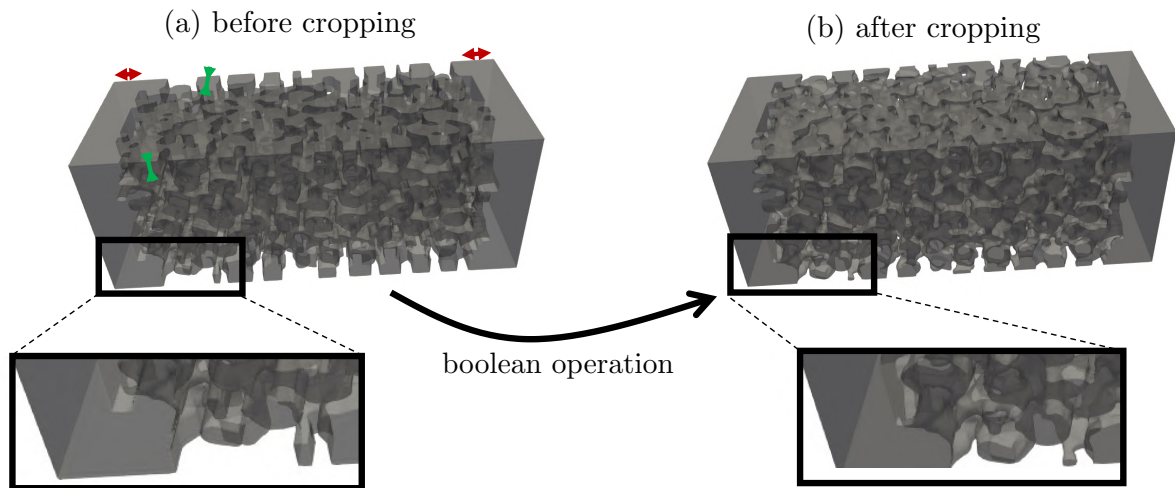


Figure 5.6. – Artificial padding of the fluid domain (a) then cropping (b). Green arrows: side padding. Red arrows: inlet and outlet padding.

5.2.4.2. STL topological cleaning

Before moving on to the meshing itself, a certain topological cleaning of the STL surfaces must be performed. Indeed, although constraints C1-C4 are enforced, the steps described above do not guarantee the fundamental property required for a surface+volume meshing, that is, **a correct STL topological connectivity**. The STL format consists in a series of nodes and triangles. For the surface to be “meshable”, it must be mathematically *manifold*, that is, the triangles must be correctly-connected, without holes on the surface, and defined in a unequivocal fashion. Problems encountered are illustrated in Figure 5.8. In topological terms, this implies that:

- **Man1:** each node and triangle must be unique ;
- **Man2:** each triangle must have strictly positive surface ;
- **Man3:** each triangle must exactly have three neighbors.

Unfortunately, these properties are not ensured from the various operation performed in BLENDER (boolean cropping, filling, etc.). Also, even before these operations the script DICOM2STL is not always conservative, especially due to a necessary simplification step. Additional difficulties lie in the fact that some of these issues may fall within threshold detection and, whilst not visible

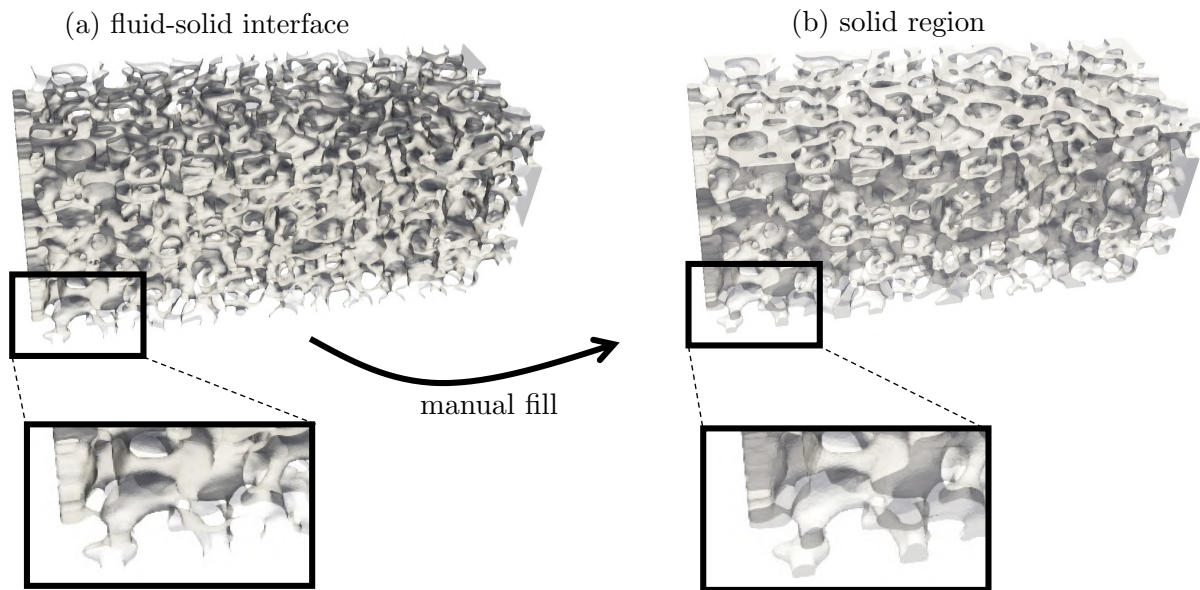


Figure 5.7. – Construction of the solid phase from the fluid-solid interface (a) then filled manually with BLENDER (b).

to the eye, do not allow to proceed to the final meshing steps (or yield elements very distorted). This is why a **cleaning operation** must be carried out. There exists automatic cleaning scripts in the softwares MESH LAB, MESH MIXER or BLENDER, but these do not necessarily enforce the properties $\text{Man1} \rightarrow \text{Man3}$ and they fail given the variety of issues encountered and the complexity of the mesh. A vast majority of the problems are found at the mesh boundaries, near the sharp edges, and arise from the cropping procedure. These issues can be fixed manually in BLENDER, in *edit mode*. We now provide very technical tips to fix these issues, which may be of use for future researchers.

Detecting topological issues: in the *3D printing* panel (must be enabled first in the settings) click *check all* to see all the degenerated nodes, edges, and surfaces, holes, triangles without neighbors, etc. This panel does not directly detect problems with $\text{Man1} \rightarrow \text{Man3}$ but they hint towards “weird” regions which may be problematic. Notably, considering Figure 5.8(a): *non-manifold edges* hint towards the geometrical defects ; *zero faces / zero edges / thin faces* hint towards degenerated geometry. The wrong number of neighbors is more complex to investigate, so a general cleaning of the edges may be necessary. Tip: click on the results to see issues by individual type on the mesh, but beware: because edges and surfaces are often hard to see, switch to node view to see them more evidently.

Fixing topological issues: depending on the situation, mesh, etc., various healing procedures may perform better than others. Also, because healing is applied with a threshold, a certain degree of generality cannot be given here. Nonetheless, for problems situated at the boundaries, here are some tips: select the problematic nodes through the *3D print* panel then switch to node view (alternatively, select all the sharp edges directly with *select* \rightarrow *by: sharp edges*). Then click *select* \rightarrow *more* 2-3 times to “thicken” the selection. This thickening allows to use the local geometry for cleaning. Then, click *mesh* \rightarrow *cleanup* \rightarrow *degenerate dissolve* or *limited dissolve* or *decimate geometry*. The filter *degenerate dissolve* tendentially removes the small, useless geometry. *limited dissolve* simplifies the surface by finding locally larger surface polygons - which also tendentially removes non-manifold geometry (hence the need to thicken

the selection first). *decimate geometry* simplifies the mesh, but be careful, this may destroy the geometry. Each of these filters depend on a given threshold which must be specified. Tip: note that in general, BLENDER is adapted to object sizes of the order of 1-100 units, so one may consider to resize temporarily the meshes otherwise the thresholds may fall within numerical error.

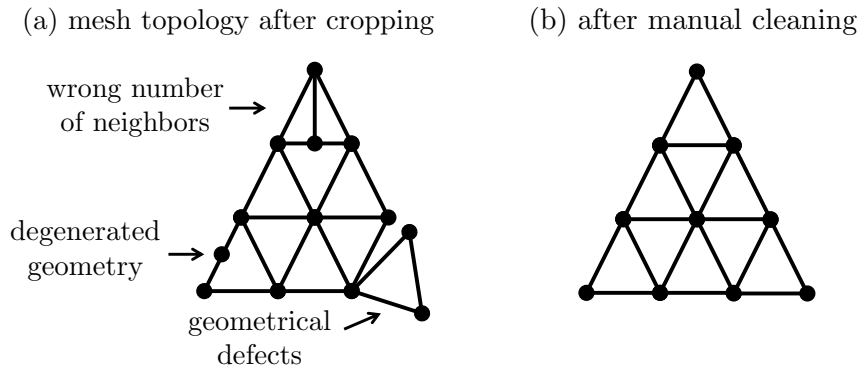


Figure 5.8. – Topological problems on the STL generated.

5.2.4.3. Meshing strategies

Now that STL surface geometries are clean and topologically-correct, one only needs to mesh the surface and the volumes. Note that, with the present coupling strategy in the codes AVBP and AVTP, the mesh nodes do not need to be exactly coincident. However, the mesh sizes must be comparable to avoid conservation errors. There exists a methodology to create perfectly-fitting meshes, but this requires more technical steps with little advantages (because for mesh size control afterwards relaxing the exact geometry of the interface is necessary). Two meshing strategies were considered in this thesis and are now described.

NetGen: this free meshing software is capable of meshing geometries of arbitrary shape, thanks to frontal 2D and 3D meshing algorithms. Interestingly, NETGEN is capable of detecting “independent” boundary regions (future patches of the domain) based on an edge threshold detection. This requires perfect topology - unless which this detection fails and meshing is made impossible - hence the above cleaning procedure. A difficulty is that the edge detection is based upon two threshold parameters (angle + arc length) which may not be applicable over the entire mesh. This often results in impossible simultaneous detection of all the boundaries, because the boundary angles may span over large values due to the plane cuts on the sides. One solution is to increase the padding of the 3D voxel array so that the cutting is done over a region almost uniform, leading to near 90-degrees boundary angles. Over time, in this thesis work NETGEN was abandoned to another strategy.

MMGS/MMG3D + GMSH: the MMG softwares offer a series of remeshing features for 2D and 3D meshes upgrade. They are developed by INP/INRIA/UBordeaux/UPMC [286, 287] and popular among the industry and research. GMSH is a 3D finite element mesh generator with built-in pre and post-processing facilities [288]. Together, these softwares can be used to generate the final computational mesh from the cleaned STL:

- convert the STL geometry to *INRIA .mesh* format by using GMSH ;
- remesh the surface of the STL with MMGS with a rough mesh size. A low threshold value for angle (*-ar* option) may be selected first to avoid issues (typical values 5-20

degrees). This operation may be performed several times by increasing iteratively the angle threshold² ;

- then remesh the surface with the target mesh size ;
- open the resulting surface mesh in GMSH and create the volume mesh by selecting *geometry* → *elementary entity* → *add* → *volume*, then *mesh* → *3D* ;
- the mesh may be further improved by using MMG3D, with various target optimizations adapted to DNS computation (deletion of small-volume elements, skewness weighting, etc.).

Now contrary to NETGEN the individual patches defining the various regions must be created. This is achieved by an in-house script which changes the boundary labels in the mesh file (to that end the format *GMSH version 2 ASCII .msh* turned out handy). Eventually, GMSH may be used to convert the final meshes into any favorite numerical software. Figure 5.9 shows an example of computational mesh.

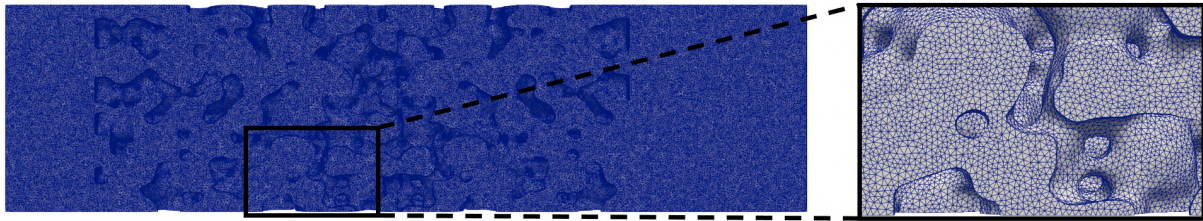


Figure 5.9. – Example of computational mesh for a 60 PPI foam, mesh size 80 μm .

5.3. Generation of lattice-based porous media

In the previous section, the computational mesh was generated from a real sample of reticulated, “random” porous foam. Although this type of burner was used extensively in the literature, it may not be suitable for applications where the internal combustion processes must be controlled exactly. If the burner geometry depends on the manufacturing process, it is therefore not excluded that system failure is reached for particular local structural arrangements. In that line of thought, a new type of tailorable, lattice-based porous burner was proposed recently by Sobhani and co-workers [154]. By using the framework of triply-periodic minimal surfaces [289, 290], a porous matrix may be generated. For a given external boundary, minimal surfaces may be defined as the surface obtained by a thin soap film of equal pressure on each side, leading to a mean-zero-curvature surface of minimal area [291]. TPMS are interesting because they offer high surface-to-volume ratio with self-supported pore connectivity by construction. Original fields of applications include bio-medicine [292] and solar cells [293]. There exists several types of minimal surfaces, the most famous being the *gyroid* and *diamond* structures. Mathematically, they are defined in reduced space as:

$$\textbf{Gyroid: } \cos(x)\sin(y) + \cos(y)\sin(z) + \cos(z)\sin(x) = 0 \quad (5.1)$$

$$\textbf{Diamond: } \sin(x)\sin(y)\sin(z) + \sin(x)\cos(y)\cos(z) + \cos(x)\sin(y)\cos(z) + \cos(x)\cos(y)\sin(z) = 0. \quad (5.2)$$

2. Tip: if the initial STL cleaning is incomplete, errors of the type “*flattened angle around ridge*” may appear, or the remeshing may fail entirely (too bad elements). In that situation either use BLENDER directly again or use the output mesh of MMGS converted back to STL - this may help topological cleaning in BLENDER!

In this thesis, only the diamond structure is considered. In physical space, Equation (5.2) can be amended by introducing a notion of wavelength in every direction (k_x, k_y, k_z) and by off-setting the zero of the function with a certain parameter t :

$$U_D(x, y, z) = \sin(k_x x)\sin(k_y y)\sin(k_z z) + \sin(k_x x)\cos(k_y y)\cos(k_z z) + \cos(k_x x)\sin(k_y y)\cos(k_z z) + \cos(k_x x)\cos(k_y y)\sin(k_z z) - t = 0. \quad (5.3)$$

Locally, the solid and fluid regions may be defined by positive and negative regions of the function U_D . The wavelengths $k_{x,y,z}$ mostly govern the pore density (thus pore size) while t mostly governs porosity (but also pore size). Moreover, if the wavelengths $k_{x,y,z}$ and threshold t depend upon space then a spatial gradation of the properties can be achieved. By choosing properly these parameters, a vast tailorable space of burner designs can be reached, with and without topological gradation. Note that from a regular lattice, geometrical deformations can also be achieved afterwards by linear, Lagrangian transformations of the spatial coordinates, which can be tuned to be porosity-conservative. For example, a linear gradation in the x direction can be achieved by the following expression:

$$\mathbf{x}(\mathbf{a}) = \mathbf{a} + (m \cdot x + p)\mathbf{a}, \quad (5.4)$$

where \mathbf{a} the coordinate in the reference configuration and $\mathbf{x}(\mathbf{a})$ the transformed coordinate. In that situation the dilatation tensor is symmetric thus $(m \cdot x + p)^3$ describes the local variation of the volumes (thus pore sizes).

The generation of the geometry from these definitions can be achieved readily by creating a spatial 3D array of voxels based upon the sign of U_D . Then the methodology presented in the previous section applies directly with the same workflow. Figure 5.10 shows an example of computational mesh for a diamond-based burner.

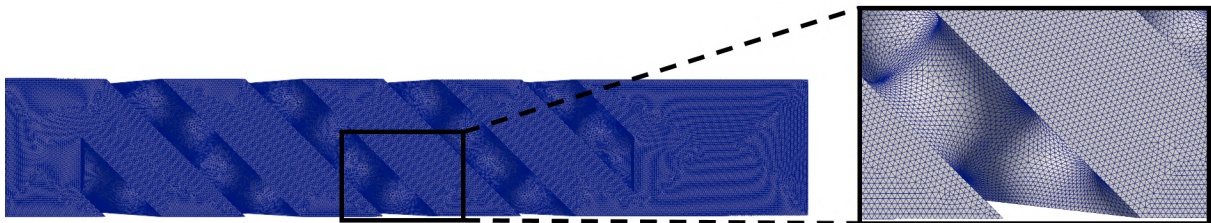


Figure 5.10. – Example of computational mesh for a 30 PPI diamond-based burner, mesh size $80 \mu\text{m}$.

5.4. Conclusions of the chapter

The generation of high-fidelity porous networks requires some technical work. For reticulated foams, a scanning procedure must be first performed, followed by filtering treatments to ensure that a resulting mesh makes physical sense and is “meshable”. In addition, the meshing procedure itself asks for extracted surfaces that are well-defined from a topological viewpoint. This requires many, lengthy hand-made corrections, and to date there does not exist a universal script/toolbox/workflow that permits to mesh any porous media scan swiftly without human intervention. Yet, in this chapter some very technical hints were given for future researchers, hoping that the present workflow be used and improved further in the future.

Relating 3D simulations and 1D models

This chapter is based on the article **Masset, P. A., Duchaine, F., Pestre & Selle, L. (2022). Modelling challenges of volume-averaged combustion within porous media. Combustion and Flame** (under review).

In porous burners, the pore size is usually larger than the flame thickness, giving rise to sharp and locally-anchored flame fronts. The presence of such steep gradients at the pore level is a major hurdle for the derivation of volume-averaged models, particularly for the highly non-linear reaction rates. So as to underline the intrinsic difficulties associated with volume-averaging for porous media combustion, this work performs 3D pore-level direct numerical simulations including conjugate heat transfer and complex chemistry in burners of finite length. The predictions from an associated volume-averaged model, whose effective properties are estimated directly on the computational domains and of identical thermo-chemical scheme, are compared to the 3D simulations. Discrepancies in terms of burning rate, physical profiles, and *a priori* analysis from the microscopic equations are found. Various pore sizes and geometries are considered. At the pore level, it is shown that flame preheating, wrinkling and wall quenching are the three main factors driving global burning rate, and that contrary to widespread perception, hydrodynamic dispersion only has an indirect role on the combustion processes. Based upon observations of combustion at pore scale, a new closure for reaction rates based on the asymptotic behavior of adiabatic laminar flames is proposed. It is meant to simulate pore-level flame wrinkling and removes the seemingly artificial increase in flame speed related to dispersion.

Overview

6.1. Introduction	128
6.2. Microscopic and macroscopic models	130
6.2.1. 3D Direct Pore-Resolved Simulations	130
6.2.2. 1D Volume-Averaged Model	134
6.3. Results and discussion	136
6.3.1. Macroscopic effective properties	136
6.3.2. Structure of the submerged flame	139
6.4. DPLS vs. VAM	142
6.4.1. Burning rate	142
6.4.2. Profiles in physical space	144
6.4.3. Other sources of error for the volume-averaged framework	145
6.4.4. Discussion on the thermal Péclet number	146
6.5. A new model for reaction rates?	147
6.5.1. Phenomenology of burning rate: DPLS <i>vs.</i> VAM	147
6.6. Conclusions of the chapter	152
6.A. Energy and mass budgets micro <i>vs.</i> macro	153
6.B. Additional plots local flame structure on \mathcal{A}	153

“In theory, there is no difference between theory and practice. But, in practice, there is.”

JAN L. A. VAN DE SNEPSCHEUT

6.1. Introduction

The combustion of a gaseous mixture in an inert solid matrix, referred to as Porous Media Combustion (PMC), is known to increase consumption speeds and enlarge flammability limits. On the lean side, this enables substantial reduction in CO and NO_x emissions [62]. The main mechanism underpinning this performance is an upstream recirculation of enthalpy from the burnt to the fresh gases through the solid matrix, leading to a preheating of the flame thus enhanced kinetics [49]. Though the general principles of PMC and main trends are well understood, the derivation of modelling strategies for the design of industrial burners is still an active field of research. Among possible macroscopic filtering strategies, the most popular framework for design is the Volume-Averaged Model (VAM). The strongly inhomogeneous, non-linear and co-dependent phenomena such as convection, diffusion, conjugate heat transfer, chemical reactions and radiation are all modelled to some extent using VAM, but they show inconsistent agreement with experiments. As recognized by many authors [29, 158, 257, 294], this is mainly due to the incomplete knowledge of combustion processes at the pore level, which drives the recent experimental and numerical efforts dedicated to characterize PMC at this scale.

On the experimental side, the opacity of the solid makes non-intrusive diagnostics of the internal flame structure notoriously difficult. 1/2D methods such as coherent anti-Stokes Raman scattering [228, 295] or laser-induced fluorescence [296] were attempted, but these require the creation of an artificial/intrusive small gap in the solid matrix or very large pores for optical access. Interestingly, the presence of local temperature maxima along the burner direction was reported in [295], suggesting the existence of non-planar flame fronts distributed longitudinally. A more direct measurement method was proposed by Dunnmon et al. [158] who used krypton as a gaseous adjuvant to perform X-ray tomography and retrieved 3D fields related to the temperature. Although the method still suffers from large uncertainties, it could be also assessed that the combustion front is largely non-planar and distributed among the pores. More recently, Fursenko et al. [257] sandwiched a 2D packing of spheres between two quartz plates to visualize directly the oscillatory nature of the flame under filtration combustion. Again, sharp and distorted fronts were observed in the voids. Those experimental strategies, although imperfect, remain more promising than the more classical, 0D and intrusive diagnostic using thermocouples inserted within the porous voids [192, 297], which have a tendency to hide short-scale variations due to both strong radiation, physical extension of the probes, and spurious contact points with the solid matrix.

On the numerical side, some direct pore-level simulations (DPLS) have been performed to study the internal structure of PMC. Those are summarized in Table 5.1 of Chapter 5, where the use of complex kinetics, radiation, mesh spacing and domain sizes are reported for comparison. In 2D, Sahraoui and Kaviany [294] were the first to propose DPLS in regular arrangements of square rods, followed by more recent works [275, 281, 282, 298]. These studies reported non-planar flame fronts, and some intrinsic discrepancies between volume-averaged models and simulations were underlined in [294]. However, a realistic simulation of intra and interphase heat transfers requires the third dimension of space. And thanks to the recent improvements in available computational resources and processing softwares, more realistic 3D geometries have also been considered. Bedoya et al. [136] presented a joint study of cylindrical and con-

ical burners, in order to compare 1D VAM, 3D DPLS and experiments. However, due to the discrepancies of hypotheses between the models and burner geometries, no conclusions on the validity of the volume-averaged model itself could be given. Billerot et al. [274] presented the first reacting simulations in regular diamond-based lattices, and reported large pore-scale inhomogeneities. Yakovlev and Zambalov [137] simulated unsteady filtration combustion in a packed bed of spheres, showing good qualitative agreement for temperature profiles against experiments. Shi et al. [280] followed through with a similar study, and compared the results to a volume-averaged model. Good agreement was observed, but since the transient displacement speed of the front in filtration combustion mode is mostly governed by a global energy budget [249], the results were less sensitive to the quality of the low-order modelling. Recently, Yakovlev et al. [259] presented simulations of a thin-layered radial burner and found large, finger-shaped flame fronts within the porous matrix. From Table 5.1, several modelling trends can be inferred. For instance, rather large mesh sizes were often employed due to the large computational costs and domain sizes simulated, what may have been an issue for the accurate representation of the flame fronts. Also, single-step kinetics still dominate the literature, what is known to present issues regarding flame response to preheating [299]. Concerning radiation, it has been increasingly included in the microscopic models. However, whilst radiation is undeniably an important mode of heat transfer affecting burner operability, it was not found to influence the combustion dynamics at the pore level. In addition, in [125] it was shown that the qualitative stabilization behavior of flames in finite-length burners was lowly affected by radiation.

In the works reported above and more generally in the vast majority of the literature of porous media combustion, the pore sizes are typically larger than the flame thermal thickness, giving rise to sharp, laminar flame fronts, very similar to the ones classically found in the wake of bluff bodies or injectors. This has major and direct consequences regarding VAM. First there is a blatant violation of length-scale separation between micro and macro-scale gradients required for upscaling procedures [160]. Moreover, there is usually the implicit assuming that the flame front is locally planar, though both experiments and pore-scale simulations suggest otherwise. In the same line of thought, VAM usually oversee the response of flame fronts to stretching, curvature, non-homogeneous preheating or near-wall quenching taking place in the interstitial flow at the pore level. Finally, though some classical assumptions of VAM for PMC are well documented, such as a interphase heat exchange, or the existence of an effective solid conductivity, the role of hydrodynamic dispersion within PMC remains unsettled. Although dispersion undeniably occurs within porous burners, its macroscale modelling through an increase in diffusivities also leads to a flame acceleration in the VAM which has not yet been linked to the pore-scale combustion processes. This increase in diffusivities implicitly assumes perfect mixing and subsequent combustion in volume at the macroscale, which is in contradiction with the observed thin flame fronts.

Fundamentally, all these remarks are related to the commutation errors between the averaging procedure and the pointwise operators, suggesting an analogy with the modelling issues of turbulent combustion. Similarly, an appropriate closure for the strongly non-linear reaction rates is crucial to retrieve a correct burning rate and the global behaviour at the burner scale. Unfortunately, to the authors' knowledge no such closure model was proposed to date for PMC. By means of 3D DPLS and associated VAM simulations for various pore sizes and geometries, this paper addresses the intrinsic modelling difficulties of volume-averaging for porous media combustion - when the pore size is larger than the flame thickness. It is shown that, even when the VAM is fed with effective parameters estimated directly on the simulated domains, large errors regarding VAM predictions for flame acceleration and spatially-averaged profiles are observed. The factors driving burning rate locally, such as flame surface density, preheating, wall quenching and stretch are investigated. Also, an *a priori* analysis is performed from the microscopic governing equations to address the sources of error in the intensity and functional

form of the macroscopic volume-averaged terms. Eventually, based upon a flamelet approach at pore scale, this study leads to the formulation of a new macroscale model for reaction rates. It includes flame wrinkling in the volume-averaged reaction terms and removes the artificial increase in flame speed related to hydrodynamic dispersion.

The paper is organised as follows. In Section 2 the 3D DPLS are presented, as well as the corresponding VAM. In Section 3, the effective properties fed in the VAM are computed, and the pore-level structure of the submerged flames is described. In Section 4, the relationships between the DPLS and the VAM are investigated - notably in the perspective micro *vs.* macroscale burning rate. Eventually, Section 5 presents an attempt at closing the gap between the DPLS and the VAM through a closure model for reaction rates based on the observations from the DPLS.

6.2. Microscopic and macroscopic models

6.2.1. 3D Direct Pore-Resolved Simulations

6.2.1.1. Computational domains

As depicted in Figure 6.1, five different computational domains are considered: R2, R1, D4, D2 and D1, whose general characteristics are given in Table 6.1. Mean porosity $\bar{\epsilon}$ represents the mean void fraction within the porous structure and L the length of the solid matrix. The domains comprise gaseous inlet and outlet regions of respectively 3 and 6 mm. The letter in their denomination refers to their type of matrix topology: either a reticulated random foam (R)

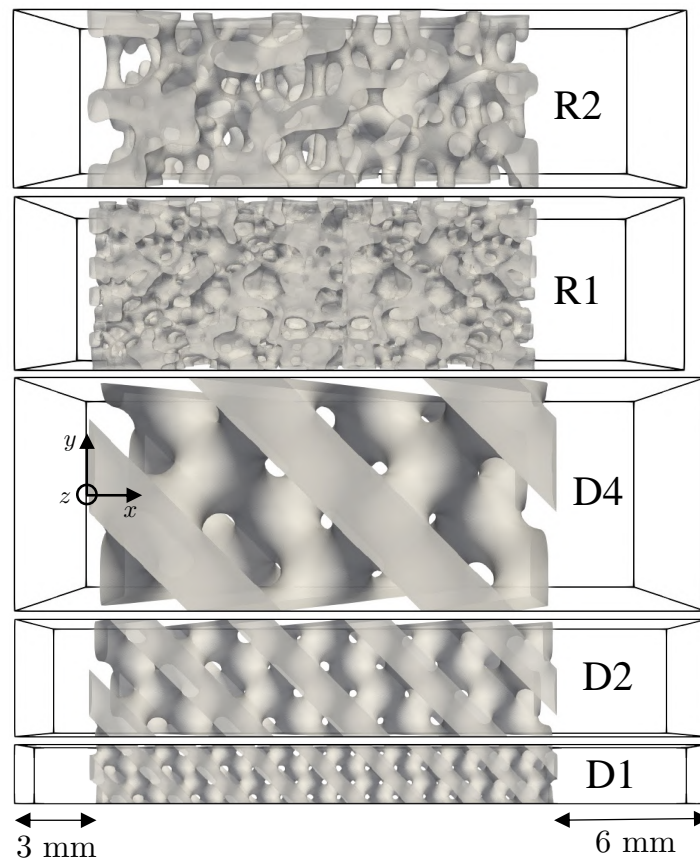


Figure 6.1. – Computational domains. Flow from left to right.

obtained via X-Ray tomography of a SiC foam, or a regular lattice (D) based on the diamond Triply-Periodic Minimal Surface:

$$\begin{aligned} \text{solid region} \iff & \sin(kx)\sin(ky)\sin(kz) \\ & + \sin(kx)\cos(ky)\cos(kz) \\ & + \cos(kx)\sin(ky)\cos(kz) \\ & + \cos(kx)\cos(ky)\sin(kz) > t, \end{aligned} \quad (6.1)$$

where k is the spatial wavenumber and here $t = 0.27$ yields a mean porosity $\bar{\epsilon}$ near 0.6. The associated numeral (1, 2 or 4) refers to their approximate mean pore diameter \bar{d}_p in mm, computed by a local thickness filter on the final geometry. A more local information about the topology of the computational domains is given in Figure 6.2(a) with the pore size density and Figure 6.2(b) with the transverse-averaged (slice) porosity $\langle \epsilon \rangle_x$. In Figure 6.2 it is observed that quite large variations of transversal porosity occur along the burner axis, foreshadowing a possible hydrodynamic anchoring of the flame.

The meshes consist of unstructured tetrahedra. In the gas phase, the prescribed mesh size is uniform (80 μm), yielding an error below 2% on flame speed at 300 K and 600 K in planar 1D adiabatic free flames. In the solid phase, the mesh size is similar ($< 100 \mu\text{m}$). Note that compared to previous studies shown in Table 5.1, our work may be considered well resolved. A mesh convergence study was performed down to 40 μm and found that the resolution of 80 μm was sufficient in the 3D case, which is expected because the flame fronts are the most stringent constraint.

Due to heat recirculation, at least a convective time scale within the gas phase must be computed ($\sim 10^{-2}$ s). The small mesh size requirement imposes a time step of the order of 10^{-9} s, so typically the convergence of one solution point requires 10^7 iterations. The computational cost for one simulation point was approximately 10^6 core-hours. The simulations were performed on the clusters MareNostrum 4, BSC, Spain and Jean-Zay, Idris, France.

Table 6.1. – Characterisation of the computational domains.

	\bar{d}_p (mm)	$\bar{\epsilon}$ (-)	L (mm)	nb. cells gas (million)	nb. cells solid (million)
R2	1.75	0.61	18.2	21.3	3.8
R1	1.08	0.59	18.1	19.9	7.0
D4	3.90	0.63	18.8	37.6	6.5
D2	2.02	0.62	18.8	4.8	2.5
D1	1.07	0.63	18.8	2.4	0.8

6.2.1.2. Gaseous phase

In the gaseous phase, the compressible reactive Navier-Stokes parallel solver AVBP is used with the TTGC scheme [300], which is third order in space and time. No subgrid scale model is used. Inlet and outlet boundaries are treated via the NSCBC formalism [301]. At the inlet, a CH_4 -air mixture is injected at constant velocity U_{in} and temperature $T_{\text{in}} = 300$ K. At the outlet, a constant pressure of 1 atm is imposed. On the sides, symmetry conditions are adopted. We

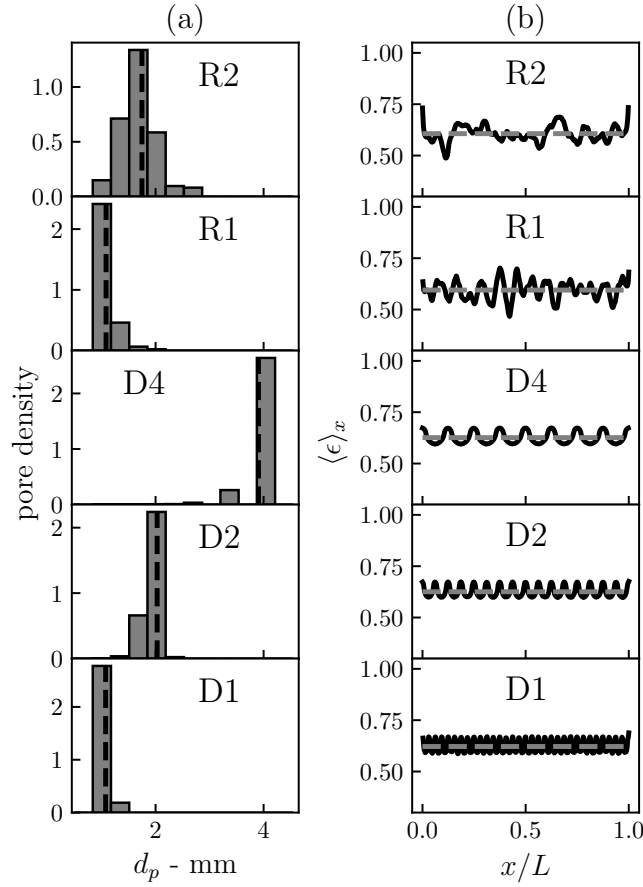


Figure 6.2. – Local characterization of the geometries.

recall the pointwise (microscopic) governing equations in AVBP:

$$\frac{\partial \rho_{g,k}}{\partial t} + \nabla \cdot (\rho_{g,k} \mathbf{u}) + \nabla \cdot \mathbf{J}_k - \dot{\omega}_k = 0, \quad (6.2)$$

$$\frac{\partial \rho_g \mathbf{u}}{\partial t} + \nabla \cdot (\rho_g \mathbf{u} \mathbf{u}) + \nabla \cdot [\mathbf{P}\underline{\underline{I}} - \underline{\underline{\tau}}] = 0, \quad (6.3)$$

$$\frac{\partial \rho_g E}{\partial t} + \nabla \cdot (\rho_g E \mathbf{u}) + \nabla \cdot [\mathbf{u} \cdot (\mathbf{P}\underline{\underline{I}} - \underline{\underline{\tau}}) + \mathbf{q}] - \dot{\omega}_T^0 = 0. \quad (6.4)$$

The underlying hypotheses are described in detail in Chapter 2. So as to simulate a realistic behavior of the flame front, an Analytically-Reduced Chemistry (ARC) is derived from a hierarchical kinetic mechanism developed by the CRECK modelling Group [302]. The reduction is performed using ARCANE [303] based on DRGEP method and the Quasi-Steady-State formalism (QSS). During the reduction laminar CH_4 -air premixed flames are used to target laminar flame speeds and adiabatic temperatures with less than 5% and 1% error respectively on the whole range of flammability for pressures between 0.3 and 5 bar. Auto-ignition times are also targeted with less than 5% deviation in constant pressure reactors with initial temperatures from 2000 K to 3000 K. The resulting chemical scheme (available in the general Appendix A at the end of this thesis) is labeled CH4_15_138_9_AP and comprises 15 transported species N_2 , H_2 , H , O_2 , O , H_2O , OH , CO , CO_2 , CH_4 , CH_3 , CH_2O , C_2H_6 , C_2H_2 , CH_2 and 9 QSS species HO_2 , CH_3OH , CH_2OH , HCO , C_2H_5 , C_2H_4 , C_2H_3 , CH_2CO for a total of 138 reversible reactions. The intrinsic characterisation of the inlet mixture (equivalence ratio ϕ , reference flame speed S_L^0 , thermal flame thickness δ_L^0 and equilibrium temperature T_{ad}) are given in Table 6.2.

ϕ	S_L^0	δ_L^0	T_{ad}
0.72	20 cm s ⁻¹	0.63 mm	1883 K

Table 6.2. – Adiabatic free-flame properties.

Because the response of the flame to preheating is absolutely crucial in PMC, we show in Figure 6.3 a plot of the flame acceleration in terms of mass flux, $\Gamma_p = \dot{m}/\rho_{\text{in}}S_L^0$, for the considered mixture. It is observed that the ARC mechanism adequately retrieves the response to the temperature $T_{\text{preheating}}$. A best fit of Γ_p is shown and used for post-processing.

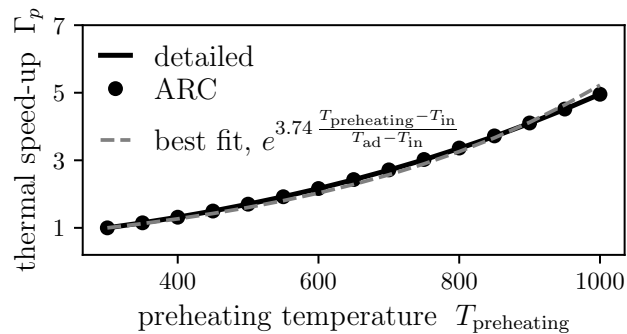


Figure 6.3. – Flame acceleration due to preheating.

6.2.1.3. Solid phase

In the solid phase, the solver AVTP [304] is used to compute the heat equation assuming Fourier's law:

$$\rho_s c_s \frac{\partial T_s}{\partial t} - \nabla \cdot [\lambda_s \nabla T_s] = 0, \quad (6.5)$$

Spatial discretization uses second-order Galerkin diffusion scheme, and time integration is performed with an implicit first-order forward Euler scheme. The resolution of the implicit system is achieved through a parallel matrix-free conjugate gradient method [305]. Adiabatic walls are prescribed on the sides. Conductivity λ_s is set constant to 10 W m⁻¹ K⁻¹.

6.2.1.4. A word on radiation

There exists *a priori* three modes of internal radiative heat transfer within porous media. The first concerns gas↔gas and gas↔solid heat transfer, but those have been neglected in previous studies because the gases are deemed transparent. For solid↔solid heat transfer, it is usually assumed that the porous network acts as an effective medium where the Radiative Transfer Equation (RTE) applies with effective macroscale coefficients. The determination of these effective properties, and the conditions under which this modelling is valid is an open question. Nonetheless, it has now become standard to resolve numerically the RTE or its various approximations in VAM, what allows to retrieve with more or less accuracy experimental temperature profiles [34, 159, 216]. The progressive influence of radiation on the stability of burners of finite length was studied by Sathe et al. [217], where it was found that the qualitative behavior of the flame is lowly affected by radiation. Similar conclusions were obtained by Mendes et al. [125]. Physically-speaking, radiation does change the macroscopic temperature profile due to external heat losses and increased heat recirculation, which in turn changes the burner operability - but from the point of view of the intertwined flame front and the general mechanism

of heat recirculation, radiation has negligible local influence at pore scale. Its inclusion would, in fact, be detrimental to the goal of comparing DPLS and VAM, because it introduces a further confounding factor and requires an elaborate study of the upscaled radiative model. So, for the sake of simplicity and pedagogy, and without altering the physics of the flame front, radiation is not considered in our numerical model.

6.2.1.5. Coupling strategy

The two softwares AVBP and AVTP are coupled through the library CWIPI [304]. At the gas/solid boundary \mathcal{A}_{gs} , AVTP imposes the temperature and AVBP the energy flux, so that:

$$\lambda_g \nabla T_g \cdot \mathbf{n}_{gs} = \lambda_s \nabla T_s \cdot \mathbf{n}_{gs} \quad \text{and} \quad T_s = T_g \quad \text{on } \mathcal{A}_{gs}. \quad (6.6)$$

\mathbf{n}_{gs} is the unit normal vector gas \rightarrow solid, as shown in Figure 6.4. The AVBP-AVTP coupling strategy was tested on various configurations and shows good agreement with experimental data [306]. Since only steady states are of interest, the two solvers are not synchronized and the solid is typically computed over a time span several thousands of times larger than the fluid. This time-decoupling strategy was used in packed-bed combustion [137] and yielded the same results than matched time steps. In addition, the no-slip and non-permeable-inert conditions at the gas/solid interface imposes:

$$\mathbf{u} = 0 \quad \text{and} \quad \mathbf{J}_k \cdot \mathbf{n}_{gs} = 0 \quad \text{on } \mathcal{A}_{gs}. \quad (6.7)$$

6.2.2. 1D Volume-Averaged Model

Figure 6.4 presents the principle of volume-averaging used in the present work, adapted to the framework of porous burners with a preferential flow direction (here x). The integration domain, centered on \mathbf{x} , is also called Representative Elementary Volume (REV), and has a thickness of $2r_0$. In our simulations it was found that a value of $r_0 \sim d_p/2$ could smooth local variations and avoid macroscopic gradients so the typical size of the REV is chosen to be equal to d_p for all domains. Moderate modifications to this integration size led to neither qualitatively nor quantitatively different conclusions. The integration is performed over \mathbf{y} . The intrinsic averages in the gas $\langle \cdot \rangle^g$ and solid $\langle \cdot \rangle^s$ phases are defined by:

$$\langle \psi \rangle^g = \frac{1}{\mathcal{V}_g} \int_{\mathcal{V}_g} \psi \, dV \quad \text{and} \quad \langle \psi \rangle^s = \frac{1}{\mathcal{V}_s} \int_{\mathcal{V}_s} \psi \, dV \quad (6.8)$$

where \mathcal{V}_g and \mathcal{V}_s are the gas and solid regions contained within the REV.

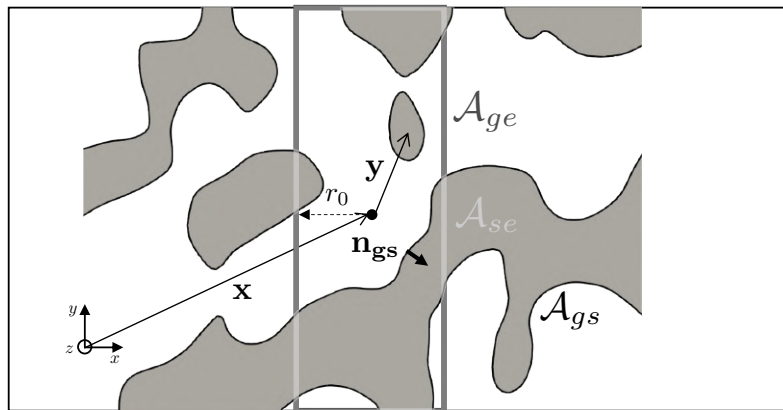


Figure 6.4. – Principle of volume-averaging and shape of the REV.

6.2.2.1. Governing equations

The classical 1D volume-averaged equations for porous media combustion are [29, 34, 136, 159, 220, 307]:

$$\epsilon \langle \rho_g \rangle^g \langle u \rangle^g \partial_x \langle Y_k \rangle^g + \partial_x \left[\epsilon J_k^{\text{eff}} \right] - \epsilon \langle \dot{\omega}_k \rangle^g = 0, \quad (6.9)$$

$$\begin{aligned} & \epsilon \langle \rho_g \rangle^g \langle u \rangle^g \langle c_{p_g} \rangle^g \partial_x \langle T_g \rangle^g - \partial_x \left[\epsilon \langle \rho_g \rangle^g \langle c_{p_g} \rangle^g D_{th}^{\text{eff}} \partial_x \langle T_g \rangle^g \right] \\ & + \sum_k \epsilon \langle c_{p_g,k} \rangle^g J_k^{\text{eff}} \partial_x \langle T_g \rangle^g + \epsilon \langle \dot{\omega}_T \rangle^g + h_V (\langle T_g \rangle^g - \langle T_s \rangle^s) = 0, \end{aligned} \quad (6.10)$$

$$\partial_x \left[\lambda_s^{\text{eff}} \partial_x \langle T_s \rangle^s \right] + h_V (\langle T_g \rangle^g - \langle T_s \rangle^s) = 0, \quad (6.11)$$

where ϵ is the local porosity, $\langle T_s \rangle^s$ the solid temperature, h_V the interphase heat transfer coefficient. The macroscale effective diffusive flux J_k^{eff} is:

$$J_k^{\text{eff}} = - \langle \rho_g \rangle^g \left[D_k^{\text{eff}} \frac{W_k}{\langle W \rangle^g} \partial_x \langle X_k \rangle^g - \langle Y_k \rangle^g V_c^{\text{eff}} \right], \quad (6.12)$$

where $\langle W \rangle^g$ is the mean molar mass, $\langle X_k \rangle^g$ the molar fractions and V_c^{eff} the macroscale correction velocity:

$$V_c^{\text{eff}} = \sum_{k=1}^N D_k^{\text{eff}} \frac{W_k}{\langle W \rangle^g} \partial_x \langle X_k \rangle^g. \quad (6.13)$$

The dispersion coefficient D^{dis} , defined later in Equation (6.21), gives:

$$D_k^{\text{eff}} = \langle D_k \rangle^g + D^{\text{dis}} \quad (6.14)$$

and:

$$D_{th}^{\text{eff}} = \frac{\langle \lambda_g \rangle^g}{\langle \rho_g \rangle^g \langle c_{p_g} \rangle^g} + D^{\text{dis}}. \quad (6.15)$$

These equations are standard but not derived via an exact mathematical procedure since commutations between averages, products and operators were required. They are to some extent *ad hoc* and the dispersion coefficient D^{dis} is an important model parameter. From the perspective of combustion, the main model is $\langle \dot{\omega}_k \rangle^g$, which is usually assumed as a simple commutation with the averages:

$$\langle \dot{\omega}_k \rangle^g = \dot{\omega}_k \left(\langle \rho_g \rangle^g, \langle T_g \rangle^g, \langle Y_k \rangle^g \right). \quad (6.16)$$

The volume-averaged heat release rate is:

$$\langle \dot{\omega}_T \rangle^g = \sum_k \langle h_k \rangle^g \langle \dot{\omega}_k \rangle^g. \quad (6.17)$$

Contrary to Equation (6.4), Equation (6.10) is based on the temperature, therefore the volume-averaged heat release rate is in fact rigorously equal to:

$$\begin{aligned} \langle \dot{\omega}_T \rangle^g &= \sum_k \langle h_{s,k} \rangle^g \langle \dot{\omega}_k \rangle^g + \langle \dot{\omega}_T^0 \rangle^g \\ &= \sum_k \langle h_{s,k} \rangle^g \langle \dot{\omega}_k \rangle^g + \sum_k \Delta h_k^{f,0}(T_{\text{ref},h}) \langle \dot{\omega}_k \rangle^g, \end{aligned} \quad (6.18)$$

but for simplicity and because the influence of sensible enthalpies is largely negligible, it is assumed that $\langle \dot{\omega}_T \rangle^g = \langle \dot{\omega}_T^0 \rangle^g$. For the numerical resolution, the software CANTERA [112] is adapted to resolve the kinetic scheme of Section 2.1.2 and the VAM governing equations. For numerical stability, the field of porosity ϵ is smoothed over 0.1 mm in CANTERA at the inlet/outlet boundaries of the solid. Also, porosity is assumed constant at the core of the solid $\epsilon = \bar{\epsilon}$. Compared to AVBP, CANTERA assumes no viscous heat production and constant pressure, two assumptions which introduce negligible errors in the present configurations.

6.3. Results and discussion

6.3.1. Macroscopic effective properties

There exists several methodologies to feed the VAM with effective properties. The first is to make use of existing correlations determined experimentally or numerically: there is, for instance, a series of estimations for heat transfer coefficient h_V [196, 197, 199, 200], each having its own range of validity in terms of temperature, flow rate, porosity, pore size, etc. Another example, in asymptotic analyses it is often assumed that the effective conductivity is simply given by the porosity so that: $\lambda_s^{\text{eff}} = (1 - \epsilon)\lambda_s$ [299, 308], an estimation retrieved during the upscaling procedure by neglecting local deviations. Correlations for dispersion can also be found in [208]. Such estimations are typically quite accurate in terms of order of magnitude, but these do not take into account the specificity of each geometrical domain and introduce uncertainties when comparing VAM and DPLS.

A second methodology, adopted in this work, is to estimate directly the effective parameters of the computational domains by performing *independent* numerical simulations in the solid and gas phases [220]. Although it is not ensured that the magnitude and functional forms of the effective macroscale models are the same in non-reactive (independent) and reactive (coupled) simulations, this corresponds to the classical methodology used to date in porous media combustion (this issue is addressed in Section 4.3). The values obtained from the 3D computational domains and reported in Table 6.3 and the procedure to obtain them, close to what could be done in experiments, is now described.

Table 6.3. – Macroscale properties of the various domains.

	h_V (W m ⁻³ K ⁻¹)	λ_s^{eff} (W m ⁻¹ K ⁻¹)	A^{dis} (m)
R2	1.0×10^5	2.3	2.6×10^{-3}
R1	4.1×10^5	2.7	1.4×10^{-3}
D4	6.3×10^4	1.8	7.3×10^{-4}
D2	2.3×10^5	1.7	6.2×10^{-4}
D1	3.6×10^5	2.0	3.4×10^{-4}

6.3.1.1. Effective thermal conductivity

The solid effective conductivity λ_s^{eff} is determined via transient simulations in the solid domain only, by excitation of the first longitudinal cosine mode with adiabatic boundary conditions. The interest of this method is the simplicity of the evolution of the system throughout time. Indeed, by setting the initial temperature at time $t = 0$ as:

$$T_s(x) = T_s^0 + \Delta T_s \cos\left(\frac{\pi x}{L}\right), \quad (6.19)$$

the solution of the equivalent, macroscopic heat equation is:

$$\langle T_s \rangle^s(x) = T_s^0 + \Delta T_s \cos\left(\frac{\pi x}{L}\right) \exp\left(\frac{-\pi^2 \lambda_s^{\text{eff}} t}{(1 - \bar{\epsilon}) \rho_s c_s L^2}\right). \quad (6.20)$$

In the simulations it is assumed that $T_s^0 = 600$ K and $\Delta T_s = 100$ K, but due to the linearity of the heat equation the exact values do not matter. A comparison between the evolution of $\langle T_s \rangle^s$ in the simulations and a best fit of λ_s^{eff} based on Equation (6.20) is shown in Figure 6.5 for domain R1. Similar agreement was found for all the geometries.

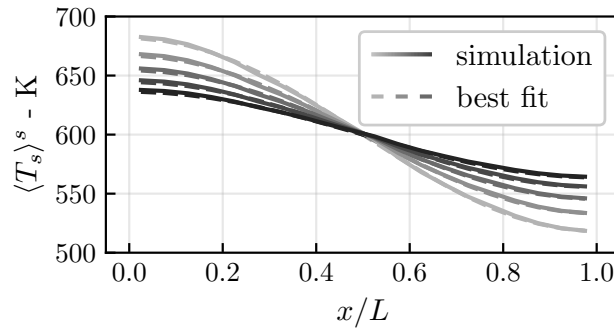


Figure 6.5. – Fitting of effective thermal conductivity for domain R1 (time computed: 21 s). Profiles evenly distributed in time.

6.3.1.2. Dispersion coefficient

A classical experiment performed to both understand and measure hydrodynamic dispersion is shown in Figure 6.6. From a steady-state cold flow solution ($T_g^0 = 300$ K), a small discontinuity of temperature ($\delta T_g = 10$ K) is imposed at time $t = 0$, with adiabatic conditions at the fluid-solid boundary. Due to the meandering nature of the flow (effects of velocity gradients, tortuosity, no-slip conditions, transverse diffusion, recirculation zones, etc.) the shape of the initial pulse is rapidly lost. At the macroscale, the averaged profiles are substantially more broadened than in a 1D free-flow: this is hydrodynamic dispersion, which is classically modelled as an increase in effective thermal diffusivity in the gas phase. The intensity of dispersion being related to the velocity fluctuations, it is often assumed that the dispersion coefficient follows a linear trend with regard to the interstitial longitudinal flow velocity $\langle u \rangle^g$. Following [136], the dispersion coefficient D^{dis} may be written accordingly as:

$$D^{\text{dis}} = 0.5 \cdot A^{\text{dis}} \cdot \langle u \rangle^g. \quad (6.21)$$

In the macroscale equation, the resulting thermal effective diffusion coefficient is therefore assumed to be of the form:

$$D_{th}^{\text{eff}} = \frac{\langle \lambda_g \rangle^g}{\langle \rho_g \rangle^g \langle c_{p_g} \rangle^g} + 0.5 \cdot A^{\text{dis}} \cdot \langle u \rangle^g. \quad (6.22)$$

where the volume-averaged values vary only slightly due to the temperature variations. Note that in the limit $\langle u \rangle^g \rightarrow 0$, the intrinsic diffusivity of gas phase is exactly retrieved, what boils down to neglecting tortuosity effects found at ultra-low velocities [208]. At the macroscopic scale, the transient governing equation of convection-diffusion is:

$$\frac{\partial \langle T_g \rangle^g}{\partial t} - D_{th}^{\text{eff}} \frac{\partial^2 \langle T_g \rangle^g}{\partial x'^2} = 0. \quad (6.23)$$

where $x' = x + \langle u \rangle^g t$ is the referential of the moving initial pulse. Its solution can be found easily through a Fourier transform, supposing an infinite medium. Back to the real space, it is:

$$\langle T_g \rangle^g(x', t) = T_g^0 + \frac{\delta T_g}{2} \sqrt{\frac{1}{\pi D_{th}^{\text{eff}} t}} \int_{-\infty}^0 \exp\left[-\frac{(x' - y')^2}{4 D_{th}^{\text{eff}} t}\right] dy', \quad (6.24)$$

where y' is a dummy integration variable. In the reference frame, this leads to:

$$\langle T_g \rangle^g(x, t) = T_0 + \frac{\delta T_g}{2} \left[1 - \text{erf}\left(\frac{x - \langle u \rangle^g t}{2 \sqrt{D_{th}^{\text{eff}} t}}\right) \right]. \quad (6.25)$$

A best fit of Equation (6.25), together with Equation (6.22) onto the simulation is shown in Figure 6.7 for domain R1, where the three solutions fields of Figure 6.6 correspond to the three leftmost profiles. A very good functional agreement is found, which confirms the existence of relatively strong dispersion potential within our geometries.

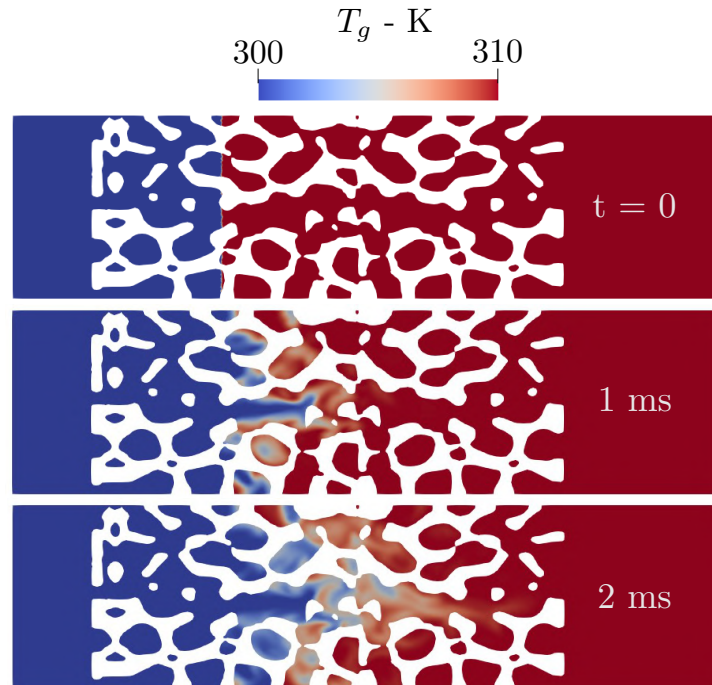


Figure 6.6. – Illustration of dispersion in physical space, slices, domain R1, from $t = 0$ to 2 ms, inlet velocity $U_{\text{in}} = 1 \text{ m s}^{-1}$.

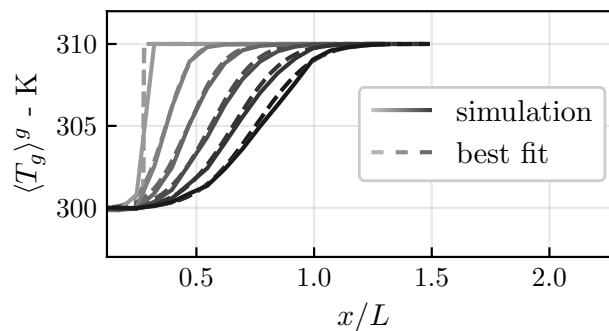


Figure 6.7. – Fitting of dispersion coefficient for domain R1 ($U_{\text{in}} = 1 \text{ m s}^{-1}$, time computed: 5 ms). Profiles evenly distributed in time: the first three profiles on the left correspond to that of Figure 6.6.

6.3.1.3. Interphase heat transfer coefficient

When there exists locally a gradient at the gas/solid interface, heat is transferred between the two phases. This typically occurs when the macroscopic temperatures of the gas $\langle T_g \rangle^g$ and solid $\langle T_s \rangle^s$ are different. Accordingly, the macroscale heat transfer per unit volume from the gas to

the solid Q_{gs} is often modelled through a heat transfer coefficient h_V as:

$$Q_{gs} = h_V [\langle T_g \rangle^g - \langle T_s \rangle^s]. \quad (6.26)$$

In some situations, this heat transfer is so large that the thermal equilibrium between the two phases is enforced. This led some authors to consider the framework of Local Thermal Equilibrium (LTE), in which the solid energy equation is discarded and the system gas+solid is viewed as an effective medium [191–193]. In porous media combustion, however, the large temperature gradients generated by the flame are mostly incompatible with LTE hypothesis. This is why the Local Thermal Non-Equilibrium hypothesis (LTNE) is rather employed through Equation (6.26), requiring a specific energy equation in the solid phase [194, 307].

Contrary to λ_s^{eff} and A^{dis} , the interphase volume heat transfer coefficient h_V is fitted directly on the DPLS, and not determined independently. This is due to the large discrepancies observed between attempted gas-only simulations (*e.g.* relaxation of gas temperature into a hot solid) and reactive gas-solid simulations. Moreover, for simplicity it is chosen to set a constant h_V in the VAM simulations, so finding a sufficiently reliable value requires a somewhat direct measurement. A best fit of Equation (6.26) is shown in Figure 6.8 for domain D2. Expectedly, the agreement is less good in the combustion zone but for the important preheating region the correlation is deemed sufficient. Other correlations have been tested including dependencies upon the Reynolds number and thermal conductivity, with minor improvements.

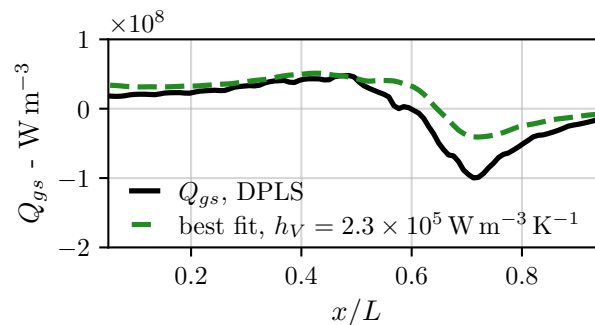


Figure 6.8. – Fit of constant h_V on domain D2.

6.3.2. Structure of the submerged flame

The pore-level structure of flames embedded in porous media is now investigated. For each domain, a steady-state condition for which the flame is fully submerged inside the porous matrix is computed. The corresponding values for inlet velocities U_{in} and pore-based Reynolds numbers $\text{Re}_p = \rho_{\text{in}} U_{\text{in}} \bar{d}_p / \mu_{\text{in}}$ are given in Tab. 6.4. Steadiness conditions were assessed through both macroscopic values such as total kinetic energy, total heat release, and total interphase heat transfer, but also based on local probes in the flow to detect local unsteady behavior. Notably, since the solid is globally adiabatic, a good indicator of convergence was found to be the integral of the interphase heat transfer Q_{gs} , which was imposed to be below 1% of the total chemical energy release per time unit. For domain D4, due to the larger pore size thus larger Reynolds number, no steady-state solution could be obtained, and an intermittent hydrodynamic cycle was observed. So as to keep a coherent steady framework it was decided to increase artificially the dynamic viscosity μ by a factor of 3, for case D4 only, hence the relatively low associated Reynolds number in Tab. 6.4. This is achieved by increasing μ_{ref} in Equation (2.33) by a factor of 3. The other intrinsic gas properties, such as thermal and species diffusivities, were kept constant by increasing the Prandtl and Schmidt numbers of the same factor. It was checked

in a 1D simulation that the resulting flame speed was unaffected. Despite this small change in operating condition, case D4 is relevant to study the influence of the ratio of pore size to flame thickness whilst remaining within steady-state framework. This observation underlines that steady-state volume-averaged models may be unadapted for burners of large pores (here D4 corresponds approximately to 10-15 PPI).

Table 6.4. – Inlet velocities U_{in} and pore-based Reynolds numbers Re_p .

	R2	R1	D4	D2	D1
$U_{\text{in}} - \text{m s}^{-1}$	0.60	0.65	0.80	0.60	0.65
Re_p	56.1	37.5	55.5	64.7	37.1

A 3D overview of the solutions is shown in Figure 6.9, where the reaction zone is colored in black (heat-release rate iso-surface). Both streamlines and the solid are colored by temperature. It is observed that the flame fronts are not planar, subject to local anchoring, and spatially distributed along the longitudinal axis, what seems inconsistent with the intrinsic hypotheses of the VAM. Also, the streamlines indicate that the flow is largely preheated by the solid matrix before reaching the reaction zone. This preheating reduces the thermal thickness below the reference value $\delta_L^0 = 0.63 \text{ mm}$, typically near 0.4-0.5 mm. From the streamlines it is inferred that the flow is more tortuous in R than D domains, which is coherent with their value of A^{dis} . Note also that between geometries D2 and D1, the anchoring pattern is similar.

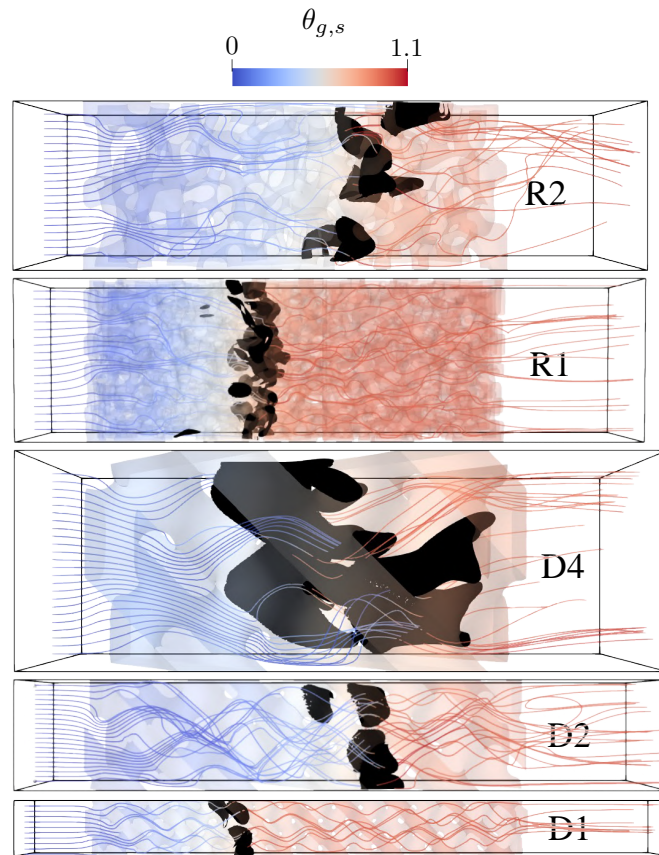


Figure 6.9. – 3D view of the solutions points used in this work. Solid/streamline coloring - blue cold, red hot regions. Black region: isocontour of heat release ($3 \times 10^9 \text{ W m}^{-3}$).

The local anchoring of the flame fronts may be further investigated in Figure 6.10, which shows

slices colored by gas and solid temperatures (blue to red), heat release rate (black), and gas \rightarrow solid heat transfer (green to purple). It is observed that flames have a tendency to stabilize in the wake of the porous obstacles, with a very large positive gas \rightarrow solid heat transfer near the flame feet (wall quenching), suggesting a combination of both thermal and hydrodynamic anchoring. In the reticulated geometries, the sign of the heat transfer does not follow easy patterns. In diamond geometries, however, it is clearly visible that mostly the upstream part of the obstacles heat up the flow. Overall, superadiabatic temperatures are observed locally, in the form of inhomogeneous pockets which rapidly equilibrate downstream of the heat release region. In domain D4, due to the low ratio \bar{d}_p/L some super and underadiabatic pockets leave the porous matrix. In all domains, some inhomogeneities in the preheating region indicate that the flow is largely three-dimensional, so one should keep in mind that slices are insufficient to comprehend the global flow structure. This also substantiates the use of a LTNE model. Figure 6.10 shows again that the flame fronts are definitely not planar, and in domain D4 the flame front is so distorted that it touches downstream pores. This finger-like structure is reminiscent of the works of [259] in a thin-layered porous burner.

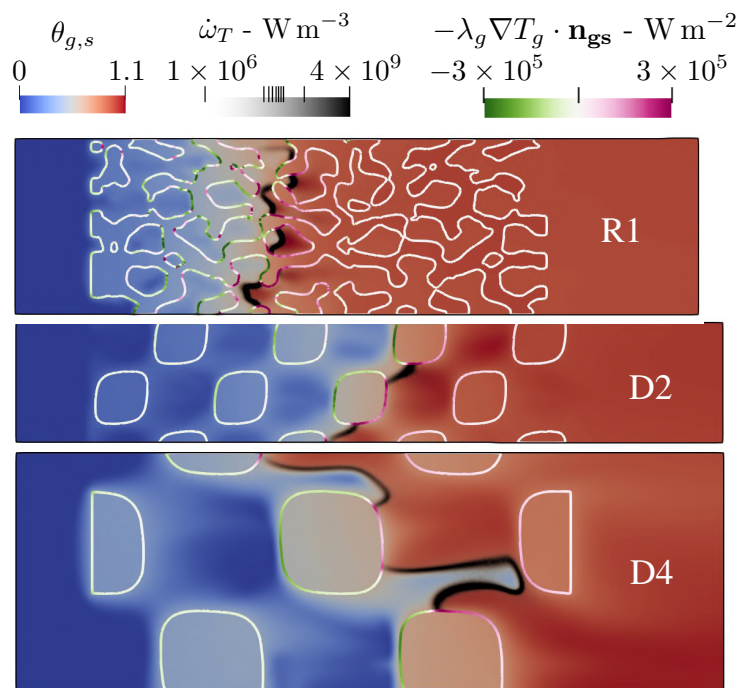


Figure 6.10. – Slices in various domains. Gas/solid temperatures, heat release rate and inter-phase heat transfer.

The 3D structure of the flame and flow is further investigated through Figure 6.11, which shows respectively the fields of (a) reduced methane mass fraction $Y_{\text{CH}_4}/\max(Y_{\text{CH}_4}^0)$, (b) reduced intermediate species H mass fraction $Y_{\text{H}}/\max(Y_{\text{H}}^0)$ and (c) longitudinal velocity component u . The 0 superscript refer to the reference laminar flame profiles. Figure 6.11(a) reveals again that the fuel is consumed over a very thin region of space, which confirms the classical vision that flames in porous media may be viewed to some extent as preheated laminar flames, and that combustion does not occur homogeneously at the scale of the REV. Figure 6.11(b) shows the multi-dimensional accumulation of the intermediate species H, a phenomenon enhanced for light species with pronounced preferential diffusion. These transverse deviations constitute a further difficulty for 1D models, expectedly leading to additional errors regarding global heat release rate and thus burning rate. In Figure 6.11(c) it is observed that there exists local constrictions and expansions of the flow, hinting that some regions may be preferential for flame anchoring,

that is, behind obstacles. A comparison between Figures 6.11(a) and (c) suggests that the flame fronts are preferentially anchored in regions of flow expansion for decreasing u values. Note that values up to 50 times the inlet velocity are attained within the porous matrix, originating from the combined effects of global porosity, tight throats and flow expansion due to combustion.

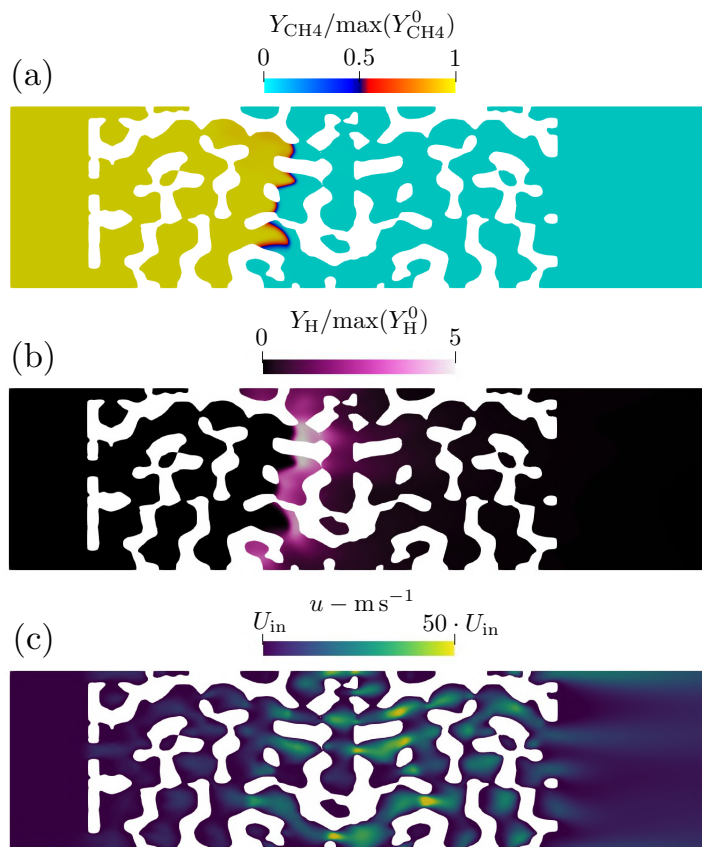


Figure 6.11. – Slices in domain R1: (a) reduced CH4 mass fraction, (b) reduced H mass fraction and (c) longitudinal velocity u .

6.4. DPLS vs. VAM

In the previous section, intrinsic discrepancies between the flame structure in the DPLS and classical derivation hypotheses of the VAM have been unveiled, such as the presence of sharp, wrinkled, and longitudinally-distributed flame fronts, but also wall quenching, a potential “discrete” hydrodynamic anchoring, and a complex 3D chemistry field. In this section, we move beyond these qualitative observations to more quantitative comments. The predictions of the VAM in terms of burning rate and physical profiles are discussed. Then, an *a priori* benchmarking of the main macroscale models such as the effective solid thermal conductivity, dispersion and reaction rates is performed, allowing to unveil additional sources of modelling errors.

6.4.1. Burning rate

Due to the preheating within the solid matrix and the multi-dimensional nature of the flame front, the burning rate of flames within porous media is known to be substantially larger than the 1D free flame at the same inlet conditions. The resulting acceleration may be measured by

the parameter Γ :

$$\Gamma = \frac{U_{\text{in}}}{\bar{\epsilon} S_L^0} = \frac{\dot{M}_{\text{in}}}{\bar{\epsilon} \dot{m}_0 \mathcal{A}_T}, \quad (6.27)$$

which compares the inlet burning velocity U_{in} to S_L^0 , mean porosity effects leading to flow constriction set aside. \dot{M}_{in} denotes the integrated inlet mass flux, \mathcal{A}_T the cross-section area of the domain and $\dot{m}_0 = \rho_{\text{in}} S_L^0$ the mass flux per surface unit of the reference laminar flame. In porous burners of finite length, 1D theory predicts that for a steady flame position in the solid matrix $x_p \in [0, L]$, only portions of the curve $\partial\Gamma/\partial x_p > 0$ are stable - which is known to occur only in the upstream half of the burner. This seems contradictory with the cases R2 and D2 of Figure 6.9, where the flame could be stabilized in the downstream half of the burner. This difference has two origins. First, in our simulations we have found that the stable range of the burners was quite narrow. This may be explained by the global adiabaticity of the solid matrix, which is known to lead to a near-plateau for the curve Γ *vs.* x_p so that downstream flames are only slightly unstable [125]. Then, this potential instability is in fact absorbed by the local changes in flame area, which constitute an additional, stabilizing degree of freedom. This is also potentially a source of hysteresis: several positions could be reached in the burner for the same U_{in} (not shown). This has important modelling implications, because the internal flame surface is absent from the VAM and *a priori* unknown for a given flame position, burning rate, etc.

Similar to LES for turbulent combustion, the filtering process is mostly problematic for the reaction rates, whose integral is directly related to Γ . And because the burning rate is very sensible to the combustion model and the (linked) physical profiles, it is expectedly a difficult quantity to predict. In that context, Figure 6.12 compares Γ values in the DPLS and corresponding VAM simulations, obtained by fixing the same position of maximum of heat release in the porous medium. Another strategy could have consisted in comparing flame positions for the same Γ values, but for a given inlet velocity it is not ensured that a stable flame position exists and the error made on Γ could not be quantified. In Figure 6.12, discrepancies between the VAM and the DPLS are observed, notably for R geometries and for the large pore case D4. Overall, the burning rate seems overestimated in R geometries, and underestimated in D geometries. This may be directly attributed to the different intensities of dispersion fed into the VAM. More especially, given the fact that between R2/D2 and R1/D1 cases, the porous length L , effective solid conductivity λ_s^{eff} , heat transfer coefficient h_V and DPLS Γ values are very close, it indicates that hydrodynamic dispersion is at least partly uncorrelated to the burning rate in real burners.

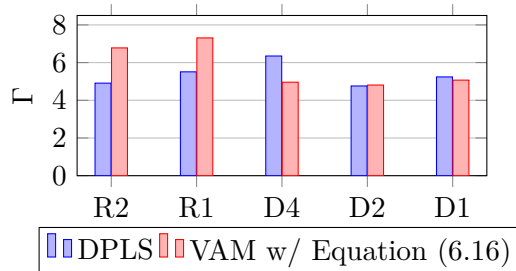


Figure 6.12. – DPLS *vs.* VAM with properties of Table 6.3.

One may understand the phenomenological issue with dispersion at the macroscale by considering the limit $h_V \rightarrow 0$. In that case Equation (6.10) becomes that of an adiabatic flame of increased thermal conductivity. However, for unity Lewis flames in adiabatic porous burners, the flame acceleration was shown to be only related to the flame surface [282], which has no reason to be quantitatively linked to the acceleration due to dispersion. Here for instance between cases R2 and D2, the flame areas are basically the same in the DPLS but intensities of

dispersion are very different which is a source of error on Γ in the VAM.

6.4.2. Profiles in physical space

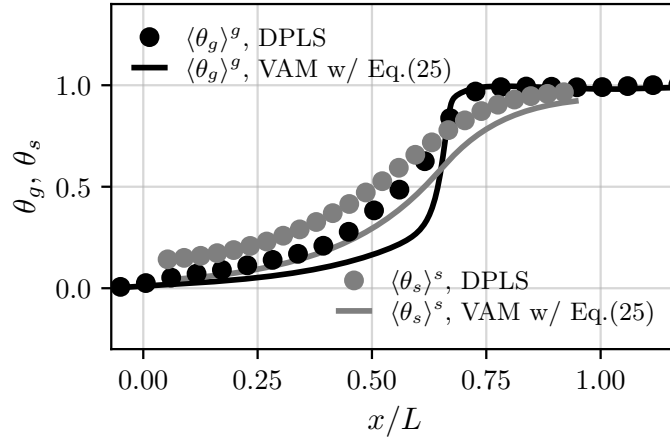


Figure 6.13. – Gas/solid temperature profiles, DPLS *vs.* VAM, domain D2.

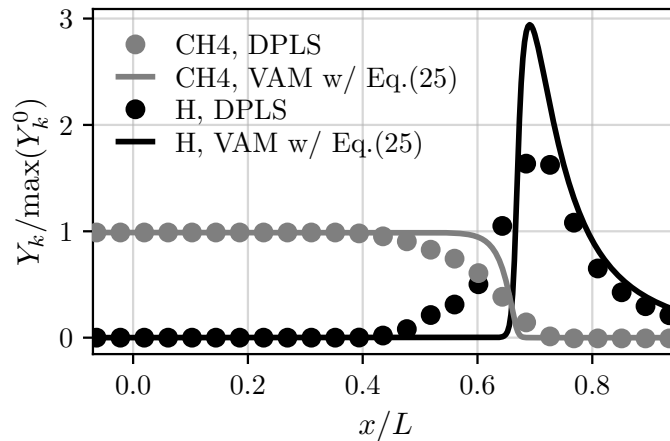


Figure 6.14. – Mass fraction profiles, DPLS *vs.* VAM, domain D2.

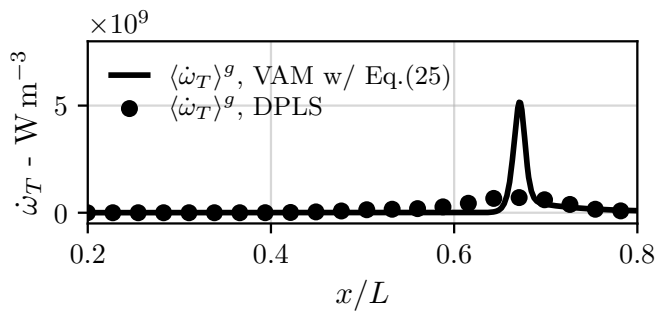


Figure 6.15. – Average HRR in the DPLS *vs.* HRR computed in the VAM, domain D2.

We now move beyond integral values to the physical space through Figures 6.13, 6.14 and 6.15, which compare DPLS and VAM profiles for gas/solid temperatures, CH4 and H reduced mass

fractions and heat release rate for domain D2. It is observed that VAM profiles only recover qualitatively that of the DPLS, with a similarity mainly originating from the matched position of the flame in the VAM. Overall, the profiles in the DPLS appear smoother, especially regarding species and heat release rate profiles. This is the signature of the longitudinal distribution of the flame fronts, as visible in Figure 6.9. Similar agreements and trends are found for the other geometries. These results suggest that, in experiments, approximate agreement of temperature profiles should not be used to discuss the quality of volume-averaged models, because similar macroscale physical profiles may show very different burning rates. The same goes for analyses of output gas compositions, which represent a rather indirect information on the quality of the solution and the actual links DPLS/VAM.

A further modelling issue may be stressed by noticing the discrepancy in (functional) shape for species concentration and heat release rate profiles between the VAM and the DPLS, hinting that a modification of the effective properties may not be sufficient to recover macroscopic profiles with more accuracy. For instance, increasing artificially dispersion to smooth further the profiles may improve the spatial agreement but may in turn largely affect Γ values. This implies that the question of whether the VAM can retrieve at the same time the burning rate and the spatial profiles, is an open and possibly uncertain question.

As a final remark, note how the local superadiabatic behavior of the flame fronts in Figure 6.10 is mostly absent from the VAM profiles of Figure 6.13, while being present locally in the 3D fields.

6.4.3. Other sources of error for the volume-averaged framework

The VAM and the DPLS share the same thermo-chemical scheme, with only very minor intrinsic differences in the modelling equations - such as constant pressure and zero viscous dissipation in CANTERA. However, these modelling differences are largely negligible compared to the other terms in the equations (for instance, typical pressure drops measured in our simulations were of the order 0.2-2% of the atmospheric pressure). Those are insufficient to account for the discrepancies in terms of burning rates and physical profiles. This leaves two possible origins for the observed differences:

- (O1): a wrong estimation of the effective properties ;
- (O2): a wrong functional form for the closure models.

To illustrate (O1), it is for instance not ensured that the effective conductivity measured in the solid phase is the same between non-reactive (independent) and reactive (coupled) situations. Estimating these parameters in the reactive coupled simulations requires the rigorous comparison of mass and energy budgets between the microscopic and macroscopic equations, a procedure which also informs about (O2). For the sake of conciseness here, this analysis is performed in Appendix 6.A based upon the upscaling procedure of Chapter 2 ; overall, it is found that the effective solid conductivity is slightly different in reactive situations though presenting good functional modelling, whilst the dispersion model struggles more to catch the complex convective and diffusive deviations from the averages, especially in the reaction zone. In agreement with our previous remarks, it is a further clue that dispersion may be incompatible with thin flame fronts.

From the point of view of combustion, the most important model is the $\langle \dot{\omega}_k \rangle^g$ and concerns directly (O2). In LES, it is notorious that the simple commutation of the reaction rates with the averages fails [115]. For filtered porous media burners, the situation is similar. Figure 6.16 illustrates the difference between the averaged heat release rate in the DPLS $\langle \dot{\omega}_T \rangle^g$ and the heat release rate value from the kinetic model computed at the averages $\dot{\omega}_T(\langle \cdot \rangle^g)$, for domains D4, D2 and D1. Clearly, Figure 6.16 shows that the simple commutation of reaction rates with their averages is fundamentally flawed. In other terms, it means that if one were to retrieve exactly

the averaged temperature and species profiles, a combustion model would be required. This lack of commutation was predicted from previous physical observations on the solutions, namely the longitudinal distribution of the flame fronts, their wrinkling, but mostly, their sharpness with regard to the size of the REV. It is noticed that the relative commutation error, which may be viewed through the ratio:

$$E_{\dot{\omega}_T} = \frac{\max[\dot{\omega}_T(\langle \cdot \rangle^g)]}{\max[\langle \dot{\omega}_T \rangle^g]}, \quad (6.28)$$

decreases with decreasing pore size (for even smaller pore sizes which were simulated but not shown here, this ratio decreases to even lower values). This may be explained by three factors. For decreasing pore size:

- the flame front becomes increasingly planar. This was notably observed by Gauthier in small heat-recirculating tubes [131] ;
- the intensity of local deviations from the averages decrease, notably in terms of temperature. Progressively, the Biot number in the gas (but also solid) phases decreases and the temperature profiles become more homogeneous. This simultaneously leads to the LTE framework, also known as hyperdiffusive [307] ;
- the size of the REV also decreases, which reduces potential windowing errors.

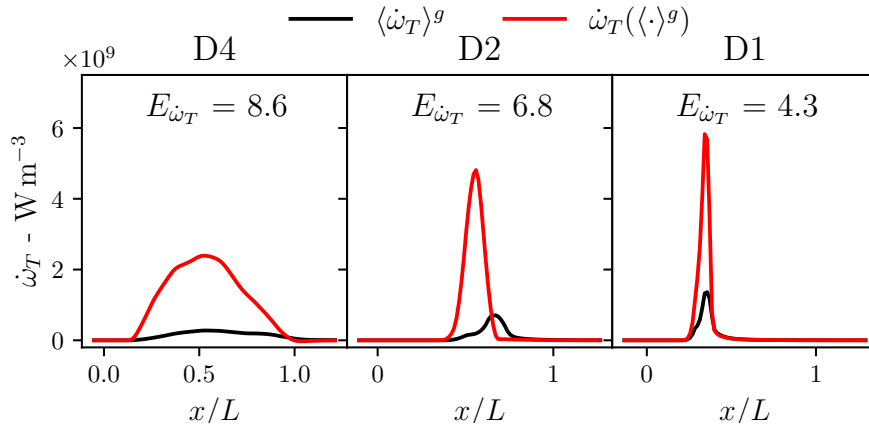


Figure 6.16. – Evaluation of the commutation error for heat release rate.

6.4.4. Discussion on the thermal Péclet number

In Chapter 2 we have seen that the ratio of pore diameter to thermal flame thickness \bar{d}_p/δ_L is equal to the thermal Péclet number $Pe_{p,th}$, and related to the macroscale commutation error of the reaction rates. In that line of thought, Figure 6.16 is complemented by cases R1 and R2 on Figure 6.17, which shows values of $E_{\dot{\omega}_T}$ for all geometries as a function of the mean pore diameter \bar{d}_p . The trend for varying pore size is seemingly validated among all geometry types. The supposed limit for infinitely small pore size is also shown, for which the gas phase becomes homogeneous at the scale of the (infinitely small) REV so that the commutation is *a priori* valid. A case with a mean pore size of 0.5 mm ($Pe_{p,th} \simeq 1$) was also performed (not shown) and appears to be consistent with the trend ($E_{\dot{\omega}_T} \sim 2$). The fact that $E_{\dot{\omega}_T} > 1$ for $Pe_{p,th} \simeq 1$ is coherent with the rationale developed in Chapter 2, arguing that the more stringent (shorter) thickness of reaction δ_R should be considered to assess the validity of the commutation. Asymptotically,

one has:

$$\delta_R \sim \frac{\delta_L}{\beta}, \quad (6.29)$$

where β is the Zel'dovich number. Supposing that the commutation error becomes negligible when $\delta_R \sim \bar{d}_p$, one finds the corresponding threshold value in terms of Péclet number:

$$\text{Pe}_{p,th}^{cr} \sim 1/\beta \sim 0.1 - 0.2, \quad (6.30)$$

above which the commutation is *a priori* invalid, and a closure model is required. We recall that, since hydrodynamic dispersion is also a function of the Péclet number and goes to zero for $\text{Pe}_{p,th} \ll 1$ [208], one can infer the important conclusion that there may be an intrinsic exclusion between the validity of the classical volume-averaged equations and the presence of hydrodynamic dispersion.

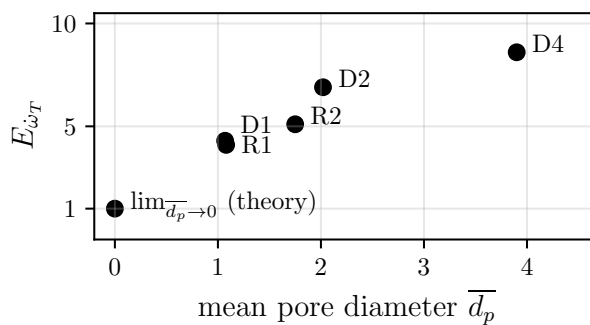


Figure 6.17. – Commutation errors for all domains.

6.5. A new model for reaction rates?

6.5.1. Phenomenology of burning rate: DPLS vs.VAM

In the spirit of closing the gap between DPLS and VAM, the mechanisms driving burning rates in the DPLS are now investigated. The aim is to propose an expression for the $\langle \dot{\omega}_k \rangle^g$ coherent with observations at the pore level. The first question to investigate is: if the flame does not burn in volume at REV scale, then which factors account for its burning rate?

In the framework of thin flames, one idea is to consider a *flamelet hypothesis*, that is, viewing the flame front as an infinitely-thin surface. Defining where and what is this surface is generally an intricate task. Usually, the fuel progress variable:

$$c_F = 1 - \frac{Y_F}{Y_{F,in}} \quad (6.31)$$

is used to near the maximum of heat release in the flame [309], and on that surface quantities such as consumption speed, stretch, species concentrations, etc. may be used to model the local consumption of the flame front. In this chapter, we have $F = \text{CH}_4$. As shown in Figure 6.18, the contour $c_F = 80\%$ (blue) seems to correlate well with heat release in our simulations, and is arguably a natural definition of “the” flame surface. However, in porous burners, contrary to classical wrinkled flames in free flows, the upstream temperatures are locally non-homogeneous - what has an influence on consumption speeds (Figure 6.3). Therefore, a local measure of preheating, upstream of the flame front, is necessary. This requirement apparently excludes the contour $c_F = 80\%$, because the influence of chemical heat release does not allow to retrieve reliably the local preheating information. One alternative solution is therefore to fix the flame

surface as the contour $c_F = 1\%$, upstream of the reaction and heat diffusion zones¹. However, as observed in Figure 6.18, this surface may differ substantially from that at $c_F = 80\%$ for the largest pore size (D4), but also in reticulated geometries (see for example R1). This may be attributed to the preferential diffusion of species, dispersion, and for geometry D4 especially, the large distortion of the flame fronts (Figure 6.9). One further alternative could consist in coming back to $c_F = 80\%$ and to measure the preheating on a corresponding point at $c_F = 1\%$, but all the tested attribution criteria (shortest geometrical distance, streamlines of velocity or progress variable) did not provide more insight on the problem or were ill-posed in some regions of the system. Therefore, being aware of the difficulties to assess where is the flame and how to measure its preheating, it is chosen to stick to the contour $c_F = 1\%$ and the flame surface \mathcal{A} is defined as:

$$\mathcal{A} \equiv \{c_F = 1\%\}. \quad (6.32)$$

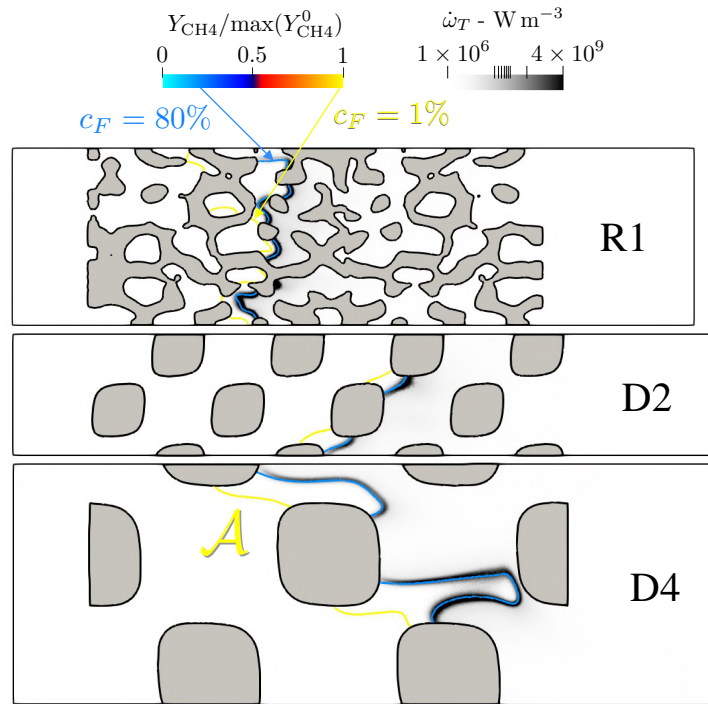


Figure 6.18. – Isocontours of 1% and 80% of fuel consumption (progress variable c_F).

On \mathcal{A} , the local temperature is noted $T_{\text{preheating}}$, the stretch rate κ , and the normal mass flux per surface unit \dot{m}_n . More precisely, by introducing the 3D field of normals to the progress variable \mathbf{n} :

$$\mathbf{n} = -\frac{\nabla c_F}{|\nabla c_F|}, \quad (6.33)$$

one can define the local mass flux as:

$$\dot{m}_n = -\rho_g \mathbf{u} \cdot \mathbf{n}, \quad (6.34)$$

and the stretch rate as:

$$\kappa = \nabla_t \cdot \mathbf{u}_t, \quad (6.35)$$

where the tangential component of velocity \mathbf{u}_t and divergence operator ∇_t on \mathcal{A} are [115]:

$$\mathbf{u}_t = \mathbf{u} - (\mathbf{u} \cdot \mathbf{n})\mathbf{n} \quad \text{and} \quad \nabla_t \cdot \mathbf{u}_t = -\mathbf{nn} : \nabla \mathbf{u}_t + \nabla \cdot \mathbf{u}_t. \quad (6.36)$$

1. this is relevant as long as $\text{Le}_{\text{CH}_4} \leq 1$, because in that case the fuel species profile is broader.

Locally, if the flame were 1D and solely governed by preheating effects, then one would find $\dot{m}_n = \dot{m}_0 \Gamma_p(T_{\text{preheating}})$. However, locally the flame front is subject to other phenomena, such as near-wall quenching and stretch within the interstitial flow. The presence of these phenomena are assessed in Figure 6.19, which shows a scatter plot of $\dot{m}_n/\dot{m}_0 \Gamma_p(T_{\text{preheating}})$ versus reduced

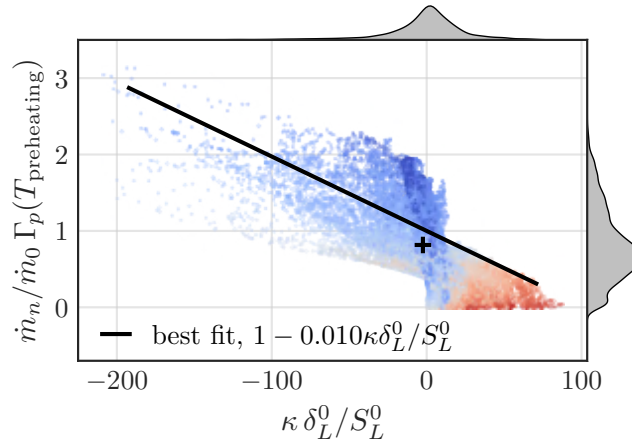


Figure 6.19. – Scatter plot and PDF on \mathcal{A} , domain D2. Blue cold (pore centers), red hot regions (near walls).

stretch rate $\kappa \delta_L^0 / S_L^0$ on \mathcal{A} for domain D2. Afferent probability density functions (PDF) are shown on the sides. The same plots for domains R1 and D4 are given in Appendix 6.B. Note that this plot resembles turbulent combustion studies [310]. Blue points indicate colder regions at the center of the pores, red points hotter regions near the walls. The cross in the middle marks the mean values. It is observed that the PDF of $\dot{m}_n/\dot{m}_0 \Gamma_p(T_{\text{preheating}})$ has a large peak and a mean value in the neighborhood of 1. This seems to show that preheating governs largely the burning rate at the pore level. The secondary peak near zero shows the influence of the walls - in these regions the flame is quenched and the no-slip condition leads to zero values of \dot{m}_n . Because there is seemingly a linear trend on the plot, we try and fit a function of the form $1 + c_F \cdot \kappa \delta_L^0 / S_L^0$, underpinning a preheated-stretched flamelet hypothesis:

$$\dot{m}_n = \dot{m}_0 \Gamma_p(T_{\text{preheating}}) \left[1 + c_F \cdot \kappa \frac{\delta_L^0}{S_L^0} \right], \quad (6.37)$$

though it is recognized that for geometries R1 and D4 there are large deviations to this model due to the difficulty in defining \mathcal{A} properly (see Appendix 6.B). In the following, $\langle \cdot \rangle^{\mathcal{A}}$ notes the integration on the flame surface \mathcal{A} . Using the symmetry conditions on the sides and the steady-state assumption, it is found that the total inlet mass flux is equal to \dot{m}_n integrated over \mathcal{A} , that is $\dot{M}_{\text{in}} = \langle \dot{m}_n \rangle^{\mathcal{A}}$. Accordingly, one can estimate the respective contributions of preheating and stretch on global burning rate by integrating and splitting Equation (6.37) into:

$$\dot{M}_{\text{in}} = \underbrace{\dot{m}_0 \langle \Gamma_p(T_{\text{preheating}}) \rangle^{\mathcal{A}}}_{C_p} + \underbrace{\dot{m}_0 c_F \frac{\delta_L^0}{S_L^0} \langle \Gamma_p(T_{\text{preheating}}) \kappa \rangle^{\mathcal{A}}}_{C_\kappa}. \quad (6.38)$$

For all five domains, it is found that $|C_\kappa| \ll C_p$, which is coherent with the fact that the reduced stretch rate is centered near zero. In Equation (6.38), one may then neglect C_κ and assume $C_p \sim \dot{M}_{\text{in}}$ which leads, by commuting further Γ_p with $\langle \cdot \rangle^{\mathcal{A}}$ to:

$$\Gamma = \Gamma_w \cdot \Gamma_p \left(\langle T_{\text{preheating}} \rangle^{\mathcal{A}} \right). \quad (6.39)$$

This commutation leads to less than a few percent difference for all domains. The flame wrinkling factor Γ_w results from the integration on \mathcal{A} :

$$\Gamma_w = \frac{\mathcal{A}}{\bar{\epsilon} \mathcal{A}_T}, \quad (6.40)$$

where it is recalled that \mathcal{A}_T is the transverse area of the domain. Equation (6.39) suggests that preheating and flame wrinkling are the two primary mechanisms for flame acceleration within PMC. Nonetheless, Table 6.5 shows that Equation (6.39) overestimates burning rate, except for case D4. This is explained by near-wall quenching, which shifts the distribution of $\dot{m}_n/\dot{m}_0\Gamma_p(T_{\text{preheating}})$ below unity in Figure 6.19. Furthermore, because these quenched regions are also the hotter regions of \mathcal{A} , there is a formal overestimation of $T_{\text{preheating}}$ and therefore of $\Gamma_p(T_{\text{preheating}})$. This overprediction is more pronounced for smaller pores, which may explain the surprisingly similar Γ values despite two-fold variations in \bar{d}_p : for decreasing pore size, there is an increase in heat recirculation but it may be compensated by larger near-wall quenching. This has potentially important practical implications, because it implies that enhancing burning rate in PMC may be preferentially achieved by increasing the solid thermal conductivity rather than reducing the pore size. To conclude, it is stressed that hydrodynamic dispersion, which is a macroscale effect, is absent from Equation (6.39) and the present local analysis of the flame front. At pore scale, it is not clear how the burning rate would be influenced by dispersion.

Table 6.5. – Γ and Γ_w values.

	R2	R1	D4	D2	D1
Γ , DPLS	4.91	5.51	6.35	4.76	5.24
Γ_w , DPLS	1.35	1.40	2.49	1.43	1.28
Γ , Equation (6.39)	7.00	10.18	6.02	6.36	9.18

We now focus on the modelling of burning rate in the VAM. Classically, reaction closure terms are simple commutations with the averages (no model):

$$\langle \dot{\omega}_k \rangle^g = \dot{\omega}_k \left(\langle \rho_g \rangle^g, \langle T_g \rangle^g, \langle Y_k \rangle^g \right). \quad (6.16)$$

If the flame front is assumed to be *locally adiabatic* in the VAM (which would correspond to the decoupled regime in [299, 307], in which the current simulations fall), then Equation (6.10) is locally the equation of a classical gaseous flame, whose burning rate is governed by the preheating of the fresh gases, but also by the increase in macroscale diffusivities due to the modelling of dispersion. Following asymptotic theory for unity Lewis flames, the burning rate increases like the square root of gas diffusivity. Accordingly we introduce the factor Γ_d , which represents the flame acceleration due to dispersion:

$$\Gamma_d = \left(\frac{\langle \lambda_g \rangle^g + \langle \rho_g \rangle^g \langle c_{pg} \rangle^g D^{\text{dis}}}{\langle \lambda_g \rangle^g} \right)^{1/2}. \quad (6.41)$$

In practice Γ_d varies a bit throughout the flame front, but an integral value for flame acceleration may be obtained in the unburnt gases. Thereafter, the resulting acceleration for the VAM is estimated to:

$$\Gamma = \Gamma_d \cdot \Gamma_p \left(\langle T_{\text{preheating}} \rangle^{\mathcal{A}} \right). \quad (6.42)$$

The difference between Equations (6.39) and (6.42) underlines the intrinsic phenomenological discrepancy between the DPLS and the VAM based on Equation (6.16), and the first-order

influence of dispersion on burning rate. It implies that in order to match to the DPLS, the burning rate of the VAM should be multiplied by Γ_w/Γ_d . To achieve this, one may consider another result of asymptotic theory which states that burning rate is proportional to the square root of the pre-exponential factors, and write:

$$\langle \dot{\omega}_k \rangle^g = \left[\frac{\Gamma_w}{\Gamma_d} \right]^2 \cdot \dot{\omega}_k \left(\langle \rho_g \rangle^g, \langle T_g \rangle^g, \langle Y_k \rangle^g \right). \quad (6.43)$$

To assess the performance of Equations (6.16) and (6.43), we perform again VAM simulations where the position of maximum of heat release is matched to the DPLS. The corresponding Γ values are reported in Figure 6.20. Also, the hypothesis $D^{\text{dis}} = 0$ with Equation (6.43) is shown.

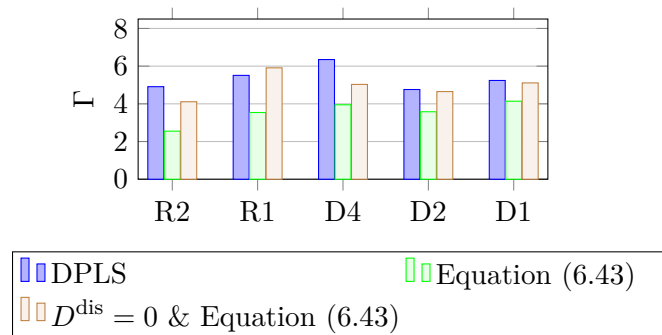


Figure 6.20. – Performance of closure models for DPLS.

In Figure 6.20, it is observed that the proposed model of Equation (6.43) always underestimates Γ . This may be attributed to the tendential underestimation of the flame surface area \mathcal{A} , but also to the absence of superadiabaticity in the VAM compared to the DPLS. Also, keep in mind that the level of non-adiabaticity of the local flame fronts in the DPLS and the VAM are not the same, because the wall quenching effects in the DPLS have not been explicitly modelled in the VAM. In addition, it is expected that this effect has the wrong trend for varying pore size: smaller pores lead to more non-adiabaticity but less dispersion, hence less non-adiabaticity in the VAM due to less broad profiles. Also, for a fixed pore size non-adiabatic effects in the DPLS are arguably very close between R and D geometries (same values for Γ and Γ_w) and non-correlated to dispersion, though the VAM seems substantially sensitive to it. Together with our previous concerns on the basic phenomenology of dispersion in the VAM, this suggests that the simultaneous coupling of dispersion, interphase heat exchange and combustion is yet to be understood properly. As intuited previously, the aggregate of macroscale modelling terms to build a VAM is therefore questionable. In order to assess the direct influence of dispersion on Γ , the hypothesis $D^{\text{dis}} = 0$ is considered in Figure 6.20. Large differences with and without dispersion, and a reasonable performance close to the original VAM model of Figure 6.12 are observed. It indicates that dispersion may not be the important parameter to consider to retrieve properly the burning rates in the VAM.

6.6. Conclusions of the chapter

3D direct numerical simulations of methane-air combustion in porous burners of finite length were conducted for various pore sizes and geometries, in cases where the flame thickness is lower than the mean pore size. A corresponding volume-averaged model based on classical equations and the same thermo-chemical scheme was fed with effective properties estimated directly on the computational domains. Direct comparisons between the 3D simulations and the 1D filtered model in terms of burning rate, physical profiles and *a priori* analysis could be achieved accordingly. This led to the following conclusions:

- in the 3D DPLS, sharp, wrinkled and longitudinally-distributed flame fronts are observed, in apparent contradiction with the upscaling hypotheses of the volume-averaged model. More especially, for 4 mm pores it was found that the flame fronts could be distorted across several pores ;
- contrary to 1D theory, flames could be stabilized in the downstream part of the burner, thanks to an adaptation mechanism through flame surface variations. Unfortunately, estimating this surface without 3D simulations is difficult ;
- substantial discrepancies in terms of burning rate and spatially-averaged profiles were observed between the VAM predictions and the DPLS ;
- an *a priori* analysis from the microscopic equations has shown that, while the effective solid conductivity and hydrodynamic dispersion can be approximately modelled by simplified macroscale closure terms with magnitudes estimated in independent (non-reactive) simulations, a very large error is introduced in the absence of a combustion model for the reaction rates ;
- the longitudinal distribution of the flame fronts along the burner axis makes the spatially-averaged profiles broader than in the VAM, which model a unique flame front ;
- tendentially, there is a mutual exclusion between the validity of current volume-averaged models and the presence of hydrodynamic dispersion ;
- hydrodynamic dispersion, although present in the system, does not appear to drive directly the burning rate of the flames at pore scale in the DPLS, contrary to the VAM where an increase in diffusivities enhances flame speeds. It was attempted to solve this phenomenological contradiction by a modification of the reaction rates, but the proposed model seems to underpredict burning rates - which may be explained by near-wall quenching ;
- locally, the burning rate of the flame fronts seems to be governed by a combination of preheating and wall quenching, while stretch effects seem to have negligible influence on average. However, the local non-adiabaticity related to this wall quenching are not modelled at the macroscale to date.

As a concluding remark, the author would like to stress that further numerical simulations are necessary to substantiate these findings, possibly in other geometries and for other pore sizes. Experiments could be useful as well, especially direct visualisations of internal flame fronts. However, measurements of temperatures, concentrations and gas output compositions, although important and necessary, will unlikely help directly in closing the gap between pore-scale combustion and volume-averaged models, which require microscale information only available to date in simulations. The fact that current state-of-the-art models suffers from such intrinsic flaws constitutes definitely an exciting direction for future research.

6.A. Energy and mass budgets micro *vs.* macro

We can now benchmark the quality of the VAM modelling terms by *a priori* analysis. The notations for the various terms in this Appendix were introduced in the upscaling procedure of Chapter 2. The magnitude of effective coefficients used for comparison are that of Table 6.3. Geometry D2 is considered, and qualitatively similar results were obtained in the other geometries enabling similar conclusions. Fundamentally, the following *a priori* analysis is aimed at answering the two following questions:

- do the effective parameters have the correct intensity (*i.e.* magnitude)?
- are the functional forms for closure models accurate representations of the microscale physics?

A look at Figures 6.21 and 6.22 allows to draw the following conclusions:

- the macroscopic mass sources seem qualitatively-well modelled by the hydrodynamic dispersion closure model, although there are some issues regarding the functional form and intensities for the fuel equation (CH₄), especially near the reaction zone. This is a likely a consequence of the sharp flame fronts ;
- the macroscale effective solid conductivity seems to follow very well the functional shape, although the magnitude may have been underestimated in the independent simulations. This change would lowly affect the resulting burning rates and profiles in the VAM ;
- concerning the dispersion of heat in the gas equation, there seems to be a major issue concerning the terms Ψ_1/Ψ_2 but those are negligible in magnitude compared to Ξ_1/Ξ_2 . The errors on Ξ_1/Ξ_2 may seem appear reasonable but they are large in magnitude, of the same order of the heat release rate. The fact that the model shows a negative peak in the reaction zone is the signature that locally, heat does not back-propagate due to the enhanced diffusivity: the gradient of macroscopic temperature is positive but the hydrodynamic field does not propagate this information through an increase in diffusivities at the macroscale. This is a direct indicator of the presence of small flame structures locally.

6.B. Additional plots local flame structure on \mathcal{A}

The plots of Figure 6.23 indicate that in cases R1 and D4, the stretch correlation are affected a lot by the difficulty to define \mathcal{A} and measure the preheating. Although the plots resemble strongly that of D2 and indicate a good overall modelling strategy, in domain R1 the randomness of the structure adds noise to the system, because different pores present different flow configurations and different preheating temperatures, but also the smaller pores disqualify the flamelet hypothesis. In domain D4, due to the largely distorted flame fronts, the inner (colder) regions can consume more fuel because \mathcal{A} is defined too upstream and not sufficiently curved “inside” the flame.

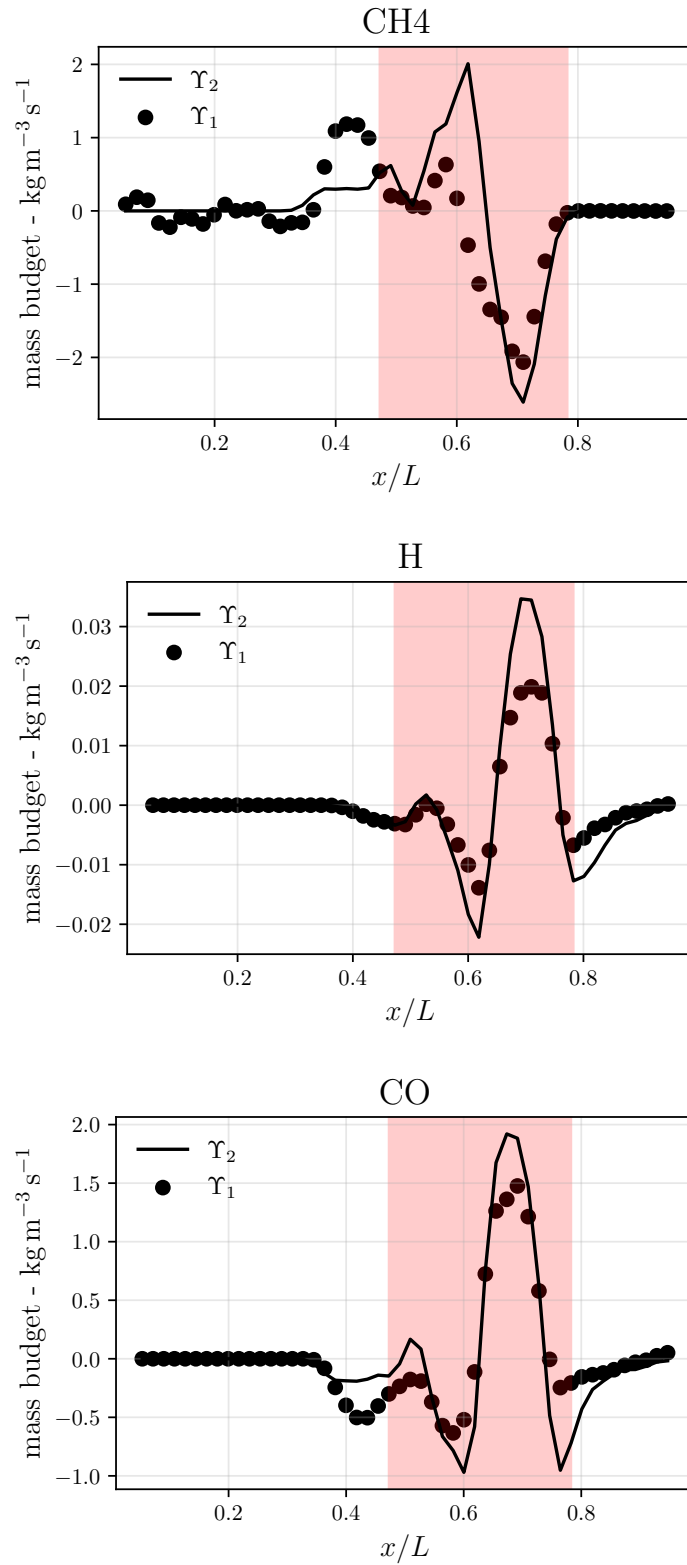


Figure 6.21. – Mass budgets: comparison of the terms Υ_1/Υ_2 (species equation) for domain D2, as defined in Equation (2.70). The red region indicates the reaction zone.

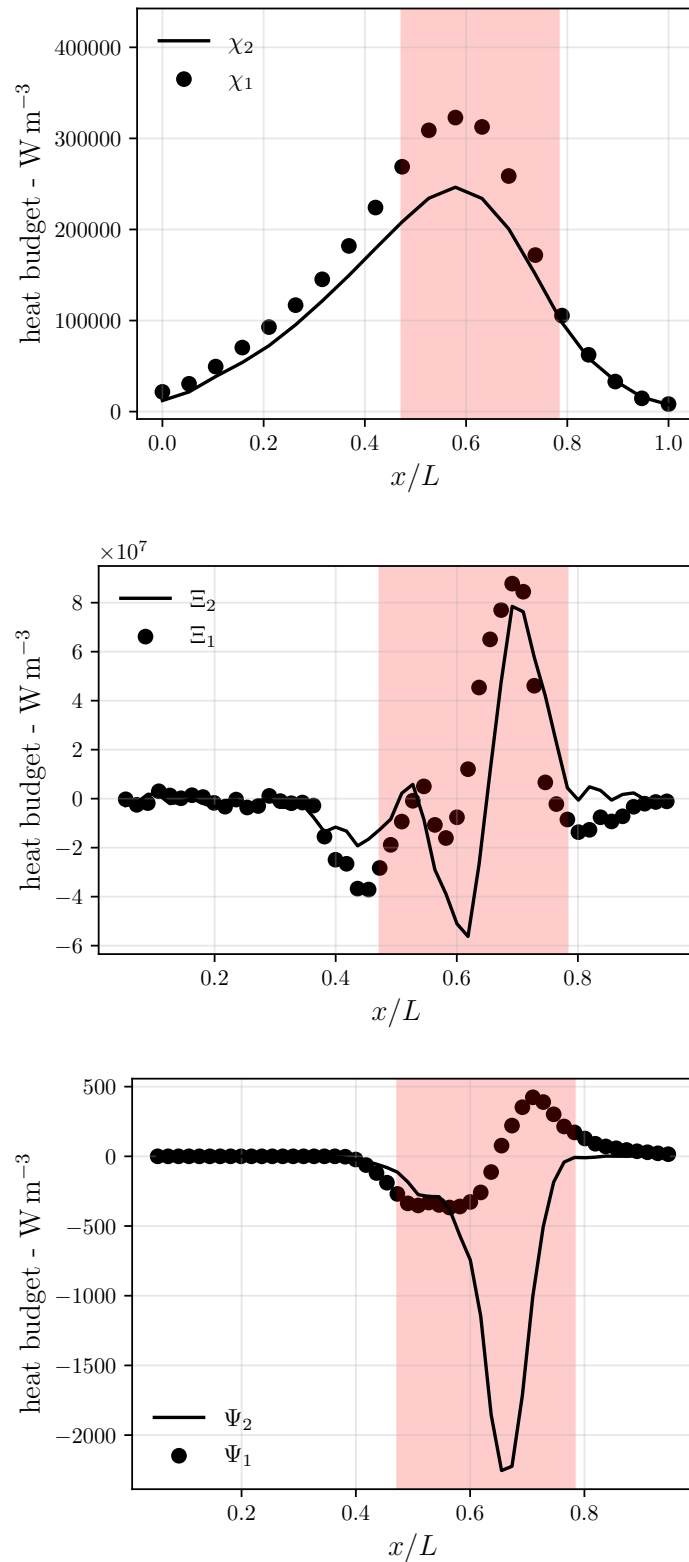


Figure 6.22. – Energy budgets: comparison of the terms χ_1/χ_2 (solid equation), Ξ_1/Ξ_2 , Ψ_1/Ψ_2 (gas equation) for domain D2, as defined in Equations (2.64), (2.78) and (2.79). The red region indicates the reaction zone.

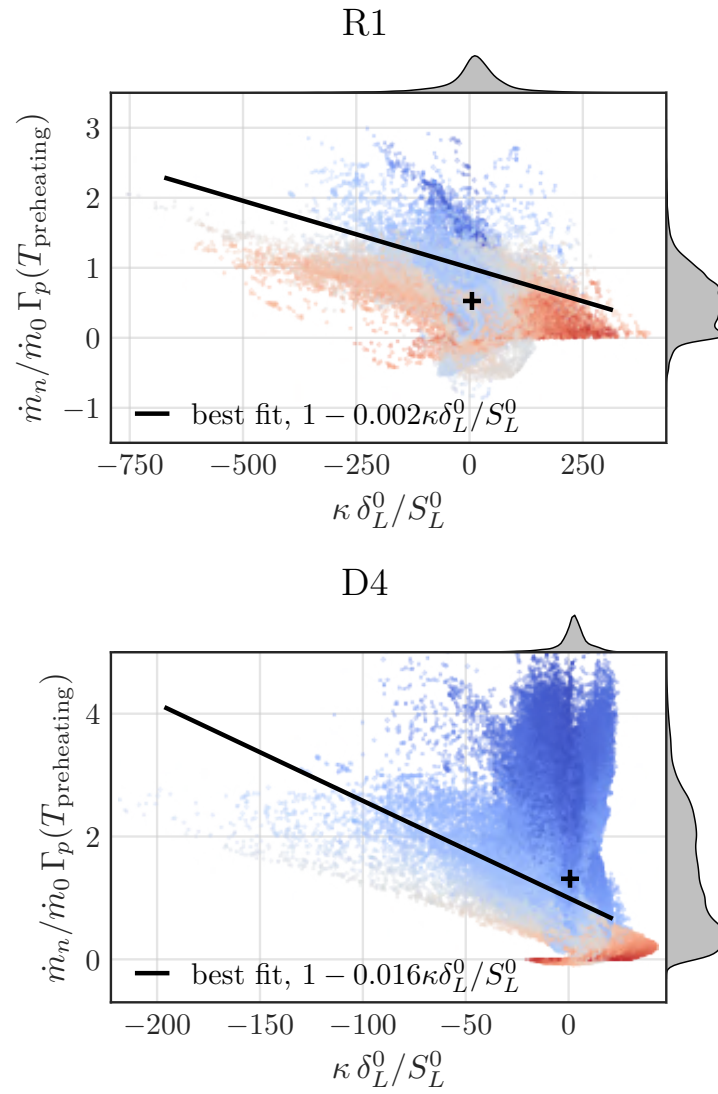


Figure 6.23. – Scatter plot and PDF on \mathcal{A} , domains D1 and D4. Blue cold (pore centers), red hot regions (near walls).

Specificities of hydrogen combustion within porous media

This last chapter presents the first pore-level simulations of hydrogen combustion within porous media. Contrary to methane-air flames, the high reactivity of hydrogen leads to larger Reynolds numbers, that is, unsteady solutions for classical pore sizes. For geometry D2, a periodic cycle is identified, and is shown to be governed mainly by the hydrodynamic field. The influence of preferential diffusion of hydrogen is then investigated in the 3D solutions. It is shown that the local flame structure is very different from methane-air mixtures. The modification of the flame shape is attributed both to the modification of the interstitial flow and preferential diffusion effects. The increased errors in terms of macroscale modelling are underlined. In order to take a step back, the chapter begins by recalling some generalities about hydrogen combustion in fields related to porous media combustion, hopefully conceptually relevant for future studies. These results are still the topic of current research and must be considered as *work in progress*.

Overview

7.1. Chapter introduction	158
7.1.1. Freely-propagating flows	160
7.1.2. Meso and microcombustion	160
7.1.3. Laminar burner-stabilized flames	161
7.1.4. Turbulent combustion	161
7.2. Hydrogen-air 1D laminar flames	162
7.3. Methodology	164
7.4. Results and discussion	164
7.4.1. Unsteady flames	164
7.4.2. Steady flames?	167
7.4.3. Local flame structure	169
7.4.4. Burning rates	170
7.4.5. Modelling of the reaction rates	172
7.4.6. Burning below the flammability limit	173
7.5. Conclusions of the chapter	173
7.A. Local flame structure in geometry D1	174

“I have no special talents. I am only passionately curious.”

ALBERT EINSTEIN

7.1. Chapter introduction

Unfortunately responsible for climate change, fossil fuels constitute the spine of modern civilizations. Today, almost every manufactured object and service finds its origin in oil extraction, either used as a chemical derivative/by-product or as a primary energy resource for heat/motion generation. The finite and declining nature of this resource constitutes definite threat of structural recession and political instabilities. Concerning energy production, there exists alternatives such as biomass or nuclear, hydro, solar and wind electricity, but those also present shortcomings (cost without abundant oil, intermittency, materials unavailability, waste, non-closed life cycle or usage conflicts). This does not stop political leaders to show some degree of optimism (not to say wishful thinking) and alternative technological solutions are put forward to decarbonize economies and become more resilient wrt. the decline in oil reserves. Hydrogen, produced from renewable energies, is one of these alternatives. It may be used for direct heat generation, or in gas turbines/internal combustion engines/fuel cells to decarbonize transport. This explains the recent efforts to understand the particular behavior of this fuel, which poses large challenges in terms of technology and safety.

Contrary to methane, lean hydrogen-air flames are characterized by substantial preferential diffusion of lightweight species, *i.e.* Lewis numbers below unity, and increased reactivity *i.e.* lower activation energies. From the viewpoint of 1D laminar flames, although a reduction in the fuel Lewis number theoretically decreases flame speed [115], the increase in reactivity related to the chemical reactions is largely dominant hence flame speeds attained with hydrogen-air mixtures are much larger (up to 3 m s^{-1}). Hydrogen flames are also characterized by larger flammability limits, faster transition to detonation and lesser visibility of the reaction zone [311]. Those come with considerable safety issues that must be handled and/or mitigated, notably in the context of household applications. Interestingly, trapping a hydrogen flame into a porous matrix may help tackle some of these challenges in different ways. Flame submersion solves the issue of visibility, for instance in the context of cooking appliances or radiant heating. Also, as shown in [34] heat recirculation theoretically enables the combustion of mixtures below the flammability limits at ambient conditions, what has a triple advantage: (1) ultra-lean combustion emits little NOx, (2) in the case of leaks the exiting mixture is not flammable, and (3) flashback is intrinsically prevented.

Surprisingly, there has been only a handful studies of “simple” hydrogen-air combustion within porous media. On the experimental side, Trimis and Wawrzinek [312] studied the critical quenching diameter of various fuels at various equivalence ratios, and found that lean hydrogen-air flames would propagate in burners of significantly smaller pore sizes. Su et al. [313] compared the stabilization of lean hydrogen-air flames in a two-staged porous burner. Two materials were compared, namely SiC and Al_2O_3 . Several combustion modes were observed, namely surface combustion, submerged and flashback. It was found that flashback was favored in Al_2O_3 burners, and combustion below the LFL was also observed. Results indicate that no stable combustion could be achieved within the upstream layer. Qu et al. [89] proposed also an experimental investigation of a two-layer burner with different fuels including pure hydrogen, and found that the burner could be operated similarly to other fuels near the flammability limit $\phi_{LFL} \sim 0.3$. Li and co-workers [98, 144, 263] proposed a series of investigations of hydrogen combustion in a 1-mm

planar microcombustor in which a porous medium of very small pore size was inserted. The proposed volume-averaged numerical model seemed to retrieve properly the experimental findings. Compared to the free-flame microcombustor, the insertion of the porous medium allowed to increase radiant efficiency by transferring a larger portion of the chemical enthalpy released to the solid boundaries. Kakutkina et al. [22] studied experimentally the filtration combustion of various fuels and found that the volume-averaged model overpredicted more the maximum temperature achieved in the domain for hydrogen. This was attributed to the local preferential diffusion effects, though the arguments used to get to this conclusion were only based upon macroscopic measurements and the volume-averaged equations. On the numerical side, only a few works are reported. Roohi et al. [314] studied H_2 -air combustion in a 2D volume-averaged model and found no particular behavior associated to the fuel. More recently, Qian et al. [149] proposed a diverging geometry for a hydrogen-air porous microcombustor and found that the flammability range and operability were largely improved by this burner design. Saldeira and Susantez [315] proposed a simplified asymptotic model allowing non-unity Lewis fuel, but no specific influence of the Lewis number on recirculation efficiency and temperature profiles were reported.

Other studies addressed the combustion of hydrogen combined with other fuels. Nozari et al. [316] studied experimentally the combustion of ammonia-hydrogen-air flames and found low NOx emissions under rich conditions. Combustion efficiency increased with hydrogen addition. Gauthier et al. [317] compared 1D numerical and experimental measurements of methane-hydrogen-air flames to account for the NOx formation mechanisms. Arrieta et al. [318] performed an experimental study with various H_2/CO mixtures in a two-staged porous burner. Increasing the proportion of hydrogen content was found to decrease CO emissions but little effect on the NOx emissions was reported, which were already very low (~ 1 ppm). Huang et al. [319] performed an experimental and numerical study of a two-staged porous burner with H_2/CO mixtures and predicted an increase in CO emissions with increasing upstream solid conductivity. Alavandi and Agrawal [31] have also shown that a two-staged porous burner could be operated with high degree of flexibility from pure hydrocarbons to syngas combustion. Tseng [320] investigated numerically the effects of hydrogen addition to methane-air flames inside porous media, and from the point of view of the 1D volume averaged equations no particular behavior except increased burning rates was reported (however, they noted that the numerical model predicted higher NOx emissions than the adiabatic laminar flame, which seems contradictory with trends in the literature, indicating that pore-level phenomena may be dominant from the determination of pollutant emissions). Dai et al. [321] proposed an original concept of hydrogen addition from the burner walls of a two-step burner, apparently showing some degree of pollutant control.

In all the above-mentioned studies, the pore-scale specificities of hydrogen could not be unveiled because experiments measured only macroscopic quantities, and because numerical simulations were solely based upon the volume-averaged equations. In VAM, preferential diffusion effects are restricted to the macroscopic scale, with little effects on the volume-averaged profiles and resulting burning rate - especially in 1D. In Chapter 6, we have seen that even for near-unity Lewis fuels the classical combustion model is already incorrect. In this line of thought, the present chapter addresses the following questions: what is the structure of a hydrogen flame inside porous burners? Do further modelling errors arise with this fuel? And what are their origins?

Because no numerical simulation or experiment has yet unveiled the structure of hydrogen-air flames inside porous burners, it is difficult to list and/or predict all the possible particularities that may arise for different pore sizes, geometries, materials, equivalence ratios, inlet velocities, burner lengths, etc. Nonetheless, previous research in related fields may provide some hints and research directions. Porous media combustion lies at the intersection between four distinct fields of investigation:

- *freely-propagating flames* for combustion occurring in possibly large porous voids ;
- *mesoscale and microscale burners*, which present large degrees of non-adiabaticity and a zoology of flame states (oscillating, repetitively extinct and ignited, asymmetric, etc.) ;
- *burner-stabilized flames*, because each pore behind a throat acts as a flame holder conceptually similar *e.g.* to perforated plates ;
- *turbulent combustion*, obviously in the presence of unsteadiness or, following the analogy developed in Chapter 2 and 6, even in steady state due to the internal convolution of the flame front.

These domains are briefly reviewed in the light of possible phenomena occurring with hydrogen as a fuel. The reader should not be surprised that some important works may have been omitted in each field, because the main focus of this chapter is not to provide a comprehensive study of hydrogen combustion but rather an overview of the possible physical phenomena that can be encountered in porous burners using hydrogen.

7.1.1. Freely-propagating flows

Inside porous voids, especially when they are much larger than the flame thickness, the flame may present instabilities found in freely-propagating flows. In addition to the natural Darrieus-Landau (hydrodynamic) instability, related to density jump between fresh and burnt gases [322], hydrogen flames present an additional destabilizing mechanism known as “thermo-diffusive” [323]. For free flows in sufficiently large domains, these instabilities lead to the formation of highly-corrugated, cellular, unsteady flame front structures, which present locally strong variations of reaction rates and increase the total flame surface, leading to substantially larger consumption speeds. Those have long been the topic of theoretical predictions [324, 325], experimental [326, 327] and numerical studies [328, 329]. Among them, the recent numerical works of Berger et al. [330] may be highlighted, which addressed thoroughly the linear and non-linear dynamics of lean hydrogen planar flames subject to small initial perturbations for varying mixture parameters. They found that instabilities were more pronounced for decreasing equivalence ratio, decreasing inlet temperature, and increasing pressure. Recast with global flame parameters, this implied an increase in growth rate for increasing expansion ratio, increasing Zel’dovich number and decreasing Lewis number. The characteristic size (wavelength) of these instabilities is typically of the order of several flame thicknesses, and they seem to be damped at lower wavelengths. This latter remark is particularly relevant for porous media combustion, because the structure of the interstitial flow and the spatial constraint related to the pore size indicate that large-scale instabilities may be reduced by the porous matrix for decreasing pore size. Also, generally-speaking preheating may have a stabilizing behavior.

7.1.2. Meso and microcombustion

Micro-scale (resp. mesoscale) burners are defined by combustion inside small channels of width near/below (resp. near/above) the quenching diameter of the mixture [331]. The sustain of combustion inside such small channels is typically enabled through heat recirculation, catalytic treatment or external heating, being conceptually close to porous media. And even though porous structures are typically more tortuous and/or random than in micro/meso combustion, the two fields share the same volume-averaged equations at the macroscopic scale - though dispersion is rarely present due to the much smaller Péclet number encountered in micro/mesoscale channels. Depending on the geometry, equivalence ratio, burning rate and channel width, a variety of steady and unsteady combustion regimes can be found. For example, for low velocities and near extinction limits a regime of flame repetitive extinction and ignition (FREI) is sometimes observed [332]. It is typically allowed by the large solid heat capacity so

this regime is also seen in externally-heated channels [333]. Other particular regimes, including mild [334], oscillatory [335], asymmetric [333] rotating [336] and spinning [337] flames have been observed. Concerning specifically hydrogen, a series of studies in micro/mesoscale combustors were conducted [338–346], some with designs close to porous media [263, 347] but the variety of flame dynamics is globally the same than for methane-air combustion. A consistent trend between methane-air and hydrogen-air combustion is that the variety of flame regimes increases with channel width [348]. The fact that the dynamics of hydrogen flames is similar to methane counterparts is partly due to the fact that when the channel size is of the order of the flame thickness, preferential diffusion effects are less visible. However, it is worth mentioning situations when the Lewis number has shown to play a role at these small scales, for instance in flashback in the study of Kurdyumov et al. [349] or in the triggering of asymmetric behavior in the works of Alipoor et al. [350]. Also, compared to tortuous and stochastic porous media, the fact that most micro/mesoscale combustors present “straight” geometries may lead to a richer variety of flame regimes. Due to the random pore distribution it is indeed possible that the various oscillations and asymmetries be damped and/or governed mostly by the interstitial hydrodynamic field. More work is required in this direction, notably through transient DPLS.

7.1.3. Laminar burner-stabilized flames

Experimentally, it has long been observed that hydrogen flames behind holes/slits are capable of flashback at much larger ratios of bulk velocity to flame speed and present larger heating of the flame holder. These features are of course undesirable from both safety and operation viewpoints. From the early critical velocity gradient theory of Von Elbe and co-workers [351, 352] much progress in the understanding of flashback dynamics was achieved and it has been shown that effects of preferential diffusion and burner pre-heating are very important for the prediction of flame shape and stability [353]. With lean hydrogen-air flames, due to the preferential diffusion of lightweight species and oxygen availability everywhere, it is classically observed that the peak of heat release rate is shifted *on the sides* of the flame holder, and an extinct zone exists downstream of the injector centerline: the flame is “open”. In other terms, the structure of non-unity Lewis number flames lies farther from their 1D laminar counterpart. In porous media, as observed in Chapter 6 there is a local anchoring of the flame fronts downstream of the porous obstacles (throats), which act locally as small laminar burners. It is therefore expected that the specificities of hydrogen for burner-stabilized flames transposes into porous media combustion: pore-scale flashback is more likely to occur.

7.1.4. Turbulent combustion

When the Reynolds number is increased, we have seen in Chapter 2 that the flow becomes progressively unsteady and chaotic inside the pores. For hydrogen combustion, the increased reaction rates may lead to higher velocities thus non-steady behavior and turbulence. There is a plethora of research regarding the modelling of turbulent combustion [115] but the synergistic influence of hydrogen combustion on turbulence and afferent modelling strategies are currently topic of active investigations. For the sake of brevity and because these issues lie partly out-of-scope, let us simply state that in porous media, the turbulence constrained inside the pores may require additional modelling subtleties in addition to the free-flow models, not to mention the influence of heat transfer to the walls and non-homogeneous preheating effects. Certainly, for very high Reynolds numbers a specific closure for reaction rates will be required in the volume-averaged model. Also, in the line of thought of viewing steady combustion inside porous media as “stationary turbulence”, such models may be implemented even in steady-state models to take into account, conceptually-speaking, the influence of preferential diffusion at the macroscale.

7.2. Hydrogen-air 1D laminar flames

Before diving into the details of the 3D DPLS, it is insightful to take a look at the 1D adiabatic laminar flames for the various mixtures considered. The same version of CANTERA than in Chapter 6 is used, that is, a version of sharing the same thermo-chemical scheme. The built-in adaptative mesh refinement is used (parameters: ratio=2, slope=0.1, curve=0.05). The flames are initialized at high inlet temperatures progressively decreased until convergence fails (*i.e.* at the lean flammability limit).

Figure 7.1 shows laminar flame speeds of various mixtures for varying unburnt inlet temperature T_u . It is observed that the response of hydrogen to temperature is much more pronounced than methane. This foreshadows the need to inject the fresh mixture at larger velocities, and a propensity of the flame to flashback more easily. Also, for temperatures approximately above 850 K, the hydrogen-air solutions computed in CANTERA become dependent upon the domain length, and the corresponding flame structures do not resemble classical laminar flames. It corresponds to the “auto-ignition” of the mixture, lying outside the self-propagating mode. Although reaching 850 K in the porous matrix requires quite large recirculation efficiencies ($\eta_{rec} \sim 0.3$ for $\phi = 0.38$) and not encountered in our simulations, following Figure 3.3 of Chapter 3 it is not excluded that a particular regime of auto-ignition occurs within porous matrices in general. The thicknesses of the temperature δ_L^0 and fuel species profiles δ_c^0 are shown in Figure 7.2. Their definition is based on the gradients as:

$$\delta_L^0 = \frac{1}{\max(|\nabla\theta_g|)} \quad \text{and} \quad \delta_c^0 = \frac{1}{\max(|\nabla c_F|)}. \quad (7.1)$$

For methane, it is observed that $\delta_L^0 > \delta_c^0$, the two values are close and follow the same trend, which is consistent with the near-unity Lewis number $Le_{CH_4} = 0.97$. This is different for hydrogen. At ambient conditions δ_c^0 is larger than δ_L^0 , consistent with the prescribed low Lewis number $Le_{H_2} = 0.30$. Interestingly, this behavior is inverted for temperatures above 580 K, and the thermal flame thickness follows a non-monotonous trend with temperature. This indicates serious modifications of the 1D flame structure at high temperatures for hydrogen and the increasing size of the reaction zone wrt. the diffusion zones. This is illustrated in Figure 7.3, which shows the spatial flame structures for two inlet temperatures $T_u = 300$ K and 800 K. Note that for H_2 at 300 K, the flame structure is already not typical of “textbook” flames. The reaction zone is already quite large and impedes largely upon the thermal diffusion length scale. At higher temperatures, the fact that heat and species diffusion length scales merge indicates that thermo-diffusive effects may be damped by preheating. In [330] it was observed that thermo-diffusive instabilities reduce largely for large preheating values. In addition to the reduction in expansion ratio for increasing preheating temperatures, it is likely that the modification of the flame structure plays a major role as well.

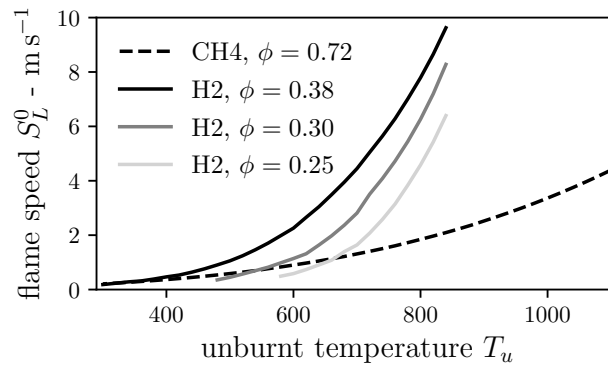


Figure 7.1. – Flame acceleration due to preheating for varying fuel and equivalence ratio.

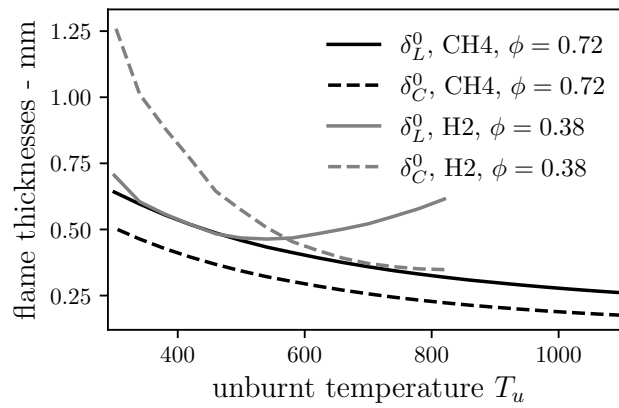


Figure 7.2. – Evolution of δ_L^0 and δ_C^0 as a function of temperature for two methane-air and hydrogen-air flames.

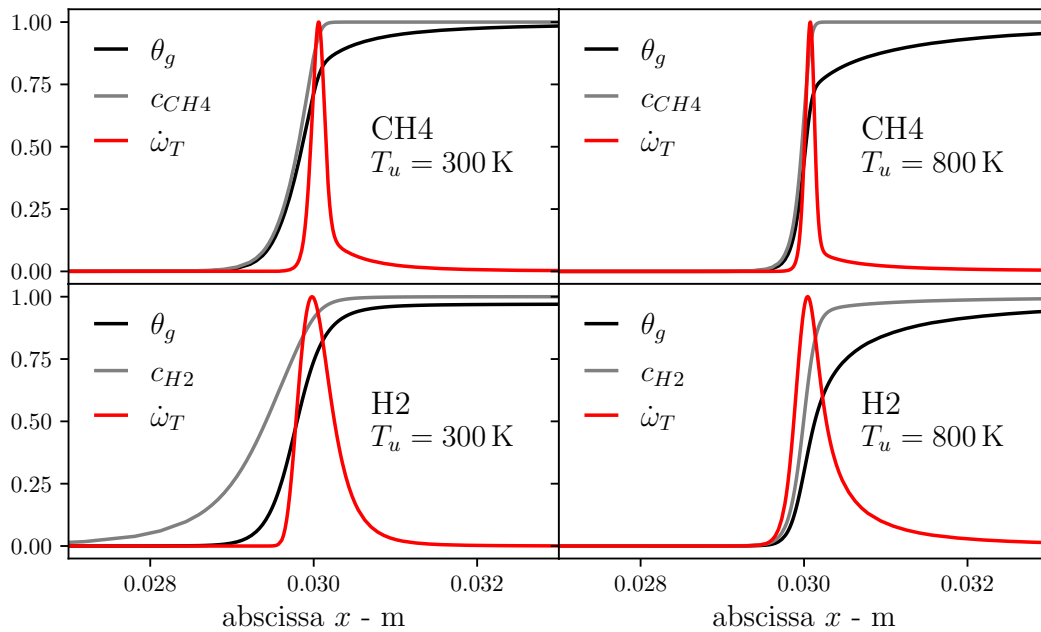


Figure 7.3. – Comparison of spatial flames structures for CH4 and H2 at 300 and 800 K.

7.3. Methodology

The combustion of H₂-air flames is considered in the previous geometries D1, D2 and R1 (see Figure 6.1 of Chapter 6). Due to the limited amount of computational resources, it was not possible to explore as many geometries, flow rates and conditions than with methane. Following the convergence study of Chapter 5, the same mesh of uniform size 80 μm is adopted. The baseline mixture has an equivalence ratio $\phi = 0.38$ (see Table 7.1), yielding the same laminar velocity than the previous CH₄-air flame at $\phi = 0.72$ at ambient conditions. The same pointwise governing equations, boundary conditions and chemical scheme are used (see Appendix A). Noteworthy, the species HO₂ is quasi-steady.

ϕ	S_L^0	δ_L^0	T_{ad}
0.38	20 cm s ⁻¹	0.65 mm	1383 K

Table 7.1. – Adiabatic free-flame properties.

In anticipation of the results, almost all computed solutions with the baseline value for dynamic viscosity are unsteady. As in Chapter 6, increases in dynamic viscosity are again considered, but given its prevalence some attention is also paid to unsteady behaviors. For transient studies, it is not affordable to match the time steps of solid and fluid domains from scratch, so the unsteady state is first approached by the decoupling method. The convergence criteria are applied to the mean values of the signals of total kinetic energy, heat release rate, mean temperatures, interphase heat transfer, etc., and the computation is then continued by matching the time steps. This avoid catching the response of the solid to short oscillations of the flame surface and position whilst keeping the total computational cost reasonable.

7.4. Results and discussion

7.4.1. Unsteady flames

Although having the same value of S_L^0 than the methane-air flames presented in Chapter 6, the present hydrogen-air mixture requires larger inlet velocity to sustain a submerged combustion mode (typically 2.0 m s⁻¹ instead of 0.6 m s⁻¹). This is a direct consequence of the higher reactivity of hydrogen chemical reactions with increasing temperature, as shown in Figure 7.1. Simultaneously, the lower adiabatic temperatures decrease the gas viscosity thus larger Reynolds number are attained within the porous voids. A consequence is that for all the geometries considered except D1, no steady behavior was observed for hydrogen flames. This constitutes a first modelling difficulty: the steady-state volume-averaged formalism may be fundamentally unadapted for classical pore sizes with H₂.

Before showing solution points where the viscosity (thus Reynolds number) was artificially modified as in Chapter 6, and the afferent consequences of this modification, it is interesting to study in more details the pore-level nature of the unsteady behavior observed inside the burners. For these unsteady solutions, it is verified that the temporal average values have converged, and the time steps of fluid and solid are matched after this convergence to make sure that the observed oscillations do not come from an artificially-fast coupling between the solid and gas phases. Figure 7.4(left) shows the temporal signal of total kinetic energy E_{cin} divided by its temporal average $\langle E_{cin} \rangle_t$, for geometry D2, inlet velocity $U_{in} = 2.0$ m s⁻¹ and matched time steps. Oscillations very close to a cosine mode are observed, with a peak-to-peak amplitude of approximately 10%. The corresponding power spectrum is shown in Figure 7.4(right), and a strong peak around the frequency $f = 1385$ Hz is clearly discernible. This indicates that the oscillations follow a quasi-periodic pattern, what is likely to emit noise in practical devices. In

order to investigate the origin of this regular pattern, one may consider the instantaneous fields at the timestamps $t_{1 \rightarrow 5}$ marked in Figure 7.4. Slices of velocity norm $|\mathbf{u}|$ and heat release rate $\dot{\omega}_T$ are shown accordingly in Figure 7.5, with the averaged field over several cycles on top. It is observed that the velocity magnitude *upstream* of the flame front shows oscillations over time, and dynamically one observes that the flame travels towards low-velocity regions (more visible in a video). These upstream oscillations result from the formation of vortices in the wake of the porous obstacles, and seem apparently periodic in time. This is reminiscent of the vortex shedding of a Von Karman street, for example behind a cylinder [354]. For such vortices, the natural frequency leads to Strouhal numbers typically near 0.2 [355]. In this line of thought, the global Strouhal number St may be defined by considering an approximation of the size of a porous obstacle d_s :

$$d_s \sim (1 - \epsilon)d_p, \quad (7.2)$$

so that:

$$St = \frac{f(1 - \epsilon)d_p}{U_{in}/\epsilon} \quad (7.3)$$

where U_{in}/ϵ is the interstitial velocity - preheating effects set aside. For the present frequency $f = 1385$ Hz, this leads to $St = 0.33$, a value very close to the classical Strouhal number for vortex shedding behind obstacles in free flows. Together with the observations of the velocity fields in the numerical simulations, it is therefore possible to conclude that the oscillations observed in the numerical simulations have a hydrodynamic origin related to the increase in Reynolds number, corresponding to the progressive onset of the transition regime (before turbulence). In order to substantiate further this claim, one may consider a cold flow simulation (isothermal 300 K) for the same inlet velocity. As shown in Figure 7.6, the signal of reduced velocity magnitude $|\mathbf{u}|/\langle|\mathbf{u}|\rangle_t$ at point P_1 and its power density spectrum present a fundamental peak of frequency close to 1385 Hz, the difference being related to preheating in the reactive case which reduces the Reynolds number through an increase in dynamic viscosity. This shows that the oscillation phenomena is somewhat independent upon combustion itself. Moreover, the fact that the peak in Figure 7.4(right) is centered mostly on a single frequency indicates that combustions acts as a filter which “selects” and amplifies the fundamental mode of the vortex street. A local measure of velocity just ahead of the flame front was used in the cold case instead of the global information $E_{cin}/\langle E_{cin} \rangle_t$ because its spectrum is not a linear comb as Figure 7.6(right). This substantiates further that combustion acts as a filter which amplifies a given mode related to the hydrodynamic field. Interestingly, in geometry R1 no particular frequency is visible in the unsteady signal of $E_{cin}/\langle E_{cin} \rangle_t$. This indicates that the noise generation from lattice-based porous media may be larger than in random geometries.

The present results exclude oscillations arising from other sources such as FREI (repetitive extinction and extinction), which typically occurs at much lower velocities [348] - and here the flame does not extinguish. The fact that similar oscillations were observed for methane in case D4 (not shown) indicate further that the oscillations are not primarily driven by thermo-diffusive instabilities and/or preferential diffusion. In general, thermo-diffusive instabilities require channels of at least, say, 10 flame thicknesses, what may occur for pore sizes of 6-7 mm or larger. Such sizes correspond to 10-15 PPI or below, and for increasing pore size the influence of turbulence will also increase. One partial conclusion is that for hydrogen-air flames, preferential diffusion may not give rise to specific oscillations for realistic geometries. Also, it is possible that some other unsteady modes of combustion observed in micro/meso-scale combustion be found in our geometries, but these were not investigated.

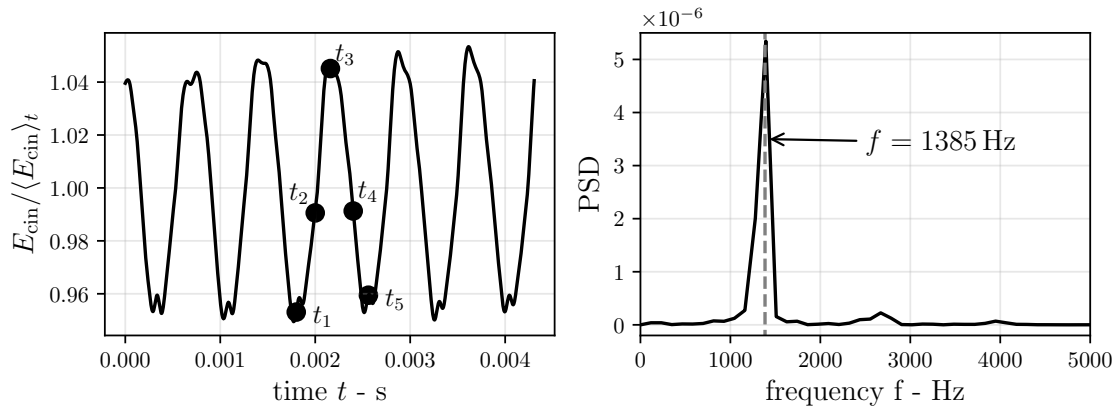


Figure 7.4. – Left: ratio of total kinetic energy E_{cin} with its temporal average. Right: power spectrum density (PSD) of the left signal. Domain D2.

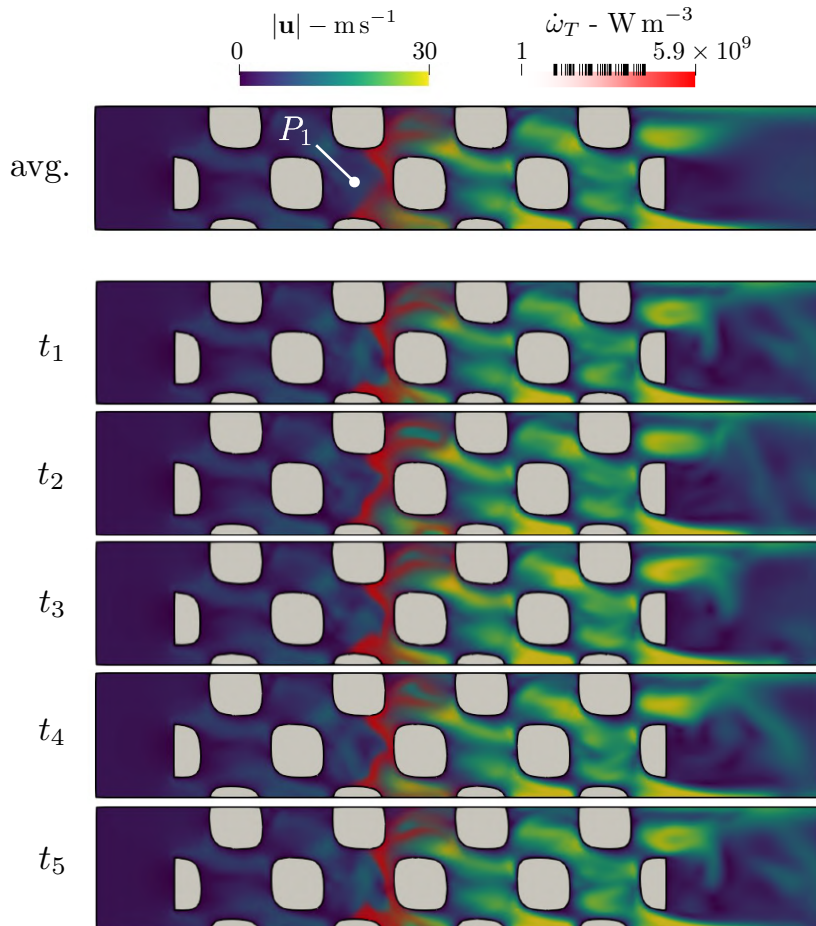


Figure 7.5. – Top: time-averaged fields of velocity norm and heat release rate. Bottom: instantaneous fields at $t_{1 \rightarrow 5}$ as defined in Figure 7.4. Domain D2, $U_{\text{in}} = 2 \text{ m s}^{-1}$, $\text{H}_2\text{-air}$, $\phi = 0.38$.

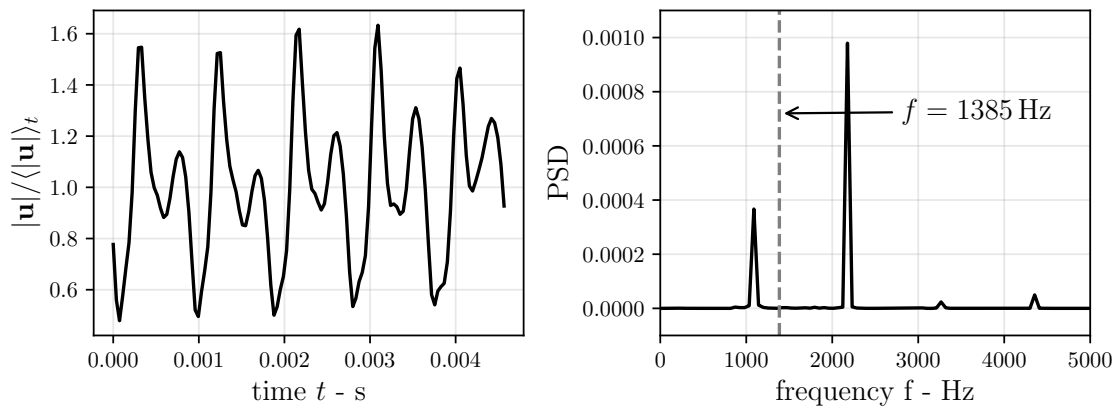


Figure 7.6. – Signal of reduced velocity magnitude at point P_1 and afferent power density spectrum.

7.4.2. Steady flames?

For all the cases considered now it is chosen to set the inlet velocity to $U_{\text{in}} = 2 \text{ m s}^{-1}$. As in Chapter 6, unsteady behavior can be damped by increasing artificially the dynamic viscosity to reduce the Reynolds number. For case D1, this is not necessary because the solution is already stationary. For case R1, a 3-fold increase of μ_{ref} is sufficient to fully stabilize the solution, because the oscillations are small.

For the case D2, the situation is different. Increasing the viscosity by a factor of 3 is not sufficient and a modification up to $\mu_{\text{ref}} \times 6$ is necessary to stabilize the flow. Nonetheless, contrary to cases R1 and the previous methane-air case D4, this forced stabilization eventually leads to flashback. This situation is illustrated in Figure 7.7. From the unsteady solution (with matched gas/solid time steps) a first 3-fold increment in viscosity is considered, followed by a 6-fold increment. To assess whether this new situation is stable, the time-step matching is stopped (solid acceleration), and one observes a flashback (a series of instantaneous fields is shown). As visible in the first flashbacking slice, upstream flame propagation is initiated from the boundary layers. The scenario observed in the simulations is the following: the re-laminarization of the flow thickens the boundary layers in which the hydrogen flame can propagate, which in turn heats up the solid and eventually leads to complete flashback. Following this idea, Figure 7.8 illustrates the modification in axial velocity profile with the increase in viscosity, along a transverse y -direction passing through point P_1 . It is clear that the velocity gradient near the wall upstream of the front near the flame feet decreases with increasing dynamic viscosity, which is favourable to flashback.

It is interesting to note that, considering the bell-shaped curve of 1D theory, the flame should have found a stable position within the solid matrix more upstream. This is not the case, and this phenomenon was observed for methane-air flames as well - to a lesser extent. For flames stabilized near the inlet, the solid temperature is very close to the adiabatic temperature. This leads to rapid ignition of the mixture near the walls, so that the flame feet propagate upstream until stabilizing outside of the porous medium. This results in highly-stretched flames anchored by the very hot solid (see last slice of Figure 7.7). This effect is purely multi-dimensional and cannot be caught by the VAM. Note that the consideration of radiative heat losses may reduce this phenomenon, which may be an artifact related to the global adiabaticity condition. In addition, for hydrogen, the higher sensitivity of the mixture to temperature (Figure 7.1) and the presence of zero-activation energy reactions involving HO_2 (reactions 4, 8 and 11 in Appendix A) lead to regions of high heat release rate near the walls, enhancing further the propensity of

hydrogen to flash back. In fact, in the present simulations it was not even possible to stabilize a hydrogen flame in the burner for case D2 in steady state. This has possibly large implications: while from the viewpoint of 1D theory flame position is dictated by the equilibrium between convection, reaction and interphase heat exchange through preheating and hyperdiffusive effects, depending on the reactivity and near-wall chemistry there may not exist a stable position for the flame in the 3D geometry. Similar to the fact that the ratio of bulk velocity to laminar flame speed is not always sufficient to predict if a flame flashes back in burner stabilization, it is *a priori* impossible to state if a flame position is stable within the porous matrix. This constitutes a further distance from 3D simulations and the 1D VAM. Also, while it was easy to stabilize flames in the 1-mm pore size geometries, it indicates that it may be difficult to handle hydrogen flames in large pores without the help of “turbulence”. Finally, it is interesting to see that the flashback phenomenon presents large hysteresis. For example, at $U_{in} = 2 \text{ m s}^{-1}$ both the submerged unsteady flame and the upstream-stabilized flame could be found, depending on ignition conditions. Unfortunately, the upstream position is very stable and the flame could resist velocities as high as $U_{in} = 5 \text{ m s}^{-1}$ anchored at the inlet, as shown in Figure 7.9. This may be an issue for practical burner operability.

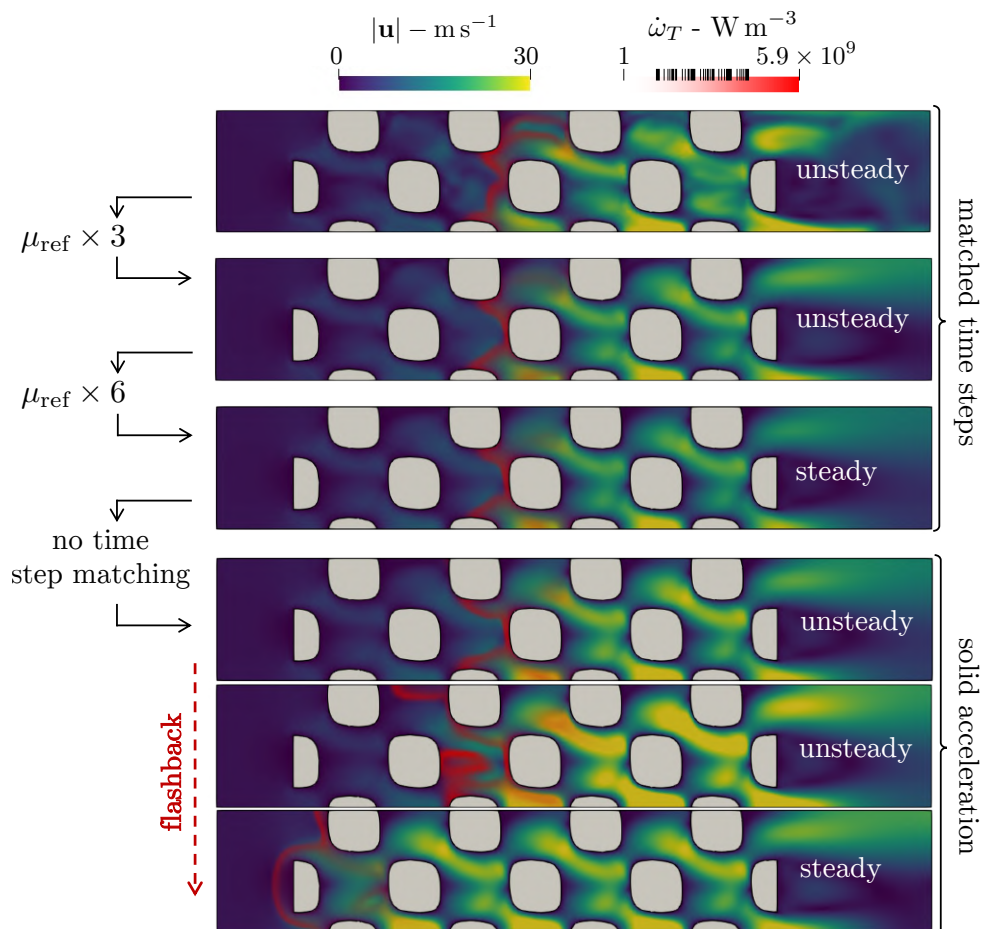


Figure 7.7. – Flashback of a hydrogen flame when passing from unsteady to steady-state by increasing the dynamic viscosity and stopping the matched time steps (solid acceleration).

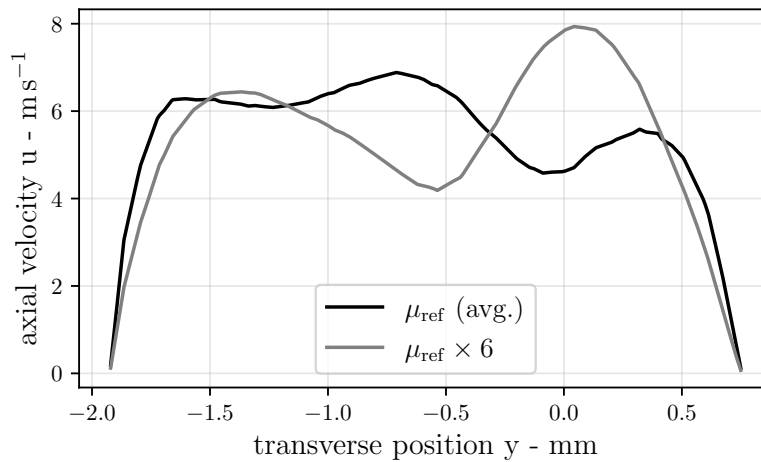


Figure 7.8. – Axial velocity component u versus transverse position y along a line passing through P1. The origin is aligned with the center of the transverse area.

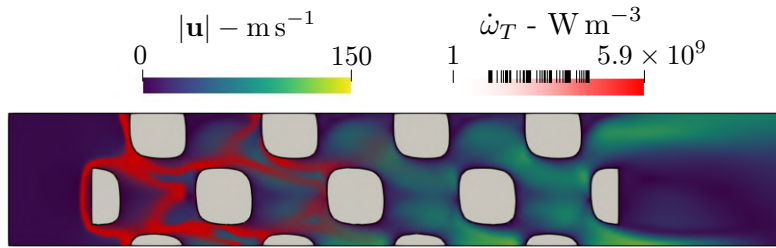


Figure 7.9. – Slice of velocity norm and heat release rate. Domain D2, $U_{\text{in}} = 5 \text{ m s}^{-1}$.

7.4.3. Local flame structure

Figure 7.10 presents a comparison between the flame structures of H_2 -air and CH_4 -air flames for the geometries D1 and R1, as in Chapter 6. It is observed that the shape of the heat release rate is very different for the two fuels: methane-air flames present closed circular arcs anchored clearly behind porous obstacles, perpendicular to the flow, while hydrogen-air flames are more distorted, and show branches/spikes more parallel to the flow. This is a direct consequence of the increased interstitial velocity, but also of the preferential diffusion effects which makes the flame burn “on the sides”, as expected from the proximity with burner-stabilized flames [353]. Accordingly, the superadiabatic pockets are not found at the exit of the flame tip as for methane but on the sides of the elongated reaction zones, which equilibrate downstream. In Figure 7.10 for geometry R1 it is also visible that some flame tips are open. Again, the fact that the H_2 R1 flame could be stabilized in the downstream part of the porous matrix indicates that there is a mechanism of flame surface adaptation. Increasing the velocity from $U_{\text{in}} = 2 \text{ m s}^{-1}$ to $U_{\text{in}} = 2.5 \text{ m s}^{-1}$ would not change the flame location (not shown).

Figure 7.10 also suggests that the local structure of the hydrogen flames is largely non-unidimensional. This effect may be investigated in more detail by introducing an interpolation operator between the adiabatic 1D laminar flame and the 3D fields from the DPLS, based on the fuel progress variable c_F . For a given quantity ψ (species mass fractions, temperature, density, heat release rate, etc.) at given point in the domain, one may associate a reference quantity ψ^0 at the same value of fuel progress variable c_F in the 1D laminar flame. The relative deviation

$\mathcal{R}(\psi)$, defined as:

$$\mathcal{R}(\psi) = \frac{\psi - \psi^0}{\psi^0} \quad (7.4)$$

allows to estimate the distance of the 3D submerged flame from its 1D adiabatic counterpart. An example is given in Figure 7.11 which shows the relative deviations of O_2 . It is observed that for H_2 -air, the intensity of deviations is larger (typically 10-15%) while for methane it is much lower (0-5%). It means that there exists regions of space in which oxygen is in default, that is, of higher equivalence ratio. These regions are typically found behind porous obstacles.

To complement further the issues related to the non-unidimensionality of the hydrogen flame in the porous matrix, the statistical reduced burning rates $\dot{m}_n/\dot{m}_0\Gamma_p(T_{\text{preheating}})$ as a function of stretch rate are given in Appendix 7.A in Figures 7.16 and 7.17, respectively for hydrogen and methane. Because hydrogen diffuses farther upstream than heat, a new flame surface \mathcal{A}^* at 10% of fuel consumption instead of 1% was used. Overall it is observed that the methane-air flame presents less variability and a clear trend regarding flame stretch, while hydrogen shows large overshoots in terms of local burning rate. This is due to the fact that \mathcal{A}^* pinpoints badly the flame surface, due to the preferential diffusion which shifts the tip of \mathcal{A}^* too upstream: in the center of the pores (coldest points in Figures 7.16) burning rates are overpredicted.

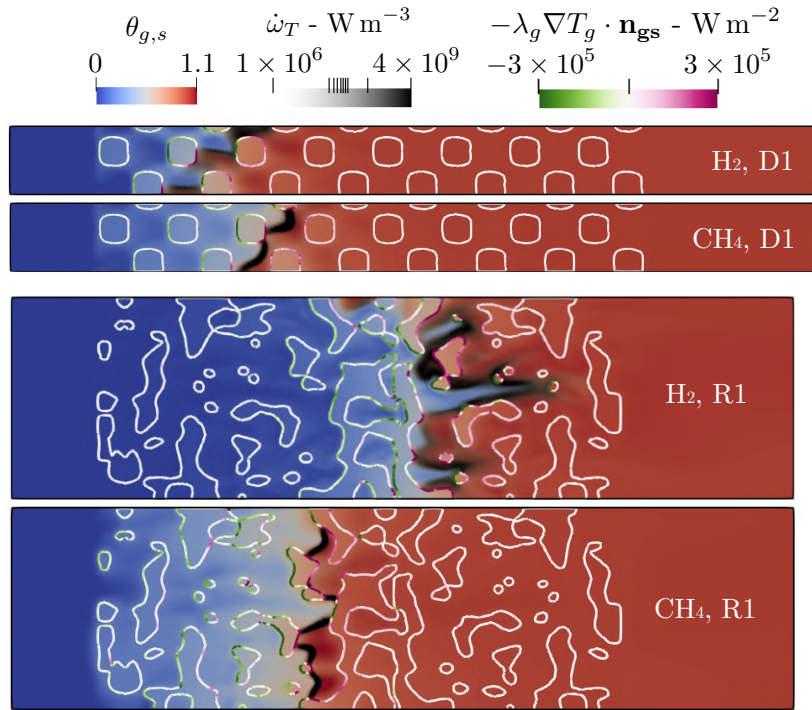


Figure 7.10. – Comparison of CH_4 -air and H_2 -air flames.

7.4.4. Burning rates

Bearing in mind that the structure of methane and hydrogen flames within porous media are substantially different, one may expect that further modelling issues arise at the macroscopic scale. To that regard, Figure 7.12 compares Γ values of the DPLS to the various models described in Chapter 6. Note that for domain D2 the VAM steady model is compared to the unsteady case and the position of maximum of heat release is matched with the time-averaged 3D field. It is observed again that the model overestimates Γ in the random geometry R1, which may be attributed to the larger intensity of dispersion. For geometries D2 and D1, the situation

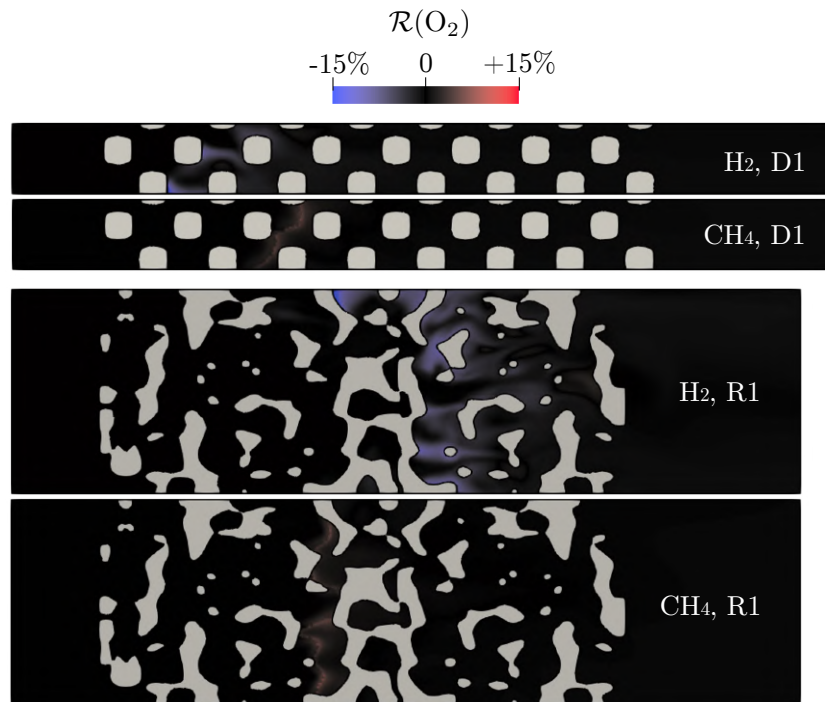


Figure 7.11. – Relative amount of O_2 compared to the adiabatic laminar flame at a given progress variable.

is much worse than in methane-air cases, with a large underprediction for all models. This is explained by the underestimation of the heat transfer coefficient h_V , which is re-estimated directly on the 3D solution as in Chapter 6 for consistency, and the corresponding fit for the case D2 is shown in Figure 7.13. It is clear that the interphase heat transfer does not follow the functional form $Q_{gs} = h_V(\langle T_g \rangle^s - \langle T_s \rangle^s)$ as correctly as for methane-air (see Figure 6.8). The reasons leading to the wrong functional estimation are still unclear and may arise from the larger interstitial velocities which render the interphase heat transfer *non-local*, and may depend upon more than just the local values of $\langle T_g \rangle^g$ and $\langle T_s \rangle^g$. Note further that the comparison between the time-average of an unsteady solution and the steady-state VAM formalism is fundamentally inconsistent. Nonetheless, as shown in the next section there is no reason to believe that for such low levels of turbulence the mean reaction rates be affected a lot by instationarity. So the present underestimation in R1 and D1 geometries is mostly attributed to the error on h_V .

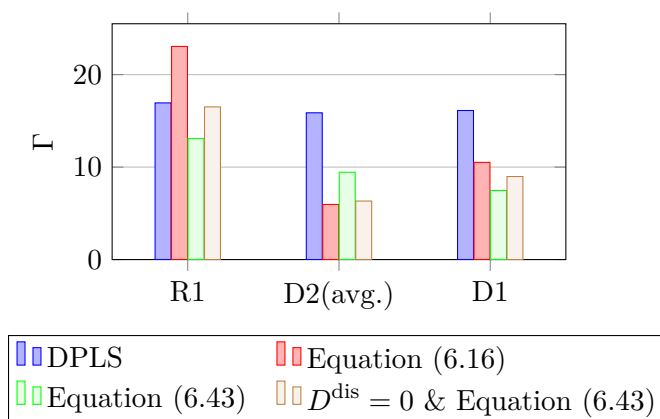


Figure 7.12. – DPLS *vs.* VAM for various H_2 -air flames. Performance of the various models.

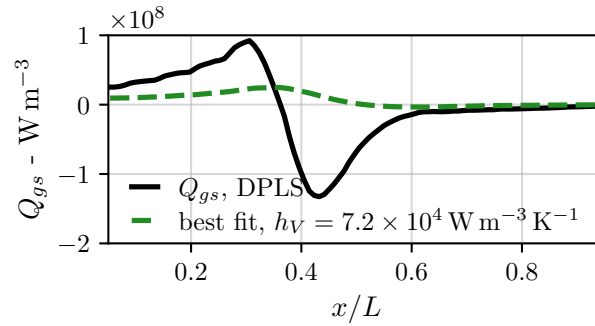


Figure 7.13. – Fit of constant h_V on domain D2 for the hydrogen-air case, on the time-averaged solution.

7.4.5. Modelling of the reaction rates

The difficulties of VAM modelling may be further explored by considering again the commutation error between of the reaction rates, as shown in Figure 7.14. Again, large discrepancies between the space average of the heat release rate $\langle \dot{\omega}_T \rangle^g$ and its *a priori* value based on the mean temperature, density and species mass fractions $\dot{\omega}_T(\langle \cdot \rangle^g)$ are observed. Note that for case R1 the presence of small isolated flame pockets upstream of the rest of the flame front lead to a secondary peak (visible in Figure 7.10). These small flame pockets are found in some corners of the domain and are likely related to some blockage of the flow near the boundaries. Fortunately it leads to the same value of $E_{\dot{\omega}_T}$ for the same pore size with D1, and again it seems that the commutation error increases with pore size. Interestingly, a comparison of $E_{\dot{\omega}_T}$ values in Figure 7.14 with the points reported for methane-air in Figure 6.17 shows that the commutation error is *lower* for hydrogen-air flames. There may be several reasons for this somewhat counter-intuitive result. First is that the characteristic flame thicknesses are systematically larger for hydrogen than methane for the mixtures considered (see Figure 7.2 and 7.3), which reduces the Péclet number and the critical threshold discussed in Chapter 6. Also, the physical extension and shape of the flame front may play a role.

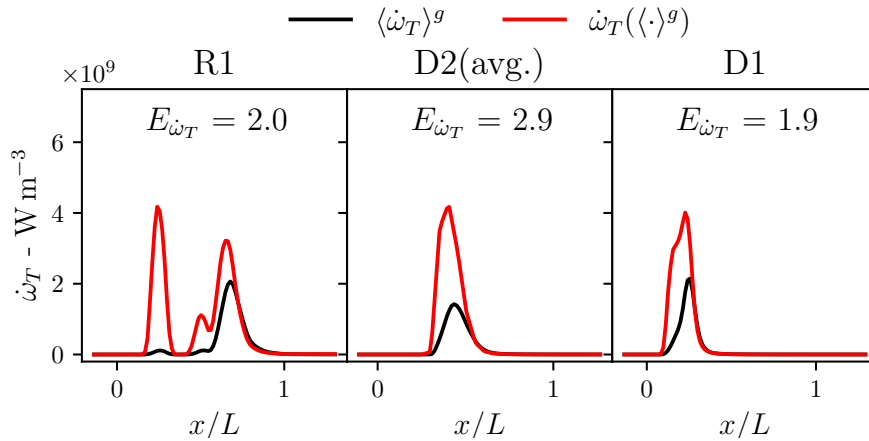


Figure 7.14. – Evaluation of the commutation error for heat release rate for hydrogen cases.

7.4.6. Burning below the flammability limit

We finish this chapter with the demonstration of combustion below the lean flammability limit at $\phi = 0.25$. Going ultra-lean is interesting in terms of safety because outside of the porous matrix, the mixture is not flammable. Figure 7.15 shows a slice of the flame structure for an inlet velocity of $U_{\text{in}} = 0.7 \text{ m s}^{-1}$, sufficiently low to yield steady-state without altering viscosity. The flame fronts are much less distorted than in Figure 7.10, and the previously-observed long fingered structures are seemingly absent - substantiating their hydrodynamic origin. However, the flame front remains largely multi-dimensional and effects of preferential diffusion are still perceivable: some flame tips are extinct.

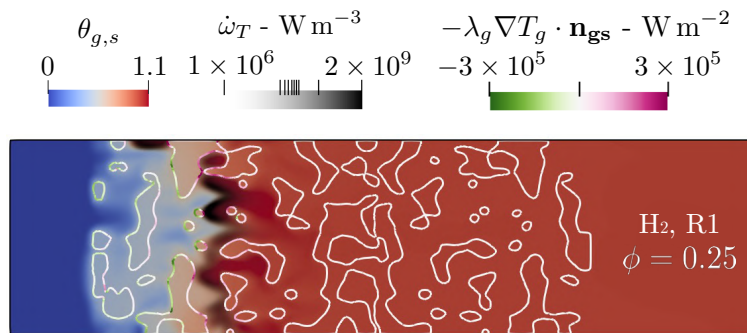


Figure 7.15. – Example of stable combustion below the flammability limit at $\phi = 0.25 < \phi_{\text{LFL}}$. Inlet velocity $U_{\text{in}} = 0.7 \text{ m s}^{-1}$.

7.5. Conclusions of the chapter

In this chapter, the first 3D numerical simulations of hydrogen-air porous media combustion have been presented, and these have been systematically compared to methane-air counterparts and again to the corresponding volume-averaged model. This led to the following conclusions:

- the high reactivity of H_2 requires large inlet velocities to sustain submerged combustion. This leads to unsteady solutions for typical pore sizes, unadapted to the steady volume-averaged framework ;
- in geometry D2, an almost periodic cycle was identified and linked to the hydrodynamic field, which may lead to some noise in practical burners. The associated Strouhal number excluding preheating effects was 0.33 ;
- reducing the Reynolds number artificially through a viscosity increase led to a boundary layer-driven flashback up to the inlet in geometry D2. This indicates that hydrogen may not be easily stabilized in large pores without the help of turbulence. Near-wall chemistry and the higher reactivity of hydrogen are fundamentally unfavourable to pore-scale stability ;
- the volume-averaged model performs poorly compared to methane-air combustion. This was attributed to the larger error made on the estimation of h_V , probably linked to the larger interstitial velocities and non-locality issues ;
- the commutation error of the reaction rates are lower than methane-air for the same pore size, what can be attributed to the larger flame thickness. This confirms that the ratio of pore size to flame thickness is an important modelling parameter, still absent from current volume-averaged models.

7.A. Local flame structure in geometry D1

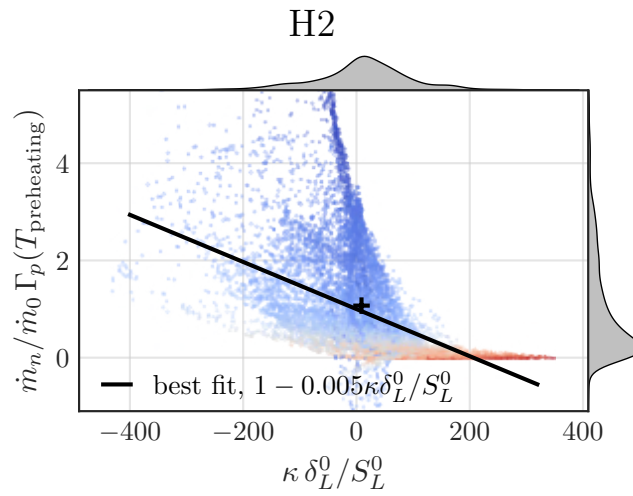


Figure 7.16. – Scatter plot and PDF on \mathcal{A}^* , domain D1, hydrogen-air flame $\phi = 0.38$. Blue cold (pore centers), red hot regions (near walls).

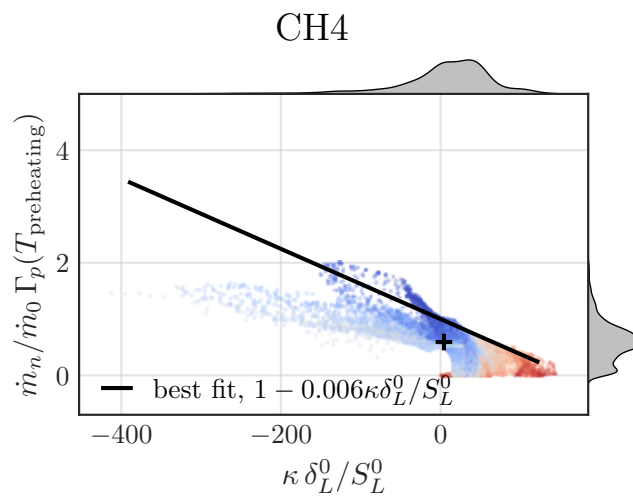


Figure 7.17. – Scatter plot and PDF on \mathcal{A} , domain D1, methane-air flame $\phi = 0.72$. Blue cold (pore centers), red hot regions (near walls).

Conclusions and future research directions

Conclusions

Heat-recirculating burners present unique technological features such as broadened flammability limits, minimal CO/NO_x emissions, fuel-flexibility, and possibly very large downturn ratios. As such, porous media combustion constitutes a serious candidate for future clean combustion systems, in prospected applications ranging from household heat generation to aeronautical engines. Unfortunately, due to the opacity and tortuosity of the porous structures, it is not yet possible to visualize with good accuracy the fine pore-scale flame structure in experiments. What is more, mesh requirements and system sizes remain computationally-prohibitive to simulate porous combustion at burner scale, which require the complex coupling between flowing-reactive gas and conductive-radiative solid phases. In the literature, there exists low-order, volume-averaged models designed to account for the burner-scale behavior at minimal cost, but these show very variable agreement to experiments, were not derived rigorously from the microscopic equations, and remain based upon and aggregate of *ad hoc* closure models whose interactions have rarely been questioned or challenged. In addition, volume-averaged models have mostly been applied to specific configurations, and little parametric analyses and regime characterisations have been proposed for porous burners, not to mention the lack of basic quantities such as intrinsic flame speed for given gas mixture and solid matrix parameters. Also, to improve operability experimentally, most porous burners are multi-layered, but the physics and stabilization at or near the interfaces are still badly predicted and understood.

These issues in mind, this Ph.D. work explored various modelling aspects of porous media combustion, either from the point of view of the 1D volume-averaged equations or through 3D pore-level numerical simulations including complex chemistry and conjugate heat transfer. Asymptotic studies have unveiled two important reduced parameters, $r_{\dot{m}}$ and r_{λ} , which allowed to classify stationary porous media combustion into three distinct regimes for increasing gas/solid thermal coupling: decoupled, intermediate and hyperdiffusive. In decoupled and hyperdiffusive regimes, fully-explicit formulae for flame speed were derived, which depend only upon $r_{\dot{m}}$ in the decoupled regime and only upon r_{λ} in the hyperdiffusive regime. Multi-layered burners were addressed theoretically for the first time, and the introduction of a contact resistance between two porous layers has proven to influence dramatically the burner stability, as well as the introduction of pore-level flame wrinkling. The theoretical results obtained in this manuscript, although overly simplified (*e.g.* no radiation) are not applicable to real burners but constitute a canonical reference unveiling unequivocally physical trends previously intuited in the literature or observed in specific configurations. For example, in the decoupled regime it was shown that recirculation efficiency (thus flame speed) decreases with equivalence ratio, porosity and ambient temperature, and increases with solid conductivity, volume heat transfer coefficient and adiabatic temperature. Other example, the ratio of diffusion to reaction length scales of the reference laminar flame was shown to be a good indicator of the maximum superadiabaticity attainable in the burner and the extent of the intermediate regime.

Current volume-averaged models were then confronted to 3D pore-level numerical simulations of methane and hydrogen combustion in air, in typical porous burner geometries and pore sizes. And although sharing the same thermo-chemical scheme and a rigorous computation of the effective properties, major intrinsic discrepancies between the two approaches were unveiled. In

the 3D simulations, the flame fronts appeared to be largely wrinkled, locally anchored behind the porous obstacles, non-homogeneously preheated, quenched near the walls, distributed longitudinally, and, importantly, thin with regard to the local pore size. For hydrogen flames, due to preferential diffusion strong 3D effects were observed near the flame front. These features are all in direct violation of the underlying hypotheses of volume-averaged models, either from the point of view of its theoretical establishment or final formulation. Notably, it is usually assumed that reaction rates commute with their average, which is expectedly incorrect in the presence of thin flame fronts due to the high non-linearity of the Arrhenius terms. This commutation error was shown to decrease with pore size, and should vanish for thermal Péclet numbers (*i.e.* ratio of pore size to flame thickness) below β^{-1} , but this regime is not typical of porous burners. A quantitative comparison between the 1D volume-averaged predictions and the 3D simulations has shown major discrepancies in terms of burning rate and physical profiles. In addition, the present work allowed to raise a major warning regarding the macroscopic interpretation of hydrodynamic dispersion. Although dispersion was shown to be undeniably present within porous burners, the thin flame fronts and absence of combustion in volume do not allow to interpret dispersion as an increase in diffusivities near the combustion zone, so the acceleration of the volume-averaged flame due to dispersion can be deemed as spurious and unrelated to local combustion processes. As such, the common interpretation that porous media combustion increases burning rates thanks to an increase in diffusivities is fundamentally flawed. Also, because dispersion occurs for thermal Péclet numbers beyond unity, there is a mutual exclusion between the validity of the classical volume-averaged models and the presence of hydrodynamic dispersion. Based upon a local flamelet hypothesis, it was attempted to include the effect of flame wrinkling and remove the acceleration related to dispersion, so as to correct macroscale burning rates in the volume-averaged model, but our best efforts proved unsuccessful in closing the gap between simulations and low-order modelling. Conceptually-speaking, the fact that the 1D volume-averaged model simulates an effective, “representative” flame front whose local environment related to the macroscale effective properties is largely different than the intertwined flame structure calls in to question whether 1D volume-averaged models ever be able to catch the pore-scale subtleties with sufficient accuracy. To this end, the improvement of current volume-averaged models constitutes a vast area of investigation, and urges for further detailed numerical simulations with corresponding volume-averaged models for rigorous comparisons, as well as the development of new experimental visualization techniques.

Future research directions

Links decoupled/intermediate/hyperdiffusive regimes *vs.* 3D flames

Although some links/discrepancies between 1D models and 3D simulations were described in the manuscript, the relations between the predicted combustion regimes (decoupled, intermediate and hyperdiffusive) and “real” flames were not assessed entirely. An intrinsic problem lies in the fact that the three regimes were defined by considering the volume-averaged equations valid as a starting point, and cannot include properly dispersion due to its phenomenological issues at the macroscale. Moreover, volume-averaged models are constructed to hide the influence of pore size in the effective parameters, so that the predicted regimes are governed by $r_{\dot{m}}$ and r_{λ} while the flame in the 3D DNS and the associated validity of volume-averaging seemed to be highly governed by the thermal Péclet number $Pe_{p,th}$. Unfortunately, there is no unequivocal relation between the couple $(r_{\dot{m}}, r_{\lambda})$ and $Pe_{p,th}$ and only qualitative arguments may be put forward. Because the intensity of interphase heat transfer and the validity of the volume-averaged equations are governed by pore size, for small pore sizes the hyperdiffusive regime will tendentially be found, while for larger pore sizes the flames will be more decoupled to the wall. These considerations may be viewed schematically in Figure 7.18, but further work is required to quantify

this intuition and explore its conceptual implications. Note that the inferred validity of the current volume-averaged models in the limit of infinitely-small pore size is logical but also requires proper validation. Unveiling the links between decoupled/intermediate/hyperdiffusive regimes and 3D flames is relevant, because differentiated corrections to the volume-averaged equations may be proposed (for instance in the present manuscript the proposed model for reaction rates implicitly assumed a decoupled behavior for the flame front). Unfortunately, the intermediate regime is likely a region where most real flames are found, where burning rate is very sensitive to the effective parameters.

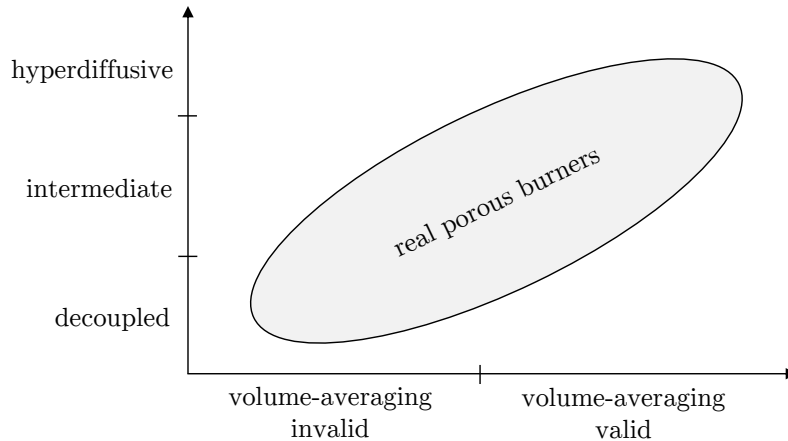


Figure 7.18. – Presence of regimes for real porous burners?

Radiation

Another limitation of the proposed work is the exclusion of radiation. Though strong arguments indicate that it should not impact significantly the present conclusions, 3D detailed numerical simulations with and without radiation, as well as a critical study of the validity of a volume-averaged radiative transfer equation, should be performed for the typical materials used in porous burners applications.

CO/NO_x emissions

Although it has been experimentally demonstrated that some porous burners may significantly reduce CO and NO_x emissions compared to traditional burners, to the author's knowledge the pore-scale mechanisms leading to such a performance has not been properly demonstrated. 3D simulations including detailed NO_x chemistry may help reproduce and unveil the mechanisms leading to a reduction in emissions.

Meshing strategy

The meshing strategy adopted in this thesis is not sufficiently sophisticated, in the sense that uniform mesh size was adopted. Although this was found to be relevant for the present application, it required extensive computational resources (approximately 30 M core-hours on a cluster in Spain, which corresponds to approximately 115 tons of equivalent CO₂, or 50 flights from New York to Melbourne¹). More advanced adaptative mesh refinement techniques specifically designed for porous media combustion may help reduced this cost sufficiently, first to compute porous combustion at the burner scale, and then to make it an available tool of design for a larger public. This also requires further developments in the automation of the process from a 3D tomographic scan to 3D conformal computational meshes, which still today require much

1. <http://www.green-algorithms.org/>

human intervention.

Hydrogen combustion

Some aspects of hydrogen combustion in porous media have been explored in Chapter 7. Larger burning rates, more unsteady flows and a greater propensity to flashback were discovered. Nonetheless, the few geometries and inlet conditions investigated are likely not representative of the rich physics attainable with hydrogen. Variations in topology, pore size, equivalence ratio, pressure, temperature and burner design must be considered, both numerically and experimentally, with the aim of achieving robust operability and safety.

Topological gradation

Topological gradation has been recently proposed in the community to improve the burner operating range, notably through a progressive modification of pore size. However, because the volume-averaged model may experience strong shortcomings and varying degrees of validity for pore size variations, it seems that the true implications of topological gradation are still to be unveiled at pore scale. For example, increasing pore sizes may lead to unsteadiness and larger flame corrugation, and this has to be verified both experimentally and numerically.

Multi-layered burners

In the literature, it is common practice to make use of two successive porous layers with different properties to help flame stabilization, notably near the interface. Usually, a fine-pored porous layer is used upstream, supposedly acting as a flame arrester, and the classical quenching theory is invoked to explain the stabilization of the flame. However, in heat-recirculating devices this conceptual framework is highly questionable, especially when the heat losses to the exterior are low. For sufficiently hot porous matrices, it is not excluded that combustion occurs for pores of arbitrarily small size, and flashback was observed in many experiments albeit satisfying the flashback criterion. 1D volume-averaged models have tried to account for this phenomenon, with little success so far. This is due to the strong assumptions made near the interface, the low validity of volume-averaged models near boundaries, the assumption of planar flame front and continuity of solid temperature. Some elements were given in the manuscript to help relax these hypotheses but the proposed toy model is not sufficient to explain counter-intuitive phenomena observed experimentally. 3D simulations including radiation and a realistic geometrical treatment of contact points between two porous layers seem mandatory and a straightforward work direction.

Towards a direct visualization of the flame structure?

Advanced experimental techniques such as X-ray computed tomography have been proposed to measure directly temperature fields within porous burners, but this required the use of krypton to increase the absorption of the gaseous phase and the method suffers from large uncertainties. Other techniques are either intrusive or require the creation of gaps within the porous structure, while only recovering 1/2D information. Thanks to the 3D simulations performed in this thesis, it could be seen that the internal flame structure and corresponding macroscale operability were similar between reticulated (random) and lattice-based (regular) porous structure. Interestingly, regular geometries present several preferential directions where the flame can be directly visualized. An experimental setup was designed and built during this Ph.D. work to ensure optical access in all directions and is shown in Figure 7.19. This will allow to compare directly the results of 3D simulations, experiments and 1D models, and constitutes as such as preferential research direction.

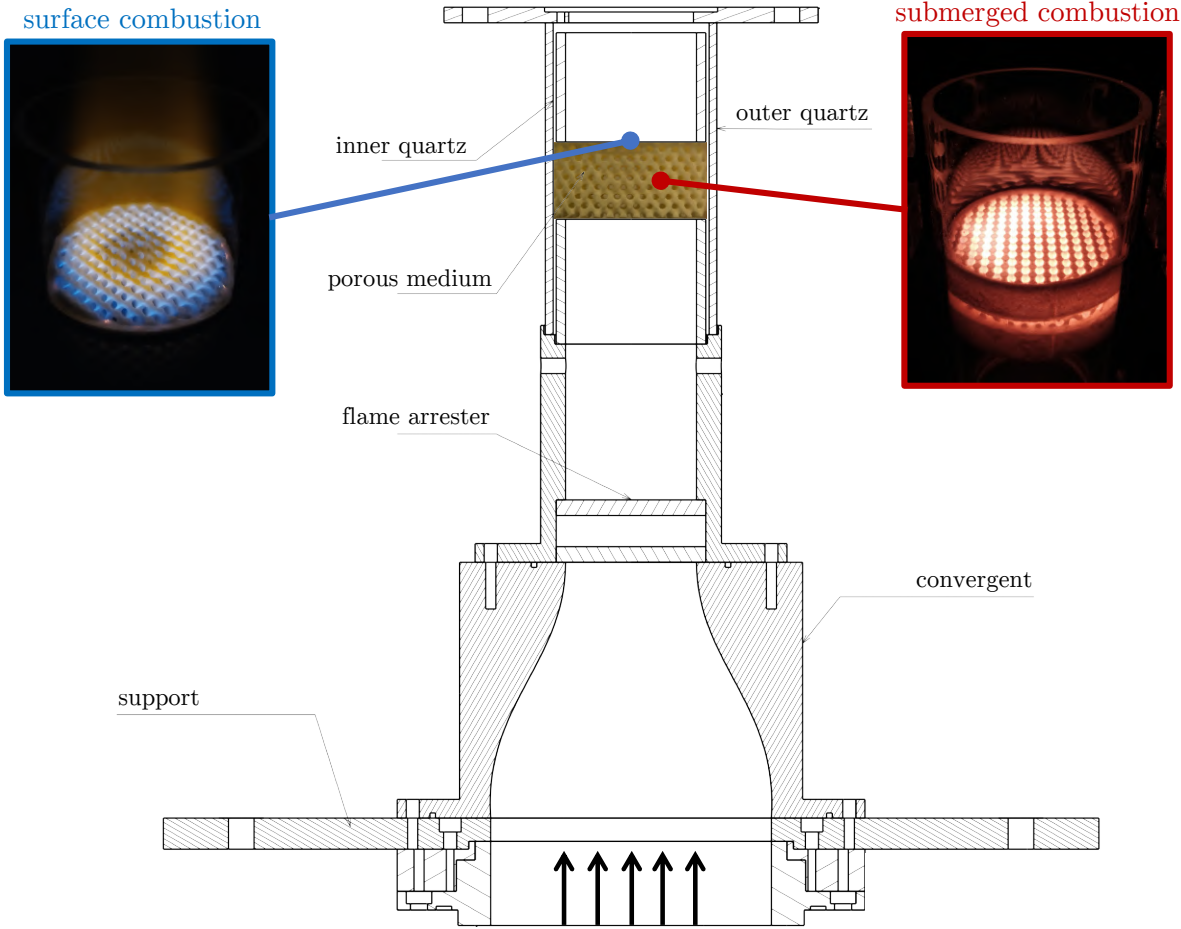


Figure 7.19. – Experimental setup to visualize directly flame fronts in lattice-based porous burners (current investigations).

Appendices

Characteristics of CH4_15_138_9_AP mechanism

The reduced ARC mechanism generated by ARCANE comprises 15 transported species, 138 reactions and 9 species in Quasi-Steady State:

- Transported species: N_2 , H_2 , H , O_2 , O , H_2O , OH , CO , CO_2 , CH_4 , CH_3 , CH_2O , C_2H_6 , C_2H_2 , $CH_2(L_1)$
- QSS species: HO_2 , CH_3OH , CH_3O , CH_2OH , HCO , C_2H_5 , C_2H_4 , C_2H_3 , CH_2CO

Detailed description of the reactions is given in Table A.1. Downloadable .cti and validation files are available at <https://chemistry.cerfacs.fr>

Table A.1. – List of reactions with A the pre-exponential factor in $m^{3(n-1)}/kmol^{n-1}/s$ with n the order of the reaction, b the temperature exponent and E_a the activation energy in $J/kmol$. In the case of fall-off reactions, two sets of Arrhenius coefficients are specified, the first one being the low temperature set and the second one the high temperature set.

No.	Reaction	A	b	E_a
1	$H_2 + O \leftrightarrow H + OH$	5.080000E+01	2.670000E+00	2.632573E+07
2	$H_2 + OH \leftrightarrow H + H_2O$	4.380000E+10	0.000000E+00	2.924616E+07
3	$H + O_2 \leftrightarrow O + OH$	1.140000E+11	0.000000E+00	6.395662E+07
4	$H + OH + M \leftrightarrow H_2O + M$	3.500000E+16	-2.000000E+00	0.000000E+00
	Species efficiencies : CH4:2.00E+00 H2O:3.65E+00			
5	$H_2O + O \leftrightarrow 2 OH$	6.700000E+04	1.704000E+00	6.270477E+07
6	$H + HO_2 \leftrightarrow 2 OH$	7.079000E+10	0.000000E+00	1.234280E+06
7	$H + HO_2 \leftrightarrow H_2 + O_2$	1.140200E+07	1.082700E+00	2.317016E+06
8	$HO_2 + O \leftrightarrow O_2 + OH$	3.250000E+10	0.000000E+00	0.000000E+00
9	$HO_2 + OH \leftrightarrow H_2O + O_2$	7.000000E+09	0.000000E+00	-4.572945E+06
10	$HO_2 + OH \leftrightarrow H_2O + O_2$	4.500000E+11	0.000000E+00	4.572945E+07
11	$H + O_2 (+M) \leftrightarrow HO_2 (+M)$	1.737000E+13	-1.230000E+00	0.000000E+00
	Troe coefficients : 6.70E-01 1.00E-30 1.00E+30 1.00E+30	4.650000E+09	4.400000E-01	0.000000E+00
	Species efficiencies : CH4:2.0E+00 CO:1.9E+00 CO2:3.8E+00 H2O:1.0E+01			
12	$CO + O (+M) \leftrightarrow CO_2 (+M)$	1.173000E+18	-2.790000E+00	1.753514E+07
	Troe coefficients : -	1.362000E+07	0.000000E+00	9.974656E+06
	Species efficiencies : CO:1.8E+00 CO2:3.6E+00 H2O:1.2E+01			
13	$CO + OH \leftrightarrow CO_2 + H$	7.015000E+01	2.053000E+00	-1.488249E+06
14	$CO + OH \leftrightarrow CO_2 + H$	5.757000E+09	-6.640000E-01	1.388251E+06
15	$CH_3 + H (+M) \leftrightarrow CH_4 (+M)$	2.477000E+27	-4.760000E+00	1.020896E+07
	Troe coefficients : 7.83E-01 7.40E+01 2.94E+03 6.96E+03	1.270000E+13	-6.300000E-01	1.602472E+06
	Species efficiencies : CH4:2.0E+00 CO:1.5E+00 CO2:2.0E+00 H2O:6.0E+00			
16	$CH_4 + H \leftrightarrow CH_3 + H_2$	6.140000E+02	2.500000E+00	4.011201E+07
17	$CH_4 + O \leftrightarrow CH_3 + OH$	1.020000E+06	1.500000E+00	3.598240E+07
18	$CH_4 + OH \leftrightarrow CH_3 + H_2O$	5.830000E+01	2.600000E+00	9.162960E+06
19	$CH_3 + HO_2 \leftrightarrow CH_4 + O_2$	1.160000E+02	2.230000E+00	-1.264405E+07
20	$CH_2(L1) + CH_4 \leftrightarrow 2 CH_3$	1.326516E+04	1.785451E+00	3.663295E+07
21	$CH_2(L1) + O_2 \rightarrow CO + H + OH$	1.746412E+02	1.988656E+00	-1.763074E+07

No.	Reaction	A	b	E_a
22	CH2(L1) + O2 \leftrightarrow CO + H2O	7.484624E+01	1.988656E+00	-1.763074E+07
23	CH2(L1) + O \leftrightarrow CO + H2	9.355780E+01	1.988656E+00	-1.763074E+07
24	CH2(L1) + O \leftrightarrow H + HCO	9.355780E+01	1.988656E+00	-1.763074E+07
25	CH2(L1) + H2 \leftrightarrow CH3 + H	4.366031E+02	1.988656E+00	-1.763074E+07
26	CH2(L1) + OH \leftrightarrow CH2O + H	1.871156E+02	1.988656E+00	-1.763074E+07
27	CH2(L1) + CO2 \leftrightarrow CH2O + CO	8.732062E+01	1.988656E+00	-1.763074E+07
28	CH2(L1) + H (+M) \leftrightarrow CH3 (+M)	1.725550E+22	-3.354549E+00	7.177589E+06
	Troe coefficients : 6.80E-01 7.80E+01 2.00E+03 5.59E+03	1.348086E+14	-1.014549E+00	2.031268E+06
	Species efficiencies : CH4:2.0E+00 CO:1.5E+00 CO2:2.0E+00 H2O:6.0E+00			
29	CH2(L1) + O2 \leftrightarrow HCO + OH	5.715883E+10	-2.145491E-01	8.307269E+06
30	CH2(L1) + O2 \rightarrow CO2 + 2 H	1.423578E+10	-2.145491E-01	8.307269E+06
31	CH2(L1) + O \rightarrow CO + 2 H	2.696171E+11	-2.145491E-01	2.031268E+06
32	CH3 + O2 \leftrightarrow CH3O + O	7.546000E+09	0.000000E+00	1.184909E+08
33	CH3 + O2 \leftrightarrow CH2O + OH	2.641000E-03	3.283000E+00	3.391132E+07
34	CH3 + O \leftrightarrow CH2O + H	5.540000E+10	5.000000E-02	-5.690240E+05
35	CH3 + OH \leftrightarrow CH2(L1) + H2O	5.282000E+14	-1.518000E+00	7.414048E+06
36	CH3 + OH \leftrightarrow CH2OH + H	4.686000E+07	8.330000E-01	1.492014E+07
37	CH3 + OH \leftrightarrow CH3O + H	1.230000E+06	1.011000E+00	4.999880E+07
38	CH3 + OH \leftrightarrow CH2(L1) + H2O	4.293000E+01	2.568000E+00	1.672680E+07
39	CH3 + HO2 \leftrightarrow CH3O + OH	1.000000E+09	2.690000E-01	-2.876500E+06
40	CH3OH (+M) \leftrightarrow CH3 + OH (+M)	1.500000E+40	-6.995000E+00	4.099994E+08
	Troe coefficients : -4.75E-01 3.56E+04 1.12E+03 9.02E+03	2.084000E+18	-6.150000E-01	3.871899E+08
41	CH3OH (+M) \leftrightarrow CH2(L1) + H2O (+M)	1.430000E+44	-8.227000E+00	4.159611E+08
	Troe coefficients : 2.54E+00 3.29E+03 4.73E+04 4.71E+04	3.121000E+18	-1.017000E+00	3.837230E+08
42	CH3OH + H \leftrightarrow CH3O + H2	1.990000E+02	2.560000E+00	4.309520E+07
43	CH3OH + H \leftrightarrow CH2OH + H2	3.070000E+02	2.550000E+00	2.276096E+07
44	CH3OH + O \leftrightarrow CH3O + OH	3.880000E+01	2.500000E+00	1.288672E+07
45	CH3OH + O \leftrightarrow CH2OH + OH	3.880000E+02	2.500000E+00	1.288672E+07
46	CH3OH + OH \leftrightarrow CH3O + H2O	1.500000E-01	3.030000E+00	-3.192392E+06
47	CH3OH + OH \leftrightarrow CH2OH + H2O	3.080000E+01	2.650000E+00	-3.375233E+06
48	CH3 + CH3OH \leftrightarrow CH3O + CH4	3.220000E+00	2.425000E+00	3.589663E+07
49	CH2OH + O2 \leftrightarrow CH2O + HO2	1.510000E+12	-1.000000E+00	0.000000E+00

No.	Reaction	A	b	E_a
50	CH2OH + O2 \leftrightarrow CH2O + HO2	2.410000E+11	0.000000E+00	2.099113E+07
51	CH2OH + H \leftrightarrow CH2O + H2	6.000000E+09	0.000000E+00	0.000000E+00
52	CH2OH + OH \leftrightarrow CH2O + H2O	2.400000E+10	0.000000E+00	0.000000E+00
53	CH2OH + O \leftrightarrow CH2O + OH	4.200000E+10	0.000000E+00	0.000000E+00
54	CH3O + O2 \leftrightarrow CH2O + HO2	4.380000E-22	9.500000E+00	-2.301618E+07
55	CH3O + H \leftrightarrow CH2O + H2	2.000000E+10	0.000000E+00	0.000000E+00
56	CH3 + CH3O \leftrightarrow CH2O + CH4	1.200000E+10	0.000000E+00	0.000000E+00
57	H + HCO (+M) \leftrightarrow CH2O (+M)	1.350000E+18	-2.570000E+00	5.962200E+06
	Troe coefficients : 7.82E-01 2.71E+02 2.76E+03 6.57E+03	1.090000E+09	4.800000E-01	-1.087840E+06
	Species efficiencies : CH4:2.0E+00 CO:1.5E+00 CO2:2.0E+00 H2O:6.0E+00			
58	CO + H2 (+M) \leftrightarrow CH2O (+M)	5.070000E+21	-3.420000E+00	3.529120E+08
	Troe coefficients : 9.32E-01 1.97E+02 1.54E+03 1.03E+04	4.300000E+04	1.500000E+00	3.330464E+08
	Species efficiencies : CH4:2.0E+00 CO:1.5E+00 CO2:2.0E+00 H2O:6.0E+00			
59	CH2O + O \leftrightarrow HCO + OH	6.260000E+06	1.150000E+00	9.455840E+06
60	CH2O + H \leftrightarrow H2 + HCO	5.740000E+04	1.900000E+00	1.146416E+07
61	CH2O + OH \leftrightarrow H2O + HCO	7.820000E+04	1.630000E+00	-4.414120E+06
62	CH2O + CH3 \leftrightarrow CH4 + HCO	3.830000E-02	3.360000E+00	1.804141E+07
63	HCO + M \leftrightarrow CO + H + M	5.700000E+08	6.600000E-01	6.221608E+07
	Species efficiencies : CH4:2.00E+00 CO:1.50E+00 CO2:2.00E+00 H2O:6.00E+00			
64	HCO + O2 \leftrightarrow CO + HO2	7.580000E+09	0.000000E+00	1.715440E+06
65	HCO + O \leftrightarrow CO + OH	3.020000E+10	0.000000E+00	0.000000E+00
66	H + HCO \leftrightarrow CO + H2	7.340000E+10	0.000000E+00	0.000000E+00
67	HCO + OH \leftrightarrow CO + H2O	3.011000E+10	0.000000E+00	0.000000E+00
68	CH3 + HCO \leftrightarrow CH4 + CO	2.650000E+10	0.000000E+00	0.000000E+00
69	HCO + O \leftrightarrow CO2 + H	3.000000E+10	0.000000E+00	0.000000E+00
70	CH2O + H (+M) \leftrightarrow CH2OH (+M)	1.270000E+26	-4.820000E+00	2.732152E+07
	Troe coefficients : 7.19E-01 1.03E+02 1.29E+03 4.16E+03	5.400000E+08	4.540000E-01	1.506240E+07
	Species efficiencies : CH4:2.0E+00 CO:1.5E+00 CO2:2.0E+00 H2O:6.0E+00			
71	CH3O (+M) \leftrightarrow CH2O + H (+M)	1.867000E+22	-3.000000E+00	1.017005E+08
	Troe coefficients : 9.00E-01 2.50E+03 1.30E+03 1.00E+99	6.800000E+13	0.000000E+00	1.094953E+08
	Species efficiencies : CH4:2.0E+00 CO:1.5E+00 CO2:2.0E+00 H2O:6.0E+00			
72	2 CH3 (+M) \leftrightarrow C2H6 (+M)	8.054000E+25	-3.750000E+00	4.107014E+06

No.	Reaction	A	b	E_a
	Troe coefficients : 0.00E+00 5.70E+02 1.00E+30 1.00E+30 Species efficiencies : CO:2.0E+00 CO2:3.0E+00 H2O:5.0E+00	2.277000E+12	-6.900000E-01	7.317816E+05
73	C2H5 + H (+M) \leftrightarrow C2H6 (+M) Troe coefficients : 8.42E-01 1.25E+02 2.22E+03 6.88E+03 Species efficiencies : CH4:2.0E+00 CO:1.5E+00 CO2:2.0E+00 H2O:6.0E+00	1.990000E+35 5.210000E+14	-7.080000E+00 -9.900000E-01	2.797004E+07 6.610720E+06
74	C2H6 + O \leftrightarrow C2H5 + OH	3.550000E+03	2.400000E+00	2.439272E+07
75	C2H6 + H \leftrightarrow C2H5 + H2	1.150000E+05	1.900000E+00	3.150552E+07
76	C2H6 + OH \leftrightarrow C2H5 + H2O	1.480000E+04	1.900000E+00	3.974800E+06
77	C2H6 + CH3 \leftrightarrow C2H5 + CH4	5.550000E-07	4.720000E+00	1.351850E+07
78	C2H4 + H (+M) \leftrightarrow C2H5 (+M) Troe coefficients : 5.69E-01 2.99E+02 -9.15E+03 1.52E+02 Species efficiencies : CH4:2.0E+00 CO:1.5E+00 CO2:2.0E+00 H2O:6.0E+00	1.419000E+33 9.569000E+05	-6.642000E+00 1.463000E+00	2.413750E+07 5.669320E+06
79	C2H5 + CH3 \leftrightarrow C2H4 + CH4	1.180000E+01	2.450000E+00	-1.222146E+07
80	2 CH3 \leftrightarrow C2H5 + H	3.100000E+11	-3.620000E-01	5.595054E+07
81	C2H3 + H (+M) \leftrightarrow C2H4 (+M) Troe coefficients : 7.82E-01 2.07E+02 2.66E+03 6.10E+03 Species efficiencies : CH4:2.0E+00 CO:1.5E+00 CO2:2.0E+00 H2O:6.0E+00	1.400000E+24 6.080000E+09	-3.860000E+00 2.700000E-01	1.389088E+07 1.171520E+06
82	C2H4 + M \leftrightarrow C2H2 + H2 + M Species efficiencies : CH4:2.00E+00 CO:1.50E+00 CO2:2.00E+00 H2O:6.00E+00	2.610000E+13	0.000000E+00	2.837714E+08
83	C2H4 + H \leftrightarrow C2H3 + H2	5.070000E+04	1.930000E+00	5.418280E+07
84	C2H4 + OH \leftrightarrow C2H3 + H2O	2.230000E+01	2.745000E+00	9.269652E+06
85	C2H4 + CH3 \leftrightarrow C2H3 + CH4	9.760000E-01	2.947000E+00	6.337923E+07
86	C2H4 + CH3 \leftrightarrow C2H3 + CH4	8.130000E-08	4.417000E+00	3.696899E+07
87	C2H4 + O \leftrightarrow CH3 + HCO	7.453000E+03	1.880000E+00	7.656720E+05
88	CH2(L1) + CH3 \leftrightarrow C2H4 + H	1.247437E+02	1.988656E+00	-1.763074E+07
89	C2H2 + H (+M) \leftrightarrow C2H3 (+M) Troe coefficients : 7.88E-01 -1.02E+04 1.00E-30 0.00E+00 Species efficiencies : CH4:2.0E+00 CO:1.5E+00 CO2:2.0E+00 H2O:6.0E+00	6.346000E+25 1.710000E+07	-4.664000E+00 1.266000E+00	1.581552E+07 1.133446E+07
90	C2H3 + O2 \leftrightarrow C2H2 + HO2	2.150000E+04	1.190000E+00	1.408753E+07
91	C2H3 + O2 \leftrightarrow C2H2 + HO2	4.600000E-02	2.760000E+00	-2.061875E+06
92	C2H3 + O2 \leftrightarrow CH2CO + OH	1.060000E+00	2.390000E+00	2.585712E+07
93	C2H3 + O2 \leftrightarrow CH2CO + OH	5.260000E-04	3.010000E+00	7.434968E+06

No.	Reaction	A	b	E_a
94	$C_2H_3 + O_2 \leftrightarrow CH_2O + HCO$	2.730000E+32	-7.320000E+00	4.945488E+07
95	$C_2H_3 + O_2 \leftrightarrow CH_2O + HCO$	6.080000E+12	-1.310000E+00	2.701609E+06
96	$C_2H_3 + O_2 \rightarrow CH_2O + CO + H$	6.360000E+32	-7.320000E+00	4.945488E+07
97	$C_2H_3 + O_2 \rightarrow CH_2O + CO + H$	1.420000E+13	-1.310000E+00	2.701609E+06
98	$C_2H_3 + O_2 \leftrightarrow CH_3O + CO$	1.030000E+08	-3.300000E-01	-3.128795E+06
99	$C_2H_3 + O_2 \leftrightarrow CH_3O + CO$	5.770000E+18	-3.540000E+00	1.996605E+07
100	$C_2H_3 + O_2 \leftrightarrow CH_3 + CO_2$	7.250000E+28	-6.700000E+00	4.368096E+07
101	$C_2H_3 + O_2 \leftrightarrow CH_3 + CO_2$	5.320000E+10	-1.140000E+00	1.868993E+06
102	$C_2H_3 + H \leftrightarrow C_2H_2 + H_2$	9.635250E+10	0.000000E+00	0.000000E+00
103	$C_2H_3 + OH \leftrightarrow C_2H_2 + H_2O$	3.011000E+10	0.000000E+00	0.000000E+00
104	$C_2H_2 + O \leftrightarrow CH_2(L1) + CO$	7.395000E+05	1.280000E+00	1.034285E+07
105	$C_2H_2 + HCO \leftrightarrow C_2H_3 + CO$	1.000000E+04	2.000000E+00	2.510400E+07
106	$C_2H_2 + OH \leftrightarrow CH_2CO + H$	7.528000E+03	1.550000E+00	8.811504E+06
107	$C_2H_2 + OH \leftrightarrow CH_3 + CO$	1.277000E+06	7.300000E-01	1.079054E+07
108	$CH_2CO (+M) \leftrightarrow CH_2(L1) + CO (+M)$	3.000000E+12	0.000000E+00	2.384880E+08
	Troe coefficients : -	3.000000E+13	0.000000E+00	2.970640E+08
	Species efficiencies : CH4:2.0E+00 CO:1.5E+00 CO2:2.0E+00 H2O:6.0E+00			
109	$C_2H_3 + O \leftrightarrow CH_2CO + H$	3.000000E+10	0.000000E+00	0.000000E+00
110	$CH_2CO + H \leftrightarrow CH_3 + CO$	7.770000E+05	1.450000E+00	1.163152E+07
111	$CH_2CO + OH \leftrightarrow CH_2OH + CO$	2.000000E+09	0.000000E+00	-4.225840E+06
112	$C_2H_4 + CH_2(L1) \leftrightarrow C_2H_3 + CH_3$	4.160000E+21	-3.190000E+00	4.083584E+07
113	$C_2H_4 + CH_2(L1) \leftrightarrow C_2H_3 + CH_3$	4.920000E+06	1.020000E+00	2.509438E+06
114	$C_2H_2 + O \rightarrow CH_2CO$	1.000000E+10	0.000000E+00	6.276000E+07
115	$CH_2CO + O \rightarrow 2 HCO$	2.000000E+10	0.000000E+00	9.623200E+06
116	$CH_2CO + OH \rightarrow CH_3 + CO_2$	1.000000E+10	0.000000E+00	0.000000E+00
117	$O + OH + M \leftrightarrow HO_2 + M$	1.000000E+10	0.000000E+00	0.000000E+00
118	$C_2H_5 + O_2 \rightarrow CH_2O + CH_3O$	1.000000E+11	0.000000E+00	1.004160E+08
119	$CH_2(L1) + HCO \leftrightarrow CH_3 + CO$	1.078469E+11	-2.145491E-01	2.031268E+06
120	$CH_2(L1) + O \leftrightarrow CO + H_2$	2.696171E+11	-2.145491E-01	2.031268E+06
121	$CH_2(L1) + OH \leftrightarrow CH_2O + H$	1.617703E+11	-2.145491E-01	2.031268E+06
122	$CH_2(L1) + CO_2 \leftrightarrow CH_2O + CO$	5.931577E+08	-2.145491E-01	6.215269E+06
123	$CH_2(L1) + O \leftrightarrow CO + 2 H$	1.871156E+02	1.988656E+00	-1.763074E+07

No.	Reaction	A	b	E_a
124	$\text{CH}_2(\text{L1}) + \text{CH}_4 \longleftrightarrow 2 \text{CH}_3$	2.681990E+02	1.988656E+00	-1.763074E+07
125	$2 \text{CH}_3 \longrightarrow \text{C}_2\text{H}_4 + \text{H}_2$	5.000000E+11	0.000000E+00	1.338880E+08
126	$2 \text{CH}_2(\text{L1}) \longrightarrow \text{C}_2\text{H}_2 + 2 \text{H}$	6.470811E+11	-2.145491E-01	2.031268E+06
127	$\text{C}_2\text{H}_6 \longleftrightarrow \text{C}_2\text{H}_4 + \text{H}_2$	3.000000E+13	0.000000E+00	3.284440E+08
128	$\text{CH}_2\text{O} + \text{O} \longrightarrow \text{CO}_2 + 2 \text{H}$	2.000000E+10	0.000000E+00	2.092000E+07
129	$\text{CH}_2\text{O} + \text{OH} \longrightarrow \text{CO}_2 + \text{H} + \text{H}_2$	1.000000E+08	0.000000E+00	0.000000E+00
130	$\text{C}_2\text{H}_2 + \text{HO}_2 \longrightarrow \text{CH}_2\text{O} + \text{HCO}$	5.000000E+09	0.000000E+00	6.276000E+07
131	$\text{CH}_3\text{O} + \text{CO} \longleftrightarrow \text{CH}_3 + \text{CO}_2$	5.000000E+08	0.000000E+00	2.719600E+07
132	$\text{C}_2\text{H}_2 + \text{O}_2 \longrightarrow \text{CH}_2\text{O} + \text{CO}$	3.000000E+08	0.000000E+00	1.087840E+08
133	$\text{C}_2\text{H}_4 + \text{O}_2 \longrightarrow 2 \text{CH}_2\text{O}$	1.000000E+11	0.000000E+00	2.008320E+08
134	$\text{C}_2\text{H}_2 + \text{O}_2 \longrightarrow 2 \text{HCO}$	3.000000E+08	0.000000E+00	1.129680E+08
135	$\text{C}_2\text{H}_4 + \text{O}_2 \longrightarrow \text{CH}_3\text{O} + \text{HCO}$	1.000000E+11	0.000000E+00	1.799120E+08
136	$\text{CH}_3 + \text{O} + \text{M} \longrightarrow \text{CH}_3\text{O} + \text{M}$	5.000000E+10	0.000000E+00	0.000000E+00
137	$\text{CH}_2\text{OH} + \text{CH}_3 \longrightarrow \text{CH}_2\text{O} + \text{CH}_4$	1.500000E+10	0.000000E+00	0.000000E+00
138	$\text{C}_2\text{H}_4 + \text{O} \longleftrightarrow \text{C}_2\text{H}_3 + \text{OH}$	1.083000E+04	2.000000E+00	3.674372E+07

List of Figures

1.1.	CO ₂ emissions <i>vs.</i> GDP per capital throughout the world.	3
1.2.	Power-to-gas strategy, from the International Renewable Energy Agency (IRENA). Fields of application for porous burners are shown in dashed purple.	4
1.3.	Examples of combustion devices of large surface-to-volume ratio. (a) from [41]: a silica micro-fibrous porous burner of characteristic fiber size 4 μm / (b) a classical porous burner made of reticulated alumina foam (credits F. Muller, IMFT) / (c) from [42]: a two-backward-step microcombustor using hydrogen as fuel / (d) from [43]: a swiss-roll microcombustor with very low flammability limit and strong heat recirculation.	6
1.4.	Principle of heat recirculation on various configurations.	7
1.5.	Effect of heat recirculation on a premixed flame.	8
1.6.	Heat recirculation in a classical free-flame burner leading to flashback. Credits: H. Pers, IMFT.	9
1.7.	From [59–61]: examples of commercial and industrial solutions based upon porous media combustion.	9
1.8.	Equivalence ratios attained by various heat recirculating devices for methane combustion, reported from the literature. Solid line: flammability limits.	10
1.9.	Adiabatic equilibrium computations, computed with CANTERA, chemical scheme GriMech3.0. Here ppm = molar fractions × 10 ⁶	11
1.10.	Typical trends of emissions in porous burners found in the literature.	11
1.11.	From [104]: examples of porous foams used in experiments - each 10, 20 and 30 pores per inch (PPI).	12
1.12.	Adiabatic laminar free-flame of methane-air at ambient conditions for an equivalence ratio $\phi = 0.8$, computed with CANTERA [112].	14
1.13.	Effect of uniform heat losses on flame structure of laminar flames. Left: for a given heat loss, two solutions may exist, one of high velocity and one of low velocity. Right: influence of heat loss intensity on the multiplicity of solutions.	15
1.14.	Flame acceleration (speed-up) Γ_p as a function of the unburnt temperature T_u	16
1.15.	Schematic view of the flame structure inside a porous burner of finite length, illustrating heat recirculation and the various regions of heat transfer, release and diffusion.	17
1.16.	Multiplicities and flame shapes in porous burners of finite length (schematic representation, adapted from the results of [125]. In (a) → (f) the gas and solid temperature profiles are shown respectively in solid black and dashed grey, while (g) represents the diagram mass flow rate \dot{m}_∞ <i>vs.</i> position x . The porous medium is represented in light grey. \dot{m}_0 is the mass flow rate of the 1D adiabatic laminar flame.	18
1.17.	For the same flame anchoring positions within the pores, augmentation of flame surface for an increase in inlet velocity (1.0 → 1.2 m s ⁻¹). Hydrogen-air, $\phi = 0.3$, chemical scheme Boivin. The flame surface is defined by 50% of fuel consumption.	19
1.18.	Schematic representation of the pore-level anchoring influence on the stability diagram of a porous burner (strong flames only).	20

1.19. Illustration of typical pore-scale phenomenology: sharp flame fronts anchored locally.	24
1.20. Outline of the manuscript.	25
2.1. Illustration of various microscale phenomena occurring in porous media combustion on a slice extracted from a 3D DNS. Afferent notations are introduced later in this chapter. Superadiabatic regions correspond to reduced temperatures $\theta_g > 1$.	28
2.2. Illustration of pressure drop in porous media combustion. Hydrogen-air flame at equivalence ratio $\phi = 0.3$. The black line marks the isocontour 10% of H2 consumption. Inlet velocity $U_{in} = 2.5 \text{ m s}^{-1}$. Mean pore diameter $\bar{d}_p = 1 \text{ mm}$.	30
2.3. Ratio of longitudinal velocity component u to inlet velocity U_{in} , for increasing pore-based Reynolds numbers Re_p . Each case corresponds to a different listed regime.	31
2.4. Fit of constant h_V for an interphase heat exchange of the form of Equation (6.26) in a reactive coupled gas/solid 3D DNS performed in this thesis.	33
2.5. Illustration of dispersion.	34
2.6. Adapted from [208]: correlation of dispersion as a function of the Péclet number.	36
2.7. Illustration: smaller and larger d_p/δ_L ratios.	37
2.8. Generalized classification of flow regimes within porous media, adapted to porous media combustion, based on the notion of thermal flame thickness.	39
2.9. Best fit of effective conductivity in (a) a steady reactive coupled gas-solid simulation, yielding $\lambda_s^{\text{eff}} = 2.09 \text{ W m}^{-1} \text{ K}^{-1}$ and (b) a transient solid-only heat transfer simulation, yielding $\lambda_s^{\text{eff}} = 1.98 \text{ W m}^{-1} \text{ K}^{-1}$. A 3D view is provided for visualisation of the shape of the fields.	40
2.10. Principle of volume-averaging over a Representative Elementary Volume (REV) with (a) a centroid of radius r_0 and (b) a slice infinite in the y and z directions of thickness r_0	45
2.11. Geometrical proof of the spatial averaging theorem.	52
3.1. Principle: flame submerged within infinite porous medium.	57
3.2. Temperature profiles for four different inlet mass flow rates and $r_\lambda = 0.01$. The parameters used are: $\epsilon = 0.8$, $\lambda_s = 20 \text{ W m}^{-1} \text{ K}^{-1}$, $\lambda_g = 0.025 \text{ W m}^{-1} \text{ K}^{-1}$, $h_V = 1.2 \times 10^5 \text{ W m}^{-3} \text{ K}^{-1}$, and $c_{p_g} = 1 \times 10^3 \text{ J kg}^{-1} \text{ K}^{-1}$	61
3.3. Recirculation efficiency η_{rec} for various values of the dimensionless parameters $r_{\dot{m}}$ and r_λ . Solid lines: $r_{\dot{m}} > 0.5$ and $r_{\dot{m}}/r_\lambda > 50$. Dotted lines: $r_{\dot{m}} < 0.5$ or $r_{\dot{m}}/r_\lambda < 50$. The points (a-d) correspond to Figure 3.2.	62
3.4. Relative error between Equations (3.47) and (3.48).	65
3.5. Speed-up of the porous medium system: numerical simulations and power law correlations.	66
3.6. Validation of the speed-up $S_L^P/S_L^0(T_u)$: comparison between a reference numerical simulation with CANTERA + GRIMECH 3.0 and the various formulae derived in this chapter.	68
3.7. Illustration of flame distribution and wrinkling inside porous media.	69
3.8. Principle: flame submerged in a finite porous medium.	71
3.9. Example of temperature profiles: adiabatic and radiant heat losses cases. The solution of the equivalent infinite porous medium is superimposed for comparison. The parameters used are: $T_u = 300 \text{ K}$, $T_{ad} = 2000 \text{ K}$, $\epsilon = 0.8$, $\lambda_s = 20 \text{ W m}^{-1} \text{ K}^{-1}$, $\lambda_g = 0.025 \text{ W m}^{-1} \text{ K}^{-1}$, $h_V = 6 \times 10^4 \text{ W m}^{-3} \text{ K}^{-1}$, $c_{p_g} = 1 \times 10^3 \text{ J kg}^{-1} \text{ K}^{-1}$, $L = 2 \text{ cm}$, $\dot{m} = 1.2 \text{ kg m}^{-2} \text{ s}^{-1}$, and $x_p = L/4$	73

3.10. Recirculation efficiency versus flame position for various lengths of porous media. Solid line: adiabatic case. Dashed line: with <u>radiant heat losses</u> . Parameters used: $T_u = 300$ K, $T_{ad} = 2000$ K, $\epsilon = 0.8$ and $\sqrt{(1 - \epsilon)/h_V \lambda_s} = 2 \times 10^{-4}$ m ² K W ⁻¹ for the radiant heat losses case.	73
3.11. Speed-up ratio versus flame position for various lengths of porous media. Solid line: adiabatic case. Dashed line: with radiant heat losses. The parameters used are: $T_u = 300$ K, $T_{ad} = 2000$ K, $\epsilon = 0.8$, $\lambda_s = 20$ W m ⁻¹ K ⁻¹ , $\lambda_g = 0.025$ W m ⁻¹ K ⁻¹ , $h_V = 2.4 \times 10^5$ W m ⁻³ K ⁻¹ , $c_{p_g} = 1 \times 10^3$ J kg ⁻¹ K ⁻¹ , $\dot{m}_0 = 1.2$ kg m ⁻² s ⁻¹ , and $n_T = 1$	74
3.12. Convergence towards the infinite porous medium case - universal curve in the conditions (3.37) and (3.70).	74
3.13. Principle: theoretical modelling of multi-step burners.	75
3.14. Illustration of the stability of single and multi-layered porous burners as predicted by 1D asymptotic theory.	77
3.15. Two-step burner for increasing thermal resistance between the two layers. Thermo-physical properties: $\lambda_{s,1} = \lambda_{s,2} = 3.0$ W m ⁻¹ K ⁻¹ , $h_{V,1} = h_{V,2} = 5 \times 10^4$ W m ⁻³ K ⁻¹ , $\epsilon_1 = \epsilon_2 = 0.8$, $c_{p_g} = 1 \times 10^3$ J kg ⁻¹ K ⁻¹ , $L_1 = L_2 = 1$ cm, $\dot{m}_0 = 0.5$ kg m ⁻² s ⁻¹ , $\beta = 8.0$, $\lambda_g = 0.025$ W m ⁻¹ K ⁻¹ . Unit for R_1 is W m ⁻² K ⁻¹	77
3.16. Stability envelope for all values of resistances.	78
3.17. Profiles in the physical space for lower (a) and larger (b) surface contact resistance values, same thermo-physical properties than Figure 3.15 but this time $N = 3$ and $L_1 = L_2 = L_3 = 2/3$ cm. Unit for R_1 is W m ⁻² K ⁻¹	78
3.18. Influence of porosity step. $R_1 = 0$, same other thermo-physical properties than Figure 3.15.	79
3.19. Influence of interphase heat coefficient step, from a reference $h_V = 5 \times 10^4$ W m ⁻³ K ⁻¹ . $R_1 = 0$, same other thermo-physical properties than Figure 3.15.	80
3.20. Influence of thermal conductivity step step, from a reference $\lambda_s = 3.0$ W m ⁻¹ K ⁻¹ . $R_1 = 0$, same other thermo-physical properties than Figure 3.15.	80
3.21. Influence of flame wrinkling, with $\Gamma_w = 1$ upstream and $\Gamma_w = 2$ downstream, $R_1 = 0$, same other thermo-physical properties than Figure 3.15.	81
3.22. Influence of the number of layers N , for a fixed length L , $R_i = 0$, same other thermo-physical properties than Figure 3.22.	82
4.1. Representation of a submerged flame in infinite porous media.	92
4.2. Solid/gas temperatures, heat release rate and interphase out-of-equilibrium temperatures from the numerical simulations (SIM) and the analytical model (AM). Methane-air, single-step, $\phi = 0.5$. The unit for h_V is W.m ⁻³ .K ⁻¹ . In case (b), θ_s for (AM) and (SIM) are superimposed. In case (d), $\theta_s \sim \theta_g$ both for (AM) and (SIM).	96
4.3. Computed speed-up versus speed-up related to preheating. Methane-air, $\phi = 0.5$, single-step. Symbols: simulations (black: decoupled, medium grey: intermediate, light grey: hyperdiffusive).	98
4.4. Simplified resistive model.	98
4.5. Points of Figure 4.3 in the space ($r_{\dot{m}}, r_{\lambda}$) and various mathematical predictions. Symbols: simulations (black: decoupled, medium grey: intermediate, light grey: hyperdiffusive). Methane-air, $\phi = 0.5$, single-step.	100
4.6. Comparison between the hyperdiffusive flame of Figure 4.2(d) and its free-flame counterpart of increased thermal conductivity. Methane-air, single-step, $\phi = 0.5$	102
4.7. Structure of the flames of Figure 4.2(a-d).	103

4.8.	(a) Temperature at the maximum of heat release rate. (b) Length of the reaction zone defined as the centered segment covering 80% of the integral of heat release rate. Large symbols: simulations. Small symbols: theoretical prediction.	104
4.9.	Effect of equivalence ratio on the maximum temperature. Single-step, methane-air. The ratio of stiffnesses reads: $\gamma_{1S,\phi=1.0,CH4}/\gamma_{1S,\phi=0.5,CH4} = 0.61$	105
4.10.	Effect of fuel on the maximum temperature. Single-step, $\phi = 0.5$. The ratio of stiffness reads: $\gamma_{1S,\phi=0.5,H2}/\gamma_{1S,\phi=0.5,CH4} = 0.59$	106
4.11.	Effect of reaction scheme on the maximum temperature. Methane-air, $\phi = 0.5$. The ratio of stiffness reads: $\gamma_{GRI\text{MECH}3.0,\phi=0.5,CH4}/\gamma_{1S,\phi=0.5,CH4} = 0.84$	106
4.12.	Theoretical prediction of Equation (4.42) versus numerical simulations of methane-air, single-step, $\phi = 0.5$	108
4.13.	Structures of flames including normalized HRR, methane-air, $\phi = 0.5$, single step, $r_\lambda = 0.1$	111
4.14.	Progressive structure of a lean hydrogen-air flame for increased heat transfer, including normalized HRR. Single-step, $\phi = 0.5$, $r_\lambda = 0.01$	112
5.1.	From [137]: illustration of the pre-processing wrap algorithm used to manage the contact point problem for a finite-volume numerical simulation of porous media combustion, in the case of packed bed of spheres.	115
5.2.	Mesh convergence study for methane-air ($\phi = 0.72$) and hydrogen-air ($\phi = 0.38$) flames, with CANTERA and AVBP.	116
5.3.	From porous foam to computational mesh.	118
5.4.	Example of tomographic image of a 30 PPI foam. Note the presence of inner cavities inside the solid. Green arrow: closed cavity. Blue arrow: open cavity	119
5.5.	Voxel treatment. From tomographic slice to final domains (a) \rightarrow (e). Comparison between (a) and (e) shown in (f).	120
5.6.	Artificial padding of the fluid domain (a) then cropping (b). Green arrows: side padding. Red arrows: inlet and outlet padding.	121
5.7.	Construction of the solid phase from the fluid-solid interface (a) then filled manually with BLENDER (b).	122
5.8.	Topological problems on the STL generated.	123
5.9.	Example of computational mesh for a 60 PPI foam, mesh size 80 μm	124
5.10.	Example of computational mesh for a 30 PPI diamond-based burner, mesh size 80 μm	125
6.1.	Computational domains. Flow from left to right.	130
6.2.	Local characterization of the geometries.	132
6.3.	Flame acceleration due to preheating.	133
6.4.	Principle of volume-averaging and shape of the REV.	134
6.5.	Fitting of effective thermal conductivity for domain R1 (time computed: 21 s). Profiles evenly distributed in time.	137
6.6.	Illustration of dispersion in physical space, slices, domain R1, from $t = 0$ to 2 ms, inlet velocity $U_{in} = 1 \text{ m s}^{-1}$	138
6.7.	Fitting of dispersion coefficient for domain R1 ($U_{in} = 1 \text{ m s}^{-1}$, time computed: 5 ms). Profiles evenly distributed in time: the first three profiles on the left correspond to that of Figure 6.6.	138
6.8.	Fit of constant h_V on domain D2.	139
6.9.	3D view of the solutions points used in this work. Solid/streamline coloring - blue cold, red hot regions. Black region: isocontour of heat release ($3 \times 10^9 \text{ W m}^{-3}$).	140

6.10. Slices in various domains. Gas/solid temperatures, heat release rate and inter-phase heat transfer.	141
6.11. Slices in domain R1: (a) reduced CH ₄ mass fraction, (b) reduced H mass fraction and (c) longitudinal velocity u	142
6.12. DPLS <i>vs.</i> VAM with properties of Table 6.3.	143
6.13. Gas/solid temperature profiles, DPLS <i>vs.</i> VAM, domain D2.	144
6.14. Mass fraction profiles, DPLS <i>vs.</i> VAM, domain D2.	144
6.15. Average HRR in the DPLS <i>vs.</i> HRR computed in the VAM, domain D2.	144
6.16. Evaluation of the commutation error for heat release rate.	146
6.17. Commutation errors for all domains.	147
6.18. Isocontours of 1% and 80% of fuel consumption (progress variable c_F).	148
6.19. Scatter plot and PDF on \mathcal{A} , domain D2. Blue cold (pore centers), red hot regions (near walls).	149
6.20. Performance of closure models for DPLS.	151
6.21. Mass budgets: comparison of the terms Υ_1/Υ_2 (species equation) for domain D2, as defined in Equation (2.70). The red region indicates the reaction zone.	154
6.22. Energy budgets: comparison of the terms χ_1/χ_2 (solid equation), Ξ_1/Ξ_2 , Ψ_1/Ψ_2 (gas equation) for domain D2, as defined in Equations (2.64), (2.78) and (2.79). The red region indicates the reaction zone.	155
6.23. Scatter plot and PDF on \mathcal{A} , domains D1 and D4. Blue cold (pore centers), red hot regions (near walls).	156
7.1. Flame acceleration due to preheating for varying fuel and equivalence ratio.	163
7.2. Evolution of δ_L^0 and δ_c^0 as a function of temperature for two methane-air and hydrogen-air flames.	163
7.3. Comparison of spatial flames structures for CH ₄ and H ₂ at 300 and 800 K.	163
7.4. Left: ratio of total kinetic energy E_{cin} with its temporal average. Right: power spectrum density (PSD) of the left signal. Domain D2.	166
7.5. Top: time-averaged fields of velocity norm and heat release rate. Bottom: instantaneous fields at $t_{1 \rightarrow 5}$ as defined in Figure 7.4. Domain D2, $U_{\text{in}} = 2 \text{ m s}^{-1}$, H ₂ -air, $\phi = 0.38$	166
7.6. Signal of reduced velocity magnitude at point P_1 and afferent power density spectrum.	167
7.7. Flashback of a hydrogen flame when passing from unsteady to steady-state by increasing the dynamic viscosity and stopping the matched time steps (solid acceleration).	168
7.8. Axial velocity component u <i>versus</i> transverse position y along a line passing through P1. The origin is aligned with the center of the transverse area.	169
7.9. Slice of velocity norm and heat release rate. Domain D2, $U_{\text{in}} = 5 \text{ m s}^{-1}$	169
7.10. Comparison of CH ₄ -air and H ₂ -air flames.	170
7.11. Relative amount of O ₂ compared to the adiabatic laminar flame at a given progress variable.	171
7.12. DPLS <i>vs.</i> VAM for various H ₂ -air flames. Performance of the various models.	171
7.13. Fit of constant h_V on domain D2 for the hydrogen-air case, on the time-averaged solution.	172
7.14. Evaluation of the commutation error for heat release rate for hydrogen cases.	172
7.15. Example of stable combustion below the flammability limit at $\phi = 0.25 < \phi_{\text{LFL}}$. Inlet velocity $U_{\text{in}} = 0.7 \text{ m s}^{-1}$	173
7.16. Scatter plot and PDF on \mathcal{A}^* , domain D1, hydrogen-air flame $\phi = 0.38$. Blue cold (pore centers), red hot regions (near walls).	174

7.17. Scatter plot and PDF on \mathcal{A} , domain D1, methane-air flame $\phi = 0.72$. Blue cold (pore centers), red hot regions (near walls).	174
7.18. Presence of regimes for real porous burners?	177
7.19. Experimental setup to visualize directly flame fronts in lattice-based porous burners (current investigations).	179

List of Tables

1.1.	Properties of typical materials used in porous media combustion (at ~ 600 K). . .	13
1.2.	Various designs for porous burners encountered in the literature.	21
2.1.	Various flow regimes for increasing interstitial velocities inside porous media. . .	29
2.2.	Various expressions for interphase heat transfer found in the literature. Pr is the Prandtl number, \mathcal{S}_V is the surface density, ϵ the porosity, and λ_g the gas thermal conductivity.	33
3.1.	Relevant thermodynamic and chemical properties for two reacting mixtures used as examples.	64
4.1.	Arrhenius pre-exponential factors A , activation temperatures T_A and fuel/oxidizer orders n_F/n_O used in the single-step approximations, for a molar production rate of the form $A \left[\frac{\rho_g Y_F}{W_F} \right]^{n_F} \left[\frac{\rho_g Y_O}{W_O} \right]^{n_O} \exp \left(-\frac{T_A}{T_g} \right)$	94
5.1.	Literature review of 3D DNS for porous media combustion.	117
6.1.	Characterisation of the computational domains.	131
6.2.	Adiabatic free-flame properties.	133
6.3.	Macroscale properties of the various domains.	136
6.4.	Inlet velocities U_{in} and pore-based Reynolds numbers Re_p	140
6.5.	Γ and Γ_w values.	150
7.1.	Adiabatic free-flame properties.	164
A.1.	List of reactions with A the pre-exponential factor in $m^{3(n-1)}/kmol^{n-1}/s$ with n the order of the reaction, b the temperature exponent and E_a the activation energy in $J/kmol$. In the case of fall-off reactions, two sets of Arrhenius coefficients are specified, the first one being the low temperature set and the second one the high temperature set.	184

Bibliography

- [1] S. He, W. Shao, and J. Han, “Have artificial lighting and noise pollution caused zoonosis and the covid-19 pandemic? a review,” Environmental Chemistry Letters, vol. 19, no. 6, pp. 4021–4030, 2021.
- [2] C. Le Quéré, R. B. Jackson, M. W. Jones, A. J. Smith, S. Abernethy, R. M. Andrew, A. J. De-Gol, D. R. Willis, Y. Shan, J. G. Canadell, et al., “Temporary reduction in daily global co₂ emissions during the covid-19 forced confinement,” Nature climate change, vol. 10, no. 7, pp. 647–653, 2020.
- [3] F. Schreyer, G. Luderer, R. Rodrigues, R. C. Pietzcker, L. Baumstark, M. Sugiyama, R. J. Brecha, and F. Ueckerdt, “Common but differentiated leadership: strategies and challenges for carbon neutrality by 2050 across industrialized economies,” Environmental Research Letters, vol. 15, no. 11, p. 114016, 2020.
- [4] I. Chapman, “The end of peak oil? why this topic is still relevant despite recent denials,” Energy Policy, vol. 64, pp. 93–101, 2014.
- [5] N. Tanaka et al., “World energy outlook 2010,” International Energy Agency. Paris: IEA, 2010.
- [6] C. J. Campbell, “Peak oil,” Presentation at the Technical University of Clausthal, 2000.
- [7] C. J. Cleveland and P. A. O’connor, “Energy return on investment (eroi) of oil shale,” Sustainability, vol. 3, no. 11, pp. 2307–2322, 2011.
- [8] D. C. R. Hans-Otto Pörtner, “Climate change 2022 impacts, adaptation and vulnerability working group ii contribution to the sixth assessment report of the intergovernmental panel on climate change,” 2021.
- [9] S. D. Casler and P. D. Blair, “Economic structure, fuel combustion, and pollution emissions,” Ecological economics, vol. 22, no. 1, pp. 19–27, 1997.
- [10] A. Valera-Medina, H. Xiao, M. Owen-Jones, W. I. David, and P. Bowen, “Ammonia for power,” Progress in Energy and combustion science, vol. 69, pp. 63–102, 2018.
- [11] G. H. Markstein, “Combustion of metals,” AIAA Journal, vol. 1, no. 3, pp. 550–562, 1963.
- [12] S. Verhelst and T. Wallner, “Hydrogen-fueled internal combustion engines,” Progress in energy and combustion science, vol. 35, no. 6, pp. 490–527, 2009.
- [13] E. Erik, “World history of the automobile. warrendale, pa: Society of automotive engineers,” 2001.
- [14] P. A. Marques and R. Kempener, “The european hydrogen strategy,” Utilization of Hydrogen for Sustainable Energy and Fuels, p. 105, 2021.
- [15] J. D. Holladay, J. Hu, D. L. King, and Y. Wang, “An overview of hydrogen production technologies,” Catalysis today, vol. 139, no. 4, pp. 244–260, 2009.
- [16] A. Körner, C. Tam, S. Bennett, and J. Gagné, “Technology roadmap-hydrogen and fuel cells,” International Energy Agency (IEA): Paris, France, 2015.

-
- [17] S. S. Kumar and V. Himabindu, "Hydrogen production by pem water electrolysis—a review," Materials Science for Energy Technologies, vol. 2, no. 3, pp. 442–454, 2019.
- [18] P. Sharer and A. Rousseau, "Benefits of fuel cell range extender for medium-duty vehicle applications," World Electric Vehicle Journal, vol. 6, pp. 452–463, 06 2013.
- [19] R. U. Ayres, L. W. Ayres, and B. Warr, "Exergy, power and work in the us economy, 1900–1998," Energy, vol. 28, no. 3, pp. 219–273, 2003.
- [20] S. Dunn, "Hydrogen futures: toward a sustainable energy system," International journal of hydrogen energy, vol. 27, no. 3, pp. 235–264, 2002.
- [21] G. Gahleitner, "Hydrogen from renewable electricity: An international review of power-to-gas pilot plants for stationary applications," international Journal of hydrogen energy, vol. 38, no. 5, pp. 2039–2061, 2013.
- [22] N. Kakutkina, A. Korzhavin, and M. Mbarawa, "Filtration combustion of hydrogen-air, propane-air, and methane-air mixtures in inert porous media," Combustion, Explosion and Shock Waves, vol. 42, no. 4, pp. 372–383, 2006.
- [23] R. D. F.-G. Gaz, F. Storengy, G. Reseau, P. d. E. G. N. Syndicat, et al., "Technical and economic conditions for injecting hydrogen into natural gas networks-final report june 2019," 2019.
- [24] R. Habib, B. Yadollahi, A. Saeed, M. H. Doranehgard, and N. Karimi, "On the response of ultralean combustion of ch₄/h₂ blends in a porous burner to fluctuations in fuel flow—an experimental investigation," Energy & Fuels, vol. 35, no. 10, pp. 8909–8921, 2021.
- [25] R. S. Cherry, "A hydrogen utopia?," International Journal of Hydrogen Energy, vol. 29, no. 2, pp. 125–129, 2004.
- [26] F. Yang, T. Wang, X. Deng, J. Dang, Z. Huang, S. Hu, Y. Li, and M. Ouyang, "Review on hydrogen safety issues: Incident statistics, hydrogen diffusion, and detonation process," International journal of hydrogen energy, vol. 46, no. 61, pp. 31467–31488, 2021.
- [27] Y. S. Najjar, "Hydrogen safety: The road toward green technology," International Journal of Hydrogen Energy, vol. 38, no. 25, pp. 10716–10728, 2013.
- [28] R. Derwent, "Global warming consequences of a future hydrogen economy," 2004.
- [29] J. Howell, M. Hall, and J. Ellzey, "Combustion of hydrocarbon fuels within porous inert media," Progress in Energy and Combustion Science, vol. 22, no. 2, pp. 121 – 145, 1996.
- [30] J. L. ELLZEY and R. Goel, "Emissions of co and no from a two stage porous media burner," Combustion science and technology, vol. 107, no. 1-3, pp. 81–91, 1995.
- [31] S. Alavandi and A. Agrawal, "Experimental study of combustion of hydrogen–syngas/methane fuel mixtures in a porous burner," International journal of hydrogen energy, vol. 33, no. 4, pp. 1407–1415, 2008.
- [32] S. Gauthier, E. Lebas, and D. Baillis, "One layer porous radiant burners: experimental and numerical study," in Eurotherm Seminar, no. 81, 2007.
- [33] S. Wood and A. T. Harris, "Porous burners for lean-burn applications," Progress in Energy and Combustion Science, vol. 34, no. 5, pp. 667–684, 2008.

- [34] D. Diamantis, E. Mastorakos, and D. Goussis, "Simulations of premixed combustion in porous media," Combustion Theory and Modelling, vol. 6, no. 3, pp. 383–411, 2002.
- [35] V. Khanna, R. Goel, and J. Ellzey, "Measurements of emissions and radiation for methane combustion within a porous medium burner," Combustion science and technology, vol. 99, no. 1-3, pp. 133–142, 1994.
- [36] R. Mital, J. Gore, and R. Viskanta, "A study of the structure of submerged reaction zone in porous ceramic radiant burners," Combustion and flame, vol. 111, no. 3, pp. 175–184, 1997.
- [37] M. Kulkarni and R. Peck, "Analysis of a bilayered porous radiant burner," Numerical Heat Transfer, Part A Applications, vol. 30, no. 3, pp. 219–232, 1996.
- [38] Y. B. Zeldovich, "Theory of limit of quiet flame propagation," Zh. Prikl. Mekh. Tekh. Fiz., vol. 11, no. 1, pp. 159–169, 1941.
- [39] H. I. Joo, K. Duncan, and G. Ciccarelli, "Flame-quenching performance of ceramic foam," Combustion science and technology, vol. 178, no. 10-11, pp. 1755–1769, 2006.
- [40] V. Babkin, "The problems of porous flame-arresters," in Prevention of hazardous fires and explosions, pp. 199–213, Springer, 1999.
- [41] H. Yang, S. Minaev, E. Geynce, H. Nakamura, and K. Maruta, "Filtration combustion of methane in high-porosity micro-fibrous media," Combustion science and technology, vol. 181, no. 4, pp. 654–669, 2009.
- [42] Q. Peng, Y. Wu, J. E. W. Yang, H. Xu, and Z. Li, "Combustion characteristics and thermal performance of premixed hydrogen-air in a two-rearward-step micro tube," Applied Energy, vol. 242, pp. 424–438, 2019.
- [43] N. I. Kim, S. Aizumi, T. Yokomori, S. Kato, T. Fujimori, and K. Maruta, "Development and scale effects of small swiss-roll combustors," Proceedings of the Combustion Institute, vol. 31, no. 2, pp. 3243–3250, 2007.
- [44] V. Zamashchikov, "Experimental investigation of gas combustion regimes in narrow tubes," Combustion and Flame, vol. 108, no. 3, pp. 357–359, 1997.
- [45] D. Trimis and F. Durst, "Combustion in a porous medium-advances and applications," Combustion science and technology, vol. 121, no. 1-6, pp. 153–168, 1996.
- [46] K. J. Laidler, "The development of the arrhenius equation," Journal of chemical Education, vol. 61, no. 6, p. 494, 1984.
- [47] B. Galmiche, F. Halter, F. Foucher, and P. Dagaut, "Effects of dilution on laminar burning velocity of premixed methane/air flames," Energy & Fuels, vol. 25, no. 3, pp. 948–954, 2011.
- [48] J. Lamouroux, M. Ihme, B. Fiorina, and O. Gicquel, "Tabulated chemistry approach for diluted combustion regimes with internal recirculation and heat losses," Combustion and Flame, vol. 161, no. 8, pp. 2120–2136, 2014.
- [49] F. Weinberg, "Combustion temperatures: the future?," Nature, vol. 233, no. 5317, pp. 239–241, 1971.

-
- [50] T. Benzinger, A. Pratt, and C. Kitzinger, "The thermostatic control of human metabolic heat production," Proceedings of the National Academy of Sciences of the United States of America, vol. 47, no. 5, p. 730, 1961.
- [51] A. Mach, A. Herzog, F. von Issendorff, B. Kanka, R. Krieger, W. Pritzkow, J. Schäfer, J. Schmidt, M. Schmücker, H. Schneider, J. Stark, D. Trimis, U. Vogt, and D. Megede, "Cerpor - optimised ceramic components for the porous burner technology," InterCeram: International Ceramic Review, pp. 48–54, 01 2006.
- [52] V. Jovicic, S. Ausmeier, A. Delgado, C. Schmidt, and N. Gerlach, "Experimental results of long time tests of porous burners with ceramic housing for high temperature application in glass industry," 09 2010.
- [53] M. Ravich, "Surface flameless combustion (in russian)," Izd. Akad. Nauk SSSR, Moscow-Leningrad, 1949.
- [54] S. Bani, J. Pan, A. Tang, Q. Lu, and Y. Zhang, "Micro combustion in a porous media for thermophotovoltaic power generation," Applied Thermal Engineering, vol. 129, pp. 596–605, 2018.
- [55] I. Malico and M. Abdul Mujeebu, "Potential of porous media combustion technology for household applications," International Journal of Advanced Thermofluid Research, vol. 1, pp. 50–69, 03 2015.
- [56] S. Mishra, P. Muthukumar, and V. Pantangi, "Porous radiant burner for domestic lpg cooking device with improved thermal efficiency and reduced emissions of co and nox," Patent Application No., vol. 73, 2013.
- [57] P. Muthukumar, P. Anand, and P. Sachdeva, "Performance analysis of porous radiant burners used in lpg cooking stove," International Journal of Energy and Environment, vol. 2, no. 2, p. 367e74, 2011.
- [58] J. Howell, M. Hall, and J. Ellzey, "Combustion of hydrocarbon fuels within porous inert media," Progress in Energy and Combustion Science, vol. 22, no. 2, pp. 121–145, 1996.
- [59] "GoGas." <https://www.gogas.com/en/process-heat/gas-ir-heaters/porous-burners>. Accessed: 1st Feb 2022.
- [60] "Innovative thermal systems." <http://innovativethermalsystems.com/products/metal-foam-burner/#tab-id-2>. Accessed: 1st Feb 2022.
- [61] "Promeos." https://promeos.com/wp-content/uploads/2020/04/pro_prom_en_web.pdf. Accessed: 1st Feb 2022.
- [62] J. Ellzey, E. Belmont, and C. Smith, "Heat recirculating reactors: Fundamental research and applications," Prog. Energ. Combust., vol. 72, pp. 32–58, 2019.
- [63] J. Hoffmann, R. Echigo, H. Yoshida, and S. Tada, "Experimental study on combustion in porous media with a reciprocating flow system," Combustion and flame, vol. 111, no. 1-2, pp. 32–46, 1997.
- [64] J. Ahn, C. Eastwood, L. Sitzki, and P. D. Ronney, "Gas-phase and catalytic combustion in heat-recirculating burners," Proceedings of the Combustion Institute, vol. 30, no. 2, pp. 2463–2472, 2005.

- [65] C.-H. Chen and P. D. Ronney, “Three-dimensional effects in counterflow heat-recirculating combustors,” Proceedings of the Combustion Institute, vol. 33, no. 2, pp. 3285–3291, 2011.
- [66] C.-H. Chen and P. D. Ronney, “Scale and geometry effects on heat-recirculating combustors,” Combustion Theory and Modelling, vol. 17, no. 5, pp. 888–905, 2013.
- [67] A. Jones, S. Lloyd, and F. J. Weinberg, “Combustion in heat exchangers,” Proceedings of the Royal Society of London. A. Mathematical and Physical Sciences, vol. 360, no. 1700, pp. 97–115, 1978.
- [68] E. L. Belmont, I. Schoegl, and J. L. Ellzey, “Experimental and analytical investigation of lean premixed methane/air combustion in a mesoscale counter-flow reactor,” Proceedings of the Combustion Institute, vol. 34, no. 2, pp. 3361–3367, 2013.
- [69] P.-F. Hsu, W. D. Evans, and J. R. Howell, “Experimental and numerical study of premixed combustion within nonhomogeneous porous ceramics,” Combustion Science and Technology, vol. 90, no. 1-4, pp. 149–172, 1993.
- [70] I. Schoegl and J. L. Ellzey, “A mesoscale fuel reformer to produce syngas in portable power systems,” Proceedings of the Combustion Institute, vol. 32, no. 2, pp. 3223–3230, 2009.
- [71] L. A. Kennedy, J. P. Bingue, A. V. Saveliev, A. Fridman, and S. I. Foutko, “Chemical structures of methane-air filtration combustion waves for fuel-lean and fuel-rich conditions,” Proceedings of the Combustion Institute, vol. 28, no. 1, pp. 1431–1438, 2000.
- [72] M. K. Drayton, A. V. Saveliev, L. A. Kennedy, A. A. Fridman, and Y.-E. D. Li, “Syngas production using superadiabatic combustion of ultra-rich methane-air mixtures,” in Symposium (International) on Combustion, vol. 27, pp. 1361–1367, Elsevier, 1998.
- [73] A. Ernst and J. D. Zibrak, “Carbon monoxide poisoning,” New England journal of medicine, vol. 339, no. 22, pp. 1603–1608, 1998.
- [74] L. Grant and T. Schneider, Air pollution by nitrogen oxides. Elsevier, 2013.
- [75] M. Kampa and E. Castanas, “Human health effects of air pollution,” Environmental pollution, vol. 151, no. 2, pp. 362–367, 2008.
- [76] A. Skowron, D. Lee, and R. De León, “The assessment of the impact of aviation nox on ozone and other radiative forcing responses – the importance of representing cruise altitudes accurately,” Atmospheric Environment, vol. 74, pp. 159–168, 2013.
- [77] M. S. Celtek and A. Pınarbaşı, “Investigations on performance and emission characteristics of an industrial low swirl burner while burning natural gas, methane, hydrogen-enriched natural gas and hydrogen as fuels,” International Journal of Hydrogen Energy, vol. 43, no. 2, pp. 1194–1207, 2018.
- [78] M. T. Smucker and J. L. ELLZEY, “Computational and experimental study of a two-section porous burner,” Combustion science and Technology, vol. 176, no. 8, pp. 1171–1189, 2004.
- [79] Y. Kotani, H. Behbahani, and T. Takeno, “An excess enthalpy flame combustor for extended flow ranges,” in Symposium (International) on Combustion, vol. 20, pp. 2025–2033, Elsevier, 1985.

-
- [80] G. J. Rørtveit, K. Zepter, Ø. Skreiberg, M. Fossum, and J. E. Hustad, “A comparison of low-nox burners for combustion of methane and hydrogen mixtures,” Proceedings of the Combustion Institute, vol. 29, no. 1, pp. 1123–1129, 2002.
- [81] A. I. Bakry and K. Rabea, “Effect of offset distance on the performance of two-region porous inert medium burners at low thermal power operation,” Applied Thermal Engineering, vol. 148, pp. 1346–1358, 2019.
- [82] S. Devi, N. Sahoo, and P. Muthukumar, “Combustion of biogas in porous radiant burner: Low emission combustion,” Energy Procedia, vol. 158, pp. 1116–1121, 2019. Innovative Solutions for Energy Transitions.
- [83] J. Toof, “A model for the prediction of thermal, prompt, and fuel nox emissions from combustion turbines,” 1986.
- [84] C. P. Fenimore, “Formation of nitric oxide in premixed hydrocarbon flames,” in Symposium (international) on combustion, vol. 13, pp. 373–380, Elsevier, 1971.
- [85] P. Glarborg, J. A. Miller, and R. J. Kee, “Kinetic modeling and sensitivity analysis of nitrogen oxide formation in well-stirred reactors,” Combustion and flame, vol. 65, no. 2, pp. 177–202, 1986.
- [86] W. M. Mathis and J. L. Ellzey, “Flame stabilization, operating range, and emissions for a methane/air porous burner,” Combustion Science and Technology, vol. 175, no. 5, pp. 825–839, 2003.
- [87] C. Keramiotis, B. Stelzner, D. Trimis, and M. Founti, “Porous burners for low emission combustion: An experimental investigation,” Energy, vol. 45, no. 1, pp. 213–219, 2012. The 24th International Conference on Efficiency, Cost, Optimization, Simulation and Environmental Impact of Energy, ECOS 2011.
- [88] G. Li, D. Stankovic, N. Overman, M. Cornwell, E. Gutmark, and L. Fuchs, “Experimental study of flameless combustion in gas turbine combustors,” in 44th AIAA Aerospace Sciences Meeting and Exhibit, p. 546, 2006.
- [89] Z. Qu, H. Gao, X. Feng, and W. Tao, “Premixed combustion in a porous burner with different fuels,” Combustion Science and Technology, vol. 187, no. 3, pp. 489–504, 2015.
- [90] H. Pedersen-Mjaanes, L. Chan, and E. Mastorakos, “Hydrogen production from rich combustion in porous media,” International journal of hydrogen energy, vol. 30, no. 6, pp. 579–592, 2005.
- [91] K. Wawrzinek, A. Kesting, J. Künzel, K. Pickenäcker, O. Pickenäcker, D. Trimis, M. Franz, and G. Härtel, “Experimental and numerical study of applicability of porous combustors for hcl synthesis,” Catalysis Today - CATAL TODAY, vol. 69, pp. 393–397, 09 2001.
- [92] F. Durst and M. Weclas, “A new type of internal combustion engine based on the porous-medium combustion technique,” Proceedings of the Institution of Mechanical Engineers, Part D: Journal of Automobile Engineering, vol. 215, no. 1, pp. 63–81, 2001.
- [93] M. Weclas, “Potential of porous-media combustion technology as applied to internal combustion engines,” Journal of Thermodynamics, vol. 2010, 2010.
- [94] C. Keramiotis, B. Stelzner, D. Trimis, and M. Founti, “Porous burners for low emission combustion: An experimental investigation,” Energy, vol. 45, no. 1, pp. 213–219, 2012.

- [95] V. Pantangi, S. C. Mishra, P. Muthukumar, and R. Reddy, "Studies on porous radiant burners for lpg (liquefied petroleum gas) cooking applications," Energy, vol. 36, no. 10, pp. 6074–6080, 2011.
- [96] P. Muthukumar and P. Shyankumar, "Development of novel porous radiant burners for lpg cooking applications," Fuel, vol. 112, pp. 562–566, 2013.
- [97] A. C. Fernandez-Pello, "Micropower generation using combustion: Issues and approaches," Proceedings of the Combustion Institute, vol. 29, no. 1, pp. 883–899, 2002. Proceedings of the Combustion Institute.
- [98] J. Li, Q. Li, J. Shi, X. Liu, and Z. Guo, "Numerical study on heat recirculation in a porous micro-combustor," Combustion and flame, vol. 171, pp. 152–161, 2016.
- [99] C. Spadaccini, X. Zhang, C. Cadou, N. Miki, and I. Waitz, "Development of a catalytic silicon micro-combustor for hydrocarbon-fueled power mems," in Technical Digest. MEMS 2002 IEEE International Conference. Fifteenth IEEE International Conference on Micro Electro Mechanical Systems (Cat. No. 02CH37266), pp. 228–231, IEEE, 2002.
- [100] K. Fu, A. J. Knobloch, F. C. Martinez, D. C. Walther, C. Fernandez-Pello, A. P. Pisano, D. Liepmann, K. Miyaska, and K. Maruta, "Design and experimental results of small-scale rotary engines," in ASME International Mechanical Engineering Congress and Exposition, vol. 35524, pp. 295–301, American Society of Mechanical Engineers, 2001.
- [101] W. Lindsay, D. Teasdale, V. Milanovic, K. Pister, and C. Fernandez-Pello, "Thrust and electrical power from solid propellant microrockets. 2. actuators," in Technical Digest. MEMS 2001. 14th IEEE International Conference on Micro Electro Mechanical Systems (Cat. No.01CH37090), pp. 606–610, 2001.
- [102] M. Kamal and A. Mohamad, "Combustion in porous media," Proceedings of the Institution of Mechanical Engineers, Part A: Journal of Power and Energy, vol. 220, no. 5, pp. 487–508, 2006.
- [103] S. Chalia, M. K. Bharti, P. Thakur, A. Thakur, and S. Sridhara, "An overview of ceramic materials and their composites in porous media burner applications," Ceramics International, vol. 47, no. 8, pp. 10426–10441, 2021.
- [104] S. A. Ghorashi, S. A. Hashemi, S. M. Hashemi, and M. Mollamahdi, "Experimental study on pollutant emissions in the novel combined porous-free flame burner," Energy, vol. 162, pp. 517–525, 2018.
- [105] J. Goela, N. Brese, L. Burns, and M. Pickering, High-Thermal-Conductivity SiC and Applications, pp. 167–198. 01 2006.
- [106] R. Brandt, L. Pawlowski, G. Neuer, and P. Fauchais, "Specific heat and thermal conductivity of plasma sprayed yttria-stabilized zirconia and nial, nicr, nicral, nicrally, nicocrally coatings," High Temperatures-High Pressures, vol. 18, pp. 65–77, 01 1986.
- [107] P. Waramit, A. Namkhat, and U. Teeboonma, "The influence of stainless steel mesh porous burner on drying kinetics of nile tilapia," Key Engineering Materials, vol. 805, pp. 116–121, 06 2019.
- [108] S. Eshkabilov, I. Ara, I. Sevostianov, F. Azarmi, and X. Tangpong, "Mechanical and thermal properties of stainless steel parts, manufactured by various technologies, in relation to their microstructure," International Journal of Engineering Science, vol. 159, p. 103398, 2021.

-
- [109] K. T. Mueller, Super-adiabatic combustion in porous media with catalytic enhancement for thermoelectric power conversion. 2011.
- [110] Q. Mistarihi, M. Umer, J. Kim, S. Hong, and H. J. Ryu, “Fabrication of zro2-based nanocomposites for tru-burning inert matrix fuel,” Nuclear Engineering and Technology, vol. 78, 05 2015.
- [111] O. Kulik, “Current state of development of new ceramic materials (review of foreign literature),” Powder metallurgy and metal ceramics, vol. 38, no. 1, pp. 93–101, 1999.
- [112] D. G. Goodwin, R. L. Speth, H. K. Moffat, and B. W. Weber, “Cantera: An object-oriented software toolkit for chemical kinetics, thermodynamics, and transport processes,” 2018. Version 2.4.0.
- [113] E. Mallard and H. Le Chatelier, “Thermal model for flame propagation,” Ann. Mines, vol. 4, no. 18, pp. 379–568, 1883.
- [114] F. A. Williams, Combustion theory. CRC Press, 2018.
- [115] T. Poinsoot and D. Veynante, Theoretical and numerical combustion. RT Edwards, Inc., 2005.
- [116] H. Berestycki, B. Larrouturou, and J. Roquejoffre, “Mathematical investigation of the cold boundary difficulty in flame propagation theory,” in Dynamical Issues in Combustion Theory, pp. 37–61, Springer, 1991.
- [117] J. D. Buckmaster and G. S. S. Ludford, “Theory of laminar flames(book),” Research supported by the U. S. Army. Cambridge and New York, Cambridge University Press, 1982. 276 p, 1982.
- [118] P. Clavin, “Dynamic behavior of premixed flame fronts in laminar and turbulent flows,” Progress in energy and combustion science, vol. 11, no. 1, pp. 1–59, 1985.
- [119] D. B. Spalding, “A theory of inflammability limits and flame-quenching,” Proceedings of the Royal Society of London. Series A. Mathematical and Physical Sciences, vol. 240, no. 1220, pp. 83–100, 1957.
- [120] J. Buckmaster, “The quenching of deflagration waves,” Combustion and Flame, vol. 26, pp. 151–162, 1976.
- [121] M. G. Zabetakis, “Flammability characteristics of combustible gases and vapors,” tech. rep., Bureau of Mines Washington DC, 1965.
- [122] P. Habisreuther, F. C. C. Galeazzo, C. Prathap, and N. Zarzalis, “Structure of laminar premixed flames of methane near the auto-ignition limit,” Combustion and Flame, vol. 160, no. 12, pp. 2770–2782, 2013.
- [123] L. Roques, “Study of the premixed flame model with heat losses the existence of two solutions,” European Journal of Applied Mathematics, vol. 16, no. 6, pp. 741–765, 2005.
- [124] A. Bonnet, “Non-uniqueness for flame propagation when the lewis number is less than 1,” European Journal of Applied Mathematics, vol. 6, no. 4, pp. 287–306, 1995.
- [125] M. Mendes, J. Pereira, and J. Pereira, “A numerical study of the stability of one-dimensional laminar premixed flames in inert porous media,” Combustion and Flame, vol. 153, no. 4, pp. 525–539, 2008.

- [126] D. Lee and K. Maruta, "Heat recirculation effects on flame propagation and flame structure in a mesoscale tube," Combustion Theory and Modelling, vol. 16, no. 3, pp. 507–536, 2012.
- [127] Y. Ju and B. Xu, "Theoretical and experimental studies on mesoscale flame propagation and extinction," Proceedings of the Combustion Institute, vol. 30, no. 2, pp. 2445–2453, 2005.
- [128] J. L.-P. Chen and S. W. Churchill, "Stabilization of flames in refractory tubes," Combustion and Flame, vol. 18, no. 1, pp. 37–42, 1972.
- [129] J. L.-P. Chen and S. W. Churchill, "A theoretical model for stable combustion inside a refractory tube," Combustion and Flame, vol. 18, no. 1, pp. 27–36, 1972.
- [130] D. K. Min and H. D. Shin, "Laminar premixed flame stabilized inside a honeycomb ceramic," International journal of heat and mass transfer, vol. 34, no. 2, pp. 341–356, 1991.
- [131] G.-P. Gauthier, Combustion in heat-recirculating burners for efficient and clean power production. McGill University (Canada), 2016.
- [132] K. Hanamura and R. Echigo, "An analysis of flame stabilization mechanism in radiation burners," Wärme-und Stoffübertragung, vol. 26, no. 6, pp. 377–383, 1991.
- [133] B. J. VOGEL and J. L. ELLZEY, "Subadiabatic and superadiabatic performance of a two-section porous burner," Combustion science and technology, vol. 177, no. 7, pp. 1323–1338, 2005.
- [134] T. Takeno and K. Sato, "An excess enthalpy flame theory," Combust. Sci. Technol., vol. 20, no. 1-2, pp. 73–84, 1979.
- [135] T. Takeno, K. Sato, and K. Hase, "A theoretical study on an excess enthalpy flame," in Symposium (International) on Combustion, vol. 18, pp. 465–472, Elsevier, 1981.
- [136] C. Bedoya, I. Dinkov, P. Habisreuther, N. Zarzalis, H. Bockhorn, and P. Parthasarathy, "Experimental study, 1d volume-averaged calculations and 3d direct pore level simulations of the flame stabilization in porous inert media at elevated pressure," Combustion and Flame, vol. 162, no. 10, pp. 3740–3754, 2015.
- [137] I. Yakovlev and S. Zambalov, "Three-dimensional pore-scale numerical simulation of methane-air combustion in inert porous media under the conditions of upstream and downstream combustion wave propagation through the media," Combust. Flame, vol. 209, pp. 74–98, 2019.
- [138] J. Buckmaster and T. Takeno, "Blow-off and flashback of an excess enthalpy flame," Combustion Science and Technology, 1981.
- [139] C.-J. TSENG and J. R. Howell, "Combustion of liquid fuels in a porous radiant burner," Combustion Science and Technology, vol. 112, no. 1, pp. 141–161, 1996.
- [140] A. Bakry, A. Al-Salaymeh, H. Ala'a, A. Abu-Jrai, and D. Trimis, "Adiabatic premixed combustion in a gaseous fuel porous inert media under high pressure and temperature: Novel flame stabilization technique," Fuel, vol. 90, no. 2, pp. 647–658, 2011.
- [141] V. Babkin, A. Korzhavin, and V. Bunev, "Propagation of premixed gaseous explosion flames in porous media," Combustion and Flame, vol. 87, no. 2, pp. 182–190, 1991.

-
- [142] S. Nemoda, D. Trimis, and G. Živković, “Numerical simulation of porous burners and hole plate surface burners,” Thermal Science, vol. 8, no. 1, pp. 3–18, 2004.
- [143] T. Marbach and A. Agrawal, “Experimental study of surface and interior combustion using composite porous inert media,” J. Eng. Gas Turbines Power, vol. 127, no. 2, pp. 307–313, 2005.
- [144] J. Li, Y. Wang, J. Shi, and X. Liu, “Dynamic behaviors of premixed hydrogen–air flames in a planar micro-combustor filled with porous medium,” Fuel, vol. 145, pp. 70–78, 2015.
- [145] B. Lin, H. Dai, C. Wang, Q. Li, K. Wang, and Y. Zheng, “Combustion characteristics of low concentration coal mine methane in divergent porous media burner,” International Journal of Mining Science and Technology, vol. 24, no. 5, pp. 671–676, 2014.
- [146] A. Loukou, M. Mendes, I. Frenzel, J. Pereira, S. Ray, J. Pereira, and D. Trimis, “Experimental and numerical investigation of methane thermal partial oxidation in a small-scale porous media reformer,” International Journal of Hydrogen Energy, vol. 42, no. 1, pp. 652–663, 2017.
- [147] Z. Al-Hamamre, S. Voß, and D. Trimis, “Hydrogen production by thermal partial oxidation of hydrocarbon fuels in porous media based reformer,” International Journal of Hydrogen Energy, vol. 34, no. 2, pp. 827–832, 2009.
- [148] S. Voss, M. Mendes, J. Pereira, and D. Trimis, “Comparison of experimental and numerical results of ultra-lean h₂/co combustion within inert porous media,” in 4th European Combustion Meeting, Vienna, Austria, Citeseer, 2009.
- [149] P. Qian, M. Liu, X. Li, F. Xie, Z. Huang, C. Luo, and X. Zhu, “Combustion characteristics and radiation performance of premixed hydrogen/air combustion in a mesoscale divergent porous media combustor,” International Journal of Hydrogen Energy, vol. 45, no. 7, pp. 5002–5013, 2020.
- [150] H. Dai, H. Zhu, H. Dai, Z. Song, Z. Wang, S. He, and X. Wang, “Syngas production by methane-rich combustion in a divergent burner of porous media,” International Journal of Hydrogen Energy, vol. 46, no. 45, pp. 23279–23291, 2021.
- [151] M. Farzaneh, R. Ebrahimi, M. Shams, and M. Shafiey, “Two-dimensional numerical simulation of combustion and heat transfer in porous burners,” Engineering letters, vol. 15, no. 2, 2007.
- [152] S. M. Hashemi and S. A. Hashemi, “Numerical investigation of the flame stabilization in a divergent porous media burner,” Proceedings of the Institution of Mechanical Engineers, Part A: Journal of Power and Energy, vol. 231, no. 3, pp. 173–181, 2017.
- [153] S. Sobhani, D. Mohaddes, E. Boigne, P. Muhunthan, and M. Ihme, “Modulation of heat transfer for extended flame stabilization in porous media burners via topology gradation,” Proceedings of the Combustion Institute, vol. 37, no. 4, pp. 5697–5704, 2019.
- [154] S. Sobhani, P. Muhunthan, E. Boigné, D. Mohaddes, and M. Ihme, “Experimental feasibility of tailored porous media burners enabled via additive manufacturing,” Proceedings of the Combustion Institute, vol. 38, no. 4, pp. 6713–6722, 2021.
- [155] W. Payman and R. V. Wheeler, “Lvi.—the propagation of flame through tubes of small diameter,” Journal of the Chemical Society, Transactions, vol. 113, pp. 656–666, 1918.

- [156] S. Aly and C. Hermance, "A two-dimensional theory of laminar flame quenching," Combustion and Flame, vol. 40, pp. 173–185, 1981.
- [157] S. Voss, M. Mendes, J. Pereira, S. Ray, J. Pereira, and D. Trimis, "Investigation on the thermal flame thickness for lean premixed combustion of low calorific h₂/co mixtures within porous inert media," Proceedings of the Combustion Institute, vol. 34, no. 2, pp. 3335–3342, 2013.
- [158] J. Dunnmon, S. Sobhani, M. Wu, R. Fahrig, and M. Ihme, "An investigation of internal flame structure in porous media combustion via X-ray Computed Tomography," Proc. Combust. Inst., vol. 36, no. 3, pp. 4399–4408, 2017.
- [159] A. J. Barra and J. L. Ellzey, "Heat recirculation and heat transfer in porous burners," Combust. Flame, vol. 137, no. 1-2, pp. 230–241, 2004.
- [160] M. Quintard and S. Whitaker, "Transport in ordered and disordered porous media ii: Generalized volume averaging," Transport in porous media, vol. 14, no. 2, pp. 179–206, 1994.
- [161] M. Kaviany, Principles of heat transfer in porous media. Springer Science & Business Media, 2012.
- [162] R. G. Carbonell and S. Whitaker, "Heat and mass transfer in porous media," in Fundamentals of transport phenomena in porous media, pp. 121–198, Springer, 1984.
- [163] W. Zhong, K. Xu, X. Li, Y. Liao, G. Tao, and T. Kagawa, "Determination of pressure drop for air flow through sintered metal porous media using a modified ergun equation," Advanced Powder Technology, vol. 27, no. 4, pp. 1134–1140, 2016.
- [164] J. Bear, Dynamics of fluids in porous media. Courier Corporation, 1988.
- [165] S. Ergun, "Fluid flow through packed columns," Chem. Eng. Prog., vol. 48, pp. 89–94, 1952.
- [166] H. Darcy, Les fontaines publiques de la ville de Dijon: exposition et application... Victor Dalmont, 1856.
- [167] M. Al-Doury, "A discussion about hydraulic permeability and permeability," Petroleum science and technology, vol. 28, no. 17, pp. 1740–1749, 2010.
- [168] P. C. Carman, "Fluid flow through granular beds," Trans. Inst. Chem. Eng., vol. 15, pp. 150–166, 1937.
- [169] J. Kozeny, "Über kapillare leitung der wasser in boden," Royal Academy of Science, Vienna, Proc. Class I, vol. 136, pp. 271–306, 1927.
- [170] S. Whitaker, "Advances in theory of fluid motion in porous media," Industrial & engineering chemistry, vol. 61, no. 12, pp. 14–28, 1969.
- [171] Z. Zeng and R. Grigg, "A criterion for non-darcy flow in porous media," Transport in porous media, vol. 63, no. 1, pp. 57–69, 2006.
- [172] P. Kundu, V. Kumar, and I. M. Mishra, "Experimental and numerical investigation of fluid flow hydrodynamics in porous media: Characterization of pre-darcy, darcy and non-darcy flow regimes," Powder Technology, vol. 303, pp. 278–291, 2016.

-
- [173] P. Forchheimer, “Wasserbewegung durch boden,” Z. Ver. Deutsch, Ing., vol. 45, pp. 1782–1788, 1901.
- [174] S. Sobhani, B. Haley, D. Bartz, J. Dunnmon, J. Sullivan, and M. Ihme, “Investigation of lean combustion stability, pressure drop, and material durability in porous media burners,” in Turbo Expo: Power for Land, Sea, and Air, vol. 50893, p. V05CT17A001, American Society of Mechanical Engineers, 2017.
- [175] M.-Z. Xie, J.-R. Shi, Y.-B. Deng, H. Liu, L. Zhou, and Y.-N. Xu, “Experimental and numerical investigation on performance of a porous medium burner with reciprocating flow,” Fuel, vol. 88, no. 1, pp. 206–213, 2009.
- [176] O. Reynolds, “Xxix. an experimental investigation of the circumstances which determine whether the motion of water shall be direct or sinuous, and of the law of resistance in parallel channels,” Philosophical Transactions of the Royal society of London, no. 174, pp. 935–982, 1883.
- [177] M. Sano and K. Tamai, “A universal transition to turbulence in channel flow,” Nature Physics, vol. 12, no. 3, pp. 249–253, 2016.
- [178] Y. Zhou, “Turbulence theories and statistical closure approaches,” Physics Reports, vol. 935, pp. 1–117, 2021.
- [179] A. Dybbs and R. Edwards, “A new look at porous media fluid mechanics—darcy to turbulent,” Fundamentals of transport phenomena in porous media, pp. 199–256, 1984.
- [180] B. D. Wood, X. He, and S. V. Apte, “Modeling turbulent flows in porous media,” Annual Review of Fluid Mechanics, vol. 52, pp. 171–203, 2020.
- [181] J. Lage, M. De Lemos, and D. Nield, “Modeling turbulence in porous media,” in Transport phenomena in porous media II, pp. 198–230, Elsevier, 2002.
- [182] B. Antohe and J. Lage, “A general two-equation macroscopic turbulence model for incompressible flow in porous media,” International Journal of Heat and Mass Transfer, vol. 40, no. 13, pp. 3013–3024, 1997.
- [183] D. Getachew, W. Minkowycz, and J. Lage, “A modified form of the κ - ε model for turbulent flows of an incompressible fluid in porous media,” International Journal of Heat and Mass Transfer, vol. 43, no. 16, pp. 2909–2915, 2000.
- [184] A. Nakayama and F. Kuwahara, “A macroscopic turbulence model for flow in a porous medium,” 1999.
- [185] T. Masuoka and Y. Takatsu, “Turbulence model for flow through porous media,” International Journal of Heat and Mass Transfer, vol. 39, no. 13, pp. 2803–2809, 1996.
- [186] M. J. de Lemos, “Modeling turbulence in permeable media: The double-decomposition concept revisited,” Physics, vol. 4, no. 1, pp. 124–131, 2022.
- [187] M. J. de Lemos, “Numerical simulation of turbulent combustion in porous materials,” International Communications in Heat and Mass Transfer, vol. 36, no. 10, pp. 996–1001, 2009.
- [188] M. J. de Lemos, “Analysis of turbulent combustion in inert porous media,” International communications in heat and mass transfer, vol. 37, no. 4, pp. 331–336, 2010.

- [189] I.-G. Lim and R. D. Matthews, "Development of a model for turbulent combustion within porous inert media," International Journal of Fluid Mechanics Research, vol. 25, no. 1-3, 1998.
- [190] M. F. Uth, Y. Jin, A. V. Kuznetsov, and H. Herwig, "Turbulence in porous media: Some fundamental questions addressed by dns solutions," 2014.
- [191] A. Mohamad, S. Ramadhyani, and R. Viskanta, "Modelling of combustion and heat transfer in a packed bed with embedded coolant tubes," Int. J. Heat. Mass Tran., vol. 37, no. 8, pp. 1181–1191, 1994.
- [192] G. Brenner, K. Pickenäcker, O. Pickenäcker, D. Trimis, K. Wawrzinek, and T. Weber, "Numerical and experimental investigation of matrix-stabilized methane/air combustion in porous inert media," Combustion and flame, vol. 123, no. 1-2, pp. 201–213, 2000.
- [193] K. Chua, W. Yang, and W. Ong, "Fundamental experiment and numerical analysis of a modular microcombustor with silicon carbide porous medium," Ind. Eng. Chem. Res., vol. 51, no. 18, pp. 6327–6339, 2012.
- [194] M. Sahraoui and M. Kaviany, "Direct simulation vs volume-averaged treatment of adiabatic, premixed flame in a porous medium," International Journal of Heat and Mass Transfer, vol. 37, no. 18, pp. 2817 – 2834, 1994.
- [195] M. Quintard and S. Whitaker, "One-and two-equation models for transient diffusion processes in two-phase systems," in Advances in heat transfer, vol. 23, pp. 369–464, Elsevier, 1993.
- [196] F. Kuwahara, M. Shirota, and A. Nakayama, "A numerical study of interfacial convective heat transfer coefficient in two-energy equation model for convection in porous media," International journal of heat and mass transfer, vol. 44, no. 6, pp. 1153–1159, 2001.
- [197] N. Wakao and S. Kaguei, "Heat and mass transfer in packed beds, garden and breach sci," Publishers, New York, pp. 243–295, 1982.
- [198] M. B. Saito and M. J. de Lemos, "Interfacial heat transfer coefficient for non-equilibrium convective transport in porous media," International Communications in Heat and Mass Transfer, vol. 32, no. 5, pp. 666–676, 2005.
- [199] M. B. Saito and M. J. De Lemos, "A correlation for interfacial heat transfer coefficient for turbulent flow over an array of square rods," 2006.
- [200] A. Zukauskas, "Heat transfer from tubes in crossflow," in Advances in heat transfer, vol. 8, pp. 93–160, Elsevier, 1972.
- [201] B. Ghanbarian, A. G. Hunt, R. P. Ewing, and M. Sahimi, "Tortuosity in porous media: a critical review," Soil science society of America journal, vol. 77, no. 5, pp. 1461–1477, 2013.
- [202] L. Pisani, "Simple expression for the tortuosity of porous media," Transport in Porous Media, vol. 88, no. 2, pp. 193–203, 2011.
- [203] P. B. Lorenz, "Tortuosity in porous media," Nature, vol. 189, no. 4762, pp. 386–387, 1961.
- [204] A. Duda, Z. Koza, and M. Matyka, "Hydraulic tortuosity in arbitrary porous media flow," Phys. Rev. E, vol. 84, p. 036319, Sep 2011.

-
- [205] M. Matyka and Z. Koza, “How to calculate tortuosity easily?,” in AIP Conference Proceedings 4, vol. 1453, pp. 17–22, American Institute of Physics, 2012.
- [206] G. I. Taylor, “Dispersion of soluble matter in solvent flowing slowly through a tube,” Proceedings of the Royal Society of London. Series A. Mathematical and Physical Sciences, vol. 219, no. 1137, pp. 186–203, 1953.
- [207] R. Aris, “On the dispersion of a solute in a fluid flowing through a tube,” Proceedings of the Royal Society of London. Series A. Mathematical and Physical Sciences, vol. 235, no. 1200, pp. 67–77, 1956.
- [208] J. Delgado, “Longitudinal and transverse dispersion in porous media,” Chemical Engineering Research and Design, vol. 85, no. 9, pp. 1245–1252, 2007.
- [209] J.-R. de Dreuzy, A. Beaudoin, and J. Erhel, “Asymptotic dispersion in 2d heterogeneous porous media determined by parallel numerical simulations,” Water Resources Research, vol. 43, no. 10, 2007.
- [210] H. D. Lugo-Mendez, F. J. Valdes-Parada, and J. A. Ochoa-Tapia, “An analytical expression for the dispersion coefficient in porous media using chang’s unit cell,” Journal of Porous media, vol. 16, no. 1, 2013.
- [211] M. Dentz, M. Icardi, and J. J. Hidalgo, “Mechanisms of dispersion in a porous medium,” Journal of Fluid Mechanics, vol. 841, pp. 851–882, 2018.
- [212] R. Borghi, “Turbulent combustion modelling,” Progress in energy and combustion science, vol. 14, no. 4, pp. 245–292, 1988.
- [213] H. F. Hemond and E. J. Fechner, Chemical fate and transport in the environment. Elsevier, 2014.
- [214] P.-A. Masset, O. Dounia, and L. Selle, “Fully explicit formulae for flame speed in infinite and finite porous media,” Combust. Theor. Model., pp. 1–28, 2021.
- [215] W. Fuqiang, Z. Xinping, D. Yan, Y. Hongliang, X. Shi, L. Yang, and C. Ziming, “Progress in radiative transfer in porous medium: a review from macro scale to pore scale with experimental test,” Applied Thermal Engineering, p. 118331, 2022.
- [216] I. Malico and J. C. F. Pereira, “Numerical study on the influence of radiative properties in porous media combustion,” J. Heat Transfer, vol. 123, no. 5, pp. 951–957, 2001.
- [217] S. B. Sathe, R. E. PECK, and T. W. Tong, “Flame stabilization and multimode heat transfer in inert porous media: a numerical study,” Combustion Science and technology, vol. 70, no. 4-6, pp. 93–109, 1990.
- [218] S. Sathe, R. Peck, and T. Tong, “A numerical analysis of heat transfer and combustion in porous radiant burners,” International Journal of Heat and Mass Transfer, vol. 33, no. 6, pp. 1331–1338, 1990.
- [219] C. T. at CERFACS, “Avbp solver.”
- [220] N. Djordjevic, P. Habisreuther, and N. Zarzalis, “Numerical simulation of the combustion in porous media: relative importance of the different transport mechanisms for the flame stabilization,” in Proc. 6th Mediterranean Combustion Symposium, 2009.

- [221] A. J. Barra, G. Diepvens, J. L. Ellzey, and M. R. Henneke, "Numerical study of the effects of material properties on flame stabilization in a porous burner," Combust. Flame, vol. 134, no. 4, pp. 369–379, 2003.
- [222] F. Valdés-Parada, C. Aguilar-Madera, and J. Alvarez-Ramirez, "On diffusion, dispersion and reaction in porous media," Chemical Engineering Science, vol. 66, no. 10, pp. 2177–2190, 2011.
- [223] S. Whitaker, "A simple geometrical derivation of the spatial averaging theorem," Chemical engineering education, vol. 19, no. 1, pp. 18–52, 1985.
- [224] T. B. Anderson and R. Jackson, "Fluid mechanical description of fluidized beds. equations of motion," Industrial & Engineering Chemistry Fundamentals, vol. 6, no. 4, pp. 527–539, 1967.
- [225] W. G. Gray and P. Lee, "On the theorems for local volume averaging of multiphase systems," International Journal of Multiphase Flow, vol. 3, no. 4, pp. 333–340, 1977.
- [226] M. A. Mujeebu, M. Z. Abdullah, A. Mohamad, and M. A. Bakar, "Trends in modeling of porous media combustion," Progress in Energy and Combustion science, vol. 36, no. 6, pp. 627–650, 2010.
- [227] N. S. Kaisare and D. G. Vlachos, "A review on microcombustion: Fundamentals, devices and applications," Progress in Energy and Combustion Science, vol. 38, no. 3, pp. 321–359, 2012.
- [228] J. Kiefer, M. Weikl, T. Seeger, F. Von Issendorff, F. Beyrau, and A. Leipertz, "Non-intrusive gas-phase temperature measurements inside a porous burner using dual-pump CARS," Proc. Combust. Inst., vol. 32, no. 2, pp. 3123–3129, 2009.
- [229] Y. Yoshizawa, K. Sasaki, and R. Echigo, "Analytical study of the structure of radiation controlled flame," International Journal of Heat and Mass Transfer, vol. 31, no. 2, pp. 311–319, 1988.
- [230] P.-F. Hsu and R. D. Matthews, "The necessity of using detailed kinetics in models for premixed combustion within porous media," Combustion and flame, vol. 93, no. 4, pp. 457–466, 1993.
- [231] N. Djordjevic, P. Habisreuther, and N. Zarzalis, "A numerical investigation of the flame stability in porous burners employing various ceramic sponge-like structures," Chemical engineering science, vol. 66, no. 4, pp. 682–688, 2011.
- [232] S. Panigrahy, Investigation on combustion in porous inert burners using gaseous and liquid fuels. PhD thesis, Indian Institute of Technology Guwahati, 2018.
- [233] Z. Jia, Q. Ye, H. Wang, H. Li, and S. Shi, "Numerical simulation of a new porous medium burner with two sections and double decks," Processes, vol. 6, no. 10, p. 185, 2018.
- [234] I. Schoegl, "Radiation effects on flame stabilization on flat flame burners," Combustion and flame, vol. 159, no. 9, pp. 2817–2828, 2012.
- [235] I. Dinkov, P. Habisreuther, and H. Bockhorn, "Numerical prediction of burning velocity and flame thickness in a radial-flow porous burner," in Proceedings of the European Combustion Meeting, pp. P5–78, 2013.

-
- [236] B. Deshaies and G. Joulin, "Asymptotic study of an excess-enthalpy flame," Combustion Science and Technology, vol. 22, no. 5-6, pp. 281–285, 1980.
- [237] F. Escobedo and H. J. Viljoen, "Modeling of porous radiant burners with large extinction coefficients," The Canadian Journal of Chemical Engineering, vol. 72, no. 5, pp. 805–814, 1994.
- [238] L. Boshoff-Mostert and H. J. Viljoen, "Analysis of homogeneous combustion in monolithic structures," Chemical engineering science, vol. 51, no. 7, pp. 1107–1111, 1996.
- [239] F. M. Pereira, A. A. Oliveira, and F. F. Fachini, "Asymptotic analysis of stationary adiabatic premixed flames in porous inert media," Combustion and Flame, vol. 156, no. 1, pp. 152 – 165, 2009.
- [240] F. M. Pereira, A. A. M. Oliveira, and F. F. Fachini, "Theoretical analysis of ultra-lean premixed flames in porous inert media," Journal of Fluid Mechanics, vol. 657, p. 285–307, 2010.
- [241] F. M. Pereira, A. A. Oliveira, and F. F. Fachini, "Maximum superadiabatic temperature for stabilized flames within porous inert media," Combustion and flame, vol. 158, no. 11, pp. 2283–2288, 2011.
- [242] X. Fu, R. Viskanta, and J. Gore, "Combustion and heat transfer interaction in a pore-scale refractory tube burner," Journal of thermophysics and heat transfer, vol. 12, no. 2, pp. 164–171, 1998.
- [243] R. Fursenko, S. Minaev, and V. Babkin, "Thermal interaction of two flame fronts propagating in channels with opposing gas flows," Combustion, Explosion and Shock Waves, vol. 37, no. 5, pp. 493–500, 2001.
- [244] P. D. Ronney, "Analysis of non-adiabatic heat-recirculating combustors," Combustion and Flame, vol. 135, no. 4, pp. 421–439, 2003.
- [245] Y. Ju and C. Choi, "An analysis of sub-limit flame dynamics using opposite propagating flames in mesoscale channels," Combustion and Flame, vol. 133, no. 4, pp. 483–493, 2003.
- [246] I. Schoegl and J. L. Ellzey, "Superadiabatic combustion in conducting tubes and heat exchangers of finite length," Combustion and flame, vol. 151, no. 1-2, pp. 142–159, 2007.
- [247] A. Aldushin and S. Kasparyan, "Stability of stationary filtrational combustion waves," Combustion, Explosion and Shock Waves, vol. 17, no. 6, pp. 615–625, 1981.
- [248] V. S. Babkin, "Filtrational combustion of gases. present state of affairs and prospects," Pure and Applied Chemistry, vol. 65, no. 2, pp. 335 – 344, 1993.
- [249] S. Zhdanok, L. A. Kennedy, and G. Koester, "Superadiabatic combustion of methane air mixtures under filtration in a packed bed," Combustion and Flame, vol. 100, no. 1-2, pp. 221–231, 1995.
- [250] V. Zamashchikov, "An investigation of gas combustion in a narrow tube," Combustion science and technology, vol. 166, no. 1, pp. 1–14, 2001.
- [251] V. Bubnovich, S. Zhdanok, and K. Dobrego, "Analytical study of the combustion waves propagation under filtration of methane–air mixture in a packed bed," International Journal of Heat and Mass Transfer, vol. 49, no. 15-16, pp. 2578–2586, 2006.

- [252] A. Mohamad, “11 - combustion in porous media : fundamentals and applications,” in Transport Phenomena in Porous Media III (D. Ingham and I. Pop, eds.), pp. 287 – 304, Oxford: Pergamon, 2005.
- [253] C. K. LAW, “Propagation, structure, and limit phenomena of laminar flames at elevated pressures,” Combustion Science and Technology, vol. 178, no. 1-3, pp. 335–360, 2006.
- [254] R. M. Corless, G. H. Gonnet, D. E. Hare, D. J. Jeffrey, and D. E. Knuth, “On the lambertw function,” Advances in Computational mathematics, vol. 5, no. 1, pp. 329–359, 1996.
- [255] A. Wang and J. Zhao, “Review of prediction for thermal contact resistance,” Science China Technological Sciences, vol. 53, no. 7, pp. 1798–1808, 2010.
- [256] H. Gao, X. Feng, and Z. Qu, “Combustion in a hybrid porous burner packed with alumina pellets and silicon carbide foams with a gap,” Journal of Energy Engineering, vol. 143, no. 5, p. 04017032, 2017.
- [257] R. V. Fursenko, I. A. Yakovlev, E. S. Odintsov, S. D. Zambalov, and S. S. Minaev, “Pore-scale flame dynamics in a one-layer porous burner,” Combust. Flame, p. 111711, 2021.
- [258] T. Leach, C. Cadou, and G. Jackson, “Effect of structural conduction and heat loss on combustion in micro-channels,” Combust. Theor. Model., vol. 10, no. 1, pp. 85–103, 2006.
- [259] I. Yakovlev, A. Maznoy, and S. Zambalov, “Pore-scale study of complex flame stabilization phenomena in thin-layered radial porous burner,” Combust. Flame, vol. 231, p. 111468, 2021.
- [260] N. Djordjevic, P. Habisreuther, and N. Zarzalis, Experimental study on the influence of the pore size of SiSiC sponge on the flame stabilization in a porous burner. 4th European Combust. Meeting, 2009.
- [261] I. Malico, X. Zhou, and J. Pereira, “Two-dimensional numerical study of combustion and pollutants formation in porous burners,” Combust. Sci. Technol., vol. 152, no. 1, pp. 57–79, 2000.
- [262] X. Zhou and J. Pereira, “Comparison of four combustion models for simulating the pre-mixed combustion in inert porous media,” Fire Mater., vol. 22, no. 5, pp. 187–197, 1998.
- [263] J. Li, Q. Li, Y. Wang, Z. Guo, and X. Liu, “Fundamental flame characteristics of premixed h₂-air combustion in a planar porous micro-combustor,” Chem. Eng. J., vol. 283, pp. 1187 – 1196, 2016.
- [264] J. Jones, “A possible analog of the lewis number for gases in a porous medium,” J. Fire Sci., vol. 26, no. 3, pp. 213–215, 2008.
- [265] V. Shirsat and A. Gupta, “A review of progress in heat recirculating meso-scale combustors,” Appl. Energ., vol. 88, no. 12, pp. 4294–4309, 2011.
- [266] P. Parthasarathy, P. Habisreuther, and N. Zarzalis, “Evaluation of longitudinal dispersion coefficient in open-cell foams using transient direct pore level simulation,” Chem. Eng. Sci., vol. 90, pp. 242–249, 2013.
- [267] C. Bedoya, Stationary Flames within Porous Inert Media. PhD thesis, Karlsruher Institut für Technologie (KIT), 2016.

-
- [268] M. Sahraoui and M. Kaviany, "Slip and no-slip temperature boundary conditions at interface of porous, plain media: conduction," *Int. J. Heat. Mass Tran.*, vol. 36, no. 4, pp. 1019–1033, 1993.
- [269] M. Haq, *Fundamental studies of premixed combustion*. PhD thesis, University of Leeds, 1998.
- [270] F. Liu and Ö. Gülder, "Effects of pressure and preheat on super-adiabatic flame temperatures in rich premixed methane/air flames," *Combust. Sci. Technol.*, vol. 180, no. 3, pp. 437–452, 2008.
- [271] Y. Zha, J. Yang, J. Zeng, C.-H. M. Tso, W. Zeng, and L. Shi, "Review of numerical solution of richardson-richards equation for variably saturated flow in soils," *Wiley Interdisciplinary Reviews: Water*, vol. 6, no. 5, p. e1364, 2019.
- [272] C. W. Downer and F. L. Ogden, "Appropriate vertical discretization of richards' equation for two-dimensional watershed-scale modelling," *Hydrological Processes*, vol. 18, no. 1, pp. 1–22, 2004.
- [273] D. Or, P. Lehmann, and S. Assouline, "Natural length scales define the range of applicability of the richards equation for capillary flows," *Water Resources Research*, vol. 51, no. 9, pp. 7130–7144, 2015.
- [274] P.-L. Billerot, L. Dufresne, R. Lemaire, and P. Seers, "3D CFD analysis of a diamond lattice-based porous burner," *Energy*, vol. 207, p. 118160, 2020.
- [275] Y. Liu, Y. Deng, J. Shi, R. Xiao, and H. Li, "Pore-level numerical simulation of methane-air combustion in a simplified two-layer porous burner," *Chinese Journal of Chemical Engineering*, vol. 34, pp. 87–96, 2021.
- [276] A. G. Dixon, "Local transport and reaction rates in a fixed bed reactor tube: Endothermic steam methane reforming," *Chemical Engineering Science*, vol. 168, pp. 156–177, 2017.
- [277] "Combustion and heat transfer in model two-dimensional porous burners," *Combust. Flame*, vol. 116, no. 1, pp. 177–191, 1999.
- [278] K. Yamamoto, N. Takada, and M. Misawa, "Combustion simulation with lattice boltzmann method in a three-dimensional porous structure," *Proceedings of the Combustion Institute*, vol. 30, no. 1, pp. 1509–1515, 2005.
- [279] N. Jouybari, M. Maerefat, and M. Nimvari, "A pore scale study on turbulent combustion in porous media," *Heat and Mass Transfer*, vol. 52, no. 2, pp. 269–280, 2016.
- [280] J. Shi, J. Lv, F. Behrendt, Y. Liu, M. Mao, and F. He, "3D pore-scale simulations and 1D volume-averaged calculations of the flow and thermal non-equilibrium for low-velocity filtration combustion," *Int. J. Heat Mass Tran.*, vol. 177, p. 121532, 2021.
- [281] F. Sirotkin, R. Fursenko, S. Kumar, and S. Minaev, "Flame anchoring regime of filtrational gas combustion: Theory and experiment," *Proc. Combust. Inst.*, vol. 36, no. 3, pp. 4383–4389, 2017.
- [282] J. C. Ferguson, S. Sobhani, and M. Ihme, "Pore-resolved simulations of porous media combustion with conjugate heat transfer," *Proc. Combust. Inst.*, vol. 38, no. 2, pp. 2127–2134, 2021.

- [283] P. Virtanen, R. Gommers, T. E. Oliphant, M. Haberland, T. Reddy, D. Cournapeau, E. Burovski, P. Peterson, W. Weckesser, J. Bright, S. J. van der Walt, M. Brett, J. Wilson, K. J. Millman, N. Mayorov, A. R. J. Nelson, E. Jones, R. Kern, E. Larson, C. J. Carey, Í. Polat, Y. Feng, E. W. Moore, J. VanderPlas, D. Laxalde, J. Perktold, R. Cimrman, I. Henriksen, E. A. Quintero, C. R. Harris, A. M. Archibald, A. H. Ribeiro, F. Pedregosa, P. van Mulbregt, and SciPy 1.0 Contributors, “SciPy 1.0: Fundamental Algorithms for Scientific Computing in Python,” *Nature Methods*, vol. 17, pp. 261–272, 2020.
- [284] S. Van der Walt, J. L. Schönberger, J. Nunez-Iglesias, F. Boulogne, J. D. Warner, N. Yager, E. Gouillart, and T. Yu, “scikit-image: image processing in python,” *PeerJ*, vol. 2, p. e453, 2014.
- [285] D. T. Chen, “dicom2stl.”
- [286] C. Dobrzynski, *MMG3D: User guide*. PhD thesis, INRIA, 2012.
- [287] C. Dapogny, C. Dobrzynski, and P. Frey, “Three-dimensional adaptive domain remeshing, implicit domain meshing, and applications to free and moving boundary problems,” *Journal of Computational Physics*, vol. 262, pp. 358–378, 2014.
- [288] C. Geuzaine and J.-F. Remacle, “Gmsh: A 3-d finite element mesh generator with built-in pre-and post-processing facilities,” *International journal for numerical methods in engineering*, vol. 79, no. 11, pp. 1309–1331, 2009.
- [289] H. Karcher and K. Polthier, “Construction of triply periodic minimal surfaces,” *Philosophical Transactions of the Royal Society of London. Series A: Mathematical, Physical and Engineering Sciences*, vol. 354, no. 1715, pp. 2077–2104, 1996.
- [290] I. Maskery, L. Sturm, A. O. Aremu, A. Panesar, C. B. Williams, C. J. Tuck, R. D. Wildman, I. A. Ashcroft, and R. J. Hague, “Insights into the mechanical properties of several triply periodic minimal surface lattice structures made by polymer additive manufacturing,” *Polymer*, vol. 152, pp. 62–71, 2018.
- [291] A. L. Mackay, “Periodic minimal surfaces,” *Physica B+ C*, vol. 131, no. 1-3, pp. 300–305, 1985.
- [292] F. P. Melchels, K. Bertoldi, R. Gabbriellini, A. H. Velders, J. Feijen, and D. W. Grijpma, “Mathematically defined tissue engineering scaffold architectures prepared by stereolithography,” *Biomaterials*, vol. 31, no. 27, pp. 6909–6916, 2010.
- [293] E. J. Crossland, M. Kamperman, M. Nedelcu, C. Ducati, U. Wiesner, D.-M. Smilgies, G. E. Toombes, M. A. Hillmyer, S. Ludwigs, U. Steiner, *et al.*, “A bicontinuous double gyroid hybrid solar cell,” *Nano letters*, vol. 9, no. 8, pp. 2807–2812, 2009.
- [294] M. Sahraoui and M. Kaviany, “Direct simulation vs volume-averaged treatment of adiabatic, premixed flame in a porous medium,” *Int. J. Heat Mass Tran.*, vol. 37, no. 18, pp. 2817–2834, 1994.
- [295] M. Weikl, S. Tedder, T. Seeger, and A. Leipertz, “Investigation of porous media combustion by coherent anti-stokes raman spectroscopy,” *Experiments in fluids*, vol. 49, no. 4, pp. 775–781, 2010.
- [296] B. Stelzner, C. Keramiotis, S. Voss, M. Founti, and D. Trimis, “Analysis of the flame structure for lean methane–air combustion in porous inert media by resolving the hydroxyl radical,” *Proc. Combust. Inst.*, vol. 35, no. 3, pp. 3381–3388, 2015.

-
- [297] R. Francisco Jr, F. Rua, M. Costa, R. Catapan, and A. Oliveira, “Combustion characteristics of gaseous fuels with low calorific value in a porous burner,” in Proceedings of the European Combustion Meeting, Citeseer, 2009.
- [298] C. Hackert, J. Ellzey, and O. Ezekoye, “Combustion and heat transfer in model two-dimensional porous burners,” Combust. Flame, vol. 116, no. 1-2, pp. 177–191, 1999.
- [299] P.-A. Masset, O. Dounia, and L. Selle, “Fully explicit formulae for flame speed in infinite and finite porous media,” Combust. Theory Model., pp. 1–28, 2021.
- [300] O. Colin and M. Rudgyard, “Development of high-order Taylor–Galerkin schemes for LES,” J. Comput. Phys., vol. 162, no. 2, pp. 338–371, 2000.
- [301] T. J. Poinso and S. K. Lele, “Boundary conditions for direct simulations of compressible viscous flows,” J. Comput. Phys., vol. 101, pp. 104–129, jul 1992.
- [302] E. Ranzi, A. Frassoldati, R. Grana, A. Cuoci, T. Faravelli, A. P. Kelley, and C. K. Law, “Hierarchical and comparative kinetic modeling of laminar flame speeds of hydrocarbon and oxygenated fuels,” Prog. Energ. Combust., vol. 38, no. 4, pp. 468–501, 2012.
- [303] Q. Cazères, P. Pepiot, E. Riber, and B. Cuenot, “A fully automatic procedure for the analytical reduction of chemical kinetics mechanisms for Computational Fluid Dynamics applications,” Fuel, 2021.
- [304] F. Duchaine, S. Jauré, D. Poitou, E. Quémerais, G. Staffelbach, T. Morel, and L. Gicquel, “Analysis of high performance conjugate heat transfer with the OpenPalm coupler,” Comput. Sci. Discov., vol. 8, no. 1, p. 015003, 2015.
- [305] V. Frayssé, L. Giraud, and S. Gratton, “A set of GMRES routines for real and complex arithmetic on high performance computers, CERFACS,” 2003.
- [306] F. Duchaine, N. Maheu, V. Moureau, G. Balarac, and S. Moreau, “Large-eddy simulation and conjugate heat transfer around a low-mach turbine blade,” J. Turbomach., vol. 136, no. 5, p. 051015, 2014.
- [307] P.-A. Masset, O. Dounia, and L. Selle, “Combustion regimes in inert porous media: From decoupled to hyperdiffusive flames,” Combust. Flame, vol. 241, p. 112052, 2022.
- [308] V. N. Kurdyumov, D. Fernández-Galisteo, and C. Jiménez, “Asymptotic study of premixed flames in inert porous media layers of finite width: Parametric analysis of heat recirculation phenomena,” Combust. Flame, vol. 241, p. 112109, 2022.
- [309] T. Howarth and A. Aspden, “An empirical characteristic scaling model for freely-propagating lean premixed hydrogen flames,” Combust. Flame, vol. 237, p. 111805, 2022.
- [310] G. V. Nivarti and R. S. Cant, “Stretch rate and displacement speed correlations for increasingly-turbulent premixed flames,” Flow Turbul. Combust., vol. 102, no. 4, pp. 957–971, 2019.
- [311] R. W. Schefer, W. D. Kulatilaka, B. D. Patterson, and T. B. Settersten, “Visible emission of hydrogen flames,” Combustion and flame, vol. 156, no. 6, pp. 1234–1241, 2009.
- [312] D. Trimis and K. Wawrzinek, “Flame stabilization of highly diffusive gas mixtures in porous inert media,” J Comput Appl Mech, vol. 5, no. 2, pp. 367–381, 2004.

- [313] S.-S. Su, S.-J. Hwang, and W.-H. Lai, “On a porous medium combustor for hydrogen flame stabilization and operation,” International journal of hydrogen energy, vol. 39, no. 36, pp. 21307–21316, 2014.
- [314] R. Roohi, M. H. Akbari, and S. Samghani, “Numerical simulation of hydrogen fueled porous burner,” Journal of Thermal Science and Technology, vol. 8, no. 3, pp. 555–570, 2013.
- [315] A. B. Caldeira and Ç. Susantez, “A simplified numerical approach to hydrogen and hydrocarbon combustion in single and double-layer porous burners,” International Journal of Hydrogen Energy, vol. 45, no. 60, pp. 35235–35245, 2020.
- [316] H. Nozari, G. Karaca, O. Tuncer, and A. Karabeyoglu, “Porous medium based burner for efficient and clean combustion of ammonia–hydrogen–air systems,” International journal of hydrogen energy, vol. 42, no. 21, pp. 14775–14785, 2017.
- [317] S. Gauthier, A. Nicolle, and D. Baillis, “Investigation of the flame structure and nitrogen oxides formation in lean porous premixed combustion of natural gas/hydrogen blends,” International journal of hydrogen energy, vol. 33, no. 18, pp. 4893–4905, 2008.
- [318] C. E. Arrieta, A. M. García, and A. A. Amell, “Experimental study of the combustion of natural gas and high-hydrogen content syngases in a radiant porous media burner,” International Journal of Hydrogen Energy, vol. 42, no. 17, pp. 12669–12680, 2017.
- [319] R. Huang, L. Cheng, K. Qiu, C. Zheng, and Z. Luo, “Low-calorific gas combustion in a two-layer porous burner,” Energy & Fuels, vol. 30, no. 2, pp. 1364–1374, 2016.
- [320] C.-j. Tseng, “Effects of hydrogen addition on methane combustion in a porous medium burner,” International Journal of Hydrogen Energy, vol. 27, no. 6, pp. 699–707, 2002.
- [321] H. Dai, B. Zhang, Z. Li, and J. Wu, “Combustion characteristics of a porous media burner with partial hydrogen injection,” International Journal of Hydrogen Energy, vol. 47, no. 2, pp. 1092–1102, 2022.
- [322] C. Clanet and G. Searby, “First experimental study of the darrieus-landau instability,” Physical review letters, vol. 80, no. 17, p. 3867, 1998.
- [323] P. Clavin and J. C. Graña-Otero, “Curved and stretched flames: the two markstein numbers,” Journal of fluid mechanics, vol. 686, pp. 187–217, 2011.
- [324] M. Matalon and B. J. Matkowsky, “Flames as gasdynamic discontinuities,” Journal of Fluid Mechanics, vol. 124, pp. 239–259, 1982.
- [325] G. I. Sivashinsky, “Nonlinear analysis of hydrodynamic instability in laminar flames—i. derivation of basic equations,” Acta astronautica, vol. 4, no. 11, pp. 1177–1206, 1977.
- [326] C. K. Law, G. Jomaas, and J. K. Bechtold, “Cellular instabilities of expanding hydrogen/propane spherical flames at elevated pressures: theory and experiment,” Proceedings of the combustion institute, vol. 30, no. 1, pp. 159–167, 2005.
- [327] E. Hu, Z. Huang, J. He, and H. Miao, “Experimental and numerical study on laminar burning velocities and flame instabilities of hydrogen–air mixtures at elevated pressures and temperatures,” international journal of hydrogen energy, vol. 34, no. 20, pp. 8741–8755, 2009.

-
- [328] C. E. Frouzakis, N. Fogla, A. G. Tomboulides, C. Altantzis, and M. Matalon, “Numerical study of unstable hydrogen/air flames: shape and propagation speed,” Proceedings of the combustion institute, vol. 35, no. 1, pp. 1087–1095, 2015.
- [329] C. Altantzis, C. E. Frouzakis, A. G. Tomboulides, S. G. Kerkemeier, and K. Boulouchos, “Detailed numerical simulations of intrinsically unstable two-dimensional planar lean premixed hydrogen/air flames,” Proceedings of the combustion institute, vol. 33, no. 1, pp. 1261–1268, 2011.
- [330] L. Berger, A. Attili, and H. Pitsch, “Intrinsic instabilities in premixed hydrogen flames: parametric variation of pressure, equivalence ratio, and temperature. part 2—non-linear regime and flame speed enhancement,” Combustion and Flame, p. 111936, 2022.
- [331] E. Jiaqiang, J. Ding, J. Chen, G. Liao, F. Zhang, and B. Luo, “Process in micro-combustion and energy conversion of micro power system: A review,” Energy Conversion and Management, vol. 246, p. 114664, 2021.
- [332] D. G. Norton and D. G. Vlachos, “Combustion characteristics and flame stability at the microscale: a cfd study of premixed methane/air mixtures,” Chemical engineering science, vol. 58, no. 21, pp. 4871–4882, 2003.
- [333] G. Pizza, C. E. Frouzakis, J. Mantzaras, A. G. Tomboulides, and K. Boulouchos, “Dynamics of premixed hydrogen/air flames in microchannels,” Combustion and Flame, vol. 152, no. 3, pp. 433–450, 2008.
- [334] S. E. Hosseini and M. A. Wahid, “Investigation of bluff-body micro-flameless combustion,” Energy conversion and management, vol. 88, pp. 120–128, 2014.
- [335] K. Maruta, T. Kataoka, N. I. Kim, S. Minaev, and R. Fursenko, “Characteristics of combustion in a narrow channel with a temperature gradient,” Proceedings of the combustion institute, vol. 30, no. 2, pp. 2429–2436, 2005.
- [336] A. Fan, S. Minaev, S. Kumar, W. Liu, and K. Maruta, “Regime diagrams and characteristics of flame patterns in radial microchannels with temperature gradients,” Combustion and flame, vol. 153, no. 3, pp. 479–489, 2008.
- [337] B. Xu and Y. Ju, “Experimental study of spinning combustion in a mesoscale divergent channel,” Proceedings of the Combustion Institute, vol. 31, no. 2, pp. 3285–3292, 2007.
- [338] X. Yang, W. Yang, S. Dong, and H. Tan, “Flame stability analysis of premixed hydrogen/air mixtures in a swirl micro-combustor,” Energy, vol. 209, p. 118495, 2020.
- [339] Q. Peng, Y. Wu, E. Jiaqiang, W. Yang, H. Xu, and Z. Li, “Combustion characteristics and thermal performance of premixed hydrogen-air in a two-rearward-step micro tube,” Applied Energy, vol. 242, pp. 424–438, 2019.
- [340] A. Tang, Y. Xu, C. Shan, J. Pan, and Y. Liu, “A comparative study on combustion characteristics of methane, propane and hydrogen fuels in a micro-combustor,” International journal of hydrogen energy, vol. 40, no. 46, pp. 16587–16596, 2015.
- [341] Y. Wang, Z. Zhou, W. Yang, J. Zhou, J. Liu, Z. Wang, and K. Cen, “Combustion of hydrogen-air in micro combustors with catalytic pt layer,” Energy Conversion and Management, vol. 51, no. 6, pp. 1127–1133, 2010.

- [342] A. Fan, J. Wan, Y. Liu, B. Pi, H. Yao, and W. Liu, "Effect of bluff body shape on the blow-off limit of hydrogen/air flame in a planar micro-combustor," Applied thermal engineering, vol. 62, no. 1, pp. 13–19, 2014.
- [343] A. Rahbari, S. Homayoonfar, E. Valizadeh, M. R. Aligoodarz, and D. Toghraie, "Effects of micro-combustor geometry and size on the heat transfer and combustion characteristics of premixed hydrogen/air flames," Energy, vol. 215, p. 119061, 2021.
- [344] W. Yang, C. Deng, J. Zhou, J. Liu, Y. Wang, and K. Cen, "Experimental and numerical investigations of hydrogen–air premixed combustion in a converging–diverging micro tube," International Journal of Hydrogen Energy, vol. 39, no. 7, pp. 3469–3476, 2014.
- [345] S. Cai, W. Yang, Y. Ding, Q. Zeng, and J. Wan, "Hydrogen-air premixed combustion in a novel micro disc-burner with an annular step," Fuel, vol. 313, p. 123015, 2022.
- [346] S. M. Lee, H. J. Jang, and N. I. Kim, "Premixed flame propagation of CH_4 and C_3H_8 in a narrow-gap disk burner using constant-volume processes at elevated-pressure," Combustion and Flame, vol. 231, p. 111482, 2021.
- [347] Z. He, Y. Yan, F. Xu, Z. Yang, H. Cui, Z. Wu, and L. Li, "Combustion characteristics and thermal enhancement of premixed hydrogen/air in micro combustor with pin fin arrays," International Journal of Hydrogen Energy, vol. 45, no. 7, pp. 5014–5027, 2020.
- [348] G. Pizza, C. E. Frouzakis, J. Mantzaras, A. G. Tomboulides, and K. Boulouchos, "Three-dimensional simulations of premixed hydrogen/air flames in microtubes," Journal of Fluid Mechanics, vol. 658, pp. 463–491, 2010.
- [349] V. Kurdyumov, E. Fernandez-Tarrazo, J.-M. Truffaut, J. Quinard, A. Wangher, and G. Searby, "Experimental and numerical study of premixed flame flashback," Proceedings of the Combustion Institute, vol. 31, no. 1, pp. 1275–1282, 2007.
- [350] A. Alipoor, K. Mazaheri, A. S. Pour, and Y. Mahmoudi, "Asymmetric hydrogen flame in a heated micro-channel: Role of darrieus–landau and thermal-diffusive instabilities," International Journal of Hydrogen Energy, vol. 41, no. 44, pp. 20407–20417, 2016.
- [351] G. Von Elbe and M. Mentser, "Further studies of the structure and stability of burner flames," The Journal of Chemical Physics, vol. 13, no. 2, pp. 89–100, 1945.
- [352] B. Lewis and G. von Elbe, "Stability and structure of burner flames," The Journal of Chemical Physics, vol. 11, no. 2, pp. 75–97, 1943.
- [353] F. H. Vance, L. de Goey, and J. A. van Oijen, "Development of a flashback correlation for burner-stabilized hydrogen-air premixed flames," Combustion and Flame, p. 112045, 2022.
- [354] D. G. Crowdy and C. C. Green, "Analytical solutions for von kármán streets of hollow vortices," Physics of Fluids, vol. 23, no. 12, p. 126602, 2011.
- [355] "2 - vibration induced by cross-flow," in Flow Induced Vibrations (S. Kaneko, T. Nakamura, F. Inada, and M. Kato, eds.), pp. 29–106, Elsevier.

